

Synthesis of Porous Carbons and Their Applications in Gas Uptake

Asma Madkhali

Thesis submitted to the University of Nottingham for the degree of Doctor of Philosophy

[2023]

Abstract

The need to mitigate the negative environmental impacts of fossil fuel usage and the growing scarcity of these fuels have motivated the exploration and implementation of alternative approaches for carbon dioxide reduction and energy storage. Porous materials have been identified as a viable solution among the various strategies available. Porous carbons have exhibited considerable potential for numerous applications in this domain. The present dissertation conducts an investigation into porous carbons, with a particular emphasis on different synthesis methods and material characterisation. Additionally, the study examines the potential of these materials in terms of energy storage and gas adsorption applications.

Using zeolites as templates for producing porous carbons is a hot topic as the resultant zeolite-templated carbons (ZTCs) have a high surface area along with a narrow pore size distribution compared to other porous carbons. However, the extensive use of acids to dissolve the template during the synthesis of ZTCs is a drawback. In this thesis, Chapter 3, a new approach was examined for dissolving the template (zeolite 13X). The results show a successful removal of the template without excessive use of acid. The methane storage using these carbons showed a superior capacity compared to some of the already existing benchmark materials.

Synthesising activated carbons from renewable, cheap biomass waste using two activating agents and different synthesis routes was examined in Chapter 4. In the approach, ginkgo leaves were converted into activated carbon for CO_2

mitigation applications. The effects of the hydrothermal carbonisation temperature, direct $K_2C_2O_4$-activation, and pre-washing of the char on the activated carbon porosities were examined. The high CO_2 uptake at atmospheric pressure (up to 5 mmol/g) made the samples promising candidates for post-combustion CO_2 capture applications.

The direct synthesis of heteroatom-doped activated carbons using a self-activating organic salt (potassium hydrogen phthalate) was examined in Chapters 5 and 6. Urea and boric acid were added during the carbonisation of the self-activating salt and led to nitrogen doping. The addition of only the urea to the carbonisation mixture of the salt boosted the surface area and porosity of the produced carbons and thus their CO_2 adsorption. On the other hand, the addition of boric acid to the salt-urea mixture had a negative effect on the porosity and the CO_2 uptake capacity.

Declaration

I hereby declare that this thesis is my original work and it has been written by me in its entirety, under the supervision of Professor Robert Mokaya. It has also not been submitted for any degree in any university previously.

Name: Asma Madkhali

Signature:

Date: 04/06/2023

- **Posters:**

Asma Madkhali and Robert Mokaya, Women in Chemistry Conference, University of Nottingham, **6th March 2020,** *Zeolite-templated carbons (ZTCs) for CH_4 storage*.

Asma Madkhali and Robert Mokaya, Dan Eley symposium, University of Nottingham, **17th May 2022**, *Simple preparation of N-doped Porous Carbons for CO_2 capture*.

Asma Madkhali and Robert Mokaya, 5th Annual UK Porous Materials Conference, University of Strathclyde, **13-14th June 2022**, *Conversion Ginkgo leaves to activated carbon.*

- **Presentations:**

Asma Madkhali and Robert Mokaya, the 2020 Materials Section 2nd Year PhD Colloquia, University of Nottingham, **2nd March 2020,** *Zeolite-templated carbon*.

Asma Madkhali and Robert Mokaya, the annual School PhD Symposium, University of Nottingham, **13-15th July 2022,** *Direct synthesis of N-doped porous carbons and their application in CO_2 capture*

Acknowledgement

First and foremost, I thank Allah for His great gratitude for completing this work.

I am grateful to the government of the Kingdom of Saudi Arabia and Jazan University for sponsoring my PhD studentship.

I would like to sincerely thank my supervisor, Professor Robert Mokaya, for his particular patience and for his supervision, guidance, and assistance during my PhD years.

I am grateful for the efforts of the technicians and store staff, without whose valuable advice and assistance, this work would not have been possible.

Special thanks to Mr. Neil Barnes and Mr. Mark Guyler.

Many thanks to Dr Tong Liu for elemental (CHN) analysis.

I thank Dr Stephen Argent, manager of the X-ray lab, B15.

Thanks to all former and current group members for their assistance and cooperation.

Words cannot express how grateful I am to my parents and siblings for everything they have given and endured.

For my family, always with my love and gratitude.

List of the Abbreviations and acronyms

BEA	Beta structured zeolites
BET	Brunauer–Emmett–Teller theory
BOC	British Oxygen Company
BCN	Boron and nitrogen co-doped carbon
C	Carbon
CH_4	Methane
CHN	carbon, hydrogen and nitrogen elemental content
CO	Carbon monoxide
CO_2	Carbon dioxide
DFT	Density functional theory
EDX	Energy dispersive x-ray
FA	Furfuryl alcohol
FAU	Faujasite zeolites
GL	Ginkgo leaves
H_2	Hydrogen
IUPAC	International Union of Pure and Applied Chemistry
K	Potassium
K_2CO_3	Potassium carbonate
K_2O	Potassium oxide
KHP	Potassium hydrogen phthalate
KOH	Potassium hydroxide
NL-DFT	Non local density functional theory
PSD	Pore size distribution
SEM	Scanning electron microscopy
TGA	Thermogravimetric analysis
XPS	X-ray photoelectron spectroscopy
XRD or PXRD	X-ray diffraction or powder X-ray diffraction
ZTC	Zeolite-templated carbon

Table of Contents

Abstract I

Declaration III

Acknowledgement V

List of the Abbreviations and acronyms VI

Table of Contents VII

Chapter 1 Introduction 1

Porous materials 1

Classification of porous materials 1

Porous carbons 4

Gas adsorption applications 15

References 18

Chapter 2 Characterisation techniques 25

1. Thermal analysis 25

2. Powder X-Ray Diffraction (PXRD) 26

3. Textural properties – N_2 physisorption 29

4. Elemental analysis (CHN analysis) 35

5. X-ray Photoelectron Spectroscopy (XPS) 37

6. Scanning Electron Microscopy (SEM) 38

7. Gases uptake measurements 40

References 41

Chapter 3 Alternative template removal method for zeolite templated carbons 43

1. Introduction 43

2. Experimental 45

2.1. Materials 46

2.2. Synthesis procedures for ZTC 46

2.3. Activation of carbon/zeolite composite 47

2.4. Characterisation 47

2.5. CH_4 uptake measurements 48

3. Results 48

3.1. Zeolite-templated carbons 50

3.1.1. X-ray diffraction 50

3.1.2. SEM analysis 52

3.2. Template removal 56

3.2.1. Thermal analysis 56
3.2.2. Carbon/Zeolite-composite reaction with KOH 57
3.2.3. Surface area and porosity 59
3.2.4. Methane uptake 62
4. Conclusion 13
Acknowledgment 14
5. References 14
Chapter 4 Synthesis and Characterisation of Porous Carbon from Biomass 17
Abstract 17
1. Introduction 17
2. Experimental 19
2.1. Synthesis procedures 19
2.2. Characterisation 22
2.3. CO_2 uptake measurements 22
3. Results 23
3.1. Carbons derived from ginkgo leaves hydrochar 24
3.2. Carbons derived from air-carbonised ginkgo leaves 29
3.3. An overview of the samples and the direct activation 35
3.4. CO_2 uptake 41
4. Summary 44
Acknowledgment 45
5. References 46
Chapter 5 N-doped porous carbon from organic salts via direct doping route and its application for CO_2 uptake 48
Abstract 48
1. Introduction 48
2. Experimental 51
2.1 Synthesis procedures 51
2.2 Characterization 52
3.2 CO_2 adsorption measurements 53
3. Results 54
3.1. Textural and morphology properties and chemical composition 54
3.2. Carbonisation temperature 69
3.3. Carbonisation/activation processes 76
4. Discussion 84
4.1. Effect of P:U ratio 85

4.2. CO_2 uptake 87
5. Conclusion 98
Acknowledgment 99
6. References 99
Chapter 6 Direct synthesis approach to porous BCN for CO_2 uptake 103
Abstract 103
1. Introduction 104
2. Experimental 105
2.1. Synthesis 105
2.2. Characterisation 107
3.2 CO_2 uptake measurements 108
3. Results 108
3.1. Nature, textural properties and chemical composition of carbons 108
3.2. CO_2 uptake 121
4. Conclusion 126
5. References 126
Chapter 7 Conclusion 130

Chapter 1 Introduction

Porous materials

The porous materials occurring in nature offer a wonderful visual illustration. Honeycomb, which is composed of multiple hexagonal cells, is an excellent example of a porous material. The honeycomb can be considered the 'host' while the honeybee is the 'guest'. Other examples of porous material found in nature are rocks, soil and biological tissues (e.g. bones, wood and sponges). A generally accepted definition of porous materials is those that contain pores (cavities, channels or interstices). The features of a porous material depend on the size, order and geometry of the pores, as well as its porosity (the ratio of the total pore volume to the apparent volume of the material) and its composition. These pores can be filled with fluids such as gas or liquid under different atmospheric conditions, making them useable for a wide range of applications.

Classification of porous materials

The International Union of Pure and Applied Chemistry (IUPAC)[1] (1985 and 2015) recommended classifying porous materials into three classes based on their pore size as shown in Figure 1-1: microporous materials (with pore diameters of < 2 nm), mesoporous materials (with pore diameters between 2 and 50 nm) and macroporous materials (with pore diameters > 50 nm). The microporous materials are divided into supermicroporous, with pores of width between 0.7 nm and 2nm, ultramicroporous, with pores of width between 0.4 nm and 0.7 nm, and submicroporous, with pores of < 0.4nm in width. The term

'nanopore' refers to all three of the aforementioned types of pores, with a maximum diameter of 100 nm.

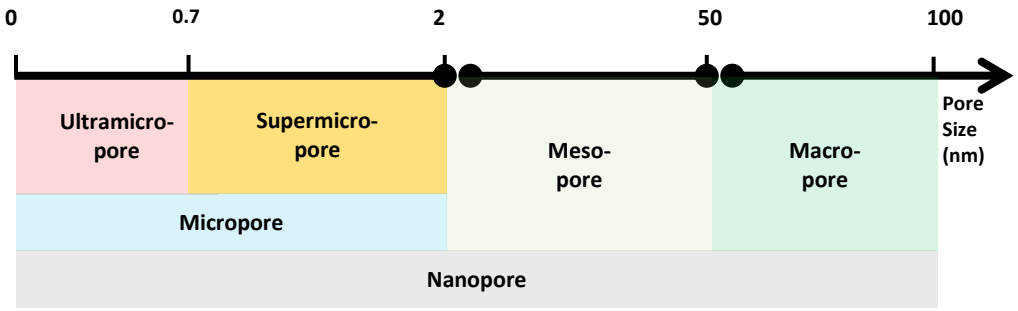


Figure 1-1 Schematic IUPAC pore classification, according to pore sizes

Therefore, these classifications, which were derived from the study of nitrogen (77 K) adsorption-desorption isotherms,[1, 2] at first appear rather arbitrary. Despite this, they continue to serve a purpose and are widely recognised for their validity. This classification was originally justified based on the critical diameter of the N_2 molecule (0.380 nm). The pore filling mechanism, which is characteristic of the micropore, is rapidly attained, due to the electrostatic force between the narrow pore walls.[3] The narrower pores would be about 0.7 nm to accommodate two layers of adsorbed N_2. Thus, 0.7 nm was considered by the IUPAC to be the maximum limit of the ultramicropore. The pores of sizes similar to the probe (N_2), which accommodate a monolayer, are considered to be the minimum pore sizes.[4]

Porous materials can either be classified as open or closed based on their permeability, i.e., fluids are able to enter, exit and move along through the network of pores extended in the material (Figure 1-2). However, all permeable

materials are also porous. In the case of materials with isolated or closed voids, the permeability could possibly be nil.[2]

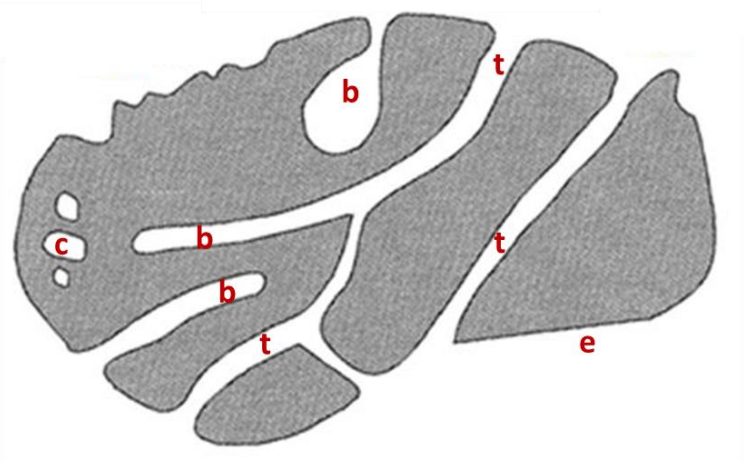


Figure 1-2 Schematic pore classification, according to their accessibility; c – closed pores, b – blind pores, t – transport or through pores and e – external surface.

Other pore classifications utilised by the IUPAC [2, 5] are based on pore geometry. The classification divides the pores based on the following geometrical shapes: cylinder, slit-shape, cone-shape and ink-bottle shape as depicted in Figure 1-3.

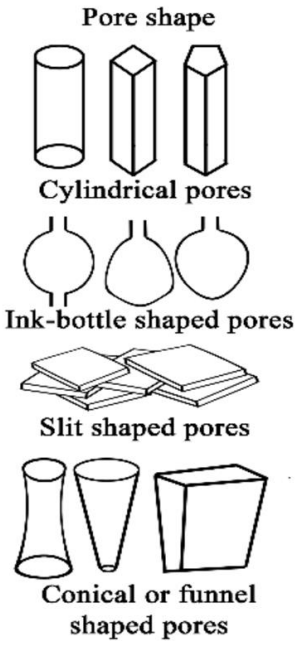


Figure 1-3 Schematic pore classification, according to their geometrical shape

Porous carbons

Carbon is one of the most abundant elements in the Universe and the nineteenth most abundant element on Earth's crust, forming a part of about 95% of all known chemical compounds.[6, 7] Carbon materials consist mainly of carbon atoms that are arranged to create different structures or forms. Graphite, graphene, carbon nanotubes, fullerenes and diamonds are all examples of such materials. Each form has unique structures, properties, applications and fabrication conditions.[8]

Since ancient times, carbon materials have been utilised in a variety of ways. Charcoal, for instance, is utilised as a generator for thermal energy and fires, and in the 1790s, was first used as adsorbent to decolourise sugar syrup in the English sugar industry. The graphite powder and soot are utilised for writing and artistic purposes. Activated carbon was primarily developed during World War I for use in air filters to remove poison gas.[9] All of the carbon materials are still undergoing adaptation and development for use in a variety of environmental, biomedical, electrochemical, electromagnetic and electronic applications.

Carbon materials containing pores of different sizes are referred to as porous carbons, which will be the focus of this thesis. Porous carbons are used for various applications, including purification, separation, electrochemical energy storage, gas storage and catalysis applications.[8] The versatility of porous carbons is due to characteristic properties such as high surface area, a wide range of pore sizes, inertness, inexpensive synthesis methods, good thermal and mechanical stabilities and hydrophobicity.[10] However, the potential employment of porous

carbons depends primarily on their textural properties, including surface area, pore size and pore volume. Microporous carbons, for example, are suitable for the adsorption of small molecules, while mesoporous carbons are suitable for electrochemical applications and for the separation of large molecules.

Synthesis methods of porous carbons

Activation and templating are the two fundamental methods for the synthesis of porous carbons.

1. Activation methods

Activation is the process of synthesising activated carbon through the partial oxidation of carbonaceous matter in order to generate pores.[8, 11, 12] Typically, certain substances (activating agents) react with carbonaceous precursors to remove a controlled number of carbon atoms, resulting in the formation of numerous internal pores in the *activated carbon*.

Activation the carbon is typically conducted by physical activation or chemical activation. In *physical activation*, the carbon source is subjected to oxidising gases (the activating agents) such as steam, ozone, carbon dioxide, or air at temperatures typically between 800 and 1000°C. These reactive oxidising gases are able to penetrate deeply into the bulk of the carbon source and gasify the carbon atoms, i.e. convert them to CO_2 and CO, with releasing other gases such as H_2O and CH_4, which ultimately leads to the opening and expansion of pores that were previously non-existent or inaccessible.[13, 14]

Another route by which the carbon can be activated is *chemical activation*. This involves prior mixing of the carbon source with an activating agent and heating the mixture, usually at high temperatures (600–1000°C) in an inert atmosphere. A variety of activating agents have been used for chemical activation. The activating agents could be acids, bases or salts;[12] for instance, nitric acid (HNO_3),[15] sulfuric acid (H_2SO_4),[16] hydrochloric acid (HCl),[17] phosphoric acid (H_3PO_4),[18] potassium hydroxide (KOH),[19] sodium hydroxide (NaOH),[20] hydrogen peroxide (H_2O_2),[21] zinc chloride ($ZnCl_2$),[22] and potassium carbonate (K_2CO_3)[23] may serve as activating agents.

Activated carbons prepared via chemical activation show superior surface area and pore volume, compared to those activated via physical activation. Moreover, chemical activation is more cost-effective as it requires lower activation temperatures, a shorter preparation time and higher carbon yield than physical activation.[18]

The most common and effective chemical activating agent is potassium hydroxide (KOH).[24] It has been widely used for commercial production of activated carbon since 1978, especially since the production of the well-known commercial activated carbons AX21 and Maxsorb.[19] KOH activation can produce activated carbons with a good micropore size distribution and a very high surface area of > 3000 m^2/g. The widely accepted activation mechanism of KOH is presented in the following chemical equations:[19]

$$6KOH + 2C \rightarrow 2K + 3H_2 + 2K_2CO_3 \text{ (1-1)}$$

$$K_2CO_3 \rightarrow K_2O + CO_2 \text{ (1-2)}$$

$$CO_2 + C \rightarrow 2CO \text{ (1-3)}$$

$$K_2CO_3 + 2C \rightarrow 2K + 3CO \text{ (1-4)}$$

$$C + K_2O \rightarrow 2K + CO \text{ (1-5)}$$

This mechanism involves the dissociation of KOH and formation of potassium carbonate at ≤ 400°C.[25] The pores are created during the activation, either chemically by oxidising the carbon via reduction of the as-prepared K-species or physically by gasifying the carbon atoms with the evolved CO_2 or other gases.

A more recent activation technique is *self-activation,* where the precursor itself contains the activating agent and can therefore generate activated type carbon during carbonisation without the need to add any other material. Such precursors offer simple and direct ways to produce activated carbons. For example, the metal cation in an organic salt can act as an activating agent when the organic salt has sufficient carbon content. To create activated carbon, metal organic salts containing a metal cation such as sodium, potassium, calcium, magnesium or zinc and a large organic component are used.[26-30] The carbonisation of potassium citrate, e.g. at 800°C, produces carbon with a high surface area of >2000 m^2/g without any additive and >3000 m^2/g with the addition of urea.[31] These surface areas comparable with those of carbons activated by conventional activators in traditional methods. Potassium hydrogen phthalate, another example of the self-activating precursor, when carbonised at 800 °C can produced activated carbon with a unimodal pore size distribution (average pore size 0.64 nm) and surface area >1200 m^2/g.[32,31]

Sometimes the carbon sources are subjected to treatments called *carbonisation* to concentrate the carbon content before the activation step. This carbonisation step involves the thermal decomposition of the starting material and the removal

of any other elements present. The remaining carbon atoms are then arranged to form carbon with varying stacking levels of graphite layers. The carbonisation process can be accomplished via the following techniques:

Pyrolysis under an inert atmosphere

Typically, in this method, the raw material is heated under an inert atmosphere at 600–900°C.[8]

Hydrothermal carbonisation

Hydrothermal and solvothermal reactions are usually performed in a sealed container or high-pressure autoclave under subcritical or supercritical solvent conditions. Hydrothermal and solvothermal reactions occur in solution, in contrast with the solid-state reactions, which depend on raw material diffusion at the interface.

The aqueous solution, which contains the dispersed carbonaceous raw material, is heated under autogenous pressure at temperatures ranging from 150 to 350°C during the hydrothermal carbonisation process.[8, 33-38]

Flash-air carbonisation

This is similar to pyrolysis, but involves low temperature thermal treatment in the presence of air for very short periods of time. In pyrolysis, the carbon source is decomposed by heat in the absence of oxygen and air to produce carbon-rich products (char), oils or liquids and gases.[39-41] On the other hand, in flash-air carbonisation, the raw material is heated in an inert atmosphere at temperatures ranging from 300 to 500°C, and then a flow of air is introduced for a few minutes before the inert flow is returned and the temperature is cooled in a quick carbonisation process.[42, 43]

There are other techniques to convert raw carbonaceous materials to carbon, e.g. heating with *microwave-assistance*.[44-47] However, overall, the carbonaceous structure and porosity of the final product are governed by the primary composition and the carbonisation conditions such as the temperature, rate of heating, duration time and carbonisation medium.

Chapter 4 in this dissertation explores an examination of the production of activated carbons by the use of two activating agents, namely potassium hydroxide (KOH) and potassium oxalate ($K_2C_2O_4$). The aim of this examination was to investigate various activation procedures for the preparation of activated carbons with different porosity levels benefiting from a biomass source, in particular "Ginkgo leaves."

2. The template method

Porous carbons can be produced without using activating agents via templating procedures wherein soft or hard templates may be used. Through these procedures, the generated carbon exhibits well-defined or uniform porosity.

In the soft templating process, the structure-directing agent (e.g. surfactants) and the carbon precursor are cooperatively assembled in solution. The templated-precursor finally undergoes polymerisation and carbonisation then, if necessary, the template is removed to leave behind a carbon framework with ordered spaces and pores. The soft templating procedure has been extensively used to prepare meso- and macro-porous carbons.[11, 48-50] For example, addition a controlled amount of Pluronic-F127 to a mixture of nanosized silica (solid template) and the thermosetting phenol resin (carbon source) improved dispersion of the silica, the hard template, and the surface area and pore volume of the produced carbon.[51] In another example, a meso/macroporous carbon nitride was prepared

with assistance of the surfactant (Pluronic-F127) in a facile procedures by mixing the carbon precursors with F127.[52]

On the other hand, in the hard templating process, a solid template with preferred porosity is chosen, and a suitable carbon precursor is then inserted into the template pores using chemical vapour deposition, liquid impregnation, or a mix of the two. The carbon precursor then undergoes polymerisation and carbonisation within the interconnected pores of the template before removal of the template to produce carbons that are an inverse mimic of the template. Many hard templates were used to produce micro, meso, and macroporous carbons, e.g., pillared clays, zeolites, silicas.[11, 53] Zeolites have been extensively explored as hard templates for producing well-controlled porous carbons. Zeolites are microporous materials that are used in a wide range of applications, including adsorption and catalysis. The crystal structure of zeolites is built up primarily by Si- and Al-tetrahedra species. Their structural formula is $M_{a/n}(AlO_2)_a(SiO_2)_b \cdot cH_2O$, where M is any alkali or alkaline earth atom that helps to balance the negative charge of the aluminium tetrahedron, n is the charge on that atom, c is the number of water molecules per unit cell, and a and b are the numbers of Al and Si tetrahedra, respectively, per unit cell. The tetrahedrons, SiO_4^{4-} and AlO_4^{5-}, are interlinked to form 3-, 4-, 5- and 6-member rings that extend the cages and channels of zeolite framework (**Error! Reference source not found.**). The differences in the b/a value, i.e. the Si/Al ratio, create variety in zeolite pore sizes and their properties. Faujasite (FAU-type) zeolites, for example, which are used in this research, are commonly used in different industrial applications due to their relatively large pores compared to other zeolites. The Si/Al ratio of FAU zeolites ranges between 1.2 and 2.6, enabling the construction of large cages

(supercages, size ~1.3 nm), beside the smaller cages (sodalite cages, size ~0.73 nm).[9, 54]

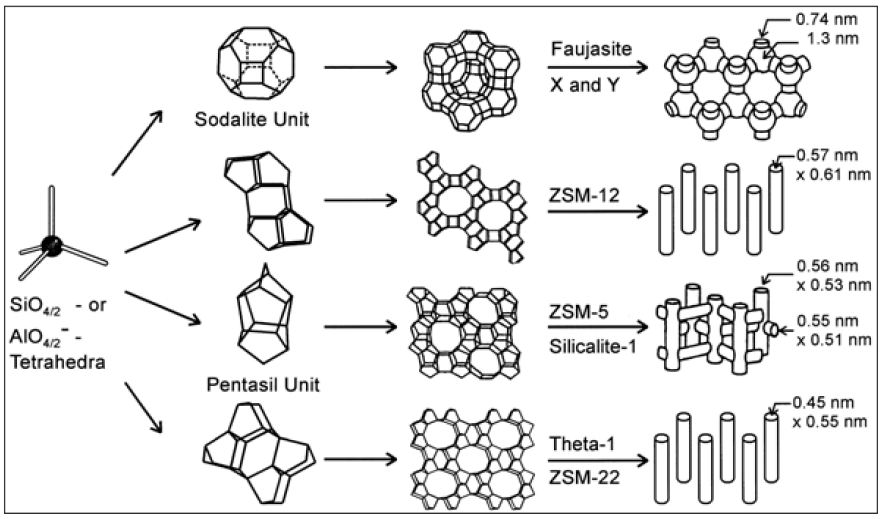


Figure 1-4 Development of four types of zeolite structures, copyright[54]

Zeolite-templated carbon

Zeolite-templated carbon (ZTC) is a type of ordered carbon resulting from the carbon replication of zeolite pores.[11, 53] The controlled synthesis conditions of ZTC generate a large surface area and narrow micropore size distributions. Besides the high surface area, the flexibility in tailoring pore volumes and particle sizes or shapes by choosing a suitable zeolite template makes ZTC a good candidate for a variety of applications.[11, 53, 55]

Structure of ZTCs

Despite the complexity of ZTC structure and the absence of ZTC crystallinity (with respect to the carbon), like most carbon forms except graphite and diamond, various models have been proposed to describe their structure. The ideal, hypothesised structure of ZTC consists of connected, opened and curved

3D graphene sheets, see Figure 1-5.[53] Nonetheless, the presence of polycyclic compounds that maintain the curvature of the ZTC framework (especially pentagonal, hexagonal, heptagonal and octagonal rings) has been theoretically confirmed.[57] There was no presence of carbon sp^3 confirmed in the ZTC framework.[56]

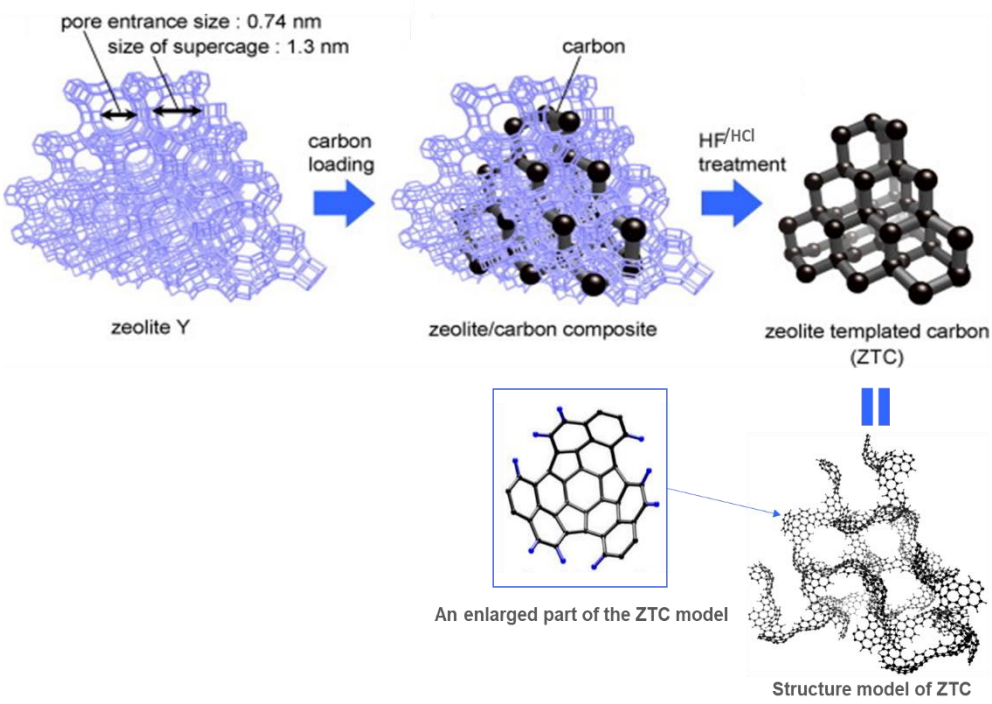


Figure 1-5 A diagram of ZTC synthesis, reprinted [56]

Synthesis of ZTCs

Since more than 200 types of zeolite frameworks have been registered to date (in the International Zeolite Association's database, IZA), it is crucial to select zeolite templates with suitable pore-entrance size and pore-connectivity dimensions in order to produce the targeted, well-defined ZTC. The ideal porous carbon will just invert the porosity of the template zeolite. According to the regularity of the zeolite pores, carbons replicated from zeolites should have a

narrow pore size distribution. The ordering of the liberated carbons from different zeolites is confirmed by the TEM and XRD patterns.[58-60] Furthermore, as an example, the templated carbon from zeolite 13X, which has a main pore size of 1.3 nm, showed good agreement with the porosity of the template. This ZTC showed a narrow PSD with a large peak at the pore size less than 1.3 nm, at about 1 nm.[61]

In terms of steps in preparation, ZTCs are made by filling the zeolite's porous framework with a carbon precursor to adopt its reverse structure. To fill the carbon precursor into the zeolite, two methods may be used: chemical vapour deposition,[62, 63] liquid impregnation, or a combination of the two.[61, 64] After that, carbonisation is performed and, in the final step, the zeolite template is dissolved using suitable acids or bases.

Chapter 3 of this thesis investigates a sustainable approach to modify the synthesis procedures of zeolite-templated carbons. The aim is to reduce or avoid the use of highly corrosive acids.

Doping of porous carbons

Doping is the method by which dopant elements can be inserted into the main material's framework. Doping carbon with heteroatoms is a method for tailoring the different properties of carbon materials, including their electroactivity, wettability, adsorption capacity, and physical and chemical stability. Therefore, heteroatom-doped carbons were utilised in energy-related applications including fuel cells, batteries, hydrogen storage, and supercapacitors.[65] Nitrogen, oxygen, sulfur, boron, and phosphorus are examples of dopants in the carbon framework.[65, 66] Typically, carbon doping is achieved by post-modification and

in-situ doping. The post-treatment method involves modifying activated carbon with heteroatom-containing precursors at a higher temperature. In-situ doping, also referred to as "direct doping," is the process of adding the dopant directly to the carbon precursor during the carbon's production processes.[67, 68]

Nitrogen is the most extensively studied dopant, and the incorporation of nitrogen heteroatoms into carbon frameworks is a successful approach to enhancing the gravimetric and volumetric performances of carbon-based supercapacitors and the hydrogen or CO_2 storage capacities of carbon materials.[66, 69] Since potassium-based salts are the most common activating agents, in order to synthesise porous N-doped carbons, there were many published papers that studied the potassium activation mechanism of nitrogen-based carbon sources.[31, 67, 70, 71] The general activation mechanism can be reduced to the following main equation:

$$K_2CO_3 + C\text{–}N \rightarrow KOCN + {-}CO_2K \quad (1\text{-}6)$$

$${-}CO_2K + C\text{–}N \rightarrow KOCN + CO \quad (1\text{-}7)$$

$$KOCN + C \rightarrow KCN + CO \quad (1\text{-}8)$$

Chapter 5 in this thesis was aimed at studying and examining the synthesis of straightforward N-doped porous carbons starting from a potassium-organic salt, potassium hydrogen phthalate, and urea. The influence of the elemental ratios N to K and N to C on the development of the N-doped carbon's porosity was investigated. Then, in Chapter 6, adding boric acid to the straightforward synthesis mixture of N-doped carbon (potassium hydrogen phthalate and urea) was examined to further investigate the effects of N:K and N:C ratios on the porosity of N-doped carbon and to produce N- and B-codoped carbons.

Gas adsorption applications

The adsorption of molecules on porous solid adsorbents is employed in a number of applications such as gas separation and gas storage. The adsorption of gases onto the surfaces of solid sorbents can either be accomplished via physical or chemical interactions. Table 1-1 summarises the differences between the two adsorption regimes. Physical adsorption is controlled by the interaction (Van der Waals force) between the adsorbent and the adsorbate (the gas molecules), while chemical adsorption is ocassioned by chemical bonding. However, the primary distinctions between physical and chemical adsorption are reversibility and adsorption heat.

Table 1-1 The differences between physical and chemical adsorption. [72]

Property	**Physical adsorption**	**Chemical adsorption**
Force of adsorption	Van der Waals	Chemical bond
Heat of adsorption	Low (< 40kJ/mole)	High (40-400kJ/mole)
Selectivity	Not selective	Selective
Reversibility	Reversible	Irreversible
Adsorption rate	Quick, no activation energy	Slow, requires activation energy
Adsorption layer	Monolayer or multilayer	Monolayer
Pressure for monolayer	$P/P_0 \approx 0.1$	$P/P_0 \ll 0.1$
Temperature	Near or below boiling point	Much higher than boiling point

Significant roles are played by gases in a variety of aspects of our daily lives. The majority of the air's components (atmospheric gases) are nitrogen (78.08%) and oxygen (20.95%). Additionally, air contains trace amounts of helium, neon,

methane, krypton, xenon, hydrogen and ozone, as well as argon (0.93%) and carbon dioxide (0.03%). Human activities have led to a growth in the levels of what are called "greenhouse gases". Major greenhouse gases include: CO_2, CH_4, N_2O and industrial gases: HFCs (hydrofluorocarbons), PFCs (perfluorocarbons), and SFs (Sulfur hexafluorides). CO_2, CH_4 and nitrogen oxides (NOx) are by-products of the incomplete combustion of fossil fuels (coal, oil, diesel and natural gas). Such an increase in these gases' concentrations contributed to the global warming issue.[73, 74]

In order to mitigate climate change and meet the growing global demand for energy, the transition toward the usage of renewable energy sources for energy production methods has become a necessity. The utilisation of greener fuels such as hydrogen, methane and biofuels as alternatives to fossil fuels is an essential step that can be taken besides the direct capture of the carbon emissions from the different emission sources.[75, 76]

For the capture, storage, or separation of GHG, a variety of solid adsorbents have been studied and applied commercially. Porous carbon adsorbents are preferred for these applications over other well-known adsorbents like zeolites and innovative adsorbents like metal organic frameworks (MOF) or covalent organic frameworks (COF) due to their distinct properties. These properties of porous carbons include chemical inertness, low atomic weight, moderate to high powder packing density, and stability under various working conditions.[77]

Carbon dioxide is a major component of the gaseous effluent produced by a variety of industrial processes, with power plants that depend on fossil fuels being the largest contributor (40% of CO_2). Physical adsorption of CO_2 onto porous materials is attractive mode of reducing such emissions and can be more

effective compared to existing commercial CO_2 separation techniques such as amine or water scrubbing. Physical adsorption has low energy requirements, is cost-effective, does not require extra water or chemicals and can be scaled to a wide range of temperature and pressure conditions. On the other hand, the amine-based commercial methods have a lot of challenges, like the generation of unwanted by-products, high energy regeneration of the absorber due to the chemical nature of the adsorption process, high corrosion (due to the nature of the amine absorbers) and low cost efficiency.[78]

Methane may be used as a cleaner energy source as it burns more cleanly and produces less CO_2 compared to other fossil fuels such as coal. The main human-made sources of methane are believed to be the production of livestock, natural gas extraction and transportation operations, landfill emissions and coal mining.[79]

For methane to be useful as a fuel, it must first be separated from other gases, purified and then stored using an efficient and effective method. For commercial uses, compressed natural gas (CNG) and liquefied natural gas (LNG), which consist mainly of methane are already being used. However, CNG faces a variety of challenges, including the need for high-pressure containers that can accommodate the necessary high storage pressure (200–300 bar) for an extended duration. On the other hand, for LNG, the need to maintain a -161°C temperature necessitates the requirement of specialised equipment. An alternative to CNG and LNG is adsorbed natural gas (ANG). In ANG, the natural gas is adsorbed on the surface of a porous material at a significantly lower pressure compared to CNG and storage can occur at much higher temperature than for LNG.[80-83] Numerous studies have examined and evaluated a wide range of adsorbents for

methane storage, including activated carbons,[43, 84-88] carbon fibers,[89] metal-organic frameworks (MOFs),[90-92] silica,[93, 94] and zeolites.[95, 96] Porous carbons are among the most effective methane storage materials due to their high porosity, high specific surface area and good chemical and thermal stability.

Effective methane storage is attractive as it goes beyond the simple use of natural gas to include renewable sources of methane via upgrading biogas to biomethane. Such upgrading involves separating the methane, which accounts for 40–70% of biogas, from the carbon dioxide, which accounts for 25–60%.[97-99] Porous carbons[100-103] and other porous materials, including zeolites,[104, 105] and metal organic frameworks (MOFs), may be used in the CH_4/CO_2 separation.[106, 107]

The motivation for this thesis arose from the harmful environmental impacts caused by fossil fuel-derived energy, which prompted the fabrication of porous materials for applications in energy storage and carbon dioxide mitigation. The thesis examined the possible uses of porous carbons in terms of energy storage and gas adsorption applications.

The methane storage capacities of the synthesised carbons and zeolite templated carbons (ZTC) were investigated in the third chapter of this thesis. The fourth chapter investigated the use of synthesised activated carbons derived from renewable biomass waste, called Ginkgo leaves, for the aim of CO_2 capture. The doped porous carbons prepared in chapters 5 and 6 were evaluated in terms of CO_2 capture and uptake capacity in comparison to conventional adsorbents.

References

1. M. Thommes, K. Kaneko, A. V. Neimark, J. P. Olivier, F. Rodriguez-Reinoso, J. Rouquerol and K. S. Sing, *Pure and applied chemistry*, 2015, **87**, 1051-1069.
2. B. D. Zdravkov, J. J. Čermák, M. Šefara and J. Janků, *Central European Journal of Chemistry*, 2007, **5**, 385-395.
3. S. Lowell, J. E. Shields, M. A. Thomas and M. Thommes, *Characterization of porous solids and powders: surface area, pore size and density*, Springer Science & Business Media, 2006.
4. M. G. Brown and D. A. Cadenhead, *Journal of Colloid and Interface Science*, 1979, **70**, 139-146.
5. K. Kaneko, *Journal of membrane science*, 1994, **96**, 59-89.
6. Encyclopædia.Britannica, carbon, https://www.britannica.com/science/carbon-chemical-element, (accessed May 10, 2023).
7. P. Nissen, Y. Chen, L. Carigi, W. Schuster and G. Zhao, *Astronomy & Astrophysics*, 2014, **568**, A25.
8. M. Inagaki and F. Kang, in *Materials Science and Engineering of Carbon: Fundamentals (2nd Edition)*, Elsevier, 2014.
9. R. T. Yang, *Adsorbents: Fundamentals and Applications*, Wiley, US, 2003.
10. M. Inagaki, F. Kang, M. Toyoda and H. Konno, in *Advanced Materials Science and Engineering of Carbon*, Elsevier.
11. Y. Xia, Z. Yang and R. Mokaya, *Nanoscale*, 2010, **2**, 639-659.
12. S. M. Manocha, *Sadhana*, 2003, **28**, 335-348.
13. B. Sajjadi, W.-Y. Chen and N. O. Egiebor, *Reviews in Chemical Engineering*, 2019, **35**, 735-776.
14. G. B. Lee, J. E. Park, S. Y. Hwang, J. H. Kim, S. Kim, H. Kim and B. U. Hong, *Carbon Letters*, 2019, **29**, 263-272.
15. P. Vinke, M. van der Eijk, M. Verbree, A. F. Voskamp and H. van Bekkum, *Carbon*, 1994, **32**, 675-686.
16. S. Karagöz, T. Tay, S. Ucar and M. Erdem, *Bioresource Technology*, 2008, **99**, 6214-6222.
17. P. Álvarez, C. Blanco and M. Granda, *Journal of Hazardous Materials*, 2007, **144**, 400-405.
18. Z. Heidarinejad, M. H. Dehghani, M. Heidari, G. Javedan, I. Ali and M. Sillanpää, *Environmental Chemistry Letters*, 2020, **18**, 393-415.
19. J. Wang and S. Kaskel, *Journal of Materials Chemistry*, 2012, **22**, 23710-23725.
20. S. Zheng, J. Zhang, H. Deng, Y. Du and X. Shi, *Journal of Bioresources and Bioproducts*, 2021, **6**, 142-151.

21. Y.-J. Heo and S.-J. Park, *Green Chemistry*, 2018, **20**, 5224-5234.
22. L. Li, F. Sun, J. Gao, L. Wang, X. Pi and G. Zhao, *RSC Advances*, 2018, **8**, 14488-14499.
23. A. F. Abbas and M. J. Ahmed, *Journal of Water Process Engineering*, 2016, **9**, 201-207.
24. M. Sevilla, N. Díez and A. B. Fuertes, *ChemSusChem*, 2021, **14**, 94-117.
25. N. C. f. B. Information, PubChem Compound Summary for CID 14797, Potassium Hydroxide, https://pubchem.ncbi.nlm.nih.gov/compound/Potassium-Hydroxide, (accessed December 1, 2022).
26. M. Sevilla and A. B. Fuertes, *Journal of Materials Chemistry A*, 2013, **1**, 13738-13741.
27. M. Sevilla and A. B. Fuertes, *ACS Nano*, 2014, **8**, 5069-5078.
28. T. Tsumura, A. Arikawa, T. Kinumoto, Y. Arai, T. Morishita, H. Orikasa, M. Inagaki and M. Toyoda, *Materials Chemistry and Physics*, 2014, **147**, 1175-1182.
29. G. A. Ferrero, M. Sevilla and A. B. Fuertes, *Carbon*, 2015, **88**, 239-251.
30. L. Tong, L.-L. Zhang, Y.-C. Wang, L.-Y. Wan, Q.-Q. Yan, C. Hua, C.-J. Jiao, Z.-Y. Zhou, Y.-W. Ding, B. Liu and H.-W. Liang, *ACS Applied Materials & Interfaces*, 2020, **12**, 25211-25220.
31. M. Sevilla, G. A. Ferrero, N. Diez and A. B. Fuertes, *Carbon*, 2018, **131**, 193-200.
32. B. Adeniran, E. Masika and R. Mokaya, *Journal of Materials Chemistry A*, 2014, **2**, 14696-14710.
33. S. Masoumi, V. B. Borugadda, S. Nanda and A. K. Dalai, *Catalysts*, 2021, **11**, 939.
34. W. Sangchoom and R. Mokaya, *ACS Sustainable Chemistry & Engineering*, 2015, **3**, 1658-1667.
35. A. Jain, R. Balasubramanian and M. P. Srinivasan, *Chemical Engineering Journal*, 2016, **283**, 789-805.
36. S. A. Nicolae, H. Au, P. Modugno, H. Luo, A. E. Szego, M. Qiao, L. Li, W. Yin, H. J. Heeres, N. Berge and M.-M. Titirici, *Green Chemistry*, 2020, **22**, 4747-4800.
37. J. A. Libra, K. S. Ro, C. Kammann, A. Funke, N. D. Berge, Y. Neubauer, M.-M. Titirici, C. Fühner, O. Bens and J. Kern, *Biofuels*, 2011, **2**, 71-106.
38. M.-M. Titirici and M. Antonietti, *Chemical Society Reviews*, 2010, **39**, 103-116.

39. S. Wang, G. Dai, H. Yang and Z. Luo, *Progress in Energy and Combustion Science*, 2017, **62**, 33-86.
40. A. Demirbas and G. Arin, *Energy sources*, 2002, **24**, 471-482.
41. M. Fang, D. Shen, Y. Li, C. Yu, Z. Luo and K. Cen, *Journal of analytical and applied pyrolysis*, 2006, **77**, 22-27.
42. E. A. Hirst, A. Taylor and R. Mokaya, *Journal of Materials Chemistry A*, 2018, **6**, 12393-12403.
43. A. Altwala and R. Mokaya, *Energy & Environmental Science*, 2020, **13**, 2967-2978.
44. J. Tan, H. Chen, Y. Gao and H. Li, *Electrochimica Acta*, 2015, **178**, 144-152.
45. H. Mao, D. Zhou, Z. Hashisho, S. Wang, H. Chen, H. Wang and M. J. Lashaki, *RSC Advances*, 2015, **5**, 36051-36058.
46. H. Xiao, H. Peng, S. Deng, X. Yang, Y. Zhang and Y. Li, *Bioresource Technology*, 2012, **111**, 127-133.
47. M. Selvam S and B. Paramasivan, *Chemosphere*, 2022, **286**, 131631.
48. C. Liang, Z. Li and S. Dai, *Angewandte Chemie International Edition*, 2008, **47**, 3696-3717.
49. B. Szczęśniak, J. Phuriragpitikhon, J. Choma and M. Jaroniec, *Journal of Materials Chemistry A*, 2020, **8**, 18464-18491.
50. H. Wang, Y. Shao, S. Mei, Y. Lu, M. Zhang, J.-k. Sun, K. Matyjaszewski, M. Antonietti and J. Yuan, *Chemical Reviews*, 2020, **120**, 9363-9419.
51. Z. Tang, Y. Song, Y. Tian, L. Liu and Q. Guo, *Microporous and Mesoporous Materials*, 2008, **111**, 48-54.
52. M. Peer, M. Lusardi and K. F. Jensen, *Chemistry of Materials*, 2017, **29**, 1496-1506.
53. H. Nishihara and T. Kyotani, *Chemical Communications*, 2018, **54**, 5648-5673.
54. J. Weitkamp, *Solid State Ionics*, 2000, **131**, 175-188.
55. S. Choi, M. A. Alkhabbaz, Y. Wang, R. M. Othman and M. Choi, *Carbon*, 2019, **141**, 143-153.
56. H. Nishihara, Q. H. Yang, P. X. Hou, M. Unno, S. Yamauchi, R. Saito, J. I. Paredes, A. Martínez-Alonso, J. M. D. Tascón, Y. Sato, M. Terauchi and T. Kyotani, *Carbon*, 2009, **47**, 1220-1230.
57. H. Nishihara, H. Fujimoto, H. Itoi, K. Nomura, H. Tanaka, M. T. Miyahara, P. A. Bonnaud, R. Miura, A. Suzuki, N. Miyamoto, N. Hatakeyama, A. Miyamoto, K. Ikeda, T. Otomo and T. Kyotani, *Carbon*, 2018, **129**, 854-862.
58. K. Kim, T. Lee, Y. Kwon, Y. Seo, J. Song, J. K. Park, H. Lee, J. Y. Park, H. Ihee, S. J. Cho and R. Ryoo, *Nature*, 2016, **535**, 131-135.

59. N. Balahmar, A. M. Lowbridge and R. Mokaya, *Journal of Materials Chemistry A*, 2016, **4**, 14254–14266.
60. Z. Ma, T. Kyotani, Z. Liu, O. Terasaki and A. Tomita, *Chemistry of Materials*, 2001, **13**, 4413-4415.
61. E. Masika and R. Mokaya, *Energy & Environmental Science*, 2014, **7**, 427-434.
62. Z. Yang, Y. Xia, X. Sun and R. Mokaya, *The Journal of Physical Chemistry B*, 2006, **110**, 18424-18431.
63. Z. Yang, Y. Xia and R. Mokaya, *Journal of the American Chemical Society*, 2007, **129**, 1673-1679.
64. N. Alam and R. Mokaya, *Energy & Environmental Science*, 2010, **3**, 1773-1781.
65. J. P. Paraknowitsch and A. Thomas, *Energy & Environmental Science*, 2013, **6**, 2839-2855.
66. S. Ghosh, S. Barg, S. M. Jeong and K. Ostrikov, *Advanced Energy Materials*, 2020, **10**, 2001239.
67. N. A. Rashidi and S. Yusup, *Journal of Energy Storage*, 2020, **32**, 101757.
68. H. Itoi, H. Nishihara and T. Kyotani, *Langmuir*, 2016, **32**, 11997-12004.
69. M. Sevilla and R. Mokaya, *Energy & Environmental Science*, 2014, **7**, 1250-1280.
70. N. Tsubouchi, M. Nishio and Y. Mochizuki, *Applied Surface Science*, 2016, **371**, 301-306.
71. J. E. Eichler, J. N. Burrow, Y. Wang, D. C. Calabro and C. B. Mullins, *Carbon*, 2022, **186**, 711-723.
72. Q. Chang, in *Colloid and Interface Chemistry for Water Quality Control*, ed. Q. Chang, Academic Press, 2016, DOI: https://doi.org/10.1016/B978-0-12-809315-3.00010-4, pp. 175-225.
73. D. Peredo-Mancilla, I. Ghouma, C. Hort, D. Bessieres and C. M. Ghimbeu, in *Char and Carbon Materials Derived from Biomass*, eds. M. Jeguirim and L. Limousy, Elsevier, 2019, DOI: https://doi.org/10.1016/B978-0-12-814893-8.00009-2, pp. 341-382.
74. D. Martin, H. McKenna and V. Livina, *The Journal of Physiological Sciences*, 2017, **67**, 97-106.
75. A. Kovač, M. Paranos and D. Marciuš, *International Journal of Hydrogen Energy*, 2021, **46**, 10016-10035.
76. V. Smil, *Natural gas: fuel for the 21st century*, John Wiley & Sons, 2015.
77. J. P. Marco-Lozar, M. Kunowsky, F. Suárez-García, J. D. Carruthers and A. Linares-Solano, *Energy & Environmental Science*, 2012, **5**, 9833-9842.

78. R. Ben-Mansour, M. A. Habib, O. E. Bamidele, M. Basha, N. A. A. Qasem, A. Peedikakkal, T. Laoui and M. Ali, *Applied Energy*, 2016, **161**, 225-255.
79. A. Alonso, J. Moral-Vico, A. Abo Markeb, M. Busquets-Fité, D. Komilis, V. Puntes, A. Sánchez and X. Font, *Science of The Total Environment*, 2017, **595**, 51-62.
80. D. Lozano-Castelló, J. Alcañiz-Monge, M. A. de la Casa-Lillo, D. Cazorla-Amorós and A. Linares-Solano, *Fuel*, 2002, **81**, 1777-1803.
81. P.-S. Choi, J.-M. Jeong, Y.-K. Choi, M.-S. Kim, G.-J. Shin and S.-J. Park, *Carbon letters*, 2016, **17**, 18-28.
82. K. V. Kumar, K. Preuss, M.-M. Titirici and F. Rodríguez-Reinoso, *Chemical Reviews*, 2017, **117**, 1796-1825.
83. DOE MOVE program, https://arpa-e-foa.energy.gov/).
84. D. Lozano-Castelló, D. Cazorla-Amorós and A. Linares-Solano, *Energy & Fuels*, 2002, **16**, 1321-1328.
85. M. E. Casco, M. Martínez-Escandell, K. Kaneko, J. Silvestre-Albero and F. Rodríguez-Reinoso, *Carbon*, 2015, **93**, 11-21.
86. J. Romanos, S. A. Dargham, M. Prosniewski, R. Roukos, F. Barakat and P. Pfeifer, *ACS Omega*, 2018, **3**, 15119-15124.
87. A. Altwala and R. Mokaya, *Journal of Materials Chemistry A*, 2022, DOI: 10.1039/D2TA00421F.
88. I. Alali and R. Mokaya, *Energy & Environmental Science*, 2022, **15**, 4710-4724.
89. N. F. Attia, M. Jung, J. Park, H. Jang, K. Lee and H. Oh, *Chemical Engineering Journal*, 2020, **379**, 122367.
90. M. Chang, T. Yan, Y. Wei, J.-X. Wang, D. Liu and J.-F. Chen, *ACS Applied Materials & Interfaces*, 2022, **14**, 25374-25384.
91. Y.-R. Lee, S.-M. Cho and W.-S. Ahn, *Korean Journal of Chemical Engineering*, 2018, **35**, 1542-1546.
92. I. Spanopoulos, C. Tsangarakis, E. Klontzas, E. Tylianakis, G. Froudakis, K. Adil, Y. Belmabkhout, M. Eddaoudi and P. N. Trikalitis, *Journal of the American Chemical Society*, 2016, **138**, 1568-1574.
93. S. Mohammed, A. K. Sunkara, C. E. Walike and G. Gadikota, *Frontiers in Climate*, 2021, **3**, 713708.
94. A.-M. Putz, A. Policicchio, S. Stelitano, P. Sfîrloagă, C. Ianăşi, R. G. Agostino and S. Cecilia, *Fullerenes, Nanotubes and Carbon Nanostructures*, 2018, **26**, 810-819.

95. S. Wang, P. Bai, Y. Wei, W. Liu, X. Ren, J. Bai, Z. Lu, W. Yan and J. Yu, *ACS Applied Materials & Interfaces*, 2019, **11**, 38955-38963.
96. H. G. T. Nguyen, C. M. Sims, B. Toman, J. Horn, R. D. van Zee, M. Thommes, R. Ahmad, J. F. M. Denayer, G. V. Baron, E. Napolitano, M. Bielewski, E. Mangano, S. Brandani, D. P. Broom, M. J. Benham, A. Dailly, F. Dreisbach, S. Edubilli, S. Gumma, J. Möllmer, M. Lange, M. Tian, T. J. Mays, T. Shigeoka, S. Yamakita, M. Hakuman, Y. Nakada, K. Nakai, J. Hwang, R. Pini, H. Jiang, A. D. Ebner, M. A. Nicholson, J. A. Ritter, J. Farrando-Pérez, C. Cuadrado-Collados, J. Silvestre-Albero, C. Tampaxis, T. Steriotis, D. Řimnáčová, M. Švábová, M. Vorokhta, H. Wang, E. Bovens, N. Heymans and G. De Weireld, *Adsorption*, 2020, **26**, 1253-1266.
97. L. A. Pellegrini, G. De Guido and S. Langé, *Renewable Energy*, 2018, **124**, 75-83.
98. M. R. Tabassum, A. Xia and J. D. Murphy, *Energy Conversion and Management*, 2018, **174**, 855-862.
99. R. Augelletti, M. Conti and M. C. Annesini, *Journal of Cleaner Production*, 2017, **140**, 1390-1398.
100. D. Saha, K. Nelson, J. Chen, Y. Lu and S. Ozcan, *Journal of Chemical & Engineering Data*, 2015, **60**, 2636-2645.
101. N. Álvarez-Gutiérrez, M. V. Gil, F. Rubiera and C. Pevida, *Fuel Processing Technology*, 2016, **142**, 361-369.
102. D.-J. Seo, Z. Gou, H. Fujita, T. Fujii and A. Sakoda, *Renewable Energy*, 2016, **86**, 693-702.
103. S. Cavenati, C. A. Grande and A. E. Rodrigues, *Energy & Fuels*, 2005, **19**, 2545-2555.
104. A. Alonso-Vicario, J. R. Ochoa-Gómez, S. Gil-Río, O. Gómez-Jiménez-Aberasturi, C. A. Ramírez-López, J. Torrecilla-Soria and A. Domínguez, *Microporous and Mesoporous Materials*, 2010, **134**, 100-107.
105. Z. Bacsik, O. Cheung, P. Vasiliev and N. Hedin, *Applied Energy*, 2016, **162**, 613-621.
106. F. A. Kloutse, A. Hourri, S. Natarajan, P. Benard and R. Chahine, *Separation and Purification Technology*, 2018, **197**, 228-236.
107. R. Zacharia, L. F. Gomez, R. Chahine, D. Cossement and P. Benard, *Microporous and Mesoporous Materials*, 2018, **263**, 165-172.

Chapter 2 Characterisation techniques

Different methods, including chemical and physical characterization, were used to obtain a comprehensive understanding of the samples. This chapter presents a summary of the methods and techniques used to characterise the samples in this thesis. Thermalgravimetric analysis (TGA), powder X-ray diffraction (XRD), textural features from nitrogen isotherms using the Brunauer, Emmett, and Teller (BET) theory, Raman spectroscopy, scanning electron microscopy (SEM), and elemental analysis using elemental microanalysis (CHN) or X-ray photoelectron spectroscopy (XPS) are the methods used to analyse porous carbons. This is in addition to the carbon dioxide and methane uptake application.

1. Thermal analysis

Thermal analysis refers to techniques that reveal changes in the chemical and physical properties of materials as a function of heating to set temperature(s). Thermal analysis techniques provide information regarding the thermal stability, decomposition behaviour, compound formation, phase transformation, and dehydration temperature of substances. We can determine the presence of impurities, the composition of the biomass starting materials, and the percentage of ash in the biomass.

Thermogravimetric analysis (TGA) and differential thermal analysis (DTA) are two of the main thermal analysis techniques for solid materials. The TGA technique automatically records the variation in sample weight as a function of temperature and is plotted out as a thermogravimetric analysis curve with steps representing major sample changes. DTA, on the other hand, monitors the

temperature difference (and behaviour variations) between a sample and an inert reference sample.[1]

In this study, thermogravimetric analysis was conducted from 50 °C to 1000 °C with a heating rate of 10°C/min under the flow of air. The thermogravimetric analyzer used was a TA Instruments Discovery or TA Instruments SDT Q600 analyzer.

2. Powder X-Ray Diffraction (PXRD)

Powder X-ray diffraction (PXRD) is a very useful analytical technique for characterising the crystal structure, lattice parameters, crystal morphology, and crystallite size of materials. The technique was pioneered by Max von Laue in 1912, who discovered that crystalline substances act as a diffraction grating for X-rays, similar to the atomic-scale plane spacing in a crystal lattice.[2] The term "powder" means that the crystalline domains are randomly oriented in the sample.[3] The X-ray diffraction pattern is unique for each crystalline substance; therefore, comparing the crystal structure of an authentic material to that of an unknown one provides information about the structure of the material under investigation. Accordingly, the XRD patterns can be compared with reference patterns from the XRD database and thus yield information about the crystalline structure of a sample. The positions and intensities of the peaks are used for identifying the underlying structure (or phase) of the material. In the experiment, a monochromatic X-ray source is utilised. In other words, the wavelength of the radiation is fixed, and the angle θ between the sample and the X-ray source is varied (by rotating the incident beam tube with the detector, see Figure *2-1*) so that diffraction from many planes can be measured. Bragg's Law (Equation 2-

1) can be used to determine the crystal structure of materials from the diffracted X-rays:

$$n\lambda = 2d \sin\theta \quad (2\text{-}1)$$

Here, λ is the wavelength of the incident X-ray beam, d is the lattice spacing, θ is the angle between the incident X-ray beam and the reflecting crystal plan, and n is an integer representing the order of the reflection (in practice, usually considered 1). Bragg's Law states that diffraction occurs when two factors are met: the incidence angle is equal to the scattering angle, and the path length difference is equal to an integer multiple of the wavelength.

XRD can be used to study partially crystalline and amorphous materials, but the detail of the output data decreases with crystallinity. Diamond, graphite, hard or soft carbon, ZTCs, and graphene can be distinguished using this method. Scientist can also study graphitizability—the ability of turbostratic carbon materials to develop to a graphite structure at high temperature.[4, 5]

The samples were prepared in a deep-well holder (diameter 10 mm, zero background plate) and the surface levelled with a minimum amount of pressure to reduce the introduction of preferred orientation stacking. Data were collected using a Malvern PANlytical Xpert MPD operating (see *Figure 2-1*) in Bragg-Brentano geometry equipped with PIXcel area detector and a sealed tube Cu source operating at 40 kV and 40 mA. A Johansson focussing beam monochromator selected pure $K_{\alpha 1}$ radiation (λ = 1.5405Å) which was then passed through 0.04 rad Soller slits to reduce axial beam divergence. Programmable Divergence Slits and Programmable Anti-Scatter Slits were used

in automatic mode to match the prepared sample length (20 mm). A fixed mask matching the prepared sample width (20 mm) and a fixed 1° anti-scatter slit were used in the incident beam path. Data were collected at room temperature with a step size of 0.013° in continuous mode and at a scan speed of 18.870 seconds/step. The sample holder was spun with a duration per spin of 8 seconds. The instrument is regularly calibrated using a silicon pressed powder sample. X-ray diffraction was used to investigate the presence of impurities and detect phases in the samples.

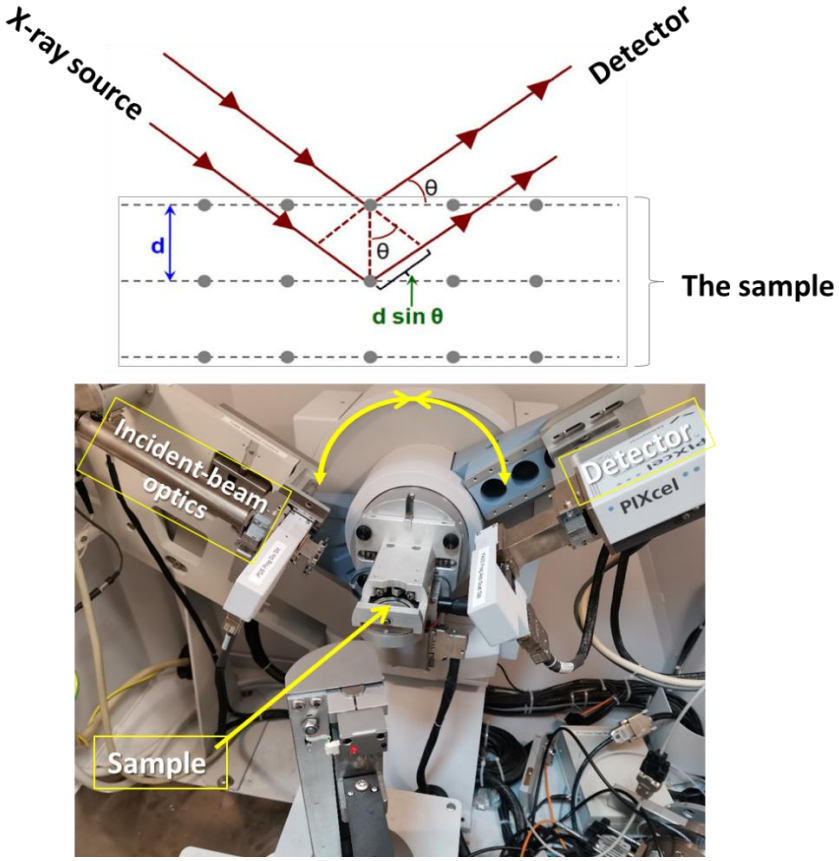


Figure 2-1 X-ray diffractometer and schematic representation of Bragg's law

3. Textural properties – N_2 physisorption

Experimentally, the physical adsorption of some gases is used to characterise the surface area and pore size/volume of porous solids. It is usually carried out at the boiling temperature of the gas to ensure that the gas particles will properly cover all of the solid surface.[6, 7] Nitrogen is a common gas that is used for measuring porosity and surface area by physisorption. The amounts of adsorbed and desorbed nitrogen at relative pressure points are measured to build the isotherm of the sample. Manometric methods are typically adopted for dosing and then evacuating certain amounts of nitrogen into the porous sample within a range of relative pressures between 10^{-7} and up to 1.

The International Union of Pure and Applied Chemistry (IUPAC) classified adsorption-desorption isotherms into six main types based on the analysis of a large range of nitrogen isotherms (Figure 2-2).

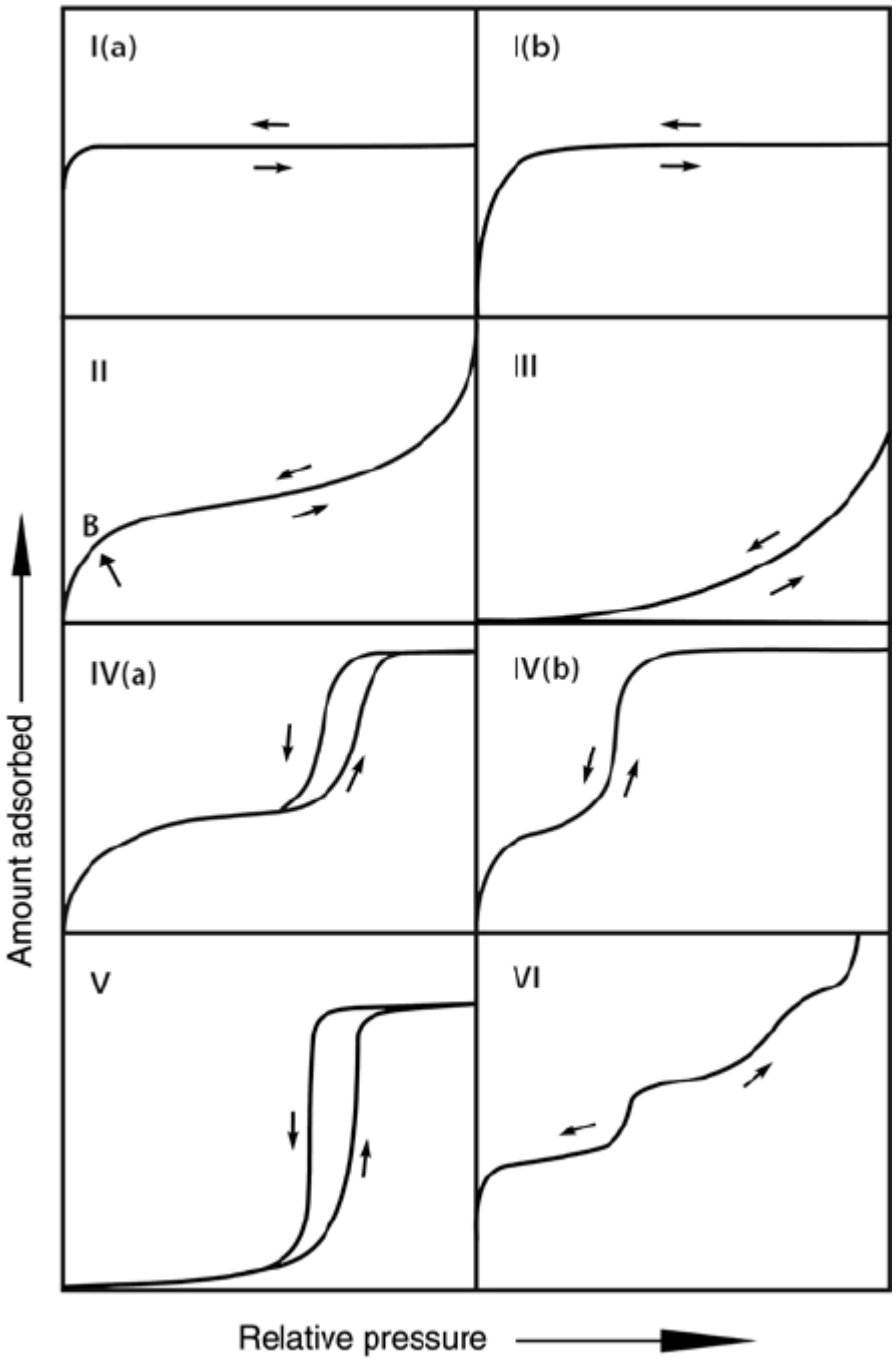


Figure 2-2 IUPAC classification of physisorption isotherms. The arrows represent adsorption or desorption direction.[7]

Type I isotherms are typically obtained in the case of microporous materials. Because of the small pore width and high adsorption energy, the high uptake at low pressures results in strong adsorbate-adsorbent interactions. This is followed by a plateau; in this case, the accessibility of the pore volume controls the

limiting uptake. Type I-a forms in narrow micropore widths, while the presence of narrow mesoporosity produces Type I-b isotherms. Most activated carbons are classified as Type I isotherms, or sometimes a mix of Type I with Type II or IV. Type II isotherms arise by adsorption on non-porous or microporous materials. Unrestricted mono-multilayer adsorption occurs in these materials up to high *p/p°*. The knee in this isotherm, referred to as "Point B," indicates the completion of the monolayer adsorption and the start of the multilayer adsorption. A weak distinction at this point means an increase in the overlap between monolayer and multilayer adsorption. Type III is a reversible isotherm along the *p/p°* range. It is not common, as only a few materials are produced. The absence of Point B from this isotherm indicates strong adsorbate-adsorbate interactions and weak adsorbate-adsorbent interactions. Type IV is provided by mesoporous materials. At low pressures, as in the case of Type II isotherms, mono-multilayer interactions take place. This is followed by pore condensation. The hysteresis loop is the most characteristic feature of Type IV-a, which is related to the pore condensation process inside the mesopores when the pore width is around 40 Å. With Type IV-b, a reversible isotherm appears due to smaller pore width and closed end pores. Type V shows pore condensation and hysteresis at higher pressures. At low pressures, the behaviour is similar to Type III and is caused by a lack of adsorbate-adsorbent interaction. Type VI isotherms are given by uniform or non-porous materials. The step shape of the isotherm arises due to the adsorbate being adsorbed layer-by-layer.

To calculate the specific surface area from an isotherm, the Brunauer-Emmett-Teller (BET) method[7] is commonly used, and the following equation is usually used:

$$a_s(BET) = n_m a_m N_A \quad (2\text{-}2)$$

Here, n_m refers to monolayer capacity (mol/g), a_m to the cross-sectional area of adsorbed gas (for nitrogen molecule, 0.162 nm^2 at –196°C (77 °K)), and the Avogadro constant is N_A.

At first, for obtaining the monolayer capacity n_m required for calculating BET surface area (Equation 2-2), the linear form of the BET equation (called the BET plot, Equation 2-4) should be plotted, $1/[n_a(1-p/p°)]$ versus $p/p°$ (Figure 2-3).

$$\frac{p/p^o}{n_a(1-p/p^o)} = \frac{1}{n_m C} + \frac{C-1}{n_m C}\frac{p}{p^o} \quad (2\text{-}3)$$

$$\frac{1}{n_a(1-p/p^o)} = \frac{1}{n_m C} + \frac{C-1}{n_m C}\frac{p}{p^o} \quad (2\text{-}4)$$

Regularly, the linear relationship is achieved in the relative pressure range of 0.05–0.30 of the isotherm.

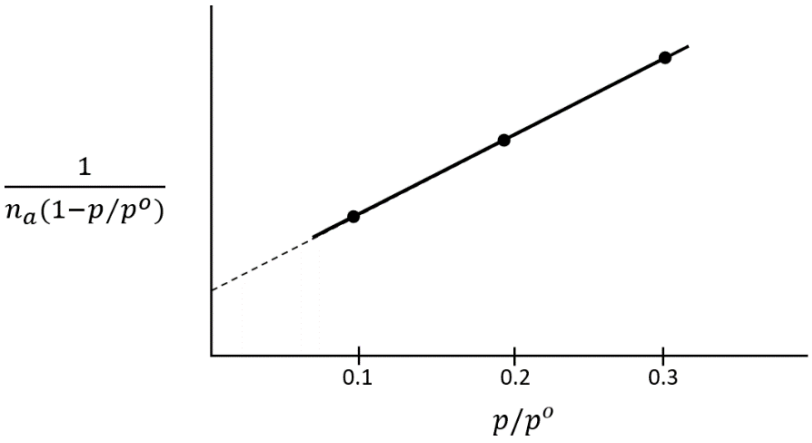


Figure 2-3 BET plot

where *na* is the adsorbed amount, $p/p°$ is the relative pressure, $p°$ is the pure adsorptive saturation vapour pressure at working temperature, p is the

equilibrium pressure at working temperature, and *C* is the BET constant related to the adsorption enthalpy. By getting the slope and the intercept of the BET plot, the value for the monolayer adsorbed capacity n_m can be solved (Equation 2-7):

$$\boldsymbol{slope} = \frac{\boldsymbol{C-1}}{\boldsymbol{n_m C}} \qquad \textit{(2-5)}$$

$$\boldsymbol{intercept} = \frac{\boldsymbol{1}}{\boldsymbol{n_m C}} \qquad \textit{(2-6)}$$

$$\boldsymbol{n_m} = \frac{\boldsymbol{1}}{\boldsymbol{slope+intercept}} \qquad \textit{(2-7)}$$

The thickness-plot (t-plot) method is adopted to determine the microporosity of the samples. In this method, the experimental isotherm of the microporous sample is compared with a standard isotherm of non-porous material (Type II). This is done by replotting volumes of adsorbed gas on the microporous sample against the thickness (t) of multilayers on non-porous reference materials, which is obtained in this report from the following Harkins and Jura equation (Equation 2-8):

$$\boldsymbol{t} = \left[\frac{\boldsymbol{13.99}}{\boldsymbol{log(p/p^o)+0.034}}\right]^{\boldsymbol{1/2}} \text{Å} \qquad \textit{(2-8)}$$

From the slope of the t-plot after this, the total surface area a_s is obtained using the following equation 2-9:

$$\boldsymbol{a_s(t)} = \boldsymbol{1.5468} \times \boldsymbol{slope} \qquad \textit{(2-9)}$$

The micropore surface area a_{micro} and micropore volume V_{micro} are calculated using the following:

$$\boldsymbol{a_{micro}} = \boldsymbol{a_s(BET)} - \boldsymbol{a_s(t)} \qquad \textit{(2-10)}$$

$$\boldsymbol{V_{micro}} = \boldsymbol{0.0015468} \times \boldsymbol{intercept} \qquad \textit{(2-11)}$$

The pore size distribution is obtained using nonlocal density functional theory (NL-DFT) via Equation 2-12. This equation calculates a series of theoretical isotherms for a series of adsorptive/adsorbent systems for a series of pore sizes.

$$N\left(\frac{p}{p^o}\right) = \int_{W_{min}}^{W_{max}} N\left(\frac{p}{p^o}, W\right) f(W)\, dW \quad \textbf{(2-12)}$$

N(p/p°) represents experimental adsorption isotherm data, *W* represents pore width, *N(p/p°,W)* represents the isotherm on a single pore of width *W*, and *f(W)* represents the pore size distribution function.

Total pore volume is taken from the total quantity of nitrogen (cm^3/g) adsorbed at *p/p°* = 0.99, at which point the system should be saturated.

In this work, analysis of porosity and determination of textural properties were performed via nitrogen sorption using a Micromeritics 3Flex sorptometer. The carbon samples were degassed under vacuum at 200 °C for 32 or 16 hours prior to analysis (at -196 °C).The surface area was calculated using the BET method applied to adsorption data within the relative pressure (P/Po) range of 0.02–0.35. The total pore volume was determined from the nitrogen uptake at close to saturation pressure (P/Po = 0.99). The micropore surface area and micropore volume were determined via t-plot analysis. Nonlocal density functional theory (NL-DFT) was applied to nitrogen adsorption isotherms on carbon (–196°C) to determine pore size distribution using a slit geometry.

4. Elemental analysis (CHN analysis)

Carbon, hydrogen, and nitrogen (CHN) analysis is used to measure carbon, hydrogen, and nitrogen elemental concentrations in the sample. A flash combustion of the sample in the presence of oxygen is used at high temperatures (800–900 °C). In this combustion process, carbon dioxide gases, water, and nitrogen are released. These are detected and their concentrations determined by measuring their thermal conductivity or through other detection methods such as infrared spectroscopy.[8] The calculated H/C and O/C ratios demonstrate the degree of transformation of the starting materials to polymeric carbon; in this case (for biomass samples), the transformation of cellulose, hemicellulose, and lignin to carbon.

Using a CE-440 Elemental Analyser manufactured by Exeter Analytical, Elemental Microanalysis was performed to determine the C, H, and N content of the carbon samples. During the analysis, approximately 2 mg of the samples were burned in a high-temperature furnace (975 °C) in pure oxygen gas (Figure 2-4). The combustion products are carried through the system by a flow of helium gas Figure 2-4). (solenoid valves A through G control the gas flow through the system; valves H and I are used for maintenance purposes). In the combustion tube, the combustion products pass over suitable reagents to ensure complete oxidation and removal of unwanted by-products such as sulphur, phosphorus, and halogen gases. Oxides of nitrogen are converted to molecular nitrogen and residual oxygen is removed in the reduction tube, which is kept at 625 °C. The sample gases are then thoroughly homogenised to a precise volume,

temperature and pressure in the mixing volume and this mixture is then released into the thermal conductivity detector.

An absorption trap between the first pair of thermal conductivity cells eliminates water from the sample gas. The differential signal measured before and after the trap reveals the water concentration and, hence, the amount of hydrogen in the initial sample.

A similar measurement is made of the signal output of a second pair of thermal conductivity cells, between which a trap removes carbon dioxide, thus determining the carbon content.

The only remaining gases are helium and nitrogen. This gas passes through a thermal conductivity cell, and the output signal is compared to the output signal of a reference cell through which pure helium flows. This provides the concentration of nitrogen.

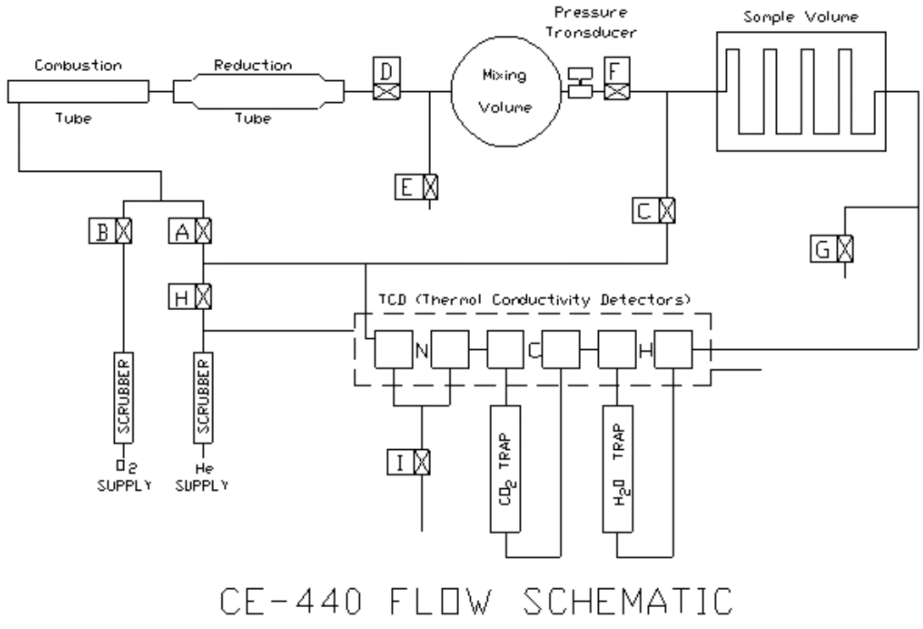


Figure 2-4 A diagram of the elemental analyser

5. X-ray Photoelectron Spectroscopy (XPS)

X-ray photoelectron spectroscopy is one of the surface analysis techniques used to detect the kinetic energy distribution of the emitted photoelectrons in order to determine the composition and electronic state of the chemical compounds on a sample surface. Photoelectron emission is produced when an X-ray from a specific source strikes the surface of a sample, causing an electron core to be ejected from its electronic shell (Figure 2-5). The kinetic energy (KE) of the ejected electron is directly proportional to the binding energy (BE) of the electron to the atom:

$$\boldsymbol{BE = h\nu - KE - \varphi_{spec}} \quad \textbf{(2-13)}$$

Here, BE is the binding energy of the particular electron to the atom, KE is the kinetic energy of the ejected electron, φ_{spec} is a correction factor that is distinctive to the instrument, and u is the frequency of the incident X-ray. MgK_a (1253.6 eV) or AlK_a (1486.6 eV) X-rays are typically used, which produce photons able to interact 1–10 micrometres from the solid surface without deeply penetrating a solid.[9, 10]

With this analysis, the functional states of carbon (or any other element) on the surface of the samples can be determined.[11] The relative percentages of all the elements included in the carbon samples (including the tiny contaminants) can be identified, though hydrogen atoms cannot be detected via XPS.

X-ray photoelectron spectroscopy (XPS) was carried out using a Kratos AXIS ULTRA with a monochromated A1 Kα X-ray source (1486.6 eV) operated at 10 mA emission current and 12 kV anode potential. The analysis chamber pressure

was better than 10−9 Torr. FAT (fixed analyzer transmission) mode was used, with pass energies of 160 eV (or 80 eV) for survey scans and 40 eV for highresolution scans. The magnetic immersion lens system allows the area of analysis to be defined by apertures, a “slot” aperture of 300 × 700 μm for wide/survey scans and a 110 μm aperture for high-resolution scans. The takeoff angle for the photoelectron analyzer was 90° and acceptance angle of 30° (in magnetic lens modes). Data analysis was carried out using CASAXPS software with Kratos sensitivity factors to determine atomic % values from the peak areas. Charge correction was applied to the data at the processing stage.

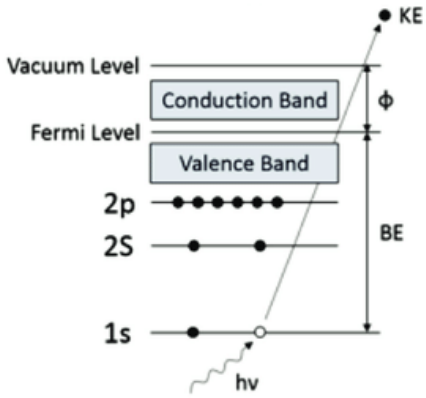


Figure 2-5 mechanism of electron emission in XPS

6. Scanning Electron Microscopy (SEM)

SEM images samples with a nanometer-scale resolution using an electron beam. In the electron source, electrons are emitted from a filament and focused into a beam. A series of lenses in the electron column then focus the beam on the surface of the sample. As a result of the electrons in the beam interacting with

the sample, a variety of signals are generated. These signals can be analysed in order to obtain information regarding the surface's topography and composition.

The interactions between the electron beam and the sample generate distinct electron and X-ray signals (Figure 2-6). The secondary electrons are one of these signals that arise from the sample's surface or near-surface areas. It arises from inelastic interactions between the incident electron beam and the material. The study of a sample's surface structure is achieved by these secondary electrons. When the incident electron beam displaces an inner shell electron and replaces it with an outer shell electron, X-rays are produced. The emitted x-rays are used to identify and quantify the elemental composition of a spot or a map based on the fact that each element has a unique energy difference between its outer and inner electron shells.[1, 12]

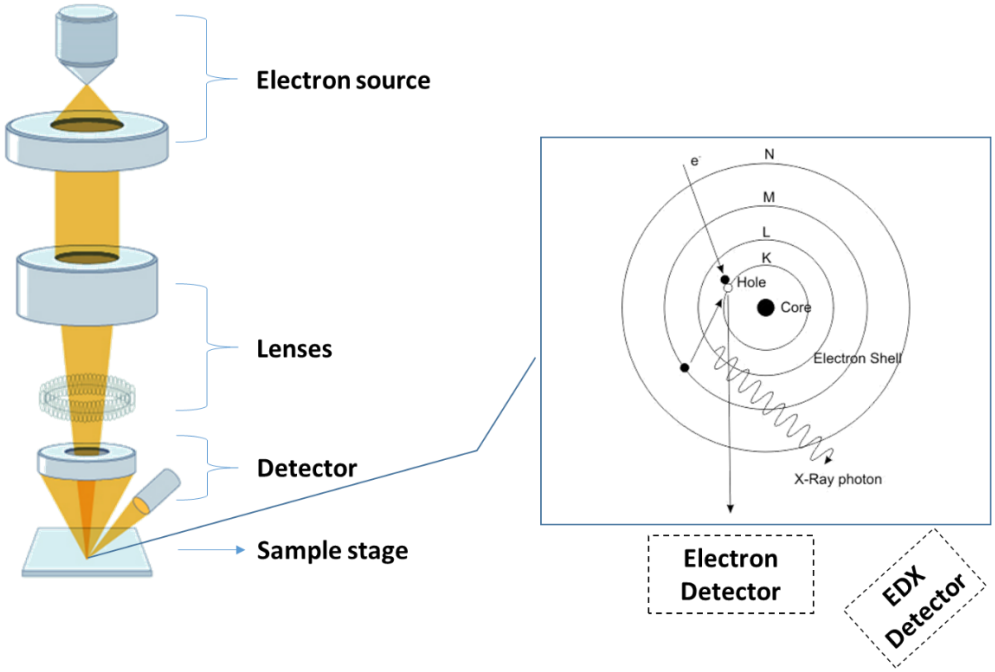


Figure 2-6 Schematic of SEM/EDX analysis

Scanning electron microscopy (SEM) images were recorded on a JEOL 7000 microscope at 15 kV accelerating voltage. Samples were mounted using conductive carbon double-sided sticky tape.

7. Gases uptake measurements

The adsorption isotherms of the targeted gases (CO_2 or CH_4) were obtained using gravimetric methods. The gravimetric technique measured the excess uptake (θ_{exc}), from which the total storage (θ_t) was calculated using the following equation:

$$\boldsymbol{\theta_t = \theta_{exc} + d_{gas} \times V_t} \quad \textbf{(2-14)}$$

where θ_t is the total gas uptake (mmol/g), θ_{exc} is the excess uptake determined by gravimetric measurement (mmol/g), V_t is the total pore volume of the adsorbent determined by nitrogen sorption analysis, and d_{gas} is the density (g/cm^3) of the gas at the relevant temperature and pressure. The density was obtained from the website of the National Institute of Standards and Technology (http:// www.nist.gov/).

The packing density of the present samples was calculated using:

$$\mathbf{d_{carbon} = (1/\rho s + V_t)^{-1}} \quad \textbf{(2-15)}$$

where d_{carbon} is the packing density of the carbon sample, ρs is skeletal density, and V_t is the total pore volume from the nitrogen physisorption analysis. The skeletal density of the carbons was determined from helium pycnometry and is usually taken to be 1.5 cm^3/g. In order to obtain the experimental packing

density, carbon samples were compressed into pellets in a 1.3 cm die at 7 MPa for approximately 5 minutes.

The targeted gas (CO_2 or CH_4) uptake capacity of the carbons was measured by gravimetric analysis with a Hiden XEMIS instrument or Intelligent Gravimetric Analysers (IGA) and a 99.9999% purity of the gas (CO_2 or CH_4). Prior to analysis, the carbon samples were degassed at 240°C at a ramp rate (10°C/min) for 3 h. The temperature of the analysis medium was controlled using a water bath.

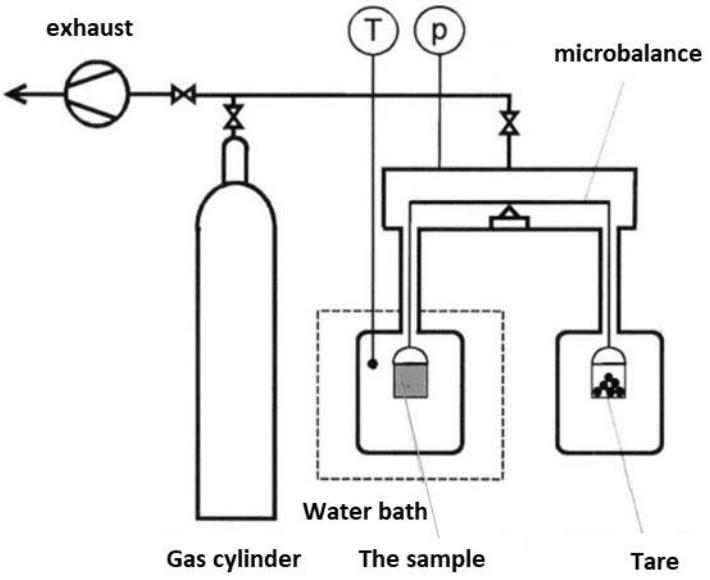


Figure 2-7 approximate scheme of the gravimetric uptake analyser

References

1. B. D. Fahlman, *Materials Chemistry by Bradley D. Fahlman. Netherlands: Springer*, 2011.
2. W. Clegg, *Oxford chemistry primers*, 1998, **60**.
3. B. E. Warren, *X-ray Diffraction*, Courier Corporation, 1990.

4. R. E. Franklin, *Proceedings of the Royal Society of London. Series A. Mathematical and Physical Sciences*, 1951, **209**, 196-218.
5. X. Dou, Karlsruher Institut für Technologie (KIT), 2019.
6. S. Lowell, J. E. Shields, M. A. Thomas and M. Thommes, *Characterization of porous solids and powders: surface area, pore size and density*, Springer Science & Business Media, 2006.
7. M. Thommes, K. Kaneko, A. V. Neimark, J. P. Olivier, F. Rodriguez-Reinoso, J. Rouquerol and K. S. Sing, *Pure and applied chemistry*, 2015, **87**, 1051-1069.
8. P. Hemming, *Exeter Analyticak (UK) Ltd*, 2018.
9. C. D. Wagner and G. E. Muilenberg, *Handbook of X-ray Photoelectron Spectroscopy: A Reference Book of Standard Data for Use in X-ray Photoelectron Spectroscopy*, Perkin-Elmer, 1979.
10. J. Chastain and R. C. King Jr, *Perkin-Elmer Corporation*, 1992, **40**, 221.
11. G. M. Burke, D. E. Wurster, M. J. Berg, P. Veng-Pedersen and D. D. Schottelius, *Pharmaceutical research*, 1992, **9**, 126-130.
12. J. Bergström, in *Mechanics of Solid Polymers*, ed. J. Bergström, William Andrew Publishing, 2015, DOI: https://doi.org/10.1016/B978-0-323-31150-2.00002-9, pp. 19-114.

Chapter 3 Alternative template removal method for zeolite templated carbons

Abstract

Zeolite-templated carbons (ZTCs) are special carbons with regular pores that reflect the pore structure of the zeolite utilised as template. Considering their exceptional performance in numerous applications, there is a need to optimise their synthesis processes. Safety issues related to the use of hydrofluoric (HF) acid for dissolving the template and obtaining the actual ZTCs have hindered the bulk manufacture of these unique carbons. We attempted to avoid using HF in this investigation by applying KOH treatment on the zeolite/carbon composite under thermal conditions as an alternative treatment. After introducing carbon into zeolite pores and conducting the KOH treatment, a diluted HCl solution was used to remove the template. The analysis showed the successful removal of the template. Even though this alternative method resulted in the destruction of a fraction of the original ZTC, the new ZTC demonstrated a high methane delivery capacity comparable to that of the ZTC prepared via conventional routes including the use of undesirable HF acid.

1. Introduction

Zeolite-templated carbons (ZTCs) are a special type of carbon, characterised by a uniform range of pores compared to the heterogeneous porosity of activated carbon. ZTCs show promising performance in gas storage,[1, 2] catalysis, battery electrodes and supercapacitor applications.[3] Lately, it has been hypothesised that zeolite-templating may be a potential synthetic method to carbon schwarzites, a class of theoretical material with fascinating properties.[4] ZTCs are typically

prepared by introducing a carbon source into zeolite pores (the template), and after removing the template, the obtained carbon has pores of the similar size and particle shape as those on the template.[5-7] Different types of zeolites, such as FAU, BEA and EMT, which contain highly 3D-ordered, interconnected large pore arrangements, are suitable for producing ordered microporous carbon frameworks.[8-11]

At each step of ZTC synthesis, the optimal conditions for replicating pores faithfully must be carefully selected. First, a template with large pores must be selected for optimal insertion of the carbon source into the majority of pores and to prevent pore blockage. FAU, BEA- and EMT-type zeolites have large pore sizes in addition to a 3D interconnected pore system, making them the ideal candidates for use as templates.[4] Choosing the carbon source, insertion method (chemical vapour deposition, liquid impregnation, or both) and controlling the thermal treatment conditions are important factors that affect the replication quality of the template pores. For example, examination of a range of CVD/carbonisation temperatures showed that the temperatures in the range 750–800 °C were optimal for the CVD of acetonitrile to replicate zeolite Y and X pores without accumulation of extra carbon layers on the surface and thus formation of graphitic stacked layers.[12]

Even if all steps were controlled to improve the quality of the resulting carbon, the problem of the last step remains, which is removing the template, as a limitation for the commercial production of ZTCs. Usually, strong acids are employed to thoroughly dissolve the template, such as concentrated HCl and HF. Hydrofluoric acid is the most effective reagent for the completion of template removal. However, commercial production of ZTCs would be

restricted due to recent concerns about HF-related health and safety risks.[13] In the same context, Park et al.[14] attempted to dissolve the template using diluted NaOH and HCl solutions, with the aim of avoiding the use of HF. They found that the weight of inorganic residues was ~2–7 % of BEA-, Zeolite Y-, and X-templated carbons.

Here, we examined the effect of KOH activation conditions, which are usually adopted in our group for carbon activation, on carbon/zeolite composite and thus on ZTC, as well as whether that would ease template removal. As it is well known, alkaline fusion is a step in one of the common techniques for preparing zeolites from Al and Si-containing natural sources. In this step, KOH can be successfully used to dissolve the aluminosilicate species prior to the crystallisation of the target zeolite at temperatures up to 600 °C.[15, 16] On the other hand, a hydrothermal treatment in the presence of KOH solution can be applied to transform FAU zeolite to CHA zeolite at low temperatures.[17] In addition, KOH is commonly used to manufacture activated carbon because it is an efficient and successful activating agent.[18]

In this work, activation of the composite facilitated the removal of the template without the need for HF. We have explored the properties and gas uptake of the resulting carbon materials and compared them to conventional ZTC prepared with the use of HF to remove the zeolite framework.

2. Experimental

2.1. Materials

Molecular sieves 13X (zeolite 13X) and furfuryl alcohol (98%) were purchased from Alfa Aesar Company. Mesitylene (99%) was purchased from Sigma Aldrich. Ethylene (Research grade purity) was obtained from BOC Ltd.

2.2. Synthesis procedures for ZTC

The ZTC was synthesised using procedures published in previous works.[10, 19] Drops of furfuryl alcohol (FA) were added to 3 g of pre-dried zeolite 13X. The FA/zeolite composite was placed in a boat and transferred to a tube furnace. The composite was then heated under N_2 flow at 80°C (with heating ramp rate of 5°C/min) for 24 hours, then at 150°C (heating ramp rate of 5°C/min) for 10 hours. The temperature was then raised (ar ramp rate of 5°C/min) and held at 700°C for 3 hours. The gas flow was changed to ethylene/ N_2 (at ratio of 1:9) for another 3 hours. Then the temperature was raised to 900°C for 3 hours (at ramp rate of 5°C/min) with only N_2 flow, followed by cooling in N_2

After cooling to room temperature, the carbon/zeolite composite was divided into a few parts. One was treated in the conventional manner by washing with 10% HF for 24 hours, followed by refluxing in concentrated HCl for 6 hours. The resulting carbon was rinsed several times under vacuum filtration with deionised water until the filtrate reached a neutral pH and dried at 100°C overnight. This carbon sample is denoted as CZ13X.

Other parts of the zeolite/carbon composite were treated as described in section 2.3 below.

2.3. Activation of carbon/zeolite composite

About 38 wt% of KOH to 30 wt% of carbon was added to a carbon/zeolite composite. The KOH was ground first, then mixed and gently ground with the composite. The mixture was then transferred to an alumina boat and heated for 1 hour at 600, 700 or 800 °C in a tube furnace under nitrogen flow and heating ramp rate of 5°C/min). Following cooling, and once the temperature reached room temperature, the template and KOH were removed by gentle stirring in a 1 M HCl solution for 48 hours, and then washed with deionised water until the filtrate had pH 7 and dried in an oven at 100°C. The activated samples are denoted as CZ13XT, where T is the activation temperature.

2.4.Characterisation

Powder XRD patterns of the samples were performed using a PANalytical X'Pert PRO diffractometer with a copper Kα and a monochromator (λ = 1.5405Å) at 40 kV and 40 mA with a step size of 0.02 and a 50 s time step. The scan was performed at room temperature. The porosity and determination of textural properties were performed via nitrogen physisorption using a Micromeritics 3Flex sorptometer. Prior to analysis (at –196°C), the carbon samples were degassed under vacuum at 230°C for 32 or 16 h. The surface area was calculated using the BET method applied to adsorption data within the relative pressure (*P/Po*) range of 0.02–0.35. The total pore volume was determined from the nitrogen uptake at close to saturation pressure (*P/Po* = 0.99). The micropore surface area and micropore volume were determined via t-plot analysis. Micromeritics' SAIEUS software was used to obtain PSDs of the samples using the 2D-NLDFT method for heterogeneous surfaces. In order to

create the most accurate PSD for carbons, the software's fitting parameter, λ, which affects the roughness of the PSD, was adjusted between 2.75 and 3.00. Scanning electron microscopy (SEM) images were recorded on a JEOL7000 microscope at 15 kV accelerating voltage. Samples were mounted using a conductive carbon double-sided sticky tape.

2.5.CH_4 uptake measurements

CH_4 uptake capacity of the carbons was measured with a Hiden Isochema XEMIS Analyser using 99.999% purity methane at 25°C and up to 100 bar of pressure. Prior to conducting the CH_4 uptake experiments, the carbons were outgassed for 3 h at 240 °C (at heating ramp rate 10°C/min) under vacuum. The measurements determined the excess CH_4 uptake directly.

3. Results

The removal of the zeolite template from the composites was tracked using powder XRD. This is possible because the zeolite template has sharp peaks, which should no longer exist if the zeolite has been successfully removed. Figure 1 shows the evolution of the XRD patterns following thermal treatment and washing of the composites. It should be noted that the zeolite peaks are expected to be removed following washing of the thermally treated composite. This is because the zeolite-13X template is thermally stable at all temperatures used.

First, 30 wt% of KOH was added to the carbon/Z13X composite, which had 30% carbon based on TGA data (not reported here), i.e., a 1:1 weight ratio of KOH

to carbon, and heated to 600°C. The carbon/Z13X/KOH composite was washed with 2 M HCl, but the template was not completely removed. This was confirmed by XRD; as depicted in Figure 3-1 (b), the carbon/Z13X composite treated with KOH at 600 °C and then washed with 2 M HCl has significant template residual peaks. As shown in Figure 3-1 (a), the XRD peaks from zeolite disappeared after a second wash using the conventional wash, i.e., a solution of 10% HF and refluxing in concentrated HCl.

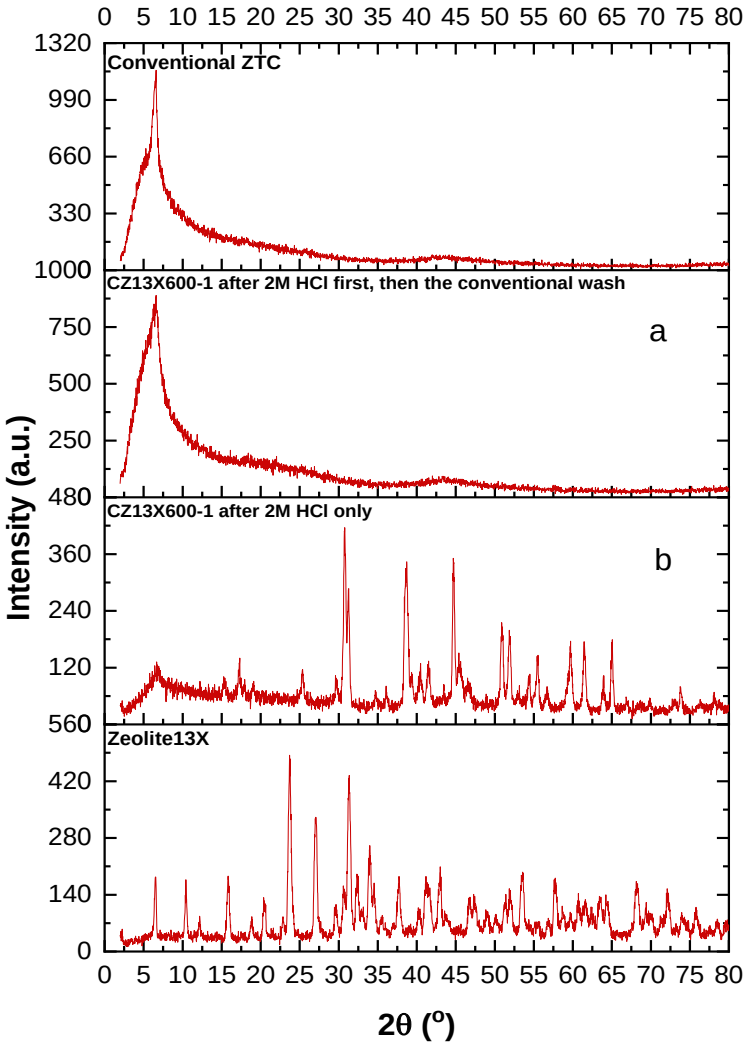


Figure 3-1 PXRD patterns of conventional ZTC, KOH-treated carbon/zeolite at 600°C using a 1:1 weight ratio of carbon to KOH (after two different wash steps, a & b), and the template zeolite 13X.

3.1. Zeolite-templated carbons

3.1.1. X-ray diffraction

The powder XRD patterns of the conventional sample (CZ13X), and the three carbon samples (CZ13XT), which were produced after treatment of the composites with KOH under thermal treatment at 600, 700 and 800^{o}C, are presented in Figure 3-2. The conventional sample, without any KOH treatment, showed the main peak of zeolite-templated carbon at 2θ = ~7°, which corresponds to a d-space = ~14 Å in FAU zeolite.[10, 11, 14, 19] Therefore, the carbon successfully replicated the structure of the template. On the other hand, the XRD patterns of the CZ13XT samples obtained via treatment with KOH (Figure 3-3) showed that the peak expected at 2θ of 7° is shifted to a lower angle or that the peak is less well developed. This indicates that the treatment with KOH had disrupted the carbon replication in some way. A possible activation reaction of the carbon by KOH or a solid-solid reaction between KOH and zeolite-13X could disrupt the regularity of the carbon and or template with the overall effect that the resulting carbon is less well ordered. The wide and weak graphitic peak at 2θ = 23^{o} in carbons treated at 600 and 700^{o}C (Figure 3-2) may be caused by a number of different mechanisms. First, this peak could appear after adding KOH when the few graphitic layers inside the cages were stacked after the cage geometry was reduced to a smaller dimension. Second, this peak could be inherited from the main ZTC before any treatment, as the previous existence of this peak will not be clearly confirmed due to its overlap with a high-intensity peak at 2θ = 7°. The intensity of the peak at 5° in KOH-treated samples decreased with increasing temperature, which would be tentatively explained by

ongoing reaction/s to destroy the Z13X replication until finally, at 800°C, an activation reaction broke down any 'zeolitic' ordering in CZ13X800.

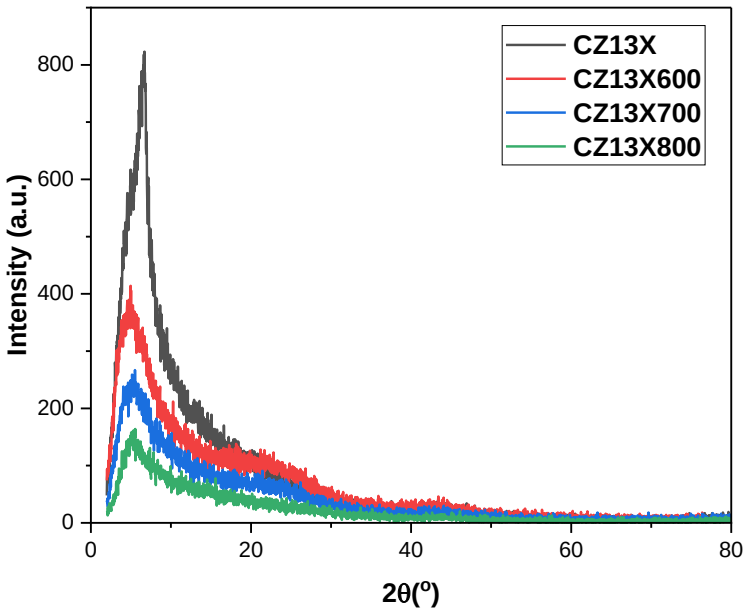


Figure 3-2 PXRD patterns of conventional ZTC and KOH-treated carbon/zeolite samples

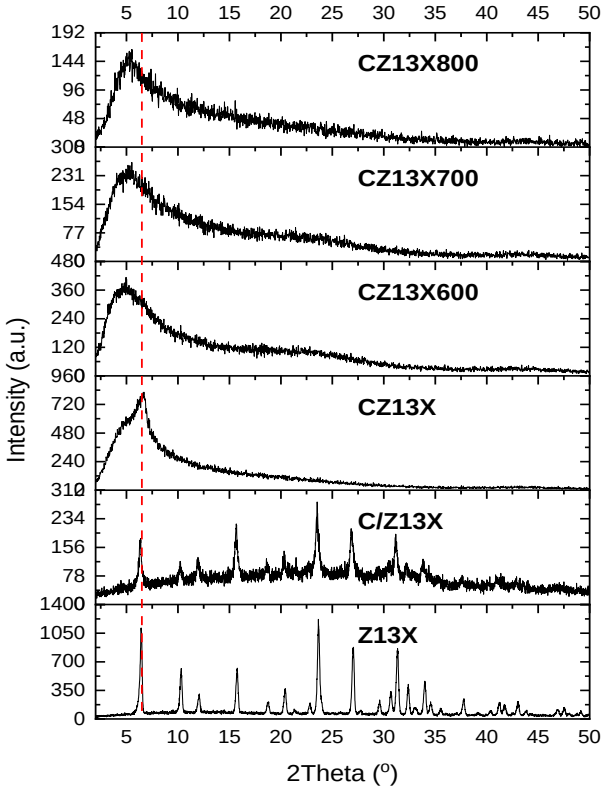


Figure 3-3 PXRD patterns of the template, zeolite13X/carbon composite, the conventional ZTC and KOH-treated carbon/zeolite samples

3.1.2. SEM analysis

The SEM images of the conventional sample (CZ13X) showed replication of the morphology of the zeolite template as shown in Figure 3-4-7. For the CZ13XT samples, the replication of morphology was to a lower extent. However, interestingly, the particles of these samples still retain many of the features of zeolite morphology – particularly the size of the particles and sharp edges (Figure 3-8). This means that some replication does still take place even though the fidelity is somewhat lower than that of the conventional ZTC.

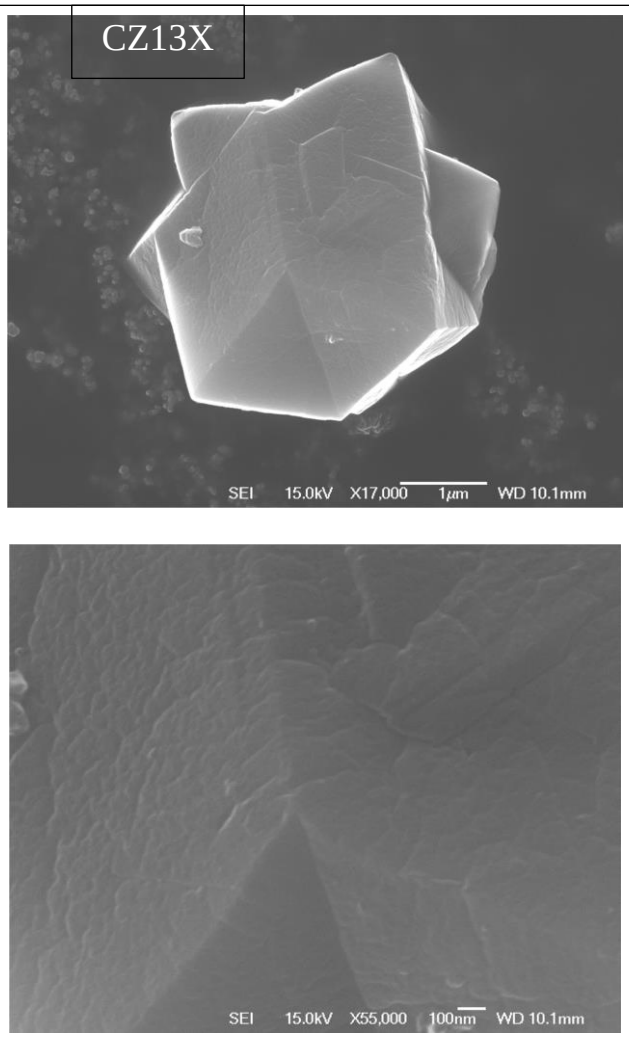


Figure 3-4 SEM images of conventional zeolite-templated carbon

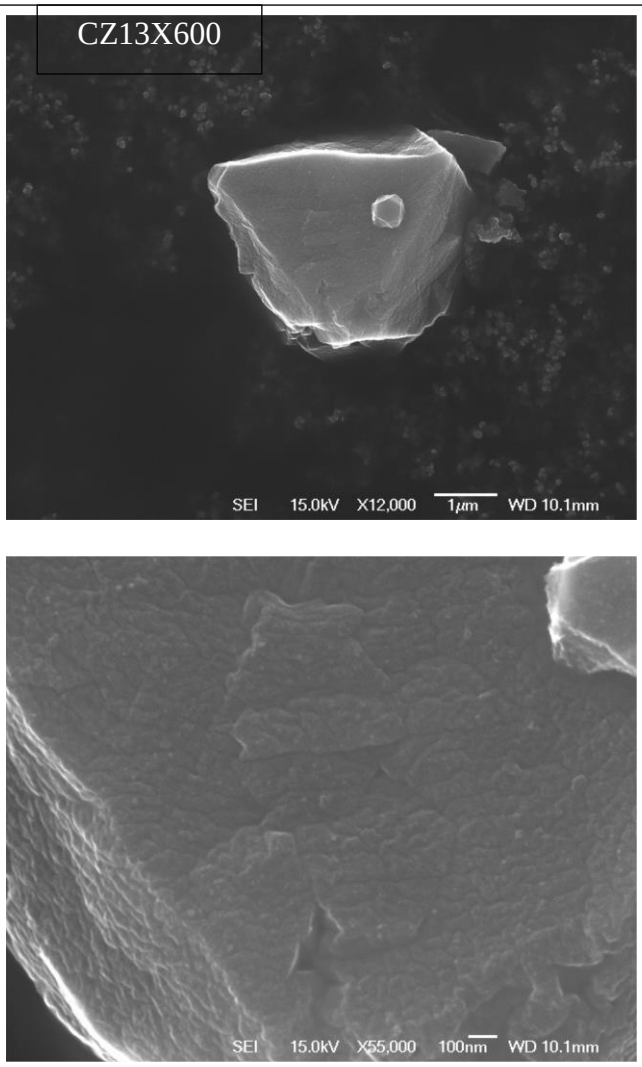


Figure 3-5 SEM images of carbon obtained from KOH-treated carbon/zeolite at 600°C

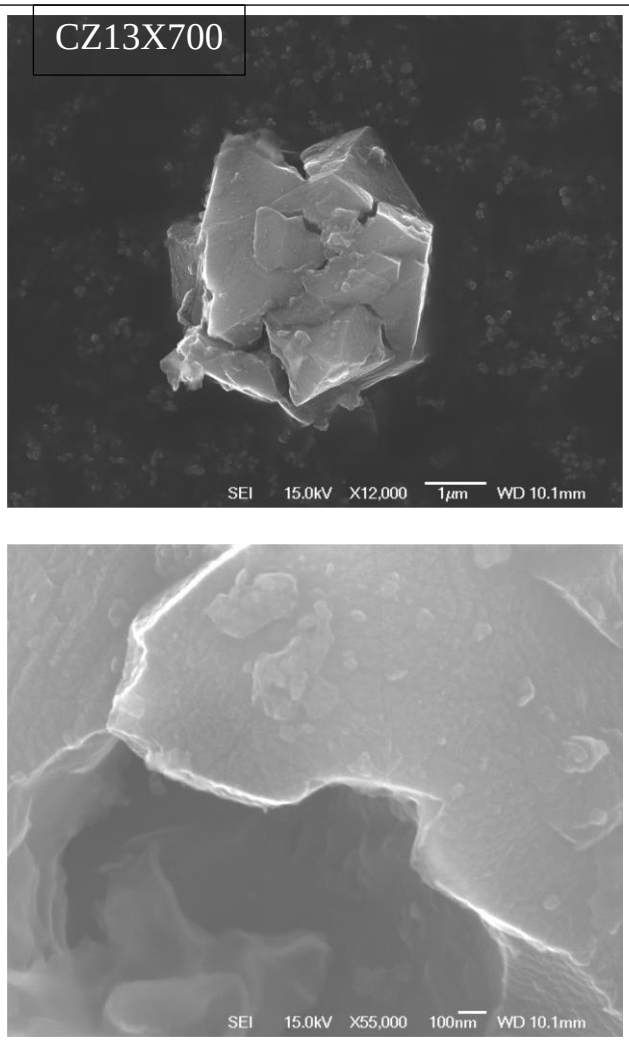


Figure 3-6 SEM images of carbon obtained from KOH-treated carbon/zeolite at 700°C

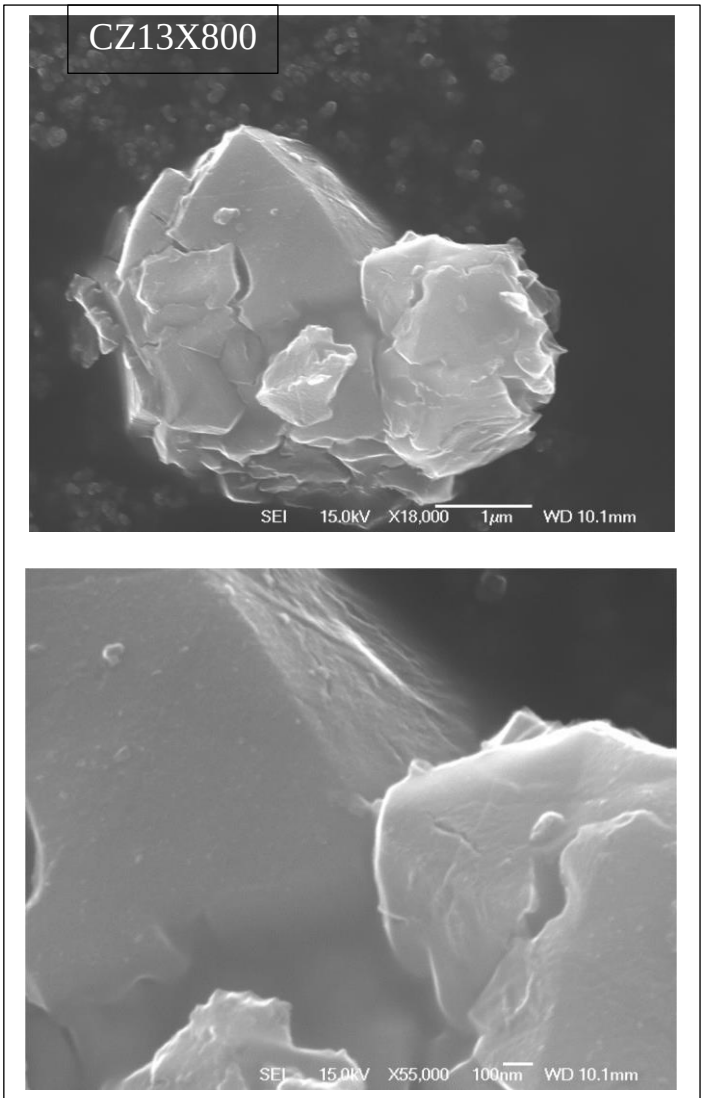


Figure 3-7 SEM images of carbon obtained from KOH-treated carbon/zeolite at 800°C

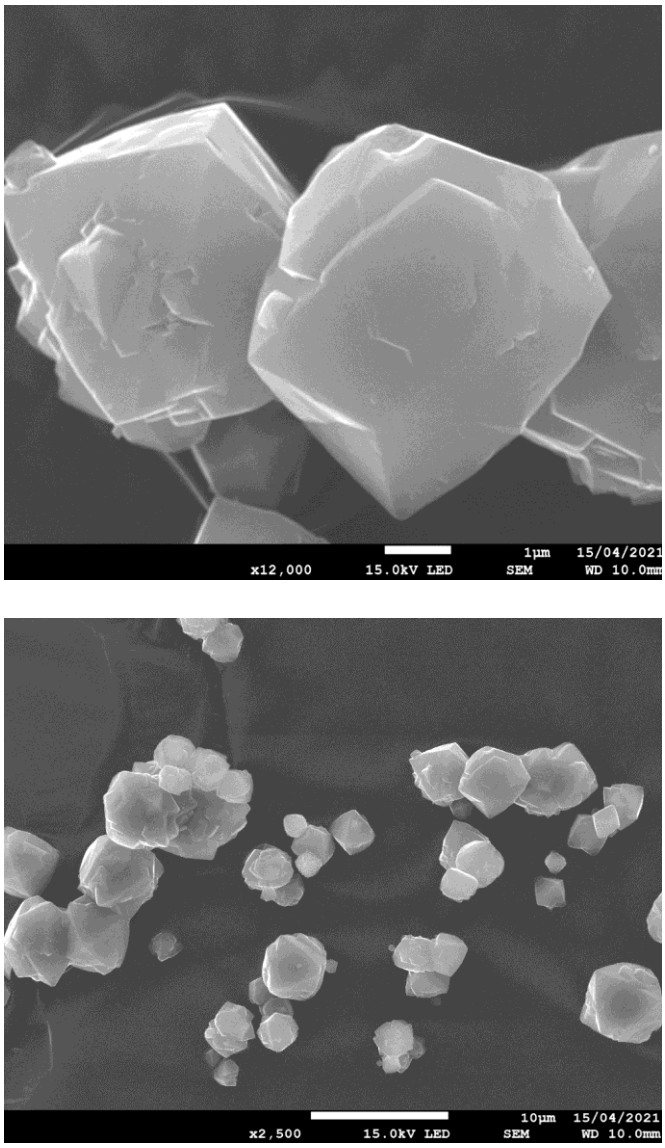


Figure 3-8 SEM image of the zeolite-13X template.

3.2. Template removal

3.2.1. Thermal analysis

Thermal analysis of the carbon/template composite and KOH-treated samples revealed the presence of template residues (see Figure 3-9). The KOH-treated sample heated at the highest temperature (800^{o}C) contained the lowest residues, 2%. For the samples treated at 600 and 700°C, the residues were 8% and 17%, respectively. Thus the CZ13X800 sample may be considered as being close to

being fully carbonaceous while the other samples still contain significant amounts of inorganic matter. This clearly indicates that a high temperature is essential for template removal via the method described here or that longer washing times are needed.

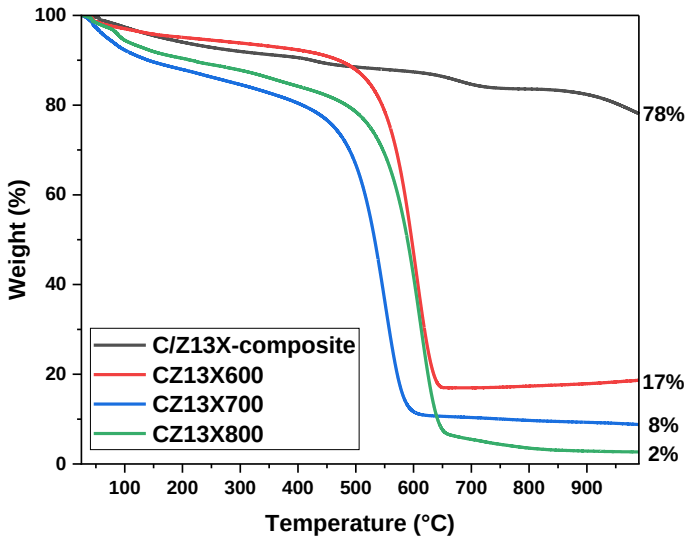


Figure 3-9 TGA curves of the samples

3.2.2. Carbon/Zeolite-composite reaction with KOH

In order to understand the nature of the KOH reaction with the carbon/zeolite composite, the PXRD patterns were collected for the carbon/zeolite/KOH composite before dissolution of the inorganic components by HCl. In addition, the PXRD patterns of the annealed zeolite with 30 wt% KOH were collected (Figure 3-10). Apparently, a reaction between Z13X and KOH occurred that produced potassium aluminium silicate as the main phase (compared with the ICDD reference: 00-032-0731 for $K_{1.25}Al_{1.25}Si_{0.75}O_4$). Consequently, the crystal

structure of the template (Zeolite X) was destroyed by heating with KOH at the targeted temperatures. This is shown by a comparison of the XRD patterns of the calcined template at 700°C (Z13X700) and the reference peaks of the zeolite X with the other patterns after KOH treatment.

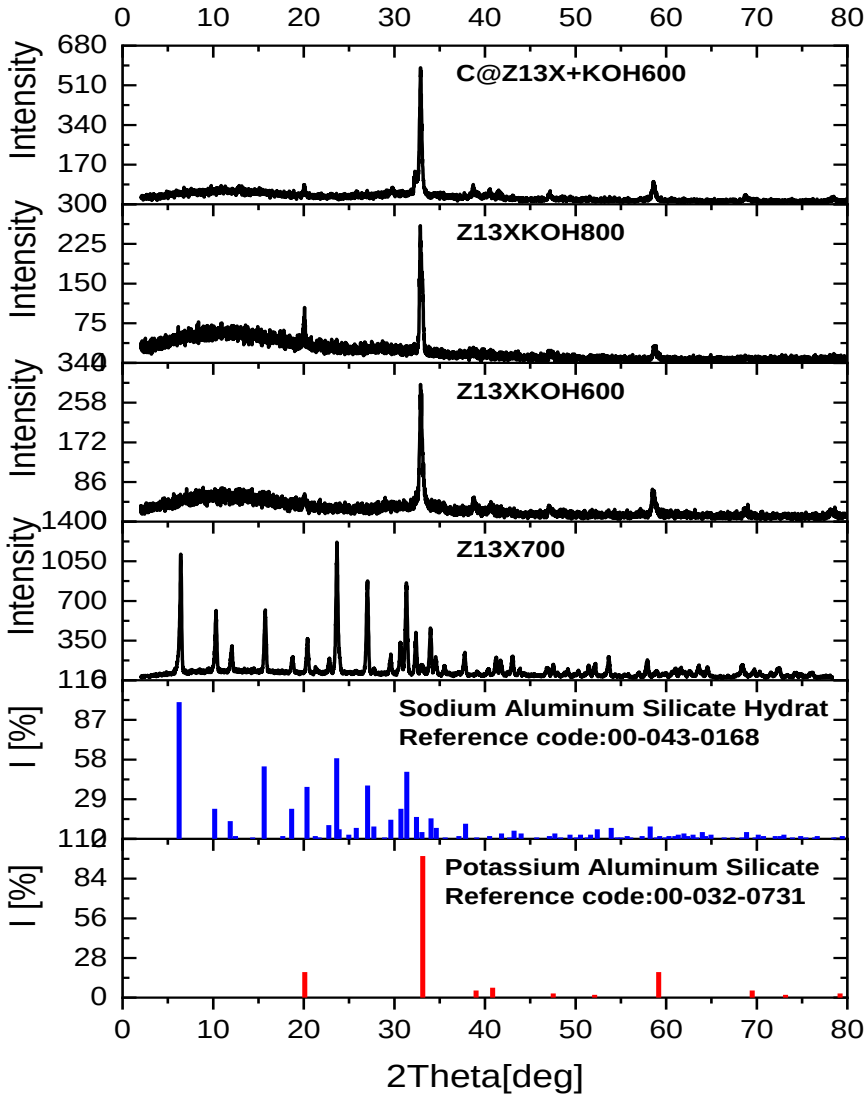


Figure 3-10 PXRD patterns of calcined zeolite13X at 700°C (Z13X700),calcined zeolite13X with KOH heated at 600 and 800°C (Z13XKOH600 and Z13XKOH800, respectively) and calcined zeolite13X/carbon composite with KOH heated at 600°C under N2 flow (C@Z13X+KOH600).

The SEM images of the annealed zeolite/KOH at 700°C (Figure 3-11) showed a change in the surface of the octagonal-structure of the zeolite particles, unlike the conventional template particles (Figure 3-8), which suggested that the template reacted with KOH. Besides that, the SEM images showed the fusion of a number of zeolite particles together due to a reaction with KOH.

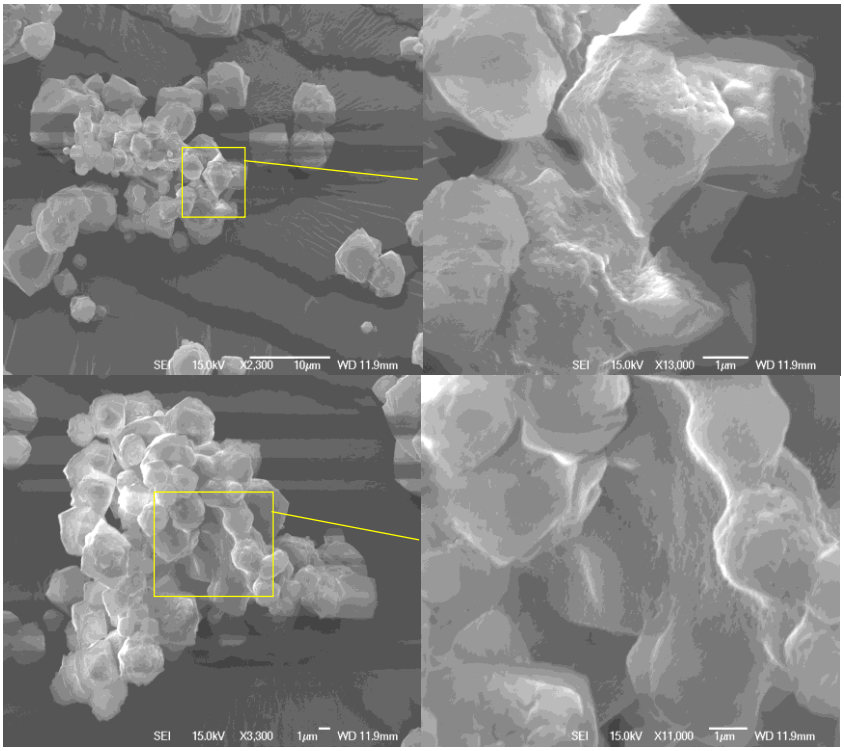
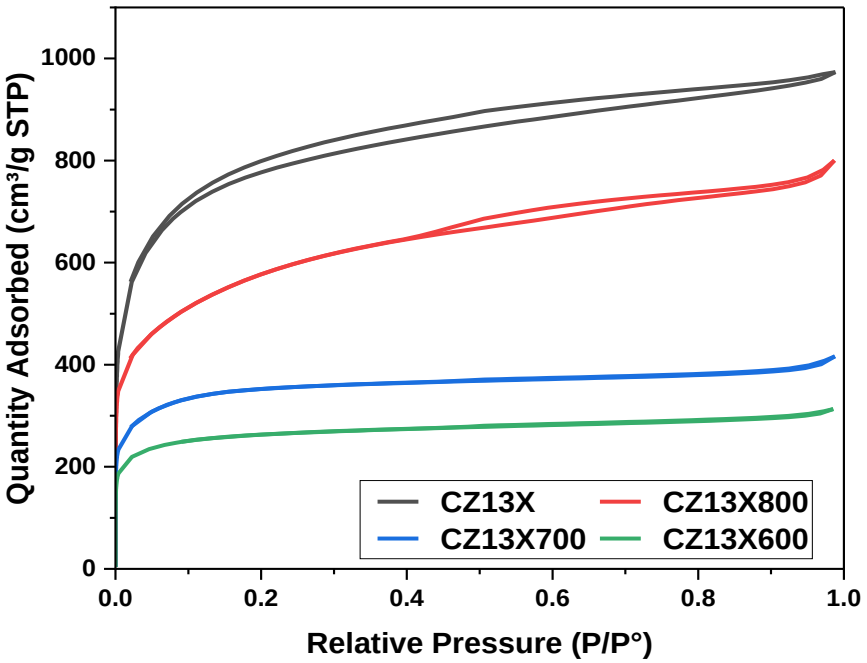


Figure 3-11 SEM images of calcined zeolite 13X with KOH heated at 700 °C under N2 flow

3.2.3. Surface area and porosity

The nitrogen sorption isotherms of the samples, as shown in Figure 3-12, are type I in accordance with IUPAC classification. Type I isotherms are usually found in microporous materials, which are accompanied by a high amount of gas adsorption at the very low relative pressures driven by pore-filling mechanisms in pore sizes less than 2nm.[20] The conventional ZTC sample,

exhibited high adsorption in the low-pressure range, and surface area of 2939 m^2/g with 55% of its surface area arising from micropores (Table 3-1). The surface area and pore volume of the conventional ZTC are close to those of ZTCs prepared at similar conditions by Masika (ca. 3300 m^2/g and 1.6 cm^3/g).[10, 21]-For samples prepared via treatment with KOH at 600–800°C, the surface area decreased to 34–71% of that of conventional ZTC. As mentioned above for the XRD patterns, the peak at $2\theta = 7^o$ was shifted and decreased in intensity, accompanied by a loss of pore sizes of around 1 nm (Figure 3-12) in the PSD curves. Also, the small peak at 23° confirmed a formation of stacked graphitic layers, which could be another reason for the decrease in surface area. According to these results, KOH seems to lead to the destruction of the crystal structure of zeolite X, or there was possibly a targeted activation of the carbon inside the zeolite cages of a size of ~1.4 nm.



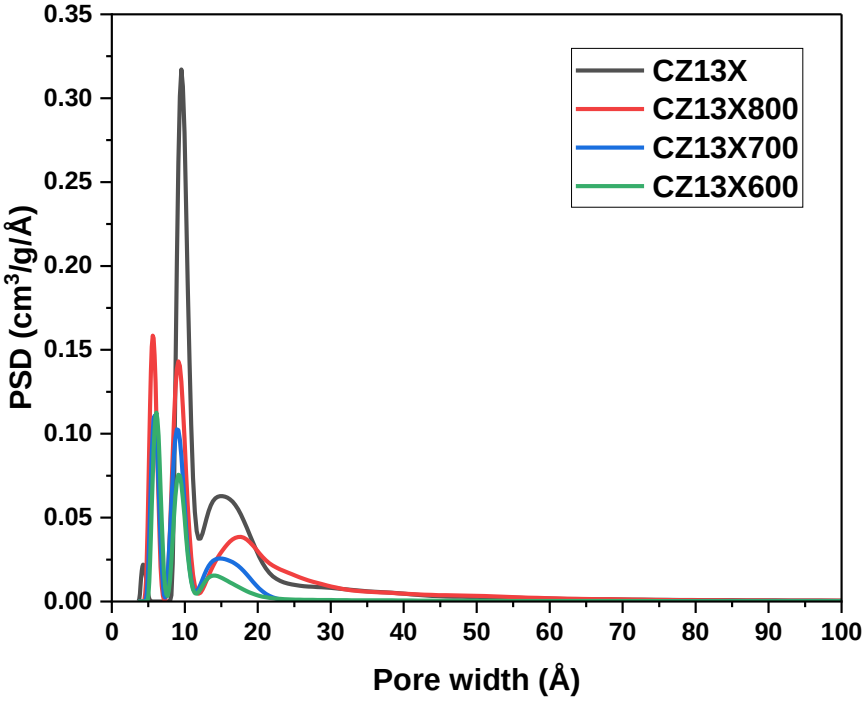


Figure 3-12 Nitrogen isotherms and 2D-NLDFT PSD of the samples

Table 3-1 Textural properties of the samples

	Surface area [a]					Pore volume [b]					
Sample	**SA**	**S_μ**	**S_{DR}**	**S_{meso}**	**S_μ**	**V_t**	**V_{DR}**	**V_μ**	**V_{meso}**	**V_μ**	**V_{DR}**
	m^2/g	**m^2/g**	**m^2/g**	**m^2/g**	**%**	**cm^3/g**	**cm^3/g**	**cm^3/g**	**cm^3/g**	**%**	**%**
CZ13X	2939	1610	3442	1329	55	1.51	1.22	0.62	0.89	41	81
CZ13X600	1012	909	1110	103	90	0.49	0.4	0.37	0.12	76	82
CZ13X700	1351	1001	1427	350	74	0.65	0.51	0.39	0.26	60	78
CZ13X800	2101	783	2186	1318	37	1.24	0.78	0.31	0.93	25	63

[a] SA is the BET surface area, S_μ is the micropore surface area, S_{DR} is the Dubinine-Radushkevich surface area, Smeso is the mesopore surface area obtained by subtracting S_μ from SA, and % is the percentages of micropore surface area (Dubinine-Radushkevich).

[b] Vt is the total pore volume, V_{DR} is the Dubinine-Radushkevich micropore volume, V_μ is micropore volume, Vmeso is the mesopore surface area obtained by subtracting V_{micro} from Vt, and % is the percentages of micropore volumes.

3.2.4. Methane uptake

The gravimetric excess uptake isotherms of the conventional and KOH-treated samples were obtained under the same conditions, which included measuring them at room temperature (25°C) and applying a pressure of 0–100 bar. It was expected that the uptake of the KOH treated samples would be lower than that of the conventional sample since the treatment decreased the porosity of the samples. The excess methane uptake isotherms of the samples are displayed in Figure 3-13 and Table 3-2. The conventional ZTC sample has the highest gravimetric uptake compared to the samples heat-treated with KOH in the range of 5–100 bar; however, there is a clear difference in the capacity for gravimetric uptake between the conventional sample and the heat-treated samples. The difference grew steadily as the pressure increased, reaching its maximum at 70 bar. Thus, at 70 bar, the difference was between 24 and 30%.

The excess methane uptake capacity of the conventional ZTC sample (Table 3-2) was 14.0 and 14.9 mmol/g at 65 and 100 bar, respectively, which is close to the values reported in the literature for such material. At 25°C and maximum pressure (90 bar), the methane uptake capacity of a ZTC-3 sample was reported to be 14.1 mmol/g,[22] which is very similar to our results. The uptake obtained by FAU-ZTC at 65 bar showed 0.26 g/g capacity,[23] near to that of the conventional sample (0.23 g/g) at the same pressure and temperature.

The difference in the gravimetric uptake between the treated samples with KOH at different temperatures was small, see Table 3-2. The maximum differences were 0.4, 1.0, and 1.3 mmol/g at 35, 65, and 100 bar, respectively. However, the differences in the volumetric uptake between them were 28, 28, and 26 cm^3_{STP}/cm^3 at 35, 65, and 100 bar, respectively. Since the volumetric uptakes are dependent on the packing density, which mainly depends on the overall sample's textural properties,[24-27] the treated samples showed higher volumetric uptake capacities compared to the conventional ZTC. The amount of the increase in the total volumetric uptake compared to the conventional ZTC was 24, 26, and 30 cm^3_{STP}/cm^3 at 35, 65, and 100 bar, respectively. The treated sample at 800 °C showed the closet gravimetric and volumetric uptake capacities to the conventional ZTC. According to the TGA results, this closeness to conventional ZTC uptake capacity is due to the removal of most of the template for CZ13X800 compared to CZ13X600 and CZ13X700, which were composed of 17 and 8% residues, respectively, resulting in pore blocking.

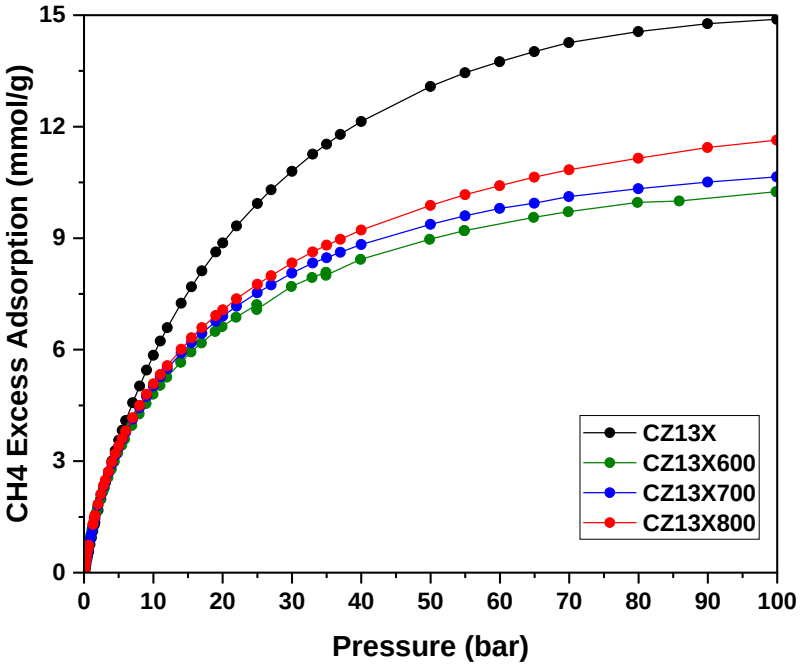


Figure 3-13 Methane uptake of the samples at 25°C

Table 3-2 Methane uptake of the samplesKOH-treated

Sample	CH_4 uptake mmol/g			Total CH_4 uptake [a] g/g			Total CH_4 uptake [a, b] $cm^3_{STP}.cm^{-3}$		
	35 bar	65 bar	100 bar	35 bar	65 bar	100 bar	35 bar	65 bar	100 bar
CZ13X	11.5	14.0	14.9	0.19	0.23	0.24	164	199	212
CZ13X600	8.9	9.6	10.3	0.13	0.15	0.16	188	225	242
CZ13X700	8.5	9.9	10.7	0.14	0.16	0.17	191	225	241
CZ13X800	8.8	10.6	11.6	0.14	0.17	0.19	163	197	216

[a] Total uptake was calculated from; $\theta_T = \theta_{Exc} + d_{CH4} \times V_T$, where; θ_T is the total uptake, θ_{Exc} is the excess uptake, d_{CH4} is the density (g/cm^3) of methane gas under the prevailing temperature and pressure, and V_T is the total pore volume (cm^3/g) of the samples from nitrogen isotherms.

[b] Volumetric uptake obtained from the calculated packing densities using $\rho D_{theo} = 1 / (VT + 1/\rho)$, where; ρD_{theo} is the theoretical packing density (g/cm^3), V_T is the total pore volume (cm^3/g) of the samples from nitrogen isotherms, and ρ is the He density (skeleton density) of the samples (ZTCs: 1.9 g/cm^3, activated carbons: 1.5 g/cm^3).

Methane uptake results were compared with other carbon samples synthesised by the activation of different carbon sources: biomass (ginkgo leaves) and synthetic organic salt (potassium hydrogen phthalate). Figure 3-15 summarise the uptake results of CZ13X and CZ13XT in comparison with the other activated carbons that were prepared in Chapters 4 and 5. Their synthesis procedures and characterisation details will be found in the next chapters. In Table 3-3, there is an extra comparison with materials from other references.

Table 3-3 Methane uptake and working capacities of the samples and different carbons

Sample	**Total CH_4 uptake (g/g) [a]**			**Total CH_4 uptake ($cm^3_{STP}.cm^{-3}$) [a, b]**			**Working capacity [c] (w_c/θ_T) [d] ($cm^3_{STP}.cm^{-3}$)**		
	35bar	65bar	100bar	35bar	65bar	100bar	35-5	65-5	100-5
CZ13X	0.19	0.23	0.24	164	199	212	113(0.69)	149(0.75)	162(0.77)
CZ13X600	0.13	0.15	0.16	188	225	242	112(0.60)	149(0.66)	166(0.69)
CZ13X700	0.14	0.16	0.17	191	225	241	115(0.60)	148(0.66)	165(0.69)
CZ13X800	0.14	0.17	0.19	163	197	216	100(0.61)	134(0.68)	153(0.71)
AcGLF-2ox-900 [e]	0.18	0.21	0.22	134	155	162	79(0.59)	101(0.65)	108(0.67)
AcGLHC300-4800 [e]	0.18	0.22	0.24	117	144	157	77(0.66)	104(0.72)	117(0.75)
AcGLF-2KOH-800 [e]	0.17	0.19	0.19	130	148	153	74(0.57)	91(0.62)	96(0.64)
AcGLFw-2KOH-800 [e]	0.17	0.19	0.19	126	141	144	68(0.54)	83(0.59)	86(0.60)
PU0.5900 [f]	0.18	0.21	0.22	133	155	165	76(0.57)	98(0.63)	108(0.65)
PU0.25900 [f]	0.17	0.20	0.21	145	169	182	81(0.56)	105(0.62)	118(0.65)
AX-21[28]				154	203	237	101(0.66)	151(0.74)	185(0.78)
MOF-5[28]				150	215	256	121(0.81)	186(0.87)	227(0.89)
PCN-14[28]				202	239	264	121(0.60)	158(0.66)	183(0.69)
HKUST-1[28]				225	263	281	145(0.65)	183(0.70)	201(0.72)
Mg2(dobdc)[28]				200	230	252	106(0.53)	137(0.59)	159(0.63)
Co2(dobdc)[28]				221	249	259	103(0.47)	131(0.53)	141(0.55)
Ni2(dobdc)[28]				231	260	277	105(0.45)	133(0.51)	151(0.54)

[a] Total uptake was calculated from; $\theta_T = \theta_{Exc} + d_{CH4} \times V_T$, where; θ_T is the total uptake, θ_{Exc} is the excess uptake, d_{CH4} is density (g/cm^3) of methane gas, and V_T is the total pore volume (cm^3/g) of the samples from nitrogen isotherms.

[b] Volumetric uptake obtained from the calculated packing densities using $\rho D_{theor} = 1 / (VT + 1/\rho)$, where; ρD_{theor} is the theoretical packing density (g/cm^3), V_T is the total pore volume (cm^3/g) of the samples from nitrogen isotherms, and ρ is the He density (skeleton density) of the samples (ZTCs: 1.9 g/cm^3, activated carbons: 1.5 g/cm^3).

[c] Working capacity is the difference in uptake between the uptake at different pressures (35, 65, and 100) bar and the uptake at 5 bar. The values in parenthesis [d] represent the ratio of working capacity 'w_c' ($cm^3_{STP}.cm^{-3}$) to total uptake (storage capacity) 'θ_T' ($cm^3_{STP}.cm^{-3}$).

[e] Activated carbons derived from biomass sources, [f] are N-doped activated carbons derived from organic salts.

Based on the data in aterials from *other references.*

Table 3-3 Methane uptake and working capacities of the samples and different carbons

Sample	**Total CH4 uptake (g/g) [a]**			**Total CH4 uptake (cm3STP.cm-3) [a, b]**			**Working capacity [c] (*wc/θT)* [d] (cm3STP.cm-3)**		
	35bar	65bar	100bar	35bar	65bar	100bar	35-5	65-5	100-5
CZ13X	0.19	0.23	0.24	164	199	212	113(0.69)	149(0.75)	162(0.77)
CZ13X600	0.13	0.15	0.16	188	225	242	112(0.60)	149(0.66)	166(0.69)
CZ13X700	0.14	0.16	0.17	191	225	241	115(0.60)	148(0.66)	165(0.69)
CZ13X800	0.14	0.17	0.19	163	197	216	100(0.61)	134(0.68)	153(0.71)
AcGLF-2ox-900 [e]	0.18	0.21	0.22	134	155	162	79(0.59)	101(0.65)	108(0.67)
AcGLHC300-4800 [e]	0.18	0.22	0.24	117	144	157	77(0.66)	104(0.72)	117(0.75)
AcGLF-2KOH-800 [e]	0.17	0.19	0.19	130	148	153	74(0.57)	91(0.62)	96(0.64)
AcGLFw-2KOH-800 [e]	0.17	0.19	0.19	126	141	144	68(0.54)	83(0.59)	86(0.60)
PU0.5900 [f]	0.18	0.21	0.22	133	155	165	76(0.57)	98(0.63)	108(0.65)
PU0.25900 [f]	0.17	0.20	0.21	145	169	182	81(0.56)	105(0.62)	118(0.65)
AX-2128				154	203	237	101(0.66)	151(0.74)	185(0.78)
MOF-528				150	215	256	121(0.81)	186(0.87)	227(0.89)
PCN-1428				202	239	264	121(0.60)	158(0.66)	183(0.69)
HKUST-128				225	263	281	145(0.65)	183(0.70)	201(0.72)
Mg2(dobdc)[28]				200	230	252	106(0.53)	137(0.59)	159(0.63)
Co2(dobdc)[28]				221	249	259	103(0.47)	131(0.53)	141(0.55)
Ni2(dobdc)[28]				231	260	277	105(0.45)	133(0.51)	151(0.54)

[a] Total uptake was calculated from; $\theta T = \theta Exc + dCH4 \times VT$, where; θT is the total uptake, θExc is the excess uptake, *dCH4* is density (g/cm3) of methane gas, and *VT* is the total pore volume (cm3/g) of the samples from nitrogen isotherms.

[b] Volumetric uptake obtained from the calculated packing densities using $\rho Dtheor = 1 / (VT+1/\rho)$, where; $\rho Dtheor$ is the theoretical packing density (g/cm3), *VT* is the total pore volume (cm3/g) of the samples from nitrogen isotherms, and ρ is the He density (skeleton density) of the samples (ZTCs: 1.9 g/cm3, activated carbons: 1.5 g/cm3).

[c] Working capacity is the difference in uptake between the uptake at different pressures (35, 65, and 100) bar and the uptake at 5 bar. The values in parenthesis [d] represent the ratio of working capacity '*wc'* (cm3STP.cm-3) to total uptake (storage capacity) '$\theta T'$ (cm3STP.cm-3).

[e] Activated carbons derived from biomass sources, [f] are N-doped activated carbons derived from organic salts.

, the conventional ZTC sample, CZ13X, displayed the highest working capacity under our measurement conditions, delivering 77% of the stored gas at 5 bar after being subjected to the maximum charging pressure of 100 bar. This result was determined by comparing the sample's working capacity at 5, 35, 65 and 100 bar, as shown in. The working capacities of the treated samples with KOH were lower than that of the conventional ZTC due to their lower porosities. The CZ13X800 showed higher working capacity than CZ13X600 and CZ13X700. The activated carbon, AcGLHC300-4800, showed the same amount of gravimetric methane uptake as conventional ZTC when subjected to the same conditions as the other carbons in the table at 100 bar. The total porosity of the conventional ZTC enhanced its volumetric uptake and, thus, the working performance of this sample among the other adsorbents, even those with the same gravimetric uptake, as can be seen in Table 3-3. A comparison of the working capacity with the common adsorbent in the literature, revealed that the delivering percentage of the conventional ZTC is comparable with that of the activated carbon AX-21[28] but with a lower working capacity by 23 $cm^3_{STP}.cm^{-3}$. Moreover, another comparison showed the low volumetric and working capacities of the conventional ZTC compared to MOFs adsorbents (MOF-5 and HKUST-1) that showed high CH_4 uptake capacities (256 and 281 $cm^3_{STP}.cm^{-3}$ uptake capacity at 100 bar, respectively) and working capacities as well (227 and 201 $cm^3_{STP}.cm^{-3}$ uptake capacity between 5 and 100 bar, respectively).[28] Despite the superiority of the MOFs capacities compared to our sample, the mechanical stability of the MOFs are poor, as it is known,[29] compared to the higher mechanical stability of the ZTCs and the carbon samples, in general.

Since the poor mechanical stability cause them to lose their high porosities and uptake capacities after a few cycles of use.

The methane uptake capacity is basically controlled by the pore size; this is due to the lack of a dipole or quadrupole in the symmetrical CH_4 molecule.[30] The analysis of the uptake results from the viewpoint of the pore size effect showed that the uptake at low pressures is governed by the presence of smaller pores, < 9 Å. The uptake on the samples in the pressure range 0–5 bar (Figure 3-14) showed similar gravimetric capacities, but after that, i.e., at pressures higher than 5 bar, the capacity varied (see Figure 3-13) according to the sample's surface area and pore volume.

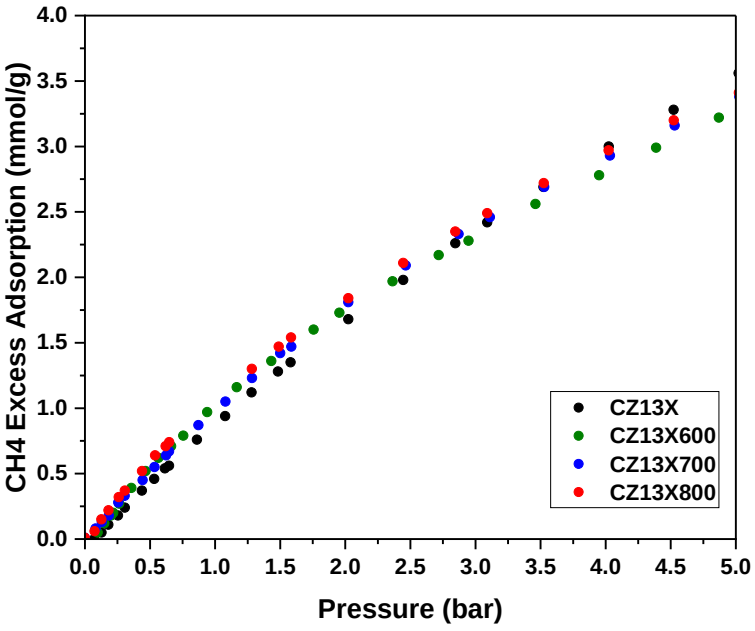
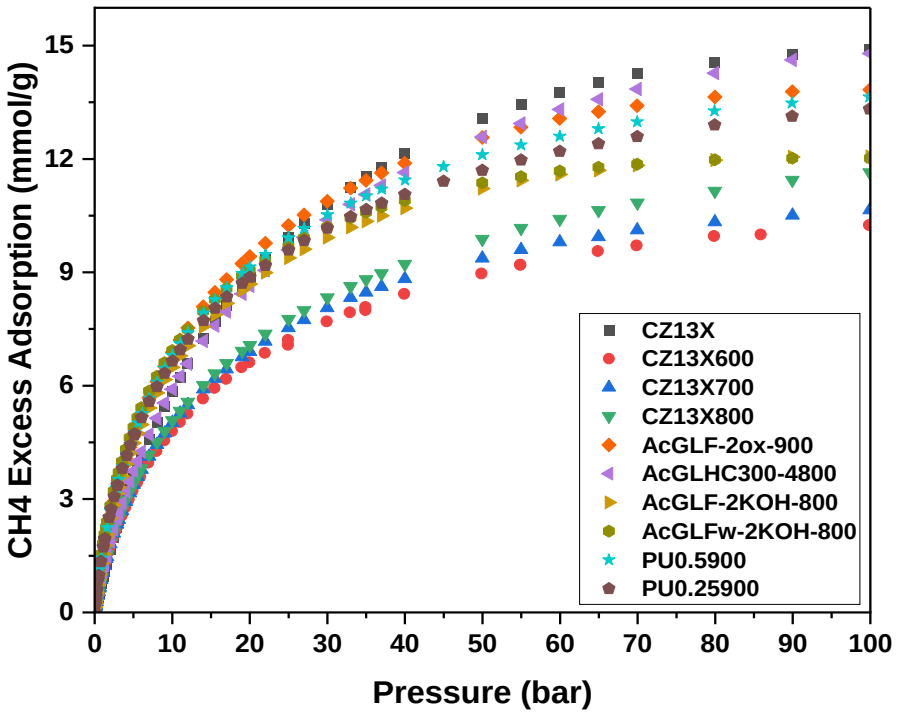


Figure 3-14 Methane uptake of the samples at 25 °C

CZ13X, CZ13XT, and activated carbon samples lied in two sets of gravimetric isotherms at low pressure, giving two uptake capacities in the pressure range

0─5 bar, as shown in Figure 3-15. In these findings we notice that the gravimetric uptake of samples and the activated carbon AcGLHC300-4800 had similar capacities in the pressure range of 0–5 bar (Figure 3-15). On the other hand, the other activated carbons in the figure showed another similar behaviour but with higher capacities in the same pressure range. The reason for these two different capacities in the 0–5 bar range could be caused by two ranges of porosities. According to Figure 3-15 and Figure 3-16, a greater number of micropores with pore sizes smaller than 0.9 nm improved the adsorption up to 5 bar, whereas the uptake at maximum pressure, 100 bar, increased as presence of the small mesopores increased. However, the pore size may not be the only factor that controls the adsorption at low pressure in the samples under study.



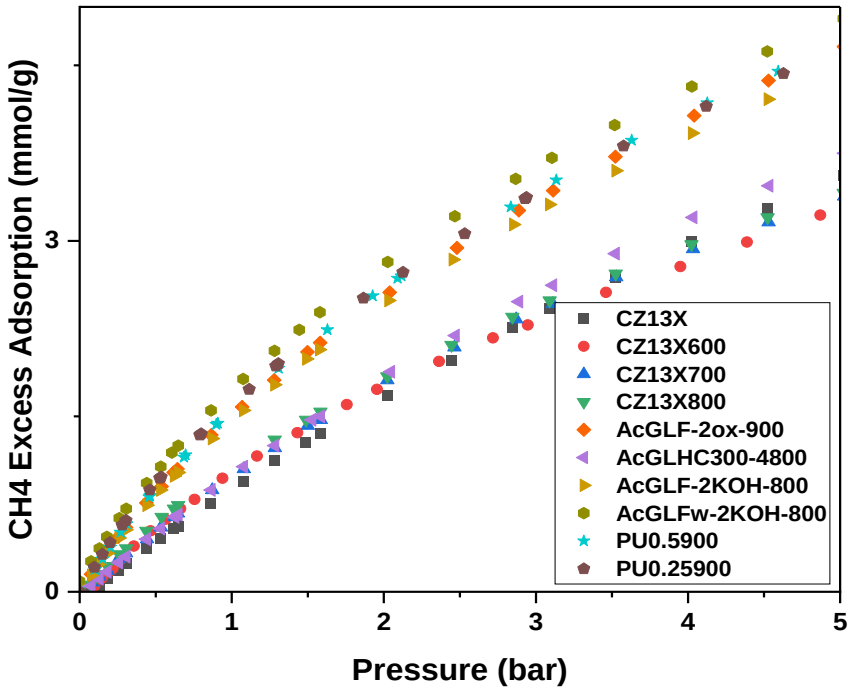


Figure 3-15 Methane uptake of the samples and activated carbons from biomass and metal organic salt sources at 25 °C, until 100 bar and 5 bar

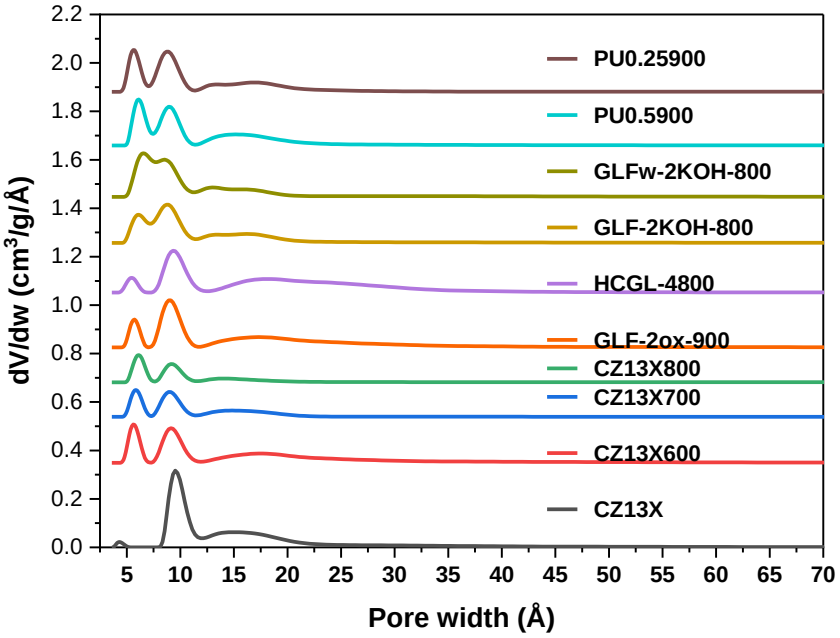


Figure 3-16 2D-NLDFT pore size distribution using a heterogeneous surface model

The relationships between the gravimetric uptake and the surface areas and the pore volumes derived from the samples and other activated carbons are presented in Figure 3-17-Figure 3-22. Figure 3-17 and Figure 3-20, show no clear effect of the micropore volumes and micropore surface area on the CH_4 uptakes at 65 and 100bar. Figure 3-18 and Figure 3-21, show that the CH_4 uptakes at 35, 65, and 100 bar are dependent on the mesopore volumes and mesopore surface area. Figure 3-19 and Figure 3-22, show that the CH_4 uptakes at 1 bar seem to be dependent on the total pore volumes and BET surface area, however, the uptakes at 35, 65, and 100 bar are clearly dependent on the same factors.

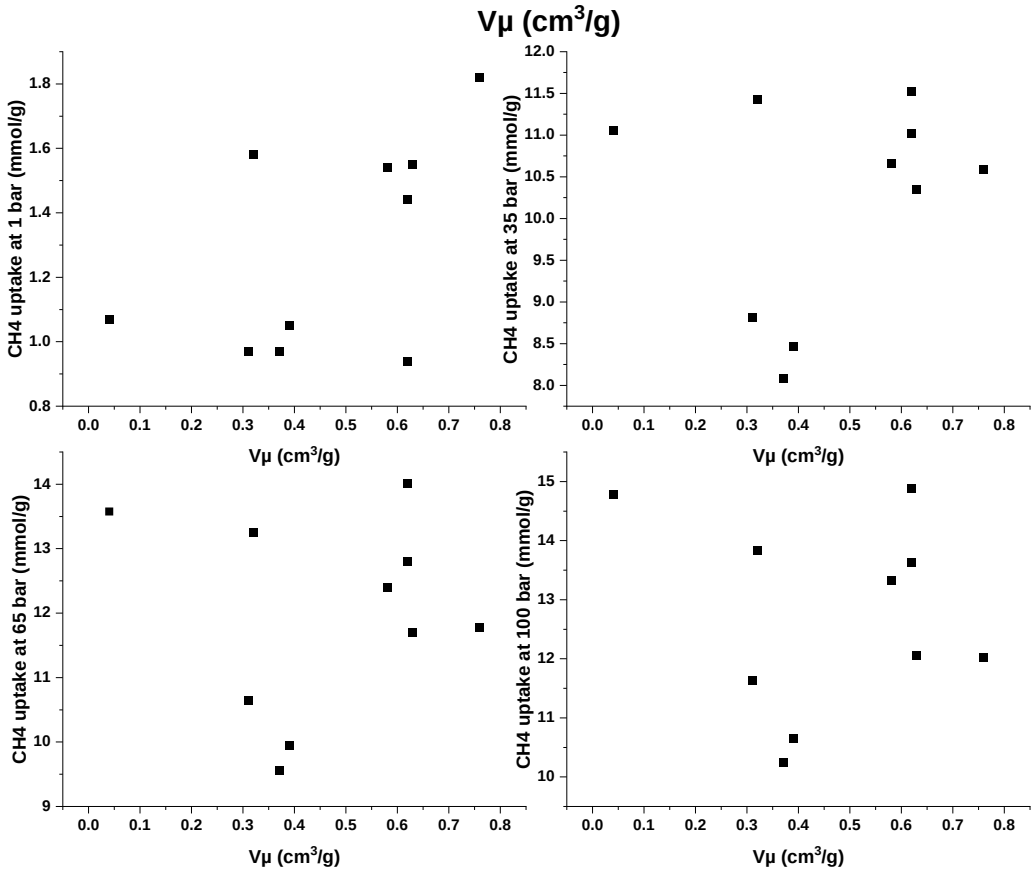


Figure 3-17 Methane uptake at 1, 35, 65, and 100 bar as a function of the t-plot micropore volume of the samples and activated carbons from biomass and metal organic salt sources at 25 °C

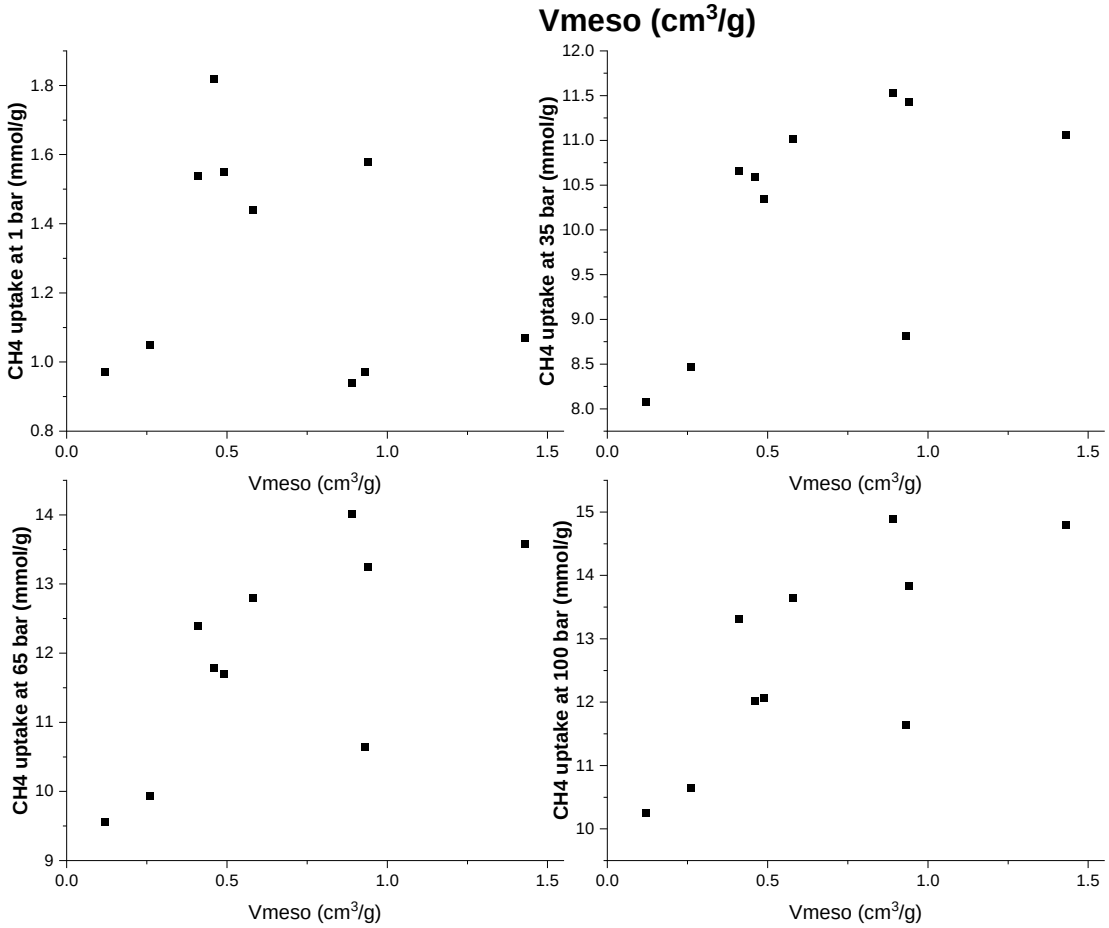


Figure 3-18 Methane uptake at 1, 35, 65, and 100 bar as a function of the mesopore volume of the samples and activated carbons from biomass and metal organic salt sources at 25 °C

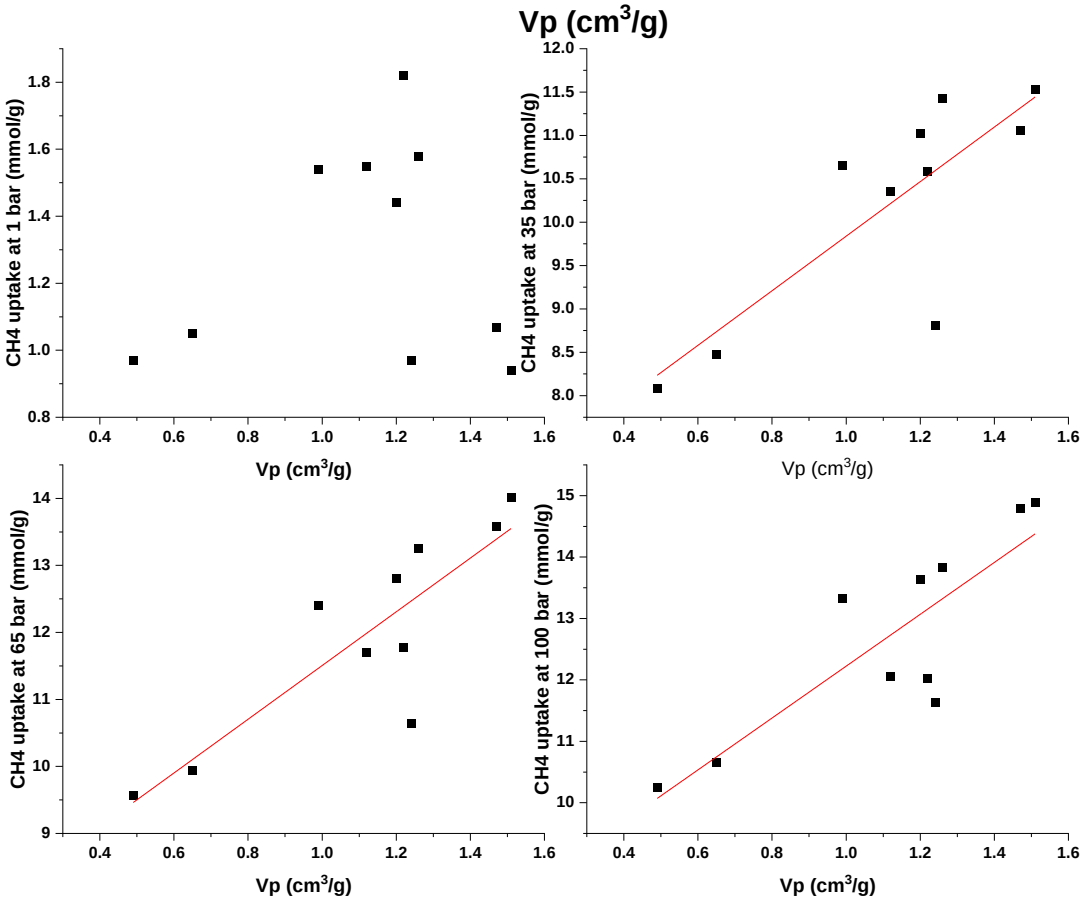


Figure 3-19 Methane uptake at 1, 35, 65, and 100 bar as a function of the total pore volume of the samples and activated carbons from biomass and metal organic salt sources at 25 °C

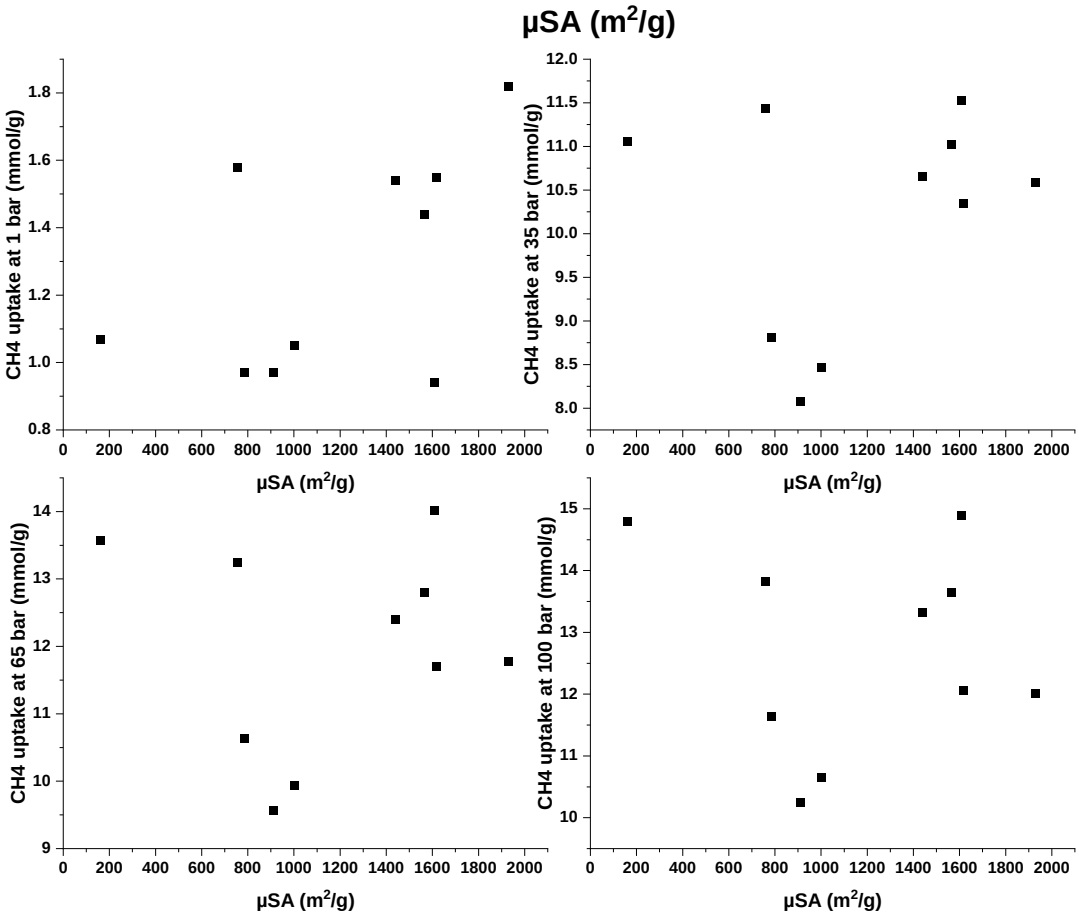


Figure 3-20 Methane uptake at 1, 35, 65, and 100 bar as a function of the t-plot surface area of the samples and activated carbons from biomass and metal organic salt sources at 25 °C

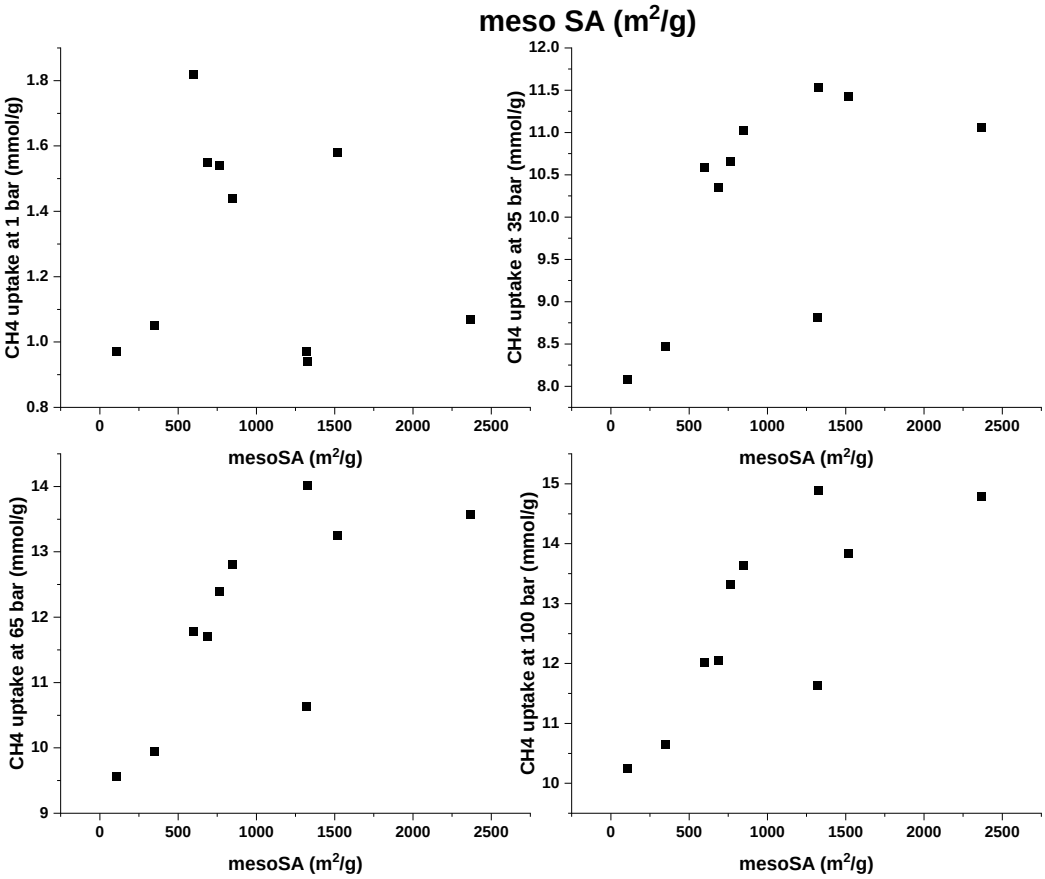


Figure 3-21 Methane uptake at 1, 35, 65, and 100 bar as a function of the mesopore surface area of the samples and activated carbons from biomass and metal organic salt sources at 25 °C

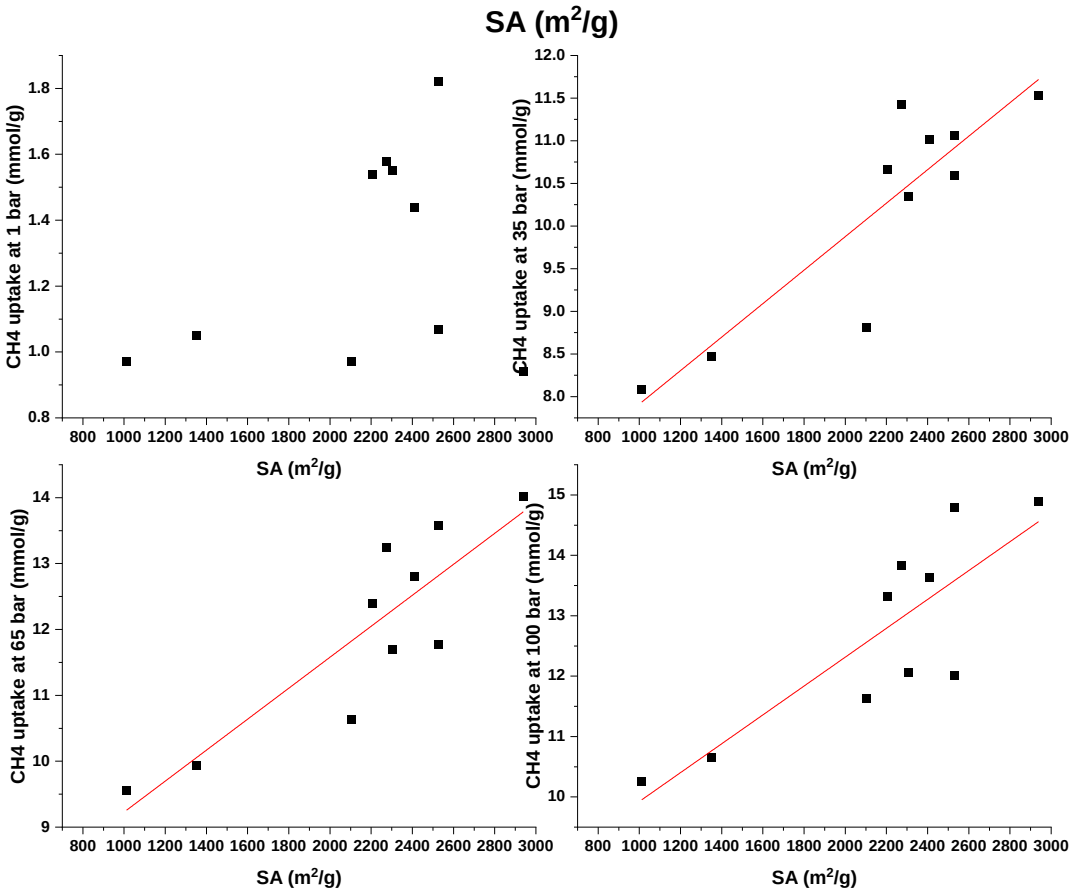


Figure 3-22 Methane uptake at 1, 35, 65, and 100 bar as a function of the BET surface area of the samples and activated carbons from biomass and metal organic salt sources at 25 °C

In summary, all the samples (i.e., CZ13X and CZ13XT) showed higher working capacity in the pressure ranges 5–35 bar, 5–65 bar, or 5–100 bar than the other carbons in the Table 3-3. The conventional ZTC sample CZ13X delivered 77% of its storage capacity and AcGLHC300-4800 delivered 75% of the adsorbed methane at 100 bar, as shown in the "$\underline{w_c/\theta_T}$" column; these two are the highest among the other samples in the table. In addition to micropores, these two samples had a lot of small mesopores and a large surface area, which enhanced

their delivering capacity. The samples that contain the majority of microporosity showed lower delivery capacity. The examined template removal in this study led to a decrease in the delivered storage capacity of the best removal condition (i.e., in CZ13X800) by 6% compared to the conventional sample. As can be seen in Figure 3-23, the conventional ZTC sample showed no change in capacity even after being subjected to three successive adsorption cycles, which is expected due to the high mechanical stability of ZTC[10, 21, 22] compared to the MOFs and other crystalline materials.

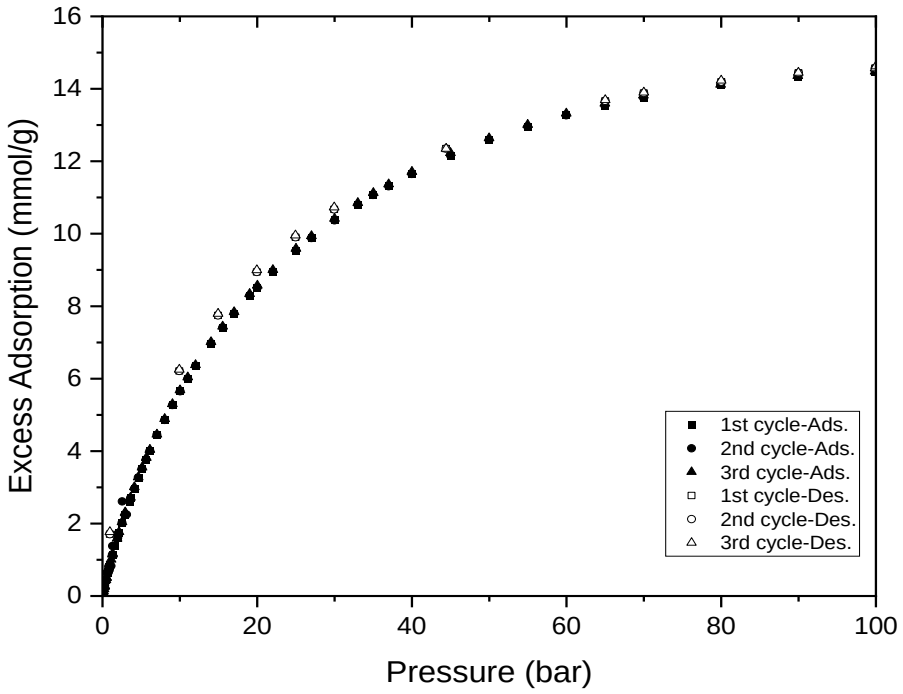


Figure 3-23 Three cycles of methane adsorption-desorption at room temperature on the conventional sample

4. Conclusion

In this study, the carbon/zeolite composites have been treated with KOH in an attempt to ease the removal of the template. In summary, the effect of KOH activation conditions on zeolite template removal from carbon/zeolite composites showed a partial removal after heating to 600°C with a 17 wt% residue of the template. This residue affected the porosity of this sample and thus also its methane uptake capacity. On the other hand, increase in temperature at which the KOH treated carbon/zeolite composite is heated to 800ºC facilitated removal of the template following dissolution using diluted HCl. Consequently, the porosity was improved by this enhanced removal of the template residues. The results showed that the template was removed by HCl without needing to use HF. The reaction between KOH and the template aided in dissolving the template by generating soluble species in HCl. Although the porosity of the carbons obtained from KOH treatment decreased compared to the conventional ZTC prepared with use of HF acid, they showed higher volumetric methane uptakes and working capacities of methane storage in the range of 5–100 bar compared to other carbon adsorbents.

Acknowledgment

I'm grateful to the Nanoscale and Microscale Research Centre (nmRC) at the University of Nottingham (especially Grace Belshaw, who imaged some of the samples for this project). I would like to thank Tara Lemercier, who performed TGA analysis of the samples.

5. References

1. Z. Yang, Y. Xia and R. Mokaya, *Journal of the American Chemical Society*, 2007, **129**, 1673-1679.
2. N. Alam and R. Mokaya, *Energy & Environmental Science*, 2010, **3**, 1773-1781.
3. J. Miao, Z. Lang, T. Xue, Y. Li, Y. Li, J. Cheng, H. Zhang and Z. Tang, *Advanced Science*, 2020, **7**, 2001335.
4. E. Braun, Y. Lee, S. M. Moosavi, S. Barthel, R. Mercado, I. A. Baburin, D. M. Proserpio and B. Smit, *Proceedings of the National Academy of Sciences*, 2018, **115**, E8116.
5. F. O. M. Gaslain, J. Parmentier, V. P. Valtchev and J. Patarin, *Chemical Communications*, 2006, DOI: 10.1039/B512002K, 991-993.
6. Y. Xia, Z. Yang and R. Mokaya, *Nanoscale*, 2010, **2**, 639-659.
7. H. Nishihara and T. Kyotani, *Chemical Communications*, 2018, **54**, 5648-5673.
8. C. Ducrot-Boisgontier, J. Parmentier and J. Patarin, *Microporous and Mesoporous Materials*, 2009, **126**, 101-106.
9. E. Masika and R. Mokaya, *Chemistry of Materials*, 2011, **23**, 2491-2498.
10. E. Masika and R. Mokaya, *Energy & Environmental Science*, 2014, **7**, 427-434.
11. K. Kim, T. Lee, Y. Kwon, Y. Seo, J. Song, J. K. Park, H. Lee, J. Y. Park, H. Ihee, S. J. Cho and R. Ryoo, *Nature*, 2016, **535**, 131-135.
12. Z. Yang, Y. Xia, X. Sun and R. Mokaya, *The Journal of Physical Chemistry B*, 2006, **110**, 18424-18431.
13. P. H. E. Centre, Hydrogen Fluoride and Hydrofluoric Acid (HF), https://assets.publishing.service.gov.uk/government/uploads/system/uploads/attachment_data/file/761014/Hydrogen_fluoride_toxicological_overview.pdf).
14. H. Park, S. K. Terhorst, R. K. Bera and R. Ryoo, *Carbon*, 2019, **155**, 570-579.
15. A. Medina, P. Gamero, J. M. Almanza, A. Vargas, A. Montoya, G. Vargas and M. Izquierdo, *Journal of Hazardous Materials*, 2010, **181**, 91-104.
16. F. R. D. de Andrade, M. T. A. G. Yogi, E. B. Gomes and M. C. Shinzato, *Environmental Earth Sciences*, 2020, **79**, 379.
17. L. Van Tendeloo, E. Gobechiya, E. Breynaert, J. A. Martens and C. E. A. Kirschhock, *Chemical Communications*, 2013, **49**, 11737-11739.
18. J. Wang and S. Kaskel, *Journal of Materials Chemistry*, 2012, **22**, 23710-23725.
19. N. Balahmar, A. M. Lowbridge and R. Mokaya, *Journal of Materials Chemistry A*, 2016, **4**, 14254–14266.
20. M. Thommes, K. Kaneko, A. V. Neimark, J. P. Olivier, F. Rodriguez-Reinoso, J. Rouquerol and K. S. Sing, *Pure and applied chemistry*, 2015, **87**, 1051-1069.

21. E. Masika and R. Mokaya, *Progress in Natural Science: Materials International*, 2013, **23**, 308-316.
22. N. P. Stadie, M. Murialdo, C. C. Ahn and B. Fultz, *Journal of the American Chemical Society*, 2013, **135**, 990-993.
23. S. Choi, M. A. Alkhabbaz, Y. Wang, R. M. Othman and M. Choi, *Carbon*, 2019, **141**, 143-153.
24. A. Altwala and R. Mokaya, *Energy & Environmental Science*, 2020, **13**, 2967-2978.
25. I. Alali and R. Mokaya, *Energy & Environmental Science*, 2022, **15**, 4710-4724.
26. A. Altwala and R. Mokaya, *Journal of Materials Chemistry A*, 2022, DOI: 10.1039/D2TA00421F.
27. M. E. Casco, M. Martínez-Escandell, E. Gadea-Ramos, K. Kaneko, J. Silvestre-Albero and F. Rodríguez-Reinoso, *Chemistry of Materials*, 2015, **27**, 959-964.
28. J. A. Mason, M. Veenstra and J. R. Long, *Chemical Science*, 2014, **5**, 32-51.
29. J. Yang, A. Sudik, C. Wolverton and D. J. Siegel, *Chemical Society Reviews*, 2010, **39**, 656-675.
30. D. Peredo-Mancilla, I. Ghouma, C. Hort, D. Bessieres and C. M. Ghimbeu, in *Char and Carbon Materials Derived from Biomass*, eds. M. Jeguirim and L. Limousy, Elsevier, 2019, DOI: https://doi.org/10.1016/B978-0-12-814893-8.00009-2, pp. 341-382.

Chapter 4 Synthesis and Characterisation of Porous Carbon from Biomass

Abstract

In this study, the synthesis of KOH-activated carbon from ginkgo leaves hydrochar is investigated. In addition to direct activation of the leaves, potassium oxalate is being studied as a milder activating agent for the activation of air-carbonised leaves. The carbon produced by direct activation of the leaves with potassium oxalate has nearly similar textural properties to the carbon produced from air-carbonised leaves. To determine the effect of the inorganic content on the porosity of the activated carbon, the activation of washed and unwashed char was compared; the results generally demonstrated that the impact of the inorganic content was modest.

The highest surface area (3366 m^2/g) was for the carbon prepared at KOH/hydrochar ratio of 4 for hydrochar prepared via hydrothermal carbonisation at 300 °C. This sample had the highest CO_2 uptake of 23 mmol/g at 25 ^oC and 20 bar.

1. Introduction

In recent years, attempts to control carbon dioxide emissions have gained a great deal of attention, as carbon dioxide is the principal human contributor to climate change.[1] Various strategies, such as moving from fossil fuels to renewable energy and capturing carbon, are being applied in order to reduce greenhouse gas emissions.[1-3] CO_2 capture by physical adsorption using porous carbons as

adsorbents is considered as a promising alternative technology to the traditional amine-based liquid absorption process. This is due to carbon's inexpensive cost, extensive availability, large surface area, easy-to-design pore structure, surface functionalization, and low regeneration energy.[4-8]

There are several techniques for manufacturing porous carbon. Typically, carbonisation of raw materials (biomass or synthetic sources) is followed by activation of the carbonised product.[9] The activation can be conducted by physical activation when oxidising gases such as carbon dioxide and steam are employed.[10] The gas is passed through appropriate precursors at high temperatures (800–1000 °C).[11] During this process, the carbon (the carbonised product) is transformed into carbon dioxide and carbon monoxide, which are then released with the consequence that pores are generated in the carbon structure. On the other hand, chemical activation is another method through which carbon may be activated. In chemical activation, the carbon precursor is mixed with an activating agent and heated at high temperatures (600–1000 °C) in an inert environment for a shorter time than in the physical activation.[10, 12] There are many activators used as activating agents, including nitric acid (HNO_3), sulfuric acid (H_2SO_4), phosphoric acid (H_3PO_4), potassium hydroxide (KOH), sodium hydroxide (NaOH), hydrogen peroxide (H_2O_2), zinc chloride ($ZnCl_2$), and potassium carbonate (K_2CO_3).[13, 14]

Biomass has become one of the most desirable starting material for porous carbon production, owing to renewability and cost-effectiveness. This chapter will focus on the synthesis and characterisation of porous carbons from biomass sources, namely ginkgo leaves. Ginkgo trees, which are seen as decorative trees,

have been widely planted everywhere along streets, in parks, etc. in many countries. The leaves and crop of ginkgo trees are employed for medical and nutritional applications.[15] Although the leaves are used for producing medical products, huge amounts are discarded as organic waste. Such waste, which is rich in carbon can be converted to carbon materials. Here we explore the synthesis of activated carbons from the ginkgo leaves using various carbonisation methods. Prior to activating the samples, hydrothermal carbonisation or flash air-carbonisation were employed to enrich the carbon content. The samples are investigated as CO_2 storage materials in a 0–20 bar pressure range at room temperature.

2. Experimental

2.1. Synthesis procedures

The biomass source in this study was ginkgo leaves, which were purchased from Amazon. Any remains of the stems or impurities were removed before grinding the leaves to a fine powder. The conversion methods of the ginkgo leaves to char and activated carbons are summarised in Scheme 1.

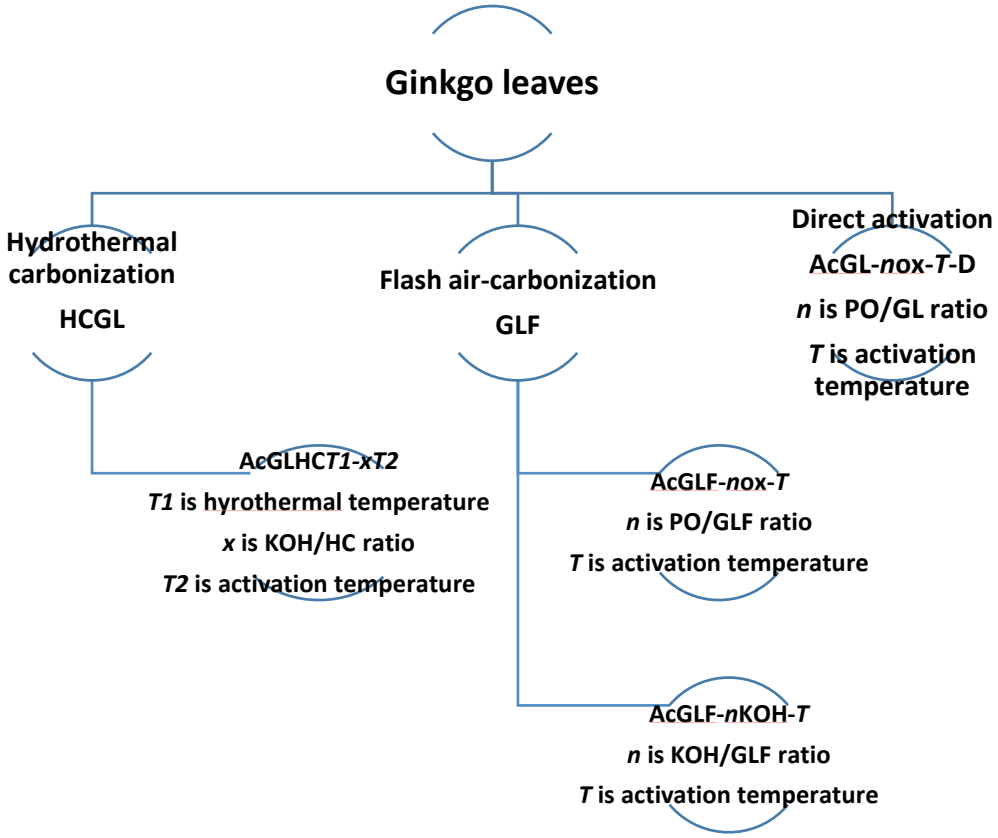
The powdered ginkgo leaves were converted to carbon using flash air carbonisation. Briefly, the ginkgo leave powder was placed in a boat and inserted into an oven. The temperature was raised to 400°C (at ramp rate of 10°C/min) under nitrogen gas flow. Once temperature arrived at 400°C, the gas flow was switched to air only for 4 minutes, then cooled down to room temperature under a nitrogen gas flow. The obtained carbon by this air carbonisation procedure was designated as GLF.

The air-carbonised ginkgo leaves (GLF) were activated using potassium oxalate (PO) at a PO/GLF weight ratio of 2. The activated carbons obtained were designated as AcGLF-.*n*ox-*T*, where *n* is the PO/GLF ratio and *T* is the activation temperature. The inorganic content of the washed, air-carbonised ginkgo leaves was removed so as to explore how it affected the activation process. The air-carbonised sample was washed in 2 M HCl for several days before being rinsed with water and dried overnight. In this case, the air carbonised sample designated as GLFw and the activated sample is denoted as AcGLFw-*n*ox-*T*. Simple direct activation of the powdered ginkgo leaves was also performed, and the resulting samples were designated as AcGL-*n*ox-*T*-D, where *n* is the PO/GL ratio and *T* is the activation temperature.

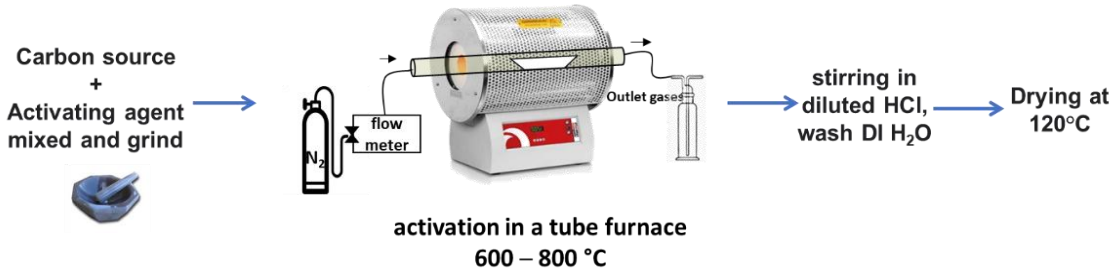
Hydrothermal carbonisation of the ginkgo leaves was also explored. To prepare the hydrochar, 3.2 g of ginkgo leaves and 10 ml of H_2O (320 g/l) were mixed in a 45-ml stainless steel autoclave, heated for 2 hours at 250°C and then allowed to cool to room temperature. The product (hydrochar) was recovered by filtration, washed several times with deionised water and then dried in an oven at 100°C overnight. The hydrochar was activated using potassium hydroxide, and the obtained samples were designated as AcGLHC*T1*-*xT2*. Here, *T1* denotes the temperature of hyrothermal treatment of the hydrochar, *x* denotes the KOH/hydrochar ratio and *T2* denotes the activation temperature.

The activation protocols for all the carbon sources in this chapter (raw leaves, hydrochar, or air-carbonised) are summarised in Scheme 2. For activation, the activating agents (PO or KOH) were thoroughly ground and mixed in an agate mortar with the carbon precursor followed by heating in a tube furnace to the

required temperature (at ramp rate of 5°C/min) and held for one hour under a N_2 atmosphere. After cooling, the activated samples were washed with 2 M HCl and then with distilled water until the filtrate attained neutral pH. The resulting samples were then dried at 100°C overnight.



Scheme 1 Conversion methods of ginkgo leaves to carbons



Scheme 2 The protocol for activating the carbon sources

2.2.Characterisation

Powder XRD patterns were performed at room temperature using a PANalytical X'Pert PRO diffractometer with a copper Kα and a monochromator source (λ = 1.5405Å) at 40 kV and 40 mA with a step size of 0.02 and a 50 s time step. The porosity and determination of textural properties were performed via nitrogen physisorption using a Micromeritics 3Flex sorptometer. Prior to analysis (at –196°C), the carbon samples were degassed under vacuum at 230°C for 32 or 16 h. The surface area was calculated using the BET method applied to adsorption data within the relative pressure (*P/Po*) range of 0.02–0.35. The total pore volume was determined from the nitrogen uptake at close to saturation pressure (*P/Po* = 0.99). The micropore surface area and micropore volume were determined via t-plot analysis. Micromeritics' SAIEUS software was used to obtain PSDs of the samples using the 2D-NLDFT method for heterogeneous surfaces. In order to create the most accurate PSD for carbons, the software's fitting parameter, *λ,* which affects the roughness of the PSD, was adjusted between 2.75 and 3.00. Scanning electron microscopy (SEM) images were recorded on a JEOL7000 microscope at 15 kV accelerating voltage. Thermogravimetric analysis (TGA) was performed on a TA Instruments Q6000 TGA system. CHN elemental analysis was performed using an Exeter Analytical CE-440 Elemental Analyser.

2.3. CO_2 uptake measurements

CO_2 uptake capacity of the carbons was measured with a Hiden Isochema Intelligent Gravimetric Analyser (IGA-003) at room temperature and up to 20 bar of pressure. Prior to conducting the CO_2 uptake experiments, the carbons

were outgassed for 3 h at 240 °C (at heating ramp rate 10°C/min) under vacuum. The measurements determined the excess CO_2 uptake directly.

3. Results

To convert the ginkgo leaves to activated carbon, first the powdered leaves were mixed and ground with KOH and heated to different temperatures to examine the easiest and most direct way to prepare the activated carbon. The yield from this approach was mostly nil and thus insufficient for any further analysis. Thus, the activation of the hydrochar of the ginkgo leaves was examined. Because of the corrosive properties of KOH on the activation equipment, impurities were produced when KOH was employed. Figure 4-1 depicts XRD peaks of alumina, which is the material of the combustion/activation boat, as a result of the harsh effect of KOH during the activation. In order to avoid corrosion of the combustion boat and any contaminants that could come from the corrosion, it was preferred to utilise PO, a milder activation agent. Air-carbonisation was chosen due to its high carbon yield and the avoidance of extra steps, such as filtration, required in hydrothermal carbonisation.[16] The XRD investigation, as depicted in Figure 4-1, shows the presence of calcium salts in the air-carbonised leaves; thus, their impact on the porosity of the activated carbon was briefly investigated.

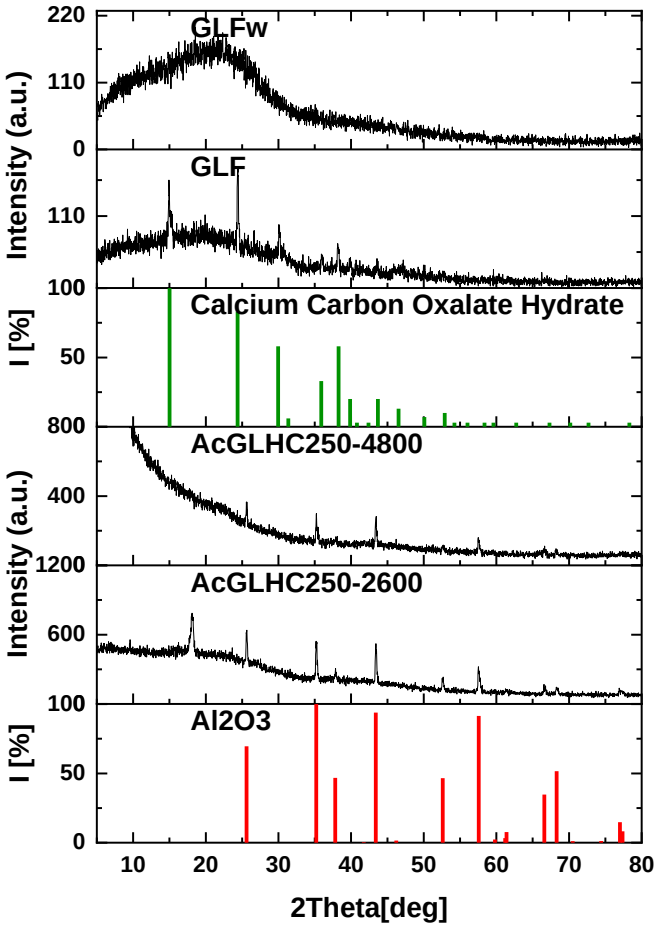


Figure 4-1 PXRD patterns of some activated carbons derived from the hyrochars of ginkgo leaves before an extra HCl wash and the patterns of washed and unwashed air-carbonised ginkgo leaves

3.1.Carbons derived from ginkgo leaves hydrochar

3.1.1. Nature, textural properties and elemental composition of carbons

The hydrochars prepared hydrothermally at 250 or at 300°C produced a filtrate with a high concentration of yellow pigments (see Figure 4-2). The yellow solution may contain flavonoids, which can be examined and recycled by concentration to be a source of carbon[17, 18] for future optimisation.



Figure 4-2 Photographic image of the yellow colour of filtrate after hydrochar filtration

The hydrothermal carbonisation at 250°C for 2 hours increased the elemental C content by 15%, while O decreased by 14% and N by ca. 1%, according to the elemental composition of the raw leaves and the hydrochar in Table 4-1. Likewise, carbonisation at higher temperature of 300°C increased the C content by 21%, while O decreased by 19% and N by ca. 1%, compared to the raw leaves. However, the H content was largely unchanged by the hydrothermal carbonisation, which is consistent to what has previously been reported.[19, 20] In regard to the yield of the obtained hydrochar, it decreased by increasing the carbonisation temperature from 61% for 250°C to 50% for 300°C.

The elemental composition of KOH-activated hydrochars shows that the C content of activated carbons ranges from 76 to 88 wt%. The maximum C content (88 wt%) is observed for carbon activated (AcGLHC300-4800) from HCGL300, which has a greater carbon content, compared to that from HCGL250 (AcGLHC250-4800). The H/C atomic ratio of activated carbons is significantly lower than that of hydrochars as a result of the greater C content and the significant decrease in H content. Similarly, the N/C and O/C ratios exhibit a significant drop in the samples following activation.

Table 4-1 elemental compositions (CHN) of raw ginkgo leaves, their hydrochars and the activated samples

	Chemical composition						
Sample	**C%**	**H%**	**N%**	**O%**	**O/C**	**N/C**	**H/C**
Raw GL	45.4	6.1	4.2	44.3	0.7	0.08	1.6
GLHC250	60.5	5.7	3.1	30.8	0.4	0.04	1.1
GLHC300	66.0	6.2	2.9	24.9	0.3	0.04	1.1
AcGLHC250-2-600	76.4	1.2	1.8	20.6	0.2	0.02	0.2
AcGLHC250-2-700	84.0	0.6	1.1	14.3	0.1	0.01	0.1
AcGLHC250-2-800	87.8	0.2	0.4	11.5	0.1	0	0
AcGLHC250-4-600	64.7	0.4	0.2		0.4	0	0.1
AcGLHC250-4-800	86.2	0.4	0.2	13.2	0.1	0	0.1
AcGLHC300-4-600							
AcGLHC300-4-800	88.2	0.1	0.2	11.5	0.1	0	0

The porosity of activated hydrochar using KOH (Table 4-2) showed an increase in surface area as the activation or carbonisation temperatures increased and as the amount of KOH increased. All the nitrogen isotherms of the activated samples were Type I typical of microporous materials (Figure 4-3). The total surface area is in the range of 1428–3366 m^2/g with pore volumes of between 0.61 and 1.65 cm^3/g, both of which are moderate to high compared to other porous carbons.[21,22] The activated samples at 800°C and KOH/hydrochar ratio of 4 exhibited high surface area, 2529 and 3366 m^2/g, respectively, from hydrochars carbonised at 250 and 300°C. As a result, the PSD (Figure 4-3) showed significant broadening of the pores in the range 12 to ca. 20Å in these two samples. More discussion of the effects of the elemental composition of the precursors on the porosity will be in Section 3.3.

Table 4-2 Textural properties of the activated hydrochars

	Surface area [a]		Pore volume [b]	
Sample	**SA_{BET} (S_{micro})**	**S_{micro}**	**V_t (V_{micro})**	**V_{micro}**
	m^2/g		**cm^3/g**	
AcGLHC250-2-600	1428 (1287)	90%	0.61 (0.50)	82%
AcGLHC250-2-700	1617 (1448)	85%	0.73 (0.53)	73%
AcGLHC250-2-800	2296 (1309)	57%	1.09 (0.52)	48%
AcGLHC250-4-600	1504 (969)	64%	0.67 (0.38)	57%
AcGLHC250-4-800	2529 (160)	6%	1.47 (0.04)	3%
AcGLHC300-4-600	1796 (1406)	78%	0.76 (0.56)	74%
AcGLHC300-4-800	3366 (2705)	80%	1.65 (1.22)	74%

a BET surface area (SA), in parenthesis: the micropore surface area (Smicro), and the proportion (%) of micropore surface area. b Total pore volume (Vt), in parenthesis: the micropore volume (Vm), and the proportion (%) of micropore volume

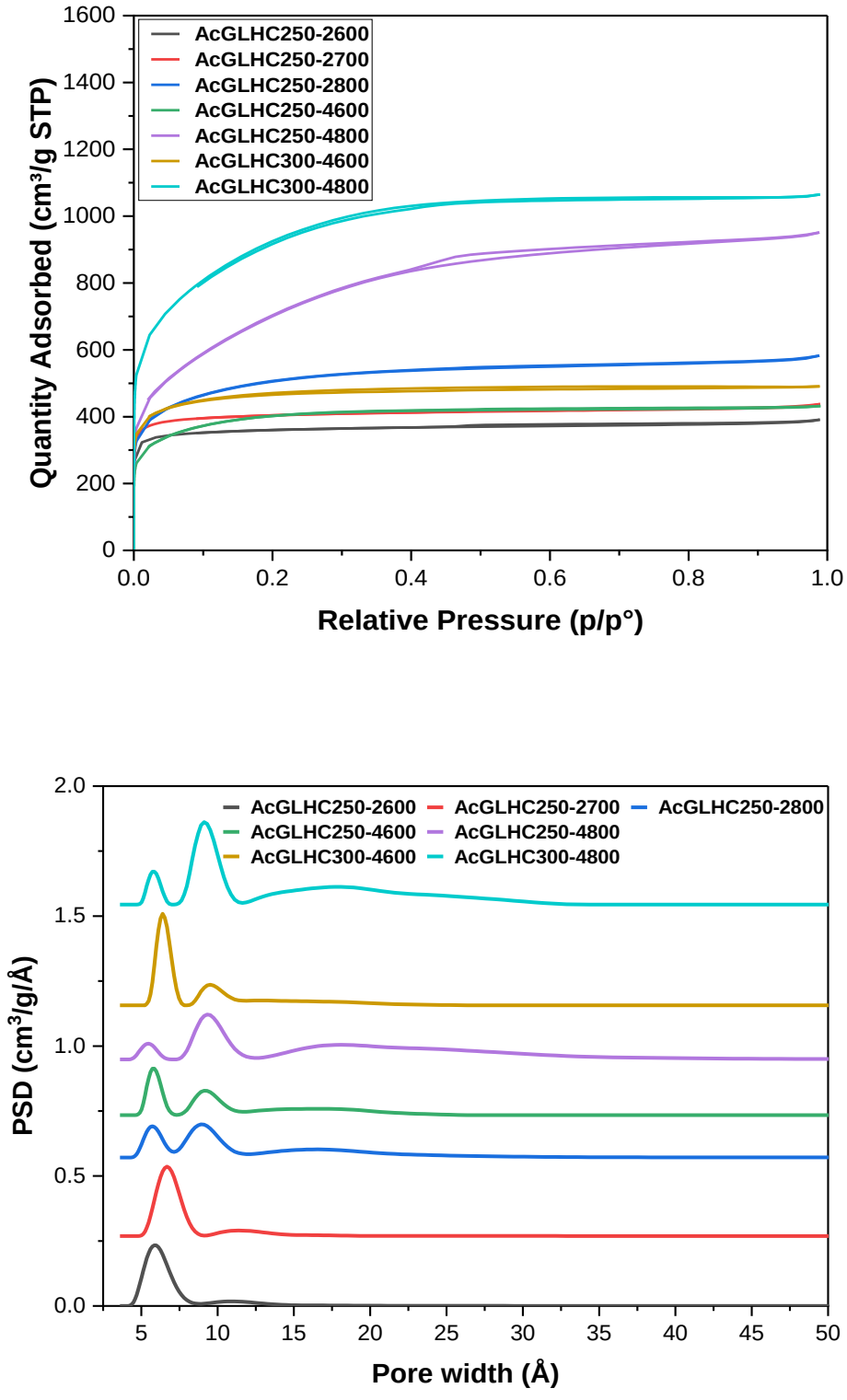


Figure 4-3 Nitrogen sorption isotherms and PSD curves of the activated carbons derived from the hydrochar of ginkgo leaves

The XRD patterns (Figure 4-4) show the amorphous nature of the activated samples. However, the samples were needed to be washed several times in HCl to remove the inorganic residues of alumina (see Figure 4-1).

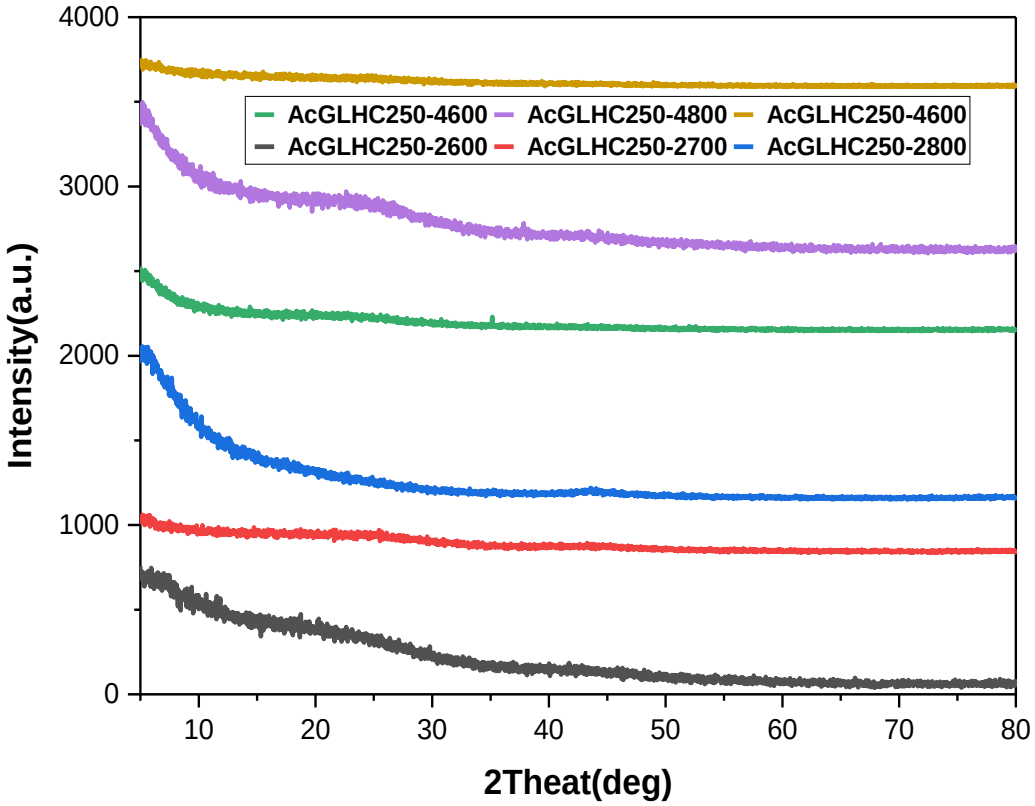


Figure 4-4 PXRD patterns of the activated carbons derived from the hyrochars of ginkgo leaves

3.2.Carbons derived from air-carbonised ginkgo leaves

3.2.1. Nature, textural properties and elemental composition of carbons

We explored air-carbonisation to produce char from ginkgo leaves and we used PO as a milder activating agent to avoid any corrosion in the boat. The flash air carbonisation at 400 °C increased the carbon from 45% in the raw leaves (GL) to 62% (GLF) (Table 4-3). It is interesting to note that the CHN analysis showed

almost similar chemical compositions between the air-carbonised leaves (GLF) and the one hydrothermally carbonised at 250°C (GLHC250), but the yield of the char was 44% in air-carbonisation compared to 61% in the hydrochar.

The carbon content of the PO-activated air-carbonised leaves (GLF), AcGLF-2ox-T, ranges from ca. 87% to ca. 90%. As in the activated hydrochars, the H/C, N/C and O/C ratios exhibit a significant drop in the samples following activation due to the boost in the C content and the significant decrease in H, N, and O contents.

Table 4-3 elemental compositions (CHN) of raw ginkgo leaves, their air-carbonised chars and the activated samples

	Chemical composition						
Sample	**C**	**H**	**N**	**O**	**O/C**	**N/C**	**H/C**
	%	**%**	**%**	**%**			
Raw GL	45.4	6.1	4.2	44.3	0.7	0.08	1.6
GLF	61.8	3.6	4.3	30.3	0.4	0.06	0.7
GLFw	70.6	4.5	4.1	20.9	0.2	0.05	0.8
AcGLF-2ox-600	86.5	0.5	1.4	11.7	0.1	0	0.1
AcGLF-2ox-700							
AcGLF-2ox-800	85.8	0.2	0.3	14.2	0.1	0	0
AcGLF-2ox-900	89.9	0.0	0.7	9.5	0.1	0	0
AcGLFw-2ox-800	89.0	0.1	0.3	10.6	0.1	0	0
AcGLF-2koh-800	84.1	0.1	0.3	15.5	0.1	0	0
AcGLFw-2koh-800	90.0	0.0	0.3	9.7	0.1	0	0
AcGL-2ox-800-D	89.1	0.1	0.3	10.5	0.1	0	0

The total surface area is in the range of 1057–2276 m^2/g with pore volumes of between 0.48 and 1.23 cm^3/g, both of which are moderate compared to other porous carbons.[21, 22] The surface area and pore size of the activated carbons derived from air-carbonised precursors at PO/GLF ratio of 2 increased at higher activation temperature (Figure 4-5 and Table 4-4). The highest surface area and pore volume were 2276 m^2/g and 1.23 cm^3/g for the sample activated by PO at 900 °C, which is consistent with the findings of activation of sawdust hydrochar

at 600─900 °C.[23] On the other hand, when KOH was used to activate the same char, the surface area was higher at 2273 m^2/g compared to 1837 m^2/g for PO. More discussion of the effects of the elemental composition of the precursors on the porosity will be in Section 3.3.

The XRD patterns (Figure 4-6) showed the amorphous nature of all the activated samples and confirmed the removal of all the inorganic residues of the activating agent.

Table 4-4 Textural properties the activated air-carbonised

	Surface area [a]		**Pore volume [b]**	
Sample	**SA(S_{micro})**	**S_{micro}**	**Vt(Vm)**	**Vm**
	m^2/g	**%**	**cc/g**	**%**
AcGLF-2ox-600	1057 (894)	84.58	0.48 (0.35)	72.92
AcGLF-2ox-700	1086 (653)	60.13	0.55 (0.27)	49.09
AcGLF-2ox-800	1837 (1486)	80.89	0.86 (0.58)	67.44
AcGLF-2ox-900	2276 (801)	35.19	1.23 (0.33)	26.83
AcGLFw-2ox-800	1745 (1574)	90.2	0.75 (0.6)	80
AcGLF-2koh-800	2273 (1771)	77.91	0.99 (0.69)	69.7
AcGLFw-2koh-800	2498 (2124)	85.03	1.06 (0.83)	78.3
AcGL-2ox-800-D	1879 (1295)	68.92	0.93 (0.51)	54.84

a BET surface area (SA), in parenthesis: the micropore surface area (Smicro), and the proportion (%) of micropore surface area. b Total pore volume (Vt), in parenthesis: the micropore volume (Vm), and the proportion (%) of micropore volume

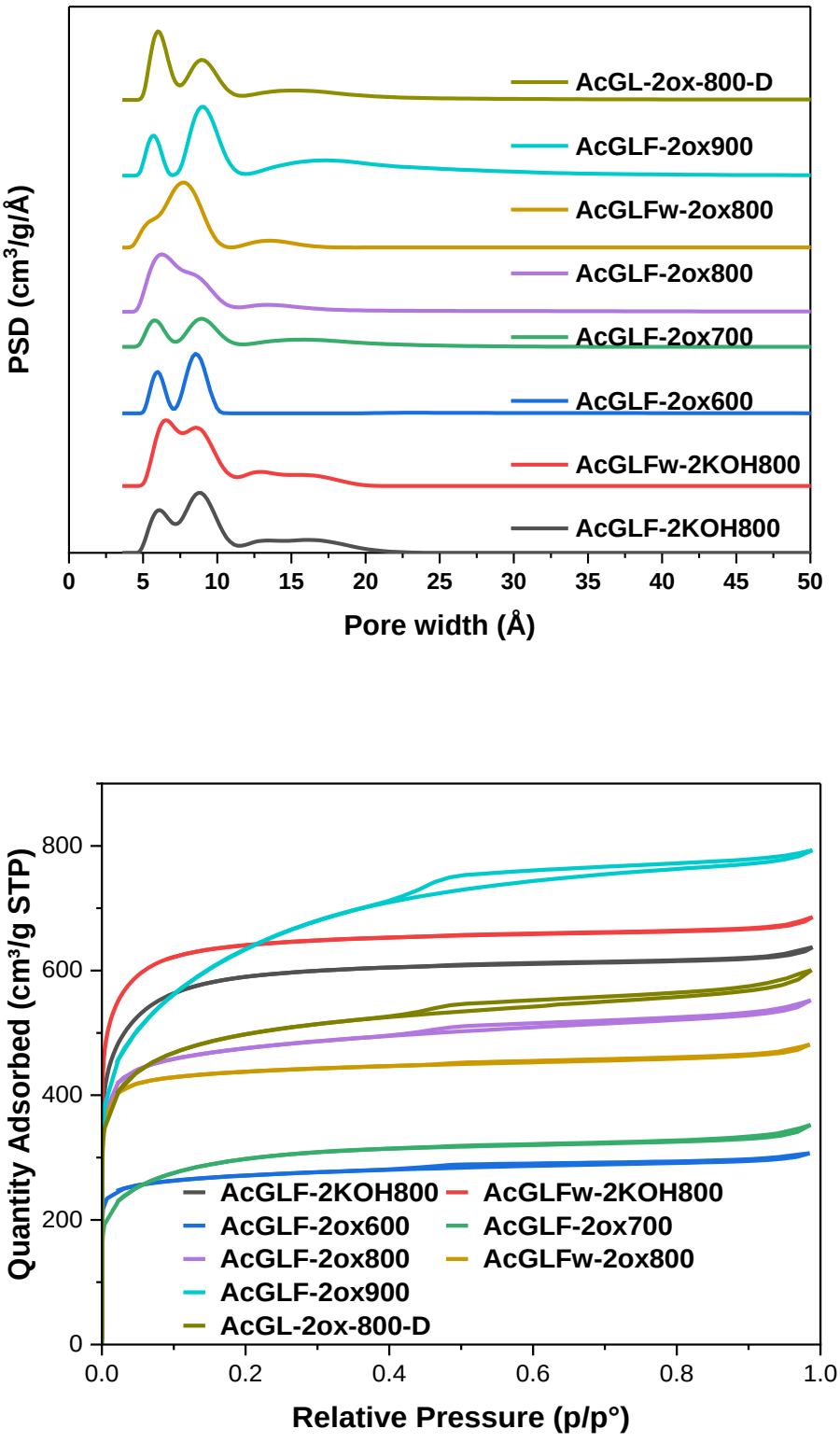


Figure 4-5 Nitrogen sorption isotherms and PSD curves of activated carbons derived from air-carbonised ginkgo leaves

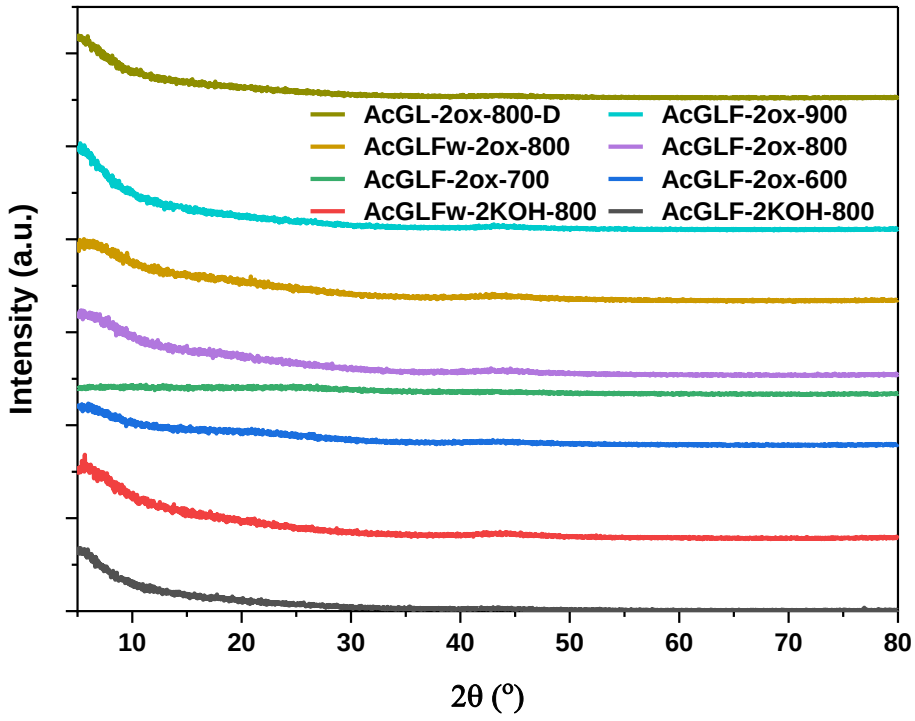


Figure 4-6 XRD patterns of activated carbons derived from air-carbonised ginkgo leaves

The analysis of the sharp peaks in the XRD patterns of the air-carbonized GLF (Figure 4-1) revealed that the peaks can be attributed to CaC_2O_4, which can be formed from ash; besides, the presence of calcium was reported as inherited inorganic content[24] in ginkgo leaves. To investigate the impact of this inorganic content on total carbon porosity, a portion of the air-carbonised leaves was washed with HCl and then activated under the same conditions. The activated samples from the washed char, AcGLFw-2ox-800 or AcGLFw-2KOH-800, showed a negligible decrease in textural properties (Table 4-4). This is consistent with the TGA result (Figure 4-7), which showed a small amount of ash, between 4 and 6 wt% of the raw ginkgo leaves. As a result, the XRD peaks (Figure 4-8) of the inorganic residues after the activation of some activated

samples show disappearance of such peaks, i.e., of calcium oxalate. Moreover, the main observable peaks are for potassium carbonate or potassium cyanide, which are the products of the activation reaction of N-containing precursors.[25-27] In terms of the chemical compositions, there were differences in the C and O contents between AcGLFw-2ox-800 or AcGLFw-2KOH-800 and the opposite samples derived from unwashed char, GLF. This difference is originated from the chemical composition of the GLF and GLFw. In brief, the impact of the inherited inorganic content was to decrease the C% and increase O% in the char and thus in the activated samples using PO or KOH, in addition to insignificant broadening of the pores.

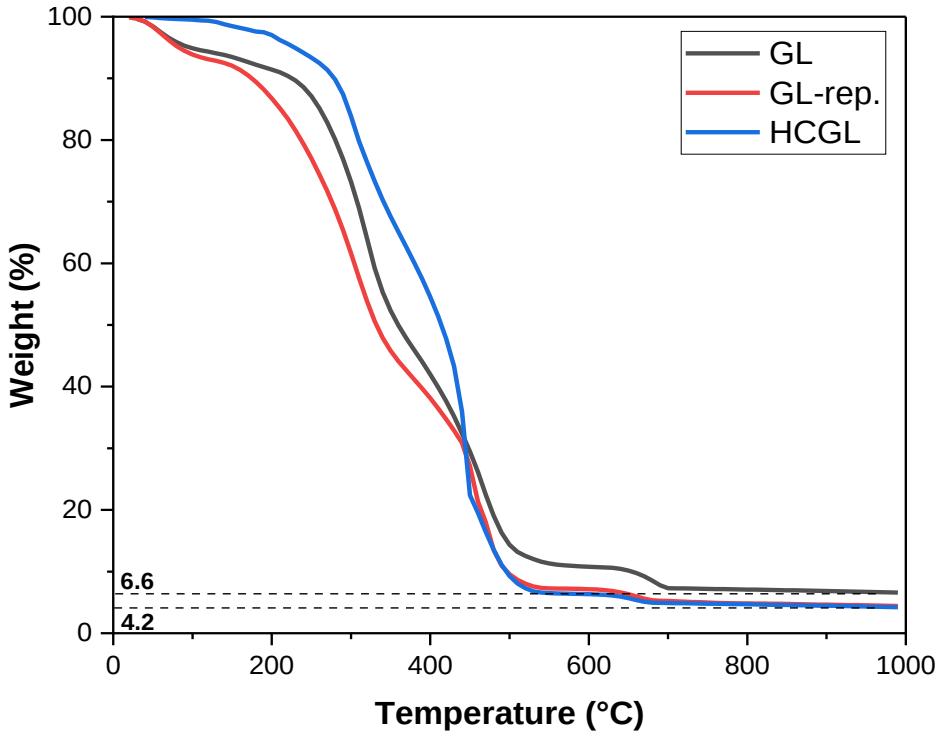


Figure 4-7 Thermogravimetric analysis (TGA) curves of raw ginkgo leaves (repeated twice, GL and GL-rep.) and hydrochar (HCGL) prepared at 250 °C

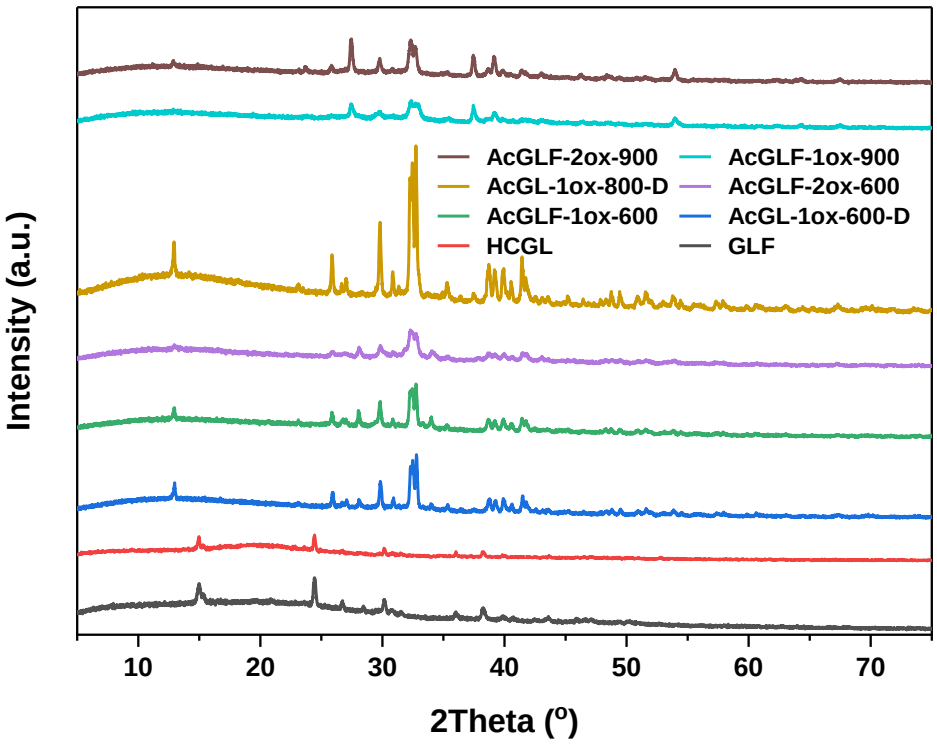


Figure 4-8 XRD patterns of unwashed air-carbonised ginkgo leaves and activated samples

3.3. An overview of the samples and the direct activation

The data in

Table 4-5 showed that there were no significant differences in the porosity between the KOH-activated samples from the hydrochar-250 or the air-carbonised char (AcGLHC250-2-800 and AcGLF-2koh-800). As we can see from the porosity of those two samples, the O/C ratio of their precursors, which we could use to predict the degree of the activation,[28, 29] was close to each other at 0.51 and 0.49, respectively. However, the increase of O/C by 0.02 in the hydrochar led to a small increase in the total pore volume and total surface area of AcGLHC250-2-800. The larger micropore surface area in AcGLF-2koh-800 compared to AcGLHC250-2-800 due to the higher C% in the air-carbonised

leaves compared to the hdyrochar, which led to etch lower amounts from the carbon framework and thus to less broadening of the pores.

The increase in hydrothermal carbonisation temperature increased the carbon content and decreased the O/C ratio, even though it produced activated carbon with a higher surface area. If this is explained by the hypothesis that some or all of the oxygen content is derived from inorganic sources, there was a decrease in the oxygen content of the char after washing with HCl and removing the inorganic content. Moreover, if we suppose that increasing the hydrothermal carbonisation temperature from 250 to 300 °C aided in the removal of inorganic residues that might hinder the activation reaction, this removal from GLHC 300 was unlikely to be a reason for the increase in surface area of their activated carbons. Since there was no significant effect of the inorganic content on the porosity (as discussed above in Section 3.2). The contribution of the inherited inorganic content in the surface area was only around 50 m^2/g, as shown in

Table 4-5 in GL800, which is a carbonised ginkgo leaves without an activating agent at 800°C. The high surface area of the activated carbons from GLHC300 is due to enriching the carbon content and thus maintaining a high amount of the carbons' framework from the overactivation.

The observed difference in the meso/microporosity ratio between AcGLHC250-4-800 and AcGLHC300-4-800, as shown in

Table 4-5, which can be ascribed to the different composition of the starting hydrochars. The notable increase in C% in GLHC300 compared to GLHC250 suggested that there was an overactivation during activation of GLHC250

carbon. This means etching or gasification a high amount of the carbon framework in GLHC250 and thus widening the majority of the pores to be in the meso-range compared to activation of GLHC300, which has higher carbons in its framework. Especially that the increase in C% did not accompany a notable change in the N/C ratio and was accompanied by a small decrease in the O/C ratio. This is consistent with what is known from the literature: the role of nitrogen in increasing the surface area by enhancing etching the carbons during K-activation[23, 25-27] and the effect of the high O/C ratio in determining the degree of the activation reaction.[28-31] The same N/C ratio in GLHC250 and GLHC300 with the higher O/C ratio of GLHC250 confirms the occurrence of an overactivation in AcGLHC250-4-800 that decreased its surface area compared to AcGLHC300-4-800. The high surface area of the KOH-activated hydrochars made them suitable for gas uptake applications at high pressures.[32]

We found that to prepare carbons with a high surface area with potassium oxalate from air-carbonised char, a higher activation temperature was needed. As we can see in

Table 4-5, the surface area reached just 2200 m^2/g at 900°C, compared to higher values for activation with KOH. As a result of the mild activation action of PO, carbons suitable for gas uptake applications at low pressures were produced.[23, 33]

The direct activation of the ginkgo leaves by KOH resulted in no yield, while the direct activation by PO produced some yield of carbon material with a high surface area. Compared to the carbonised ginkgo leaves without an activating agent, GL800, the direct activation with PO boosted the porosity of the raw

leaves (AcGL-2ox-800-D). The GL800 was prepared in the same manner and washed with HCl and water at the end of the procedure. Interestingly, the surface areas and pore volumes of the carbons produced from direct activation of the leaves (AcGL-2ox-800-D) or from air-carbonised leaves (AcGLF-2ox-800) using PO were almost identical. This is consistent with the literature[23, 33] that showed the direct activation of sawdust using PO produced activated carbon with a surface area and pore volumes similar to those of activated carbons derived from sawdust hydrochar. However, there was an increase in the meso/microporosity ratio in the direct activated leaves compared to the activated from the air carbonised leaves. The synergy of the higher compositional ratios in the raw leaves (GL) compared to the air carbonised leaves (GLF) of O/C (0.07 versus 0.04) and N/C (0.07 versus 0.04) has led to this increase in the meso/microporosity ratio. According to the literature, the nitrogen-containing carbon sources show a higher surface area, pore volume, and especially a higher meso/microporosity ratio compared to the non-nitrogen-containing sources. Figure 4-9 shows the relationship between the surface area and the elemental composition of the precursors of different activated carbons prepared using the weight ratio 2 of PO/precursor. From Figure 4-9, we can see that the surface area generally increases as the N/C ratio increases. This is in agreement with the literature, which showed clearly how the presence of nitrogen in the precursors led to an increase in the total surface area and pore volume of the PO-activated carbons. The small range of the samples in the figure, which were the ginkgo leaves and the sawdust, would limit the ability to generalise a conclusion from this figure. i.e., the effects of N/C, O/C, and H/C ratios on the surface area of activated carbons prepared using a 2-weight ratio of PO/precursor. An average

effect of these ratios, maybe with other effects like the porosities of the precursors, is what nay have affected the total porosity of the activated carbons presented in the figure. Thus, another study would be recommended to find out their effects on the pore development of the produced activated carbons.

In brief, for preparing a controlled porosity using KOH from the prepared hydrochar of the ginkgo leaves, the hydrothermal carbonisation temperature should be chosen carefully. As such, the temperature will control the elemental composition of the precursor to tailor the surface area and meso/microporosity ratio of the activated carbon. In regards to the preparation of a controlled porosity using PO from a precursor, the activation temperature plays a key role in developing the high surface area and pore volume, besides the nitrogen content mainly in the precursors. Finally, careful pre-mixing of the leaves with N-rich precursors[29] may provide another method for modulating direct PO-activation with large surface areas and at low activation temperatures for the uptake at specified pressure ranges.

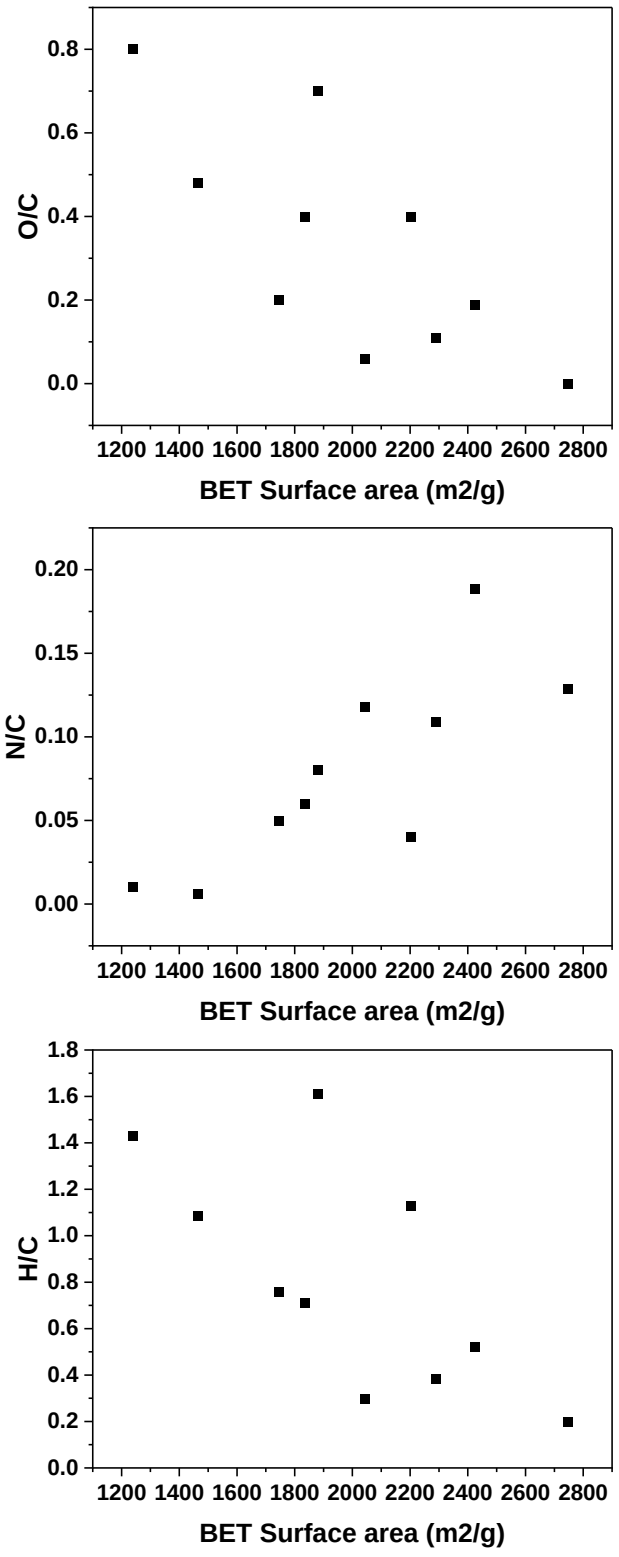


Figure 4-9 Surface area of activated carbons as a function of the O/C, N/C, and H/C ratios of their precursors. All the activated carbons were prepared at 800 °C with a PO/precursor ratio of 2.

3.4.CO_2 uptake

The CO_2 uptake at room temperature and pressure of 0 to 20 bar pressure is summarised in

Table 4-5. The gravimetric uptake at low pressures by the hydrochar-derived activated samples (Figure 4-10) showed good uptake. The highest uptake at 1 bar of 4.59 and 4.74 mmol/g was for samples activated at 600 and 700 °C, respectively. As is well known, the pores expand as the KOH/precursor ratio increases. Thus, the uptake was lower for samples prepared at KOH/precursor ratio of 4 at low pressures. Interestingly, activated carbons derived from hydrochar-300 have slightly higher uptake at low pressures. As mentioned above, the hydrothermal carbonisation at a higher temperature increased the carbon content and thus sustained higher porosity during the activation. On the other hand, the uptake on the same sample set at high pressure (20 bar) increased as the surface area increased. The highest uptake was 23.36 mmol/g for sample AcGLHC300-4-800, which has the highest surface area. This uptake is competitive when compared to other carbon adsorbents.[32]

Table 4-5 Textural properties, elemental composition (CHN) and CO_2 uptake results of all samples

Sample	SA(S_{micro})[a]	S_{micro}[b]	Vt(Vm)[c]	Vm[d]	C	H	N	O	O/C	N/C	H/C	CO_2 uptake(mmol/g)		
	m^2/g	%	cc/g	%	%	%	%	%	At.	At.	At.	0.15 bar	1 bar	20 bar
GL	-	-	-	-	45.4	6.1	4.2	44.3	0.7	0.1	1.6			
HCGL250	7 (0)	-	0.03 (0)	0	60.5	5.7	3.1	30.8	0.4	0.0	1.1			
HCGL300		0			66	6.2	2.9	24.9	0.3	0.0	1.1			
GLF	14 (0)		0.04 (0)	0	61.8	3.6	4.3	30.3	0.4	0.1	0.7			
GLFw		0			70.6	4.5	4.1	20.9	0.2	0.1	0.8			
GL800	49 (12.63)	26	0.05 (005)	0								0.81	1.8	3.07
AcGLHC250-2-600	1428 (1287)	90	0.61 (0.50)	82	76.4	1.18	1.79	20.63	0.2	0.0	0.2	1.4	4.6	10.5
AcGLHC250-2-700	1617 (1448)	90	0.68 (0.55)	81	84	0.63	1.1	14.27	0.1	0.0	0.1	1.3	4.7	12.2
AcGLHC250-2-800	2296 (1309)	57	1.09 (0.52)	48	87.82	0.21	0.44	11.53	0.1	0.0	0.0	0.8	3.7	18.5
AcGLHC250-4-600	1504 (969)	64	0.67 (0.38)	57	64.675	0.445	0.175	34.705	0.4	0.0	0.1	1.3	3.5	12.7
AcGLHC250-4-800	2529 (160)	6	1.47 (0.04)	3	86.23	0.37	0.24	13.16	0.1	0.0	0.1	0.4	2.4	19.6
AcGLHC300-4-600	1796 (1406)	78	0.76 (0.56)	74								1.2	4.3	14.3
AcGLHC300-4-800	3366 (2705)	80	1.65 (1.22)	74	88.2	0.08	0.2	11.52	0.1	0.0	0.0	0.8	3.6	23.4
AcGLF-2ox-600	1057 (894)	85	0.48 (0.35)	73	86.5	0.5	1.4	11.7	0.1	0.0	0.1	1.8	4.6	9.8
AcGLF-2ox-700	1086 (653)	60	0.55 (0.27)	49	56.7	0.2	0.3	42.9	0.6	0.0	0.0	1.9	5.0	10.3
AcGLF-2ox-800	1837 (1486)	81	0.86 (0.58)	67	85.8	0.2	0.3	14.2	0.1	0.0	0.0	1.2	4.6	14.4
AcGLF-2ox-900	2276 (801)	35	1.23 (0.33)	27	89.9	0	0.7	9.5	0.1	0.0	0.0	0.7	3.3	19.3
AcGLFw-2ox-800	1745 (1574)	90	0.75 (0.60)	80	89	0.1	0.3	10.6	0.1	0.0	0.0	1.3	4.7	13.1
AcGLF-2koh-800	2273 (1771)	78	0.99 (0.69)	70	84.1	0.1	0.3	15.5	0.1	0.0	0.0	0.8	3.8	17.5
AcGLFw-2koh-800	2498 (2124)	85	1.06 (0.83)	78	90	0	0.3	9.7	0.1	0.0	0.0	1	4.2	17.2
AcGL-2ox-800-D	1879 (1295)	69	0.93 (0.51)	55	89.1	0.1	0.3	10.5	0.1	0.0	0.0	1.1	4.0	15.5

[a] BET surface area, and the values in parenthesis are micropore surface area. [b] The percentages (%) of micropore surface area. [c] Total pore volume, and the values in parenthesis are micropore volume. [d] The percentages (%) of micropore volume.

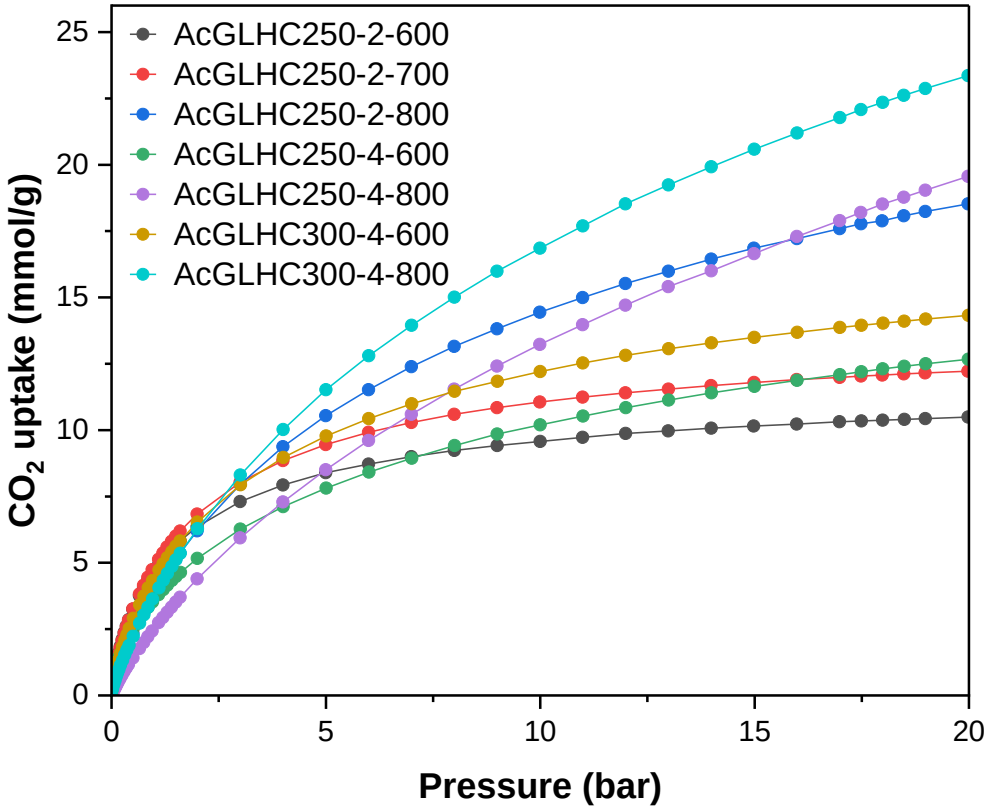


Figure 4-10 Gravimetric CO_2 uptake of activated carbons made from the hyrochars of ginkgo leaves

The gravimetric CO_2 uptake at low pressures (

Table 4-5, Figure 4-11) of the PO activated air-carbonised samples is equally attractive. The highest uptake at 1 bar was for the sample activated at 600 and 700°C: the values were 4.62 and 5.01 mmol/g, respectively. There was a minor increase in the uptake at low pressures for the samples prepared from washed char compared to those prepared from unwashed char. For example, the uptake at 0.15 and 1 bar increased from 1.15 and 4.56 mmol/g to 1.31, 4.74 mmol/g of

AcGLF-2ox-800 and AcGLFw-2ox-800, respectively. The sample with the highest surface area, AcGLF-2ox-900, had the highest uptake at 20 bar of 19.29 mmol/g. The uptake of PO-activated samples at 800°C, both directly activated and activated from air-carbonised leaves, showed a slight increase in the uptake at 20 bar by 1 mmol/g.

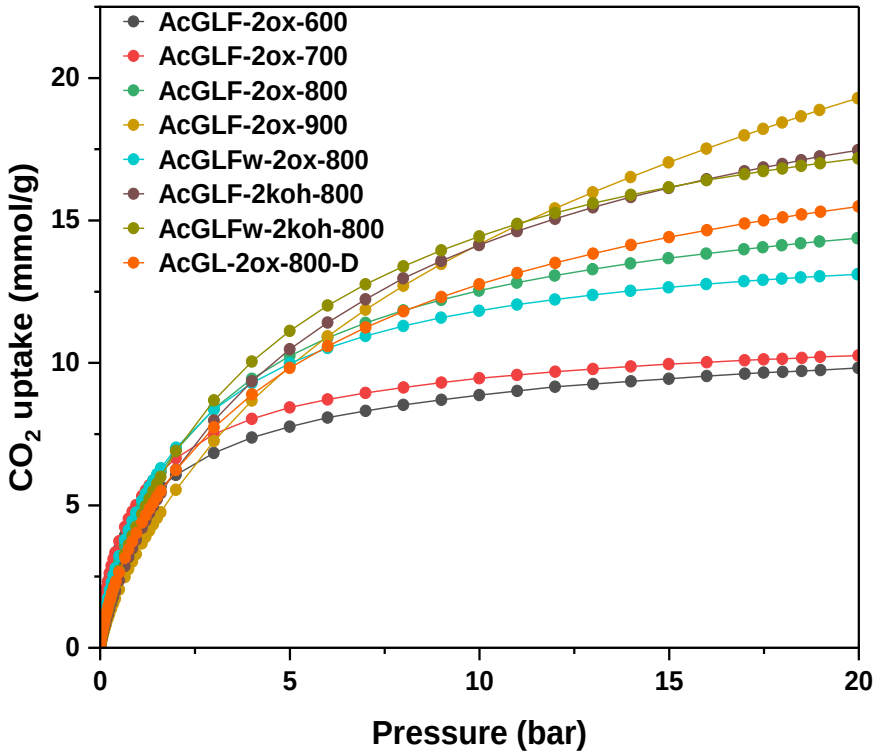


Figure 4-11 Gravimetric CO_2 uptake of activated carbons made from air-carbonised ginkgo leaves at room temperature

4. Summary

We have prepared activated carbons from ginkgo leaves as a carbon source. The hydrothermal carbonisation of the leaves was applied to enrich the carbons in

the leaves prior to the KOH activation. Two hydrothermal carbonisation temperatures were employed (250 and 300C). The higher temperature has enriched the C% in the hydrochar and led to an enhancement of the surface area of the activated carbon up to 3300 m^2/g with CO_2 uptake at 20bar up to 23 mmol/g. The other carbonisation method was flash air-carbonisation, which produced char with a similar chemical composition to the hydrothermally prepared char at 250C. This similarity in their chemical composition led to produce activated carbons, which were prepared at the same conditions, with insignificant variation in their porosities and CO_2 uptake gravimetric capacities. The air carbonisation of the leaves followed by activation with PO generated carbons with controlled porosity suitable for CO_2 uptake at low pressures. The PO-activated at 700 °C had the largest uptake at low pressures, with values of 5.01 mmol/g at 1bar. The direct activation of raw ginkgo leaves with PO offers a straightforward method for producing carbons with porosities remarkably comparable to those of samples from activated air-carbonised leaves. That emphasises the findings of the PO-directly activated sawdust, which showed similar porosities to the PO-activated sawdust hydorchar. Our investigation revealed that the presence of inorganic content in the carbon precursor led to a minor widening of the pore sizes in activated carbon.

Acknowledgment

I'm grateful to the Nanoscale and Microscale Research Centre (nmRC) at the University of Nottingham (especially Grace Belshaw, who imaged the samples for this project).

5. References

1. N. Mac Dowell, P. S. Fennell, N. Shah and G. C. Maitland, *Nature Climate Change*, 2017, **7**, 243-249.
2. E. I. S. Department for Business, *Net Zero Strategy: Build Back Greener*, HM Government, 2022, www.gov.uk/government/publications/net-zero-strategy.
3. N. K. Arora and I. Mishra, *Environmental Sustainability*, 2021, **4**, 585-588.
4. N. A. Rashidi and S. Yusup, *Journal of CO2 Utilization*, 2016, **13**, 1-16.
5. X.-q. Zhang, W.-c. Li and A.-h. Lu, *New Carbon Materials*, 2015, **30**, 481-501.
6. S. Choi, J. H. Drese and C. W. Jones, *ChemSusChem*, 2009, **2**, 796-854.
7. H. A. Patel, J. Byun and C. T. Yavuz, *ChemSusChem*, 2017, **10**, 1303-1317.
8. N. Hedin, L. Chen and A. Laaksonen, *Nanoscale*, 2010, **2**, 1819-1841.
9. S. M. Manocha, *Sadhana*, 2003, **28**, 335-348.
10. C. Goel, S. Mohan and P. Dinesha, *Science of The Total Environment*, 2021, **798**, 149296.
11. B. Sajjadi, W.-Y. Chen and N. O. Egiebor, *Reviews in Chemical Engineering*, 2019, **35**, 735-776.
12. K. S. Ukanwa, K. Patchigolla, R. Sakrabani, E. Anthony and S. Mandavgane, *Sustainability*, 2019, **11**, 6204.
13. O. Ioannidou and A. Zabaniotou, *Renewable and Sustainable Energy Reviews*, 2007, **11**, 1966-2005.
14. Z. Heidarinejad, M. H. Dehghani, M. Heidari, G. Javedan, I. Ali and M. Sillanpää, *Environmental Chemistry Letters*, 2020, **18**, 393-415.
15. E. T. Noor, R. Das, M. S. Lami, A. J. Chakraborty, S. Mitra, T. E. Tallei, I. Rinaldi, M. Amany Abdel-Rahman, M. J. Hossain, K. Dhama, G. Mostafa-Hedeab and E. Talha Bin, *Evidence - Based Complementary and Alternative Medicine*, 2022, **2022**.
16. E. A. Hirst, A. Taylor and R. Mokaya, *Journal of Materials Chemistry A*, 2018, **6**, 12393-12403.
17. J. Xu, X. Jie, F. Xie, H. Yang, W. Wei and Z. Xia, *Nano Research*, 2018, **11**, 3648-3657.
18. W.-K. Li, J.-T. Feng and Z.-Q. Ma, *Carbon*, 2020, **161**, 685-693.
19. W. Sangchoom and R. Mokaya, *ACS Sustainable Chemistry & Engineering*, 2015, **3**, 1658-1667.
20. H. M. Coromina, D. A. Walsh and R. Mokaya, *Journal of Materials Chemistry A*, 2016, **4**, 280-289.

21. A. Altwala and R. Mokaya, *RSC Advances*, 2022, **12**, 20080-20087.
22. G. Singh, K. S. Lakhi, S. Sil, S. V. Bhosale, I. Kim, K. Albahily and A. Vinu, *Carbon*, 2019, **148**, 164-186.
23. A. M. Aljumialy and R. Mokaya, *Materials Advances*, 2020, **1**, 3267-3280.
24. H. J. An, N. R. Kim, M. Y. Song, Y. S. Yun and H.-J. Jin, *Journal of Industrial and Engineering Chemistry*, 2017, **45**, 223-228.
25. M. Sevilla, G. A. Ferrero and A. B. Fuertes, *Chemistry of Materials*, 2017, **29**, 6900-6907.
26. M. Sevilla, A. S. M. Al-Jumialy, A. B. Fuertes and R. Mokaya, *ACS Applied Materials & Interfaces*, 2018, **10**, 1623-1633.
27. M. Sevilla, G. A. Ferrero, N. Diez and A. B. Fuertes, *Carbon*, 2018, **131**, 193-200.
28. L. S. Blankenship and R. Mokaya, *Materials Advances*, 2022, **3**, 1905-1930.
29. N. Balahmar and R. Mokaya, *Journal of Materials Chemistry A*, 2019, **7**, 17466-17479.
30. A. Altwala and R. Mokaya, *Energy & Environmental Science*, 2020, **13**, 2967-2978.
31. I. Alali and R. Mokaya, *Energy & Environmental Science*, 2022, **15**, 4710-4724.
32. A. A. Abd, M. R. Othman and J. Kim, *Environmental Science and Pollution Research*, 2021, **28**, 43329-43364.
33. A. Altwala and R. Mokaya, *Energy Advances*, 2022, **1**, 216-224.

Chapter 5 N-doped porous carbon from organic salts via direct doping route and its application for CO_2 uptake

Abstract

Doping with nitrogen is a successful method for enhancing some properties of activated carbon, including its specific surface area and performance in various energy storage applications. In the literature, there is much confusion regarding the effect of nitrogen on the porosity of potassium-activated carbon. Urea is a nitrogen doping reagent for activated carbon that can be utilised in both post-treatment and in-situ doping processes. In this study, we systematically examined different nitrogen ratios using urea as a dopant agent and the simplest route of activated carbon preparation. The results highlight the impact of selecting the ratios of nitrogen to potassium, carbon to oxygen, and nitrogen to carbon on the porosity of the carbon. The samples were examined for CO_2 uptake at room temperature, and the results showed that samples with N/K ratios of 1.7 and 3.4 had superior uptake at high pressure due to the higher surface area.

1. Introduction

Porous carbon is similar to most other adsorbents in that it can have a large surface area and a range of pore sizes that may be suited for the storage of small gas molecules such as carbon dioxide and methane. Additionally, most porous carbons have good stability in a wide range of conditions and are relatively low cost in terms of their synthesis.[1, 2] Porous carbons may be generated by physical activation or chemical activation of suitable carbonaceous matter or by using a

template.[3] Nitrogen doping of porous carbons is typically accomplished either through post-synthesis treatment, which involves subjecting the carbon to a flow of ammonia at elevated temperatures,[4] and/or by mixing with nitrogen-containing liquids such as HNO_3.[5, 6] The N-doping can be accomplished in situ by activating a N-containing carbon source or by mixing N-rich precursors with the carbon source during the carbon synthesis steps in manner that allows direct N-doping.[7-10]

Various studies have been conducted on the chemical activation of carbons using potassium salts as activator and in particular KOH.[11] Recent research indicates that in addition to the well-known activation mechanism of carbon by potassium salts, there are additional mechanisms that control pore evolution when N is present in the carbon framework.[12] In this regard, the activation mechanism can be highly dependent on the presence of nitrogen atoms.[12]

It is well established that a number of steps are involved in pore evolution when nitrogen-free carbon is activated using potassium-salts. For example, a redox reaction etches the carbon framework – a gasification of the carbon by the resultant H_2O and CO_2 – and the carbon framework is expanded by the as-prepared metallic potassium.[11] In the presence of nitrogen, there is another step, which is the reaction between potassium and nitrogen to form potassium cyanide or cyanate.[13] Eichler et al.[14] studied the activation of a system consisting of semi-carbonised sucrose with melamine and potassium oxalate and concluded that the N:K and N:C ratios have a key effect on the production of the pores.

Organic salts are increasingly being used as precursors for porous carbons via simple heating of carbon-rich salts such as potassium hydrogen phthalate

(KHP).[15] In such self-activation scenarios, the metal within the organic salt, if selected carefully to have porogen properties, can act as activator with the possibility of generating porosity upon thermal treatment followed by simple washing with water to remove the metal or associated residues. It is already known that carbons generated from KHP can be highly microporous and therefore suited for storage of CO_2 at low pressure.[15] However, KHP-derived carbons required temperature above 800 ^oC in order to achieve surface area above ca. 1200 m^2/g, which limits their use for high pressure CO_2 uptake.[15] Achieving higher surface area at lower temperature via self-activation of KHP or related organic salts would be desirable. One way of achieving higher surface area is to vary the N:K and N:C ratios of the self-activation mixture by adding an extra ingredient that increases the amount of N.[13,14] This expectation is based on the known effect of these ratios on pore development in activated carbons, and which suggests that the presence of N aids in pore formation.[13,14] More generally, it is possible that presence of increasing amounts of N can act as an added porogen during the self-activation process.

In this regard, the addition of an ingredient rich in N to a self-activating organic salt can enable direct doping of nitrogen and also simplify the synthesis process and lower the cost of production of high surface area N-doped carbons with respect to the temperature required. Accordingly, further studies are needed to explore new precursors and synthesis routes. Besides, a supplementary goal of investigating such straightforward synthesis routes is to further clarify the influence N:K and N:C ratios on the porosity of N-doped carbon.

In this chapter, a straightforward route was adopted to synthesise N-doped carbons by mixing KHP with a N-rich ingredient, urea, and then exposing the mixture to direct carbonisation. As a result, several processes including carbonisation, doping and activation were all performed in one step, followed by a water-only washing step. The work demonstrates that the addition of urea to KHP enables achievement of much higher surface area at temperatures no higher than 800^{o}C in a manner not possible in the absence of urea. Indeed, the surface area and overall porosity almost doubles. This means that the CO_2 uptake of the KHP derived carbons at high pressure significantly improves but without diminishing the low pressure uptake capability. Controlling the synthesis conditions besides the N/K ratio of the primary mixture were the keys to manipulating the porosity of the resulting N-doped carbons from the KHP-urea mixture.

2. Experimental

2.1 Synthesis procedures

Potassium hydrogen phthalate (KHP), hereinafter referred to as P (99%, Alfa Aesar) and urea (U) (≥99%, Sigma-Aldrich) were mechanically mixed in an agate mortar at P/U ratios of 1, 0.5 and 0.25 as shown in Table 5-1. Afterward, the mixture was placed in an alumina crucible and subjected to a thermal treatment (800°C) in a tube-furnace under N_2 flow (heating rate = 10°C min^{-1}) and held at the desired temperature for one hour before cooling. Purification of the samples was done with warm distilled water (~90°C) until a neutral pH was reached. The carbon thus produced were dried in an oven at 100°C overnight.

The resulting carbons were designated as PUxy, where x is the weight ratio and y is activation temperature.

For comparison, KHP and potassium phthalimide, PPI, (≥99%, Sigma-Aldrich) were carbonised separately under the same conditions and designated as P800 and PN800, respectively. Further samples were prepared at 600, 700 and 900ºC at P:U ratio of 0.25, 0.5 and 1.

Table 5-1 starting materials quantities of the samples

Sample	KHP (g)	Urea (g)	wt. ratio KHP:urea	Molar ratio KHP:urea
P800	4	0	-	-
PU	4	4	1:1	1:3
PU0.75	4	3	1:0.75	1:2.5
PU0.5	4	2	1:0.5	1:1.5
PU0.25	4	1	1:0.25	1:1
PU0.125	4	0.5	1:0.125	2:1
PU0.0625	4	0.25	1:0.0625	2:0.5

2.2 Characterization

Powder XRD patterns of the samples were performed via a PANalytical X'Pert PRO diffractometer using a copper Kα and a monochromator (λ = 1.5405Å) at 40 kV and 40 mA with a step size of 0.02 and a 50 s time step. The scan was achieved at room temperature. The porosity and determination of textural properties were performed via nitrogen physisorption using a Micromeritics 3Flex sorptometer. Prior to analysis (at –196°C), the carbon samples were degassed under vacuum at 230°C for 32 or 16 h. The surface area was calculated using the BET method applied to adsorption data within the relative pressure (*P/Po*) range of 0.02–0.35. The total pore volume was determined from the nitrogen uptake at close to saturation pressure (*P/Po* = 0.99). The micropore surface area and micropore volume were determined via t-plot analysis.

Micromeritics' SAIEUS software was used to obtain PSDs of the samples using the 2D-NLDFT method for heterogeneous surfaces. In order to create the most accurate PSD for carbons, the software's fitting parameter, λ, which affects the roughness of the PSD, was adjusted between 2.75 and 3.00. Scanning electron microscopy (SEM) images were recorded on a JEOL7000 microscope at 15 kV accelerating voltage. Samples were mounted using a conductive carbon double-sided sticky tape and a thin (ca. 10 nm) coating of Iridium sputter was deposited onto g-C_3N_4 sample to reduce the effects of charging. CHN elemental analysis was performed using an Exeter Analytical CE-440 Elemental Analyser. X-ray photoelectron spectroscopy (XPS) was carried out using a Kratos AXIS ULTRA with a monochromated A1 Kα X-ray source (1486.6 eV) operated at 10 mA emission current and 12 kV anode potential. The analysis chamber pressure was better than 10^{-9} Torr. FAT (fixed analyzer transmission) mode was used, with pass energies of 160 eV (or 80 eV) for survey scans and 40 eV for high-resolution scans. The magnetic immersion lens system allows the area of analysis to be defined by apertures, a "slot" aperture of 300 × 700 μm for wide/survey scans and a 110 μm aperture for high-resolution scans. The take-off angle for the photoelectron analyzer was 90° and acceptance angle of 30° (in magnetic lens modes). Data analysis was carried out using CASAXPS software with Kratos sensitivity factors to determine atomic % values from the peak areas. Charge correction was applied to the data at the processing stage. IR spectroscopy was performed using a Bruker ALPHA FTIR Spectrometer. Raman spectra were recorded using a Horiba–Jobin–Yvon LabRAM Raman microscope with a 532 nm laser.

3.2 CO_2 adsorption measurements

CO_2 uptake capacity of the carbons was measured with a Hiden Isochema XEMIS instrument at 25 °C and up to 40 bar of pressure. Prior to conducting the CO_2 uptake experiments, the carbons were outgassed for 3 h at 240 °C (heating ramp rate 10°C/min) under vacuum. Our measurements determined the excess CO_2 uptake directly.

3. Results

3.1. Textural and morphology properties and chemical composition

N-doped porous carbons were prepared by the simple carbonisation of KHP mixed with urea. To investigate the effect of doping ratios on porosity and nitrogen doping, the following ratios of P/U were used: 0.0.625, 0.125, 0.25, 0.5 and 1. At a carbonisation temperature of 800°C, the optimal P/U ratio was determined in comparison to carbonisation of KHP alone. According to the XRD patterns in Figure 5-1, all the samples are mainly amorphous carbon; however, there is a broad peak around 2θ of 23°, which may be assigned to lowly graphitic ordering for the P800 sample. After the addition of urea at low concentrations (i.e. PU0.25y and PU0.5y), the resulting carbons were amorphous. However, at the highest ratio (PUy), there is a broad peak that may be ascribed to graphitisation centred at 26.6°. This peak could be due to the formation of g-C_3N_4 or graphite-like carbon.

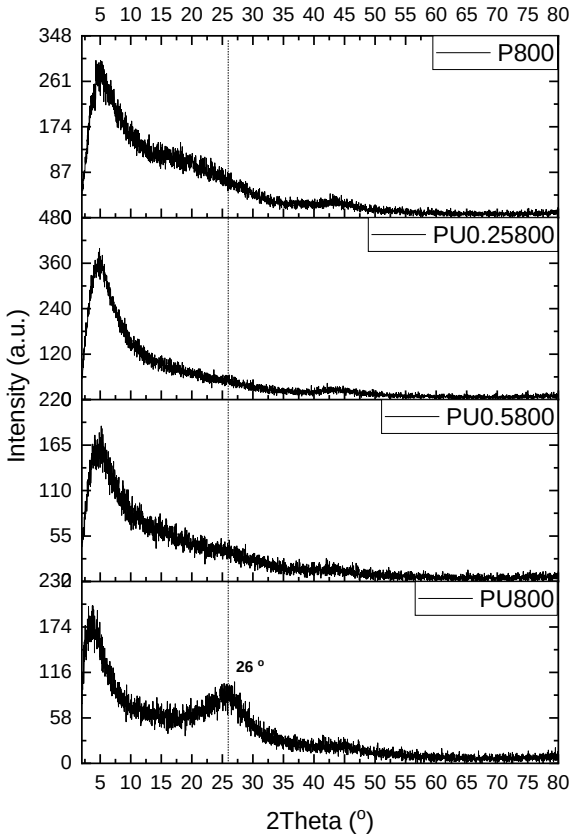


Figure 5-1 Powder XRD patterns of carbons derived from carbonisation of mixtures of urea (U) and potassium hydrogen phthalate (KHP) at 800°C.

..

Looking at nitrogen isotherms and NLDFT pore size distributions in Figure 5-2, the porosity (i.e. total nitrogen adsorbed and therefore the surface area and total pore volume) increased with adding urea to the carbonisation mixture of KHP. All the isotherms are type I, which is typical of microporous materials. The pore sizes of the N- doped carbons have two pore sizes centred in the micropore range at 0.6 and 0.9 nm. However, carbonisation of KHP itself without urea produced a uniform pore size of around 0.6 nm. Therefore, adding urea introduced new and wider pores in the carbon framework, with a size of 0.9 nm. The surface area and pore volume (Table 5-2) increased with the amount of urea added up to

P/U ratio 0.5. A higher P/U ratio led to a decrease in the surface area and pore volume. The surface area ranged from 1289 m^2/g for P800 (i.e. no urea) to 2312 m^2/g at P/U ratio 0.5, before decreasing to 1372 m^2/g at P/U ratio 1. This means that the surface area increases by up to 80% due to the addition of urea.

On the other hand, as shown in Table 5-2, the micropore surface area and micropore volume increased as the P/U ratio increased from 0 to 0.25, and after this range, any increase in the P/U ratio from 0.75 to 1 decreased the micropore surface area. The highest micropore surface area and pore volume were 1740 m^2/g and 0.73 cm^3/g, respectively, for the ratio 0.25. It is notable as well that the carbonisation at the slower ramp rate reduced the micropore surface area and micropore volume, as shown by a comparison between PU0.5800 and PU0.5800-5, or between PU800 and PU800-5, as two examples. The decrease in the micropore surface area and micropore volume were from 1654 to 1595 m^2/g and from 0.65 to 0.63 cm^3/g, respectively, when the ramp rate was reduced from 10 of PU0.5800 to 5°C/min of PU0.5800-5.

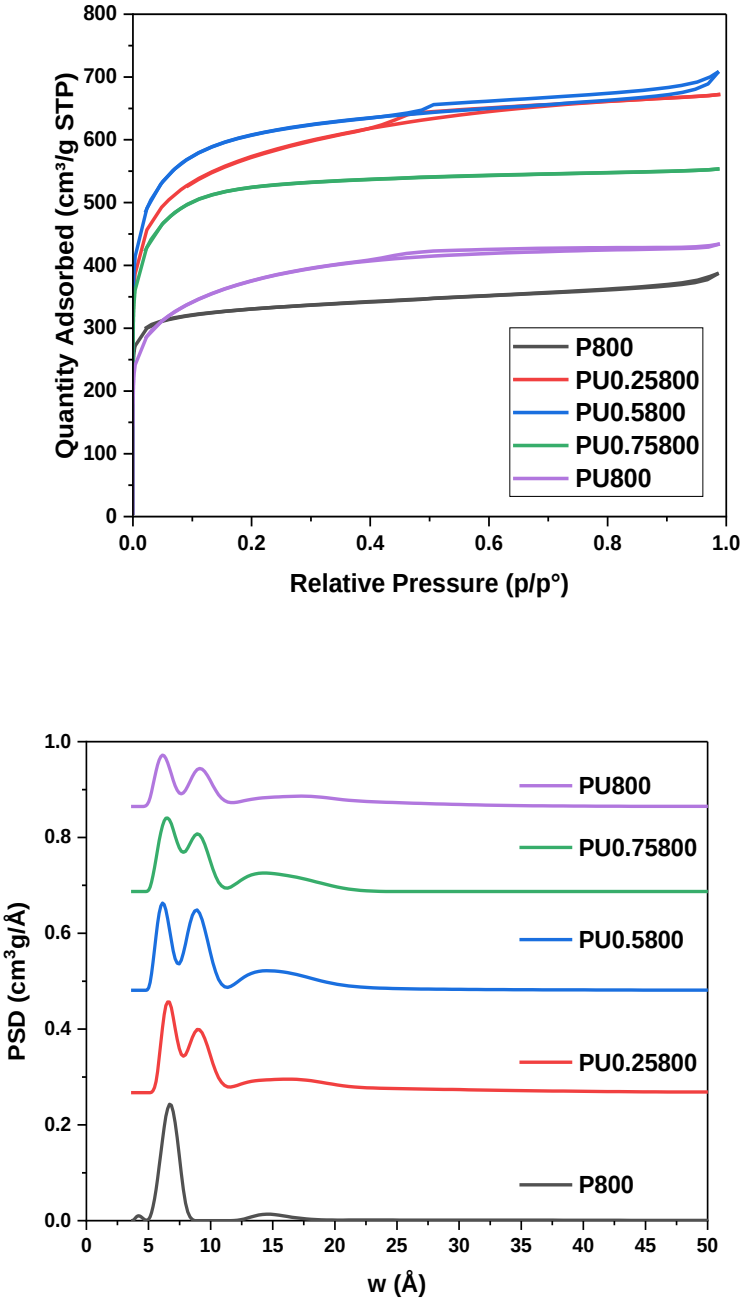


Figure 5-2 Nitrogen isotherms and NLDFT pore size distribution of carbons derived from carbonisation of mixtures of urea (U) and potassium hydrogen phthalate (KHP) at 800°C.

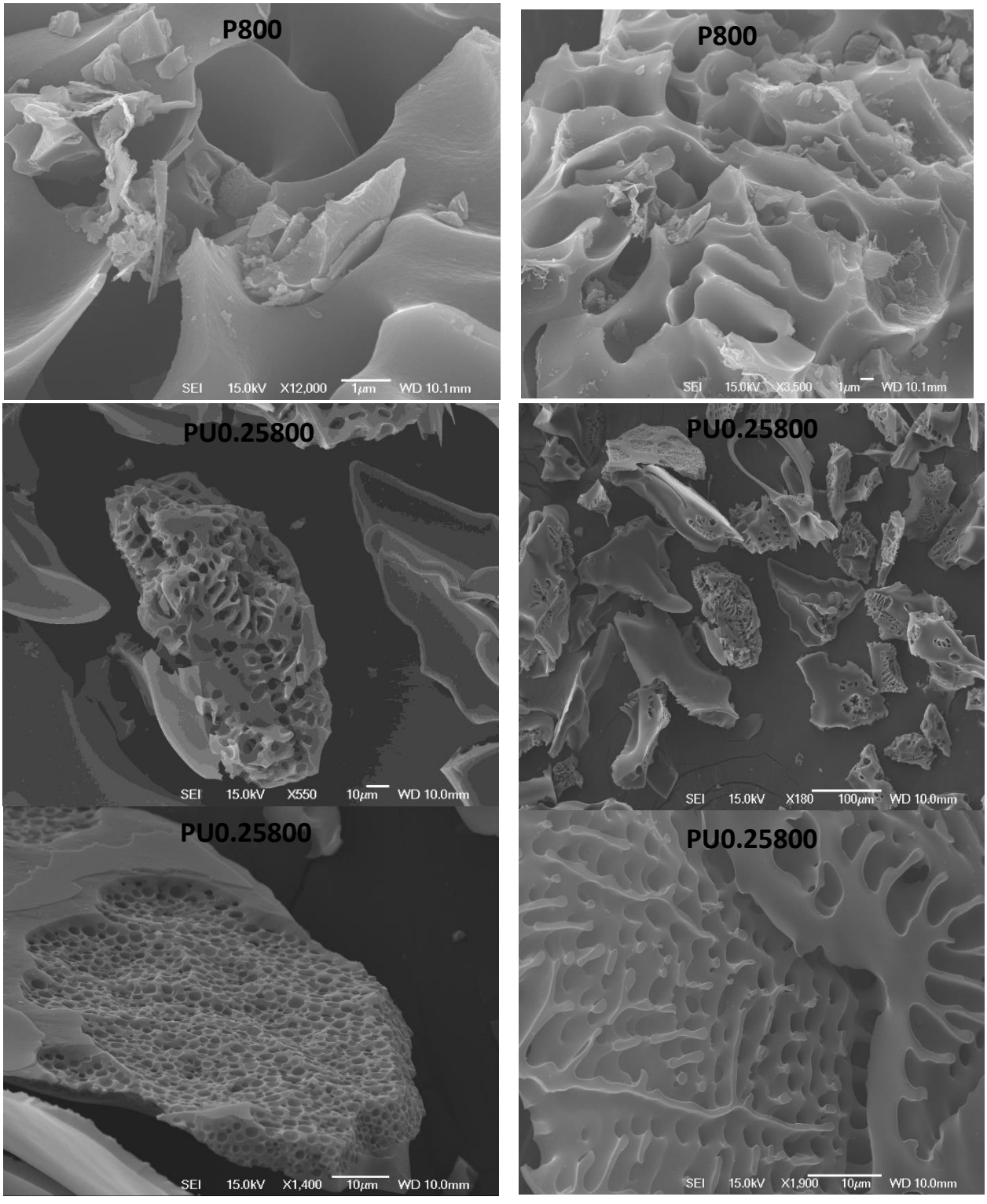
Table 5-2 textural properties and elemental analysis of the samples.

Sample	Textural properties		Elemental composition CHN				Elemental composition XPS			
	Surface area[a]	Pore volume[b]	C	H	N	~O	C	K	N	O
	m^2/g	cm^3/g	%	%	%	%	%	%	%	%
P800	1289 (1087)	0.60 (0.42)	87.98	0.20	0	11.82	67.28	3.99	0	28.73
PU0.0625800	1349 (1194)	0.61 (0.46)	90.68	0.05	0.32	8.95	-	-	-	-
PU0.125800	1510 (1324)	0.67 (0.51)	89.48	0.07	0.58	9.87	-	-	-	-
PU0.25800	2138 (1740)	1.04 (0.73)	91.34	0	0.91	8.66	88.61	0	1.01	10.37
PU0.5800	2312 (1654)	1.1 (0.65)	84.34	0.46	2.54	12.66	76.48	1.27	2.36	19.89
PU0.5800-5	2242 (1595)	1.2 (0.63)	87.27	0.15	1.25	11.33	-	-	-	-
PU0.75800	2018 (1581)	0.86 (0.62)	83.03	0.82	9.64	6.51	-	-	-	-
PU800	1374 (695)	0.67 (0.28)	74.45	0.61	12.01	12.93	75.32	0.85	12.53	11.30
PU800-5	1436 (584)	0.88 (0.24)	76.29	0.85	14.72	8.98	-	-	-	-
PN800	1565 (1163)	0.75 (0.45)	90.74	0.12	1.19	7.95	-	-	-	-

[a] The values in parenthesis are micropore surface area. [b] The values in parenthesis are micropore volume.

The morphology of the P800 and the N-doped samples are shown in the SEM images in Figure 5-3. Sample P800 and PU0.25800 both had microcracks and carbon flakes, which looked like interconnected carbon nanosheets. This morphology was a result of the carbonisation of KHP. When urea was introduced onto the carbonised KHP, holes in a sponge-like pattern developed on the carbon surface. Apart from the interconnected nanosheets of KHP carbonisation, the sponge-like pattern was created by the low amounts of added urea (sample PU0.25800). When the amount of urea was increased to P/U ratio of 0.5, well-developed interconnected pores in irregular carbon particle shapes were produced. The sponge-shaped pores seem to have a narrow range

of sizes around 100 nm. This range of pore widths became wider by adding more urea at P/U ratio 1; at this point, the irregularity in the pore sizes and the morphology of the surface also increased.



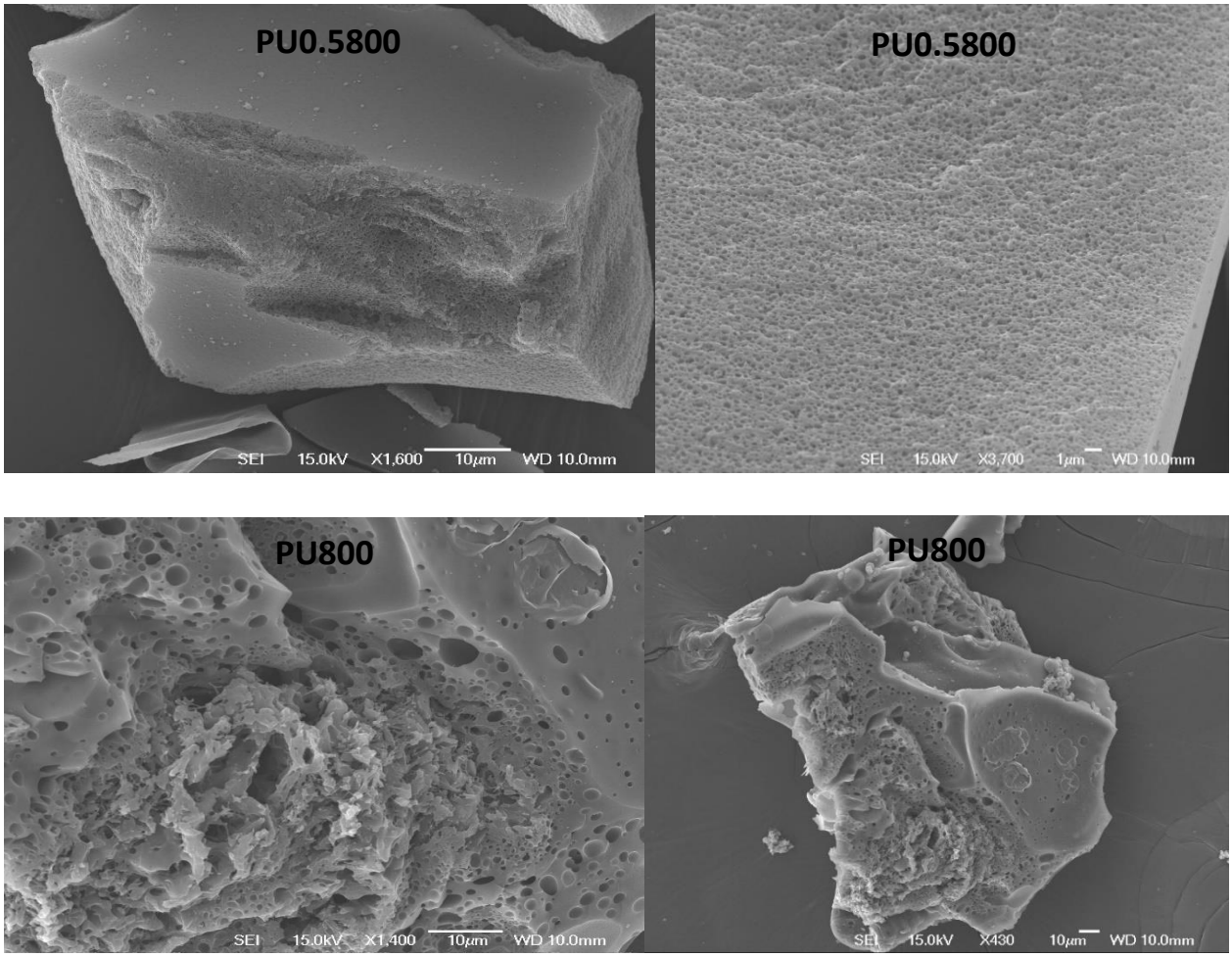


Figure 5-3 SEM images of carbons of carbons derived from carbonisation of mixtures of urea (U) and potassium hydrogen phthalate (KHP) at 800°C.

The mechanism by which KHP decomposes during the carbonisation as previously described by the group, is that the carbon framework seems to expand and then contract.[15] The change in the carbon morphology after adding urea can be interpreted as the urea acting as a directing agent for the formation of crumbled graphene layers.[12, 15, 16] On the other hand, the surface morphology seems to be developed by etching the surface as is clearly seen in Figure 5-4, which depicts the morphology of the carbonised sample PU0.25 at 600°C. A comparison between SEM images of the sponge-shaped morphology on some

parts of PU0.25800 and SEM of PU0.25600, shows how the 3D morphology in PU0.25800 started to progress on the particle surface at about 600°C.

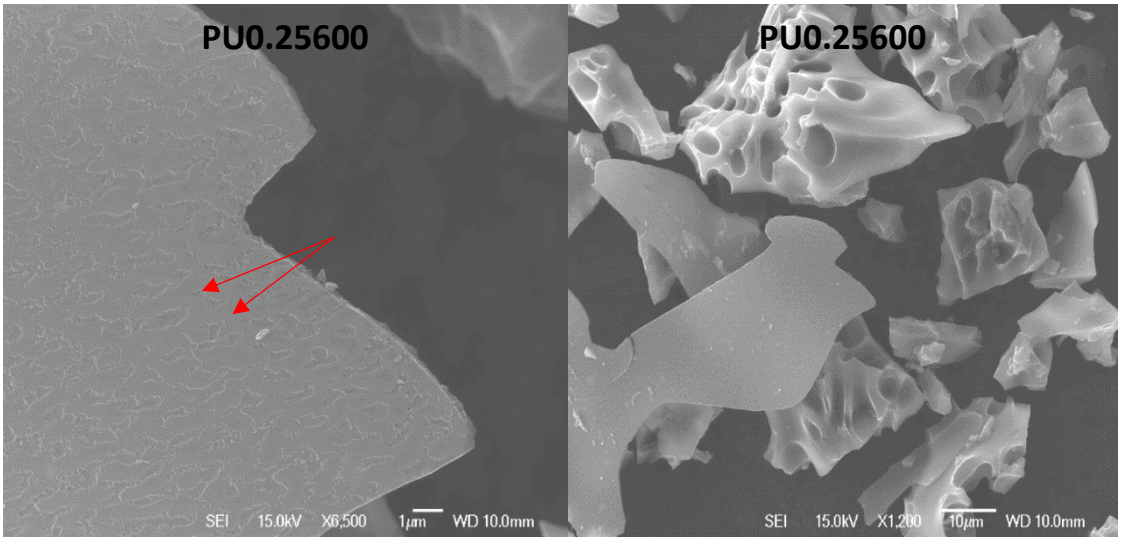


Figure 5-4 SEM images of carbon derived from carbonisation PU0.25 at 600°C.

The elemental analysis data given in Table 5-2 shows that by adding urea to the KHP carbonisation mixture, nitrogen atoms were incorporated into the carbon framework as dopants. The amount of N-doping increases with an increase in the amount of urea. Despite these features, the development of the surface area and porosity were suppressed at ratio 1. As the XRD results above show, at the highest level of N-doping (P/U ratio of 1), there is a formation of graphitic layers, which causes a reduction in the surface area and the porosity. A P/U ratio of 0.5 seems, however, to be optimum; besides significant incorporation of N, the surface area and porosity were the highest. Additionally, by comparing PU0.5800 and PU0.25800, which have nearly comparable porosity, the N content is lower for the latter.

For a comparison, an N-doped carbon was produced by the carbonisation of potassium phthalimide at the same conditions (sample PN800). Potassium

phthalimide contains only about 8%wt. of N, as shown in Table 5-3 in the pre-carbonised column, while the N content in the PU0.25 mixture was 9%. Despite this small difference in the N content, the surface area of PN800 was lower by 27%, as shown in Table 5-2 compared to the PU0.25800, which can be explained by effect of the O/C ratio. It is know that the O/C ratio has a main role in prediction of the degree of the activation. The degree of activation increase as the O/C ratio.[17] Consequently, PN800 that has lower O/C ratio compared to PU0.25800 had a lower porosity as well.

Table 5-3 Elemental composition before and after carbonisation of Urea/KHP mixtures in this work versus other works.

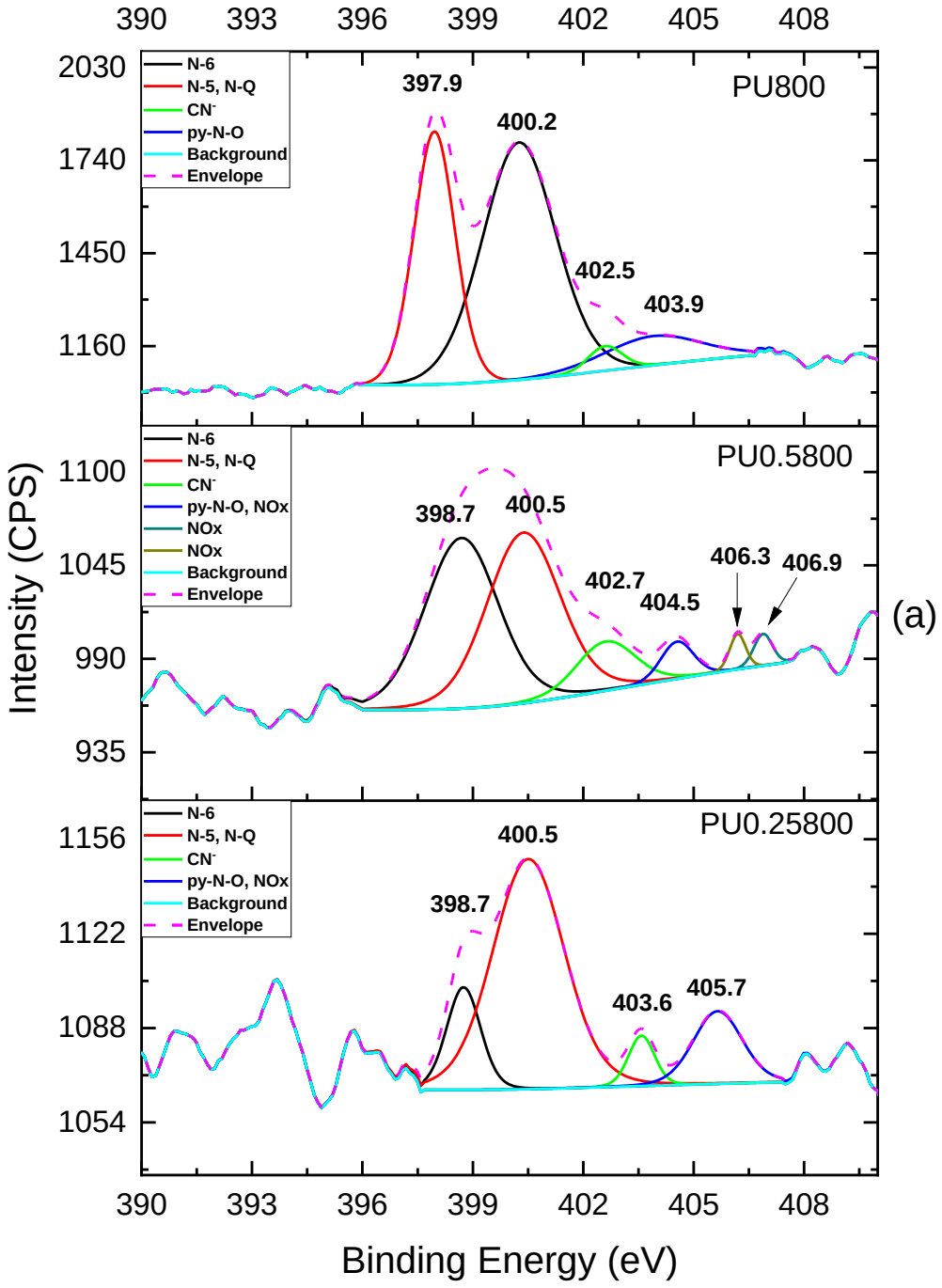
Sample	**Carbonised[a]**						
	C%	H%	N%	O%	N/H	N/C	N/O
PU800	74.45	0.61	12.01	12.93	1.41	0.14	1.06
PU0.75800							
PU0.5800	84.34	0.46	2.54	12.66	0.39	0.03	0.23
PU0.25800	91.34	0.00	0.00	8.66		0.00	0.12
PN800	90.74	0.12	1.19	7.95	0.71	0.01	0.17
PU0.125	89.48	0.07	0.58	9.87	0.59	0.01	0.07
PU0.0625	90.68	0.05	0.32	8.95	0.46	0.00	0.04
	Pre-carbonised[b]						
	C%	**N%**	**N/H**	**N/K**	**N/C**	**N/O**	
PU800	33.50	23.30	0.37	6.80	0.60	0.92	
PU0.75800	35.40	20.00	0.34	5.10	0.48	0.78	
PU0.5800	38.00	16.00	0.29	3.40	0.35	0.60	
PU0.25800	42.00	9.32	0.20	1.70	0.19	0.35	
PN800	52.00	7.56	0.25	1.00	0.13	0.50	
PU0.125	44.00	5.18	0.13	0.85	0.10	0.19	
PU0.0625	45.40	2.74	0.07	0.43	0.05	0.10	
PU800	33.50	23.30	0.37	6.80	0.60	0.92	
PU0.75800	35.40	20.00	0.34	5.10	0.48	0.78	

[a] elemental analysis of the carbonised samples collected from CHN analysis
[b] calculated from the precursors (urea + K-organic salt) and based on the weights used

Carbonisation of a potassium citrate, a potassium organic salt, with urea introduced three types of nitrogen atoms into the carbon framework: pyrrolic-N,

pyridinic-N and quaternary-N.[12] The elemental analysis was performed by XPS as well for further confirmation, especially for the type of N-content in our samples. The deconvoluted high-resolution N 1s spectra (Figure 5-5-a) of the three different ratio samples were mainly composed of two main peaks centred at 398± 0.8 eV and 400.2± 0.3 eV and smaller peaks in the range of 402–405 eV. The N1s peak's component is at 398± 0.8 eV corresponding to pyridinic nitrogen.[12, 15] It was at 398.7 eV in the two samples that had a lower urea amounts and shifted to lower binding energy in the sample with a higher amount to 397.9 eV, which could mean that the peak was related to a mix of pyridinic and tri-s-triazine rings (which increased with increasing the dopant ratio).[20] The other main component at 400.2± 0.3 eV was attributed to pyrrolic/pyridone nitrogen, and this peak could correspond to a mix of pyrrolic/pyridine and graphitic nitrogen groups.[15, 21] Therefore, there was a shift to lower binding energy in PU0.5800 and PU0.25800 (400.5 rather than 401.3 eV). This was at 400.2 eV in PU800, which could be due to the presence of a higher proportion of pyrrolic/pyridone nitrogen. The small peak at 403.6 eV in PU0.25800 corresponds to pyridine-N-oxide groups.[22-24] This peak shifted to lower binding energy with an increased dopant ratio to 402.7 and 402.5 eV in PU0.5800 and PU800, respectively.[25] There is another possibility for the origin of this peak at 402.7± 0.2 eV, which is the presence of a tiny amount of potassium as impurities, which could be in the form of KCN. According to the literature, this peak is due to the nitrogen in the cyanide group. The cyano group and heterocycles can have positive charge localisation or charging effects at 402.6 eV or 404.4 eV.[20, 26, 27] On the other hand, the other small components of the N

1s peak were in the range of 404.5–406 eV and could as well come from (R-)NOx groups, such as nitrites or nitrates, according to other literature.[28, 29]



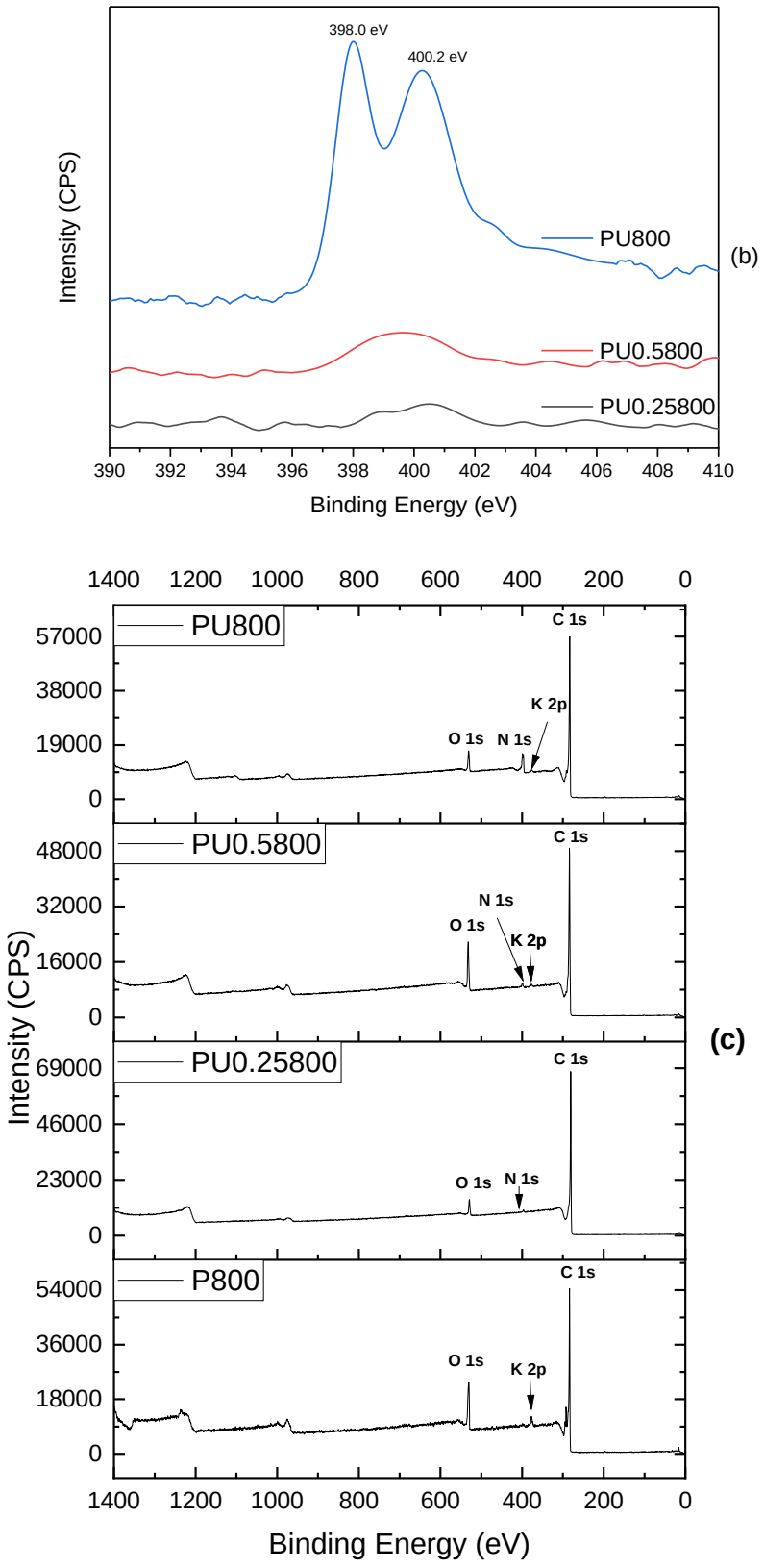
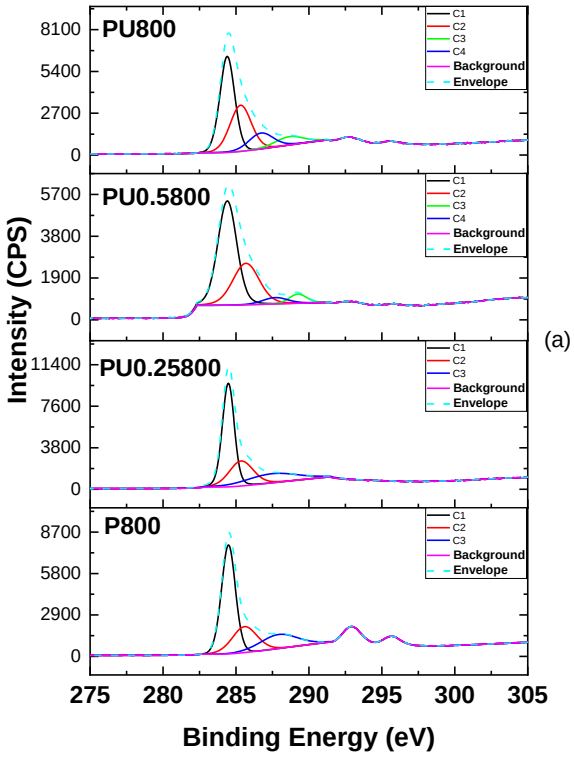


Figure 5-5 deconvoluted high-resolution N 1s spectra and XPS spectra of carbons derived from carbonisation of mixtures with various amounts of KHP and urea (U:KHP ratios of 0.25, 0.5 and 1) at 800°C for 1 h (a&b), XPS survey spectra of the same samples compared to the undoped sample (P800) (c).

The XPS wide scan of the N-doped samples and the undoped P800 sample (Figure 5-5-c) showed the presence of traces of the activating agent peak, due to an insufficient washing step. Thus, the K2p peak in P800, PU800 and PU0.5800 is present as impurities in the form of K_2CO_3 or KCN. The potassium usually appears in two peaks at around 292 and 295 eV, attributed to $K2p_{1/2}$ and $K2p_{3/2}$.[30] The K2p peaks, which originate from potassium carbonate, have to be accompanied by a peak in the high-resolution O 1s spectrum, as seen in the P800 sample at 530.0 ± 0.5 eV, and a peak in the range of 288-289 eV in the high-resolution C 1s spectrum, attributed to a -COK.[31] Also, peaks of KCN traces were possibly present in the N-doped samples PU800 and PU0.5800; there was a peak in the high-resolution C 1s spectrum in the range of 288–289 eV, as well as a peak at ~399.0 eV in the high-resolution N 1s spectrum, were attributed to the carbon and nitrogen of the CN-functional group of KCN.[32, 33]



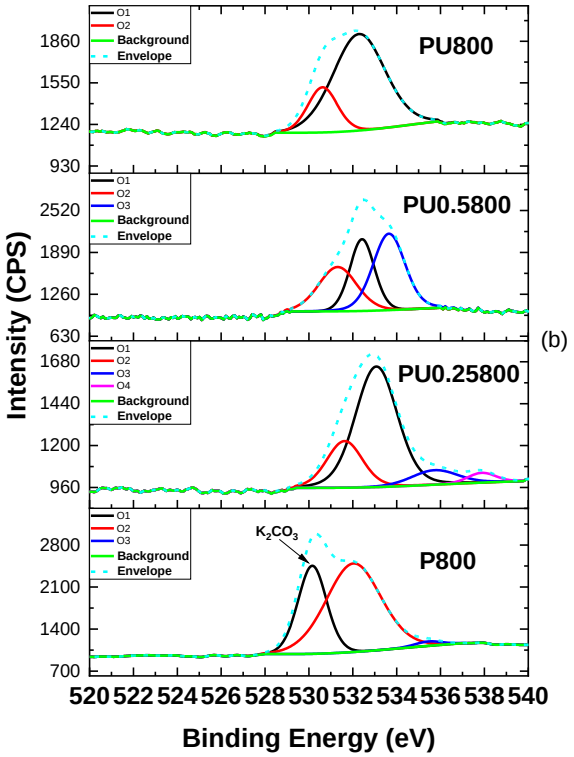


Figure 5-6 Deconvoluted high-resolution C 1s, K2p (a) and O 1s (b) spectra of carbons derived from carbonisation of mixtures with various ratios of U:KHP at 800°C for 1 h.

In summary, the XPS results showed that carbonisation of a mixture of different urea/KHP ratios has led to the doping of mainly pyridinic nitrogen and pyrrolic nitrogen and possibly a small amount of graphitic nitrogen. The results confirm the efficiency of the preparation steps in removing the inorganic species, as the inorganic impurities in the N-doped carbons were less than ca. 1%. On the other hand, the FTIR spectra (Figure 5-7) showed two main peaks attributed to N-doping located around 1650 and 1300 cm^{-1}. The peak centred at ca. 1650 cm^{-1} was assigned to the aromatic C=N bonds and the one that centred at ca. 1300 cm^{-1} was assigned to C-N bonds.[18, 34] The emergence of two peaks in PU800 and PU0.5800 can be attributed to N-doping, as evidenced by the increased intensities observed in correlation with the percentage of N present in the samples.

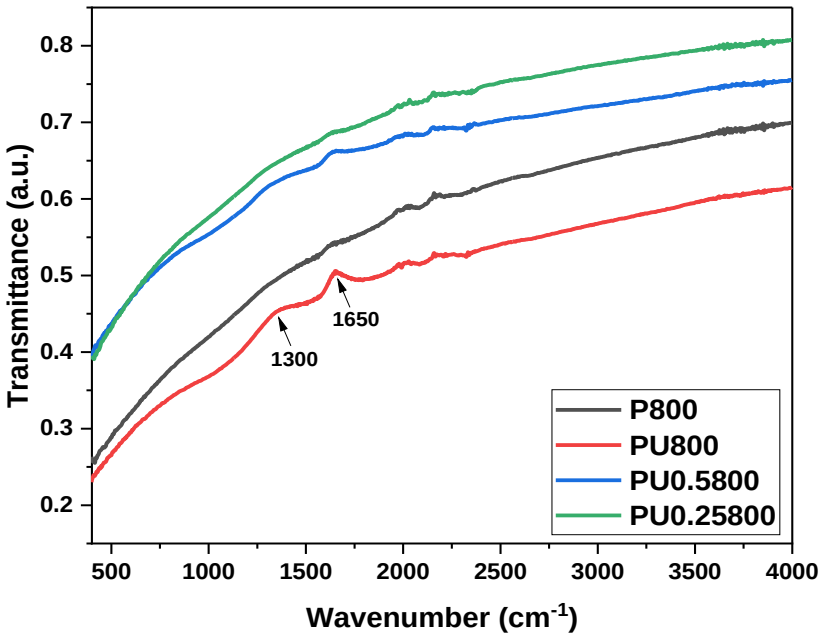


Figure 5-7 FTIR spectra of carbons derived from carbonisation of mixtures with various ratios of U:KHP mixture (0.25, 0.5 and 1) at 800°C for 1 h.

3.2.Carbonisation temperature

The effect of carbonisation temperature on porosity is summarised in

Table *5-4* and Figure 5-8. The surface area and total pore volume of the samples prepared at P/U ratio of 0.25, 0.5 and 1 increased with carbonisation temperature from 600 to 900°C. This does not include the carbonisation ratio of 0.25, because increasing the carbonisation temperature from 800 to 900 resulted in some decrease in porosity (microporosity) due to the destruction or blockage of part of the pores. Compared to the PU and PU0.5 set samples, the samples prepared at P/U ratio of 0.25 are mostly composed of KHP. The porosity from literature of carbonised KHP without urea is higher at 900°C than at 800°C.[35] On the contrary, when urea was added, the microporosity decreased when the temperature rose from 800 to 900°C, as shown in

Table *5-4*. At carbonisation temperatures greater than 700°C, i.e. at 800°C and above, the knee of the isotherms shows gradual widening compared to the isotherms of samples carbonised at 600 and 700°C. This indicated the formation of larger pore sizes at temperatures greater than 700°C.

The high ratio of urea enhanced increasing the proportion of the microporosity. As we can see in

Table *5-4*, the microporosity decreased as the carbonisation temperature increased between 600 ─ 900 °C in the samples of P/U ratio 0.5 and 1. The micropore area percentage, as example, decreased from 87% to 43% between 600 ─ 900 °C in P/U of ratio 1. On the contrary, the microporosity increased as the temperature increased between 600 ─ 800 °C in the sample of P/U ratio 0.25 then decreased again at 900 °C.

On the other hand, the micropore surface area and micropore volume increased as the carbonisation temperature increased in all P/U ratios (see

Table *5-4*). However, between 800 and 900 °C, there was a decrease in micropore surface area and micropore volume in the samples of ratios 0.25 and 0.5, while the decrease was between 700 and 800 °C in the samples of ratio 1. This notice revealed the role of a combination of activation temperature and P/U ratio in modulating the microporosity of the samples.

Table 5-4 Textural properties and CHN elemental analysis showing the effect of carbonisation temperature.

Sample	Textural properties				Chemical composition			
	Surface area[a]	Pore volume[b]	µSA[c]	µVp[c]	C	H	N	O
	m^2/g	cm^3/g	%	%	%	%	%	%
P800	**1289 (1087)**	**0.60 (0.42)**	**84**	**70**	**87.98**	**0.20**	**0**	**11.82**
PU600	577 (500)	0.27 (0.19)	87	70	61.36	1.44	22.01	15.19
PU700	1309 (993)	0.61 (0.39)	76	64	66.97	1.24	17.99	13.8
PU800	**1374 (695)**	**0.67 (0.28)**	**51**	**42**	**74.45**	**0.61**	**12.01**	**12.93**
PU900	1538 (661)	0.84 (0.27)	43	32	83.27	0.11	7.98	8.64
PU0.5600	1309 (1014)	0.56 (0.40)	77	71	74.61	0.94	6.91	17.54
PU0.5700	1723 (1331)	0.82 (0.52)	77	63	79.86	0.44	4.94	14.76
PU0.5800	**2312 (1654)**	**1.1 (0.65)**	**72**	**59**	**84.34**	**0.46**	**2.54**	**12.66**
PU0.5900	2409 (1565)	1.2 (0.62)	65	52	89.95	0.19	1.22	8.64
PU0.25600	1064 (702)	0.51 (0.28)	66	55	77.16	2.58	4.47	15.79
PU0.25700	1598 (1116)	0.73 (0.44)	70	60	80.97	0.635	3.32	15.08
PU0.25800	**2138 (1740)**	**1.04 (0.73)**	**81**	**70**	**91.34**	**0**	**0**	**8.66**
PU0.25900	2205 (1441)	0.99 (0.58)	65	59	92.25	0	0.42	7.33

[a] The values in parenthesis are micropore surface area. [b] The values in parenthesis are micropore volume. [c] Percentage of micropore surface area and percentage of micropore volume percentages.

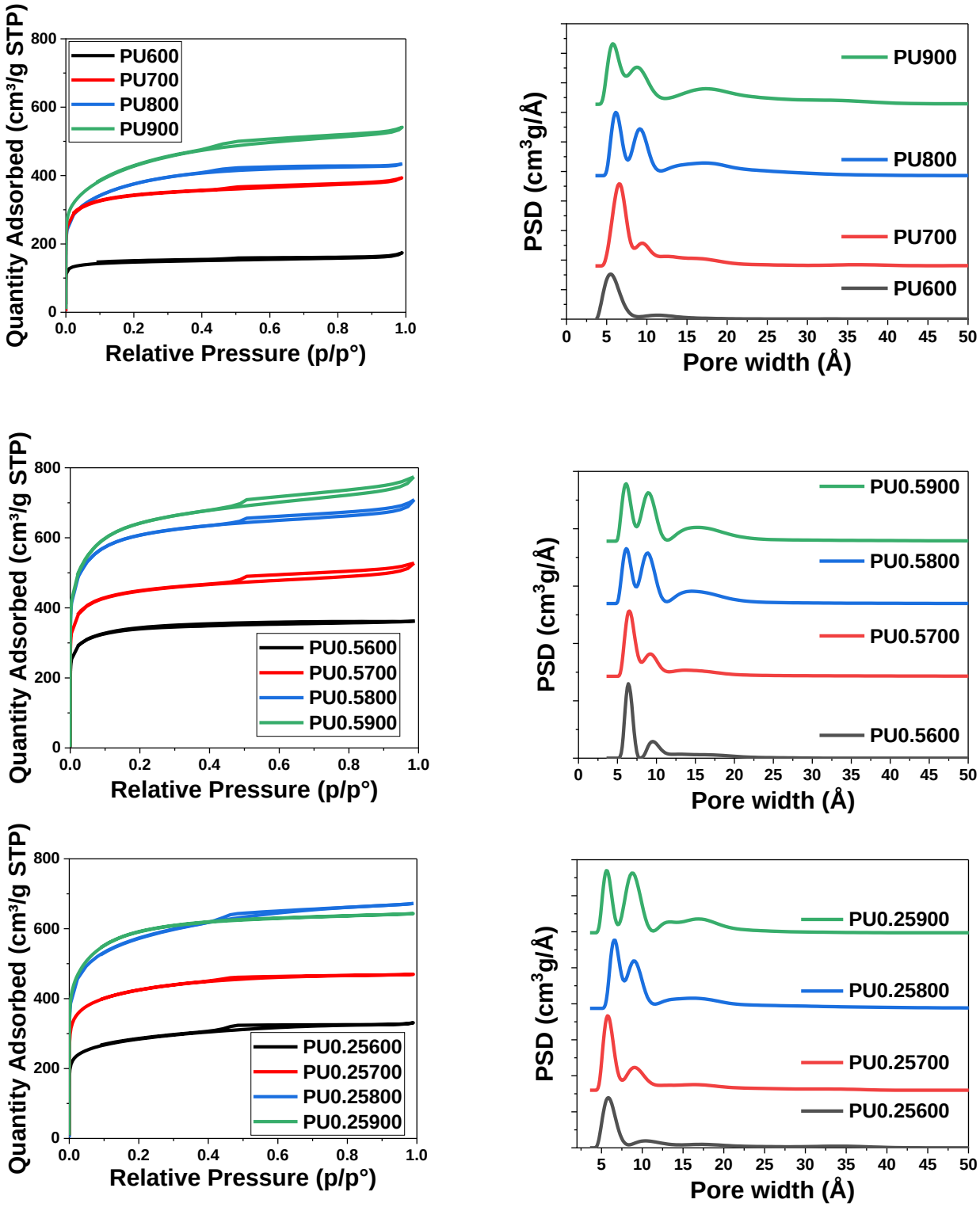


Figure 5-8 Nitrogen sorption isotherms and NLDFT PSD curves of carbons derived from carbonisation of mixtures containing various ratios of U:KHP at various temperatures.

A P/U ratio of 1 led to the formation of a large number of graphitic layers, as shown in the XRD patterns in Figure 5-11, which explains the noticeable low surface area and pore volume of this sample. The samples prepared at lower P/U ratios, Figure 5-9 and 11, showed an amorphous nature. The broad peak at 2θ of 25.5–28°C from graphitic layers was observed for all the samples prepared at P/U ratio of 1 regardless of the carbonisation temperatures. However, the intensity of this peak decreased as the carbonisation temperature increased. In the samples prepared at P/U ratio of 0.5 and 0.25, the peak was weak and only appeared for carbonisation at 600 and 700°C. Noticeably, the intensity of these graphitic peaks is related to the amount of nitrogen in the samples.

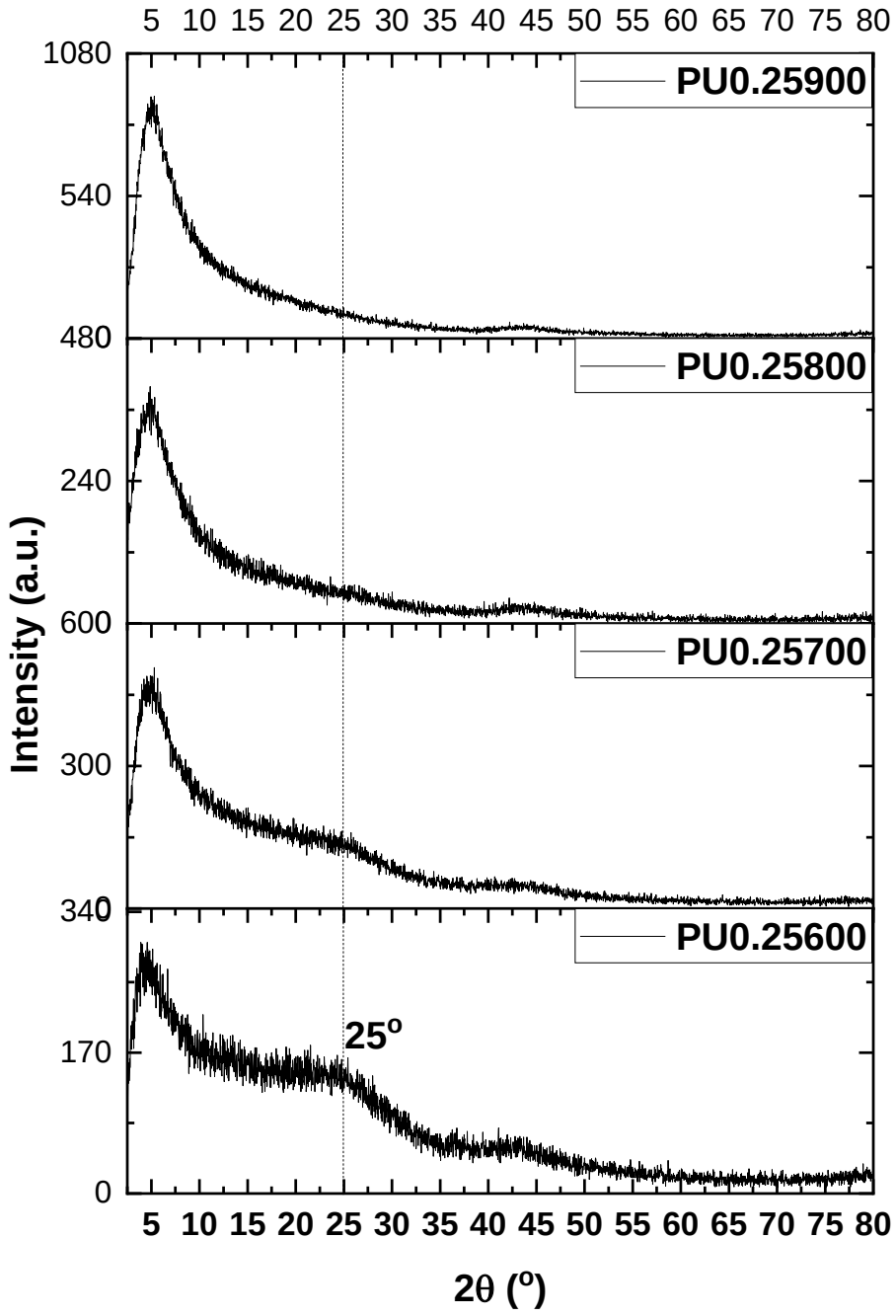


Figure 5-9 Powder XRD patterns of carbons derived from carbonisation ratio 0.25 of U:KHP at different temperatures for 1 h

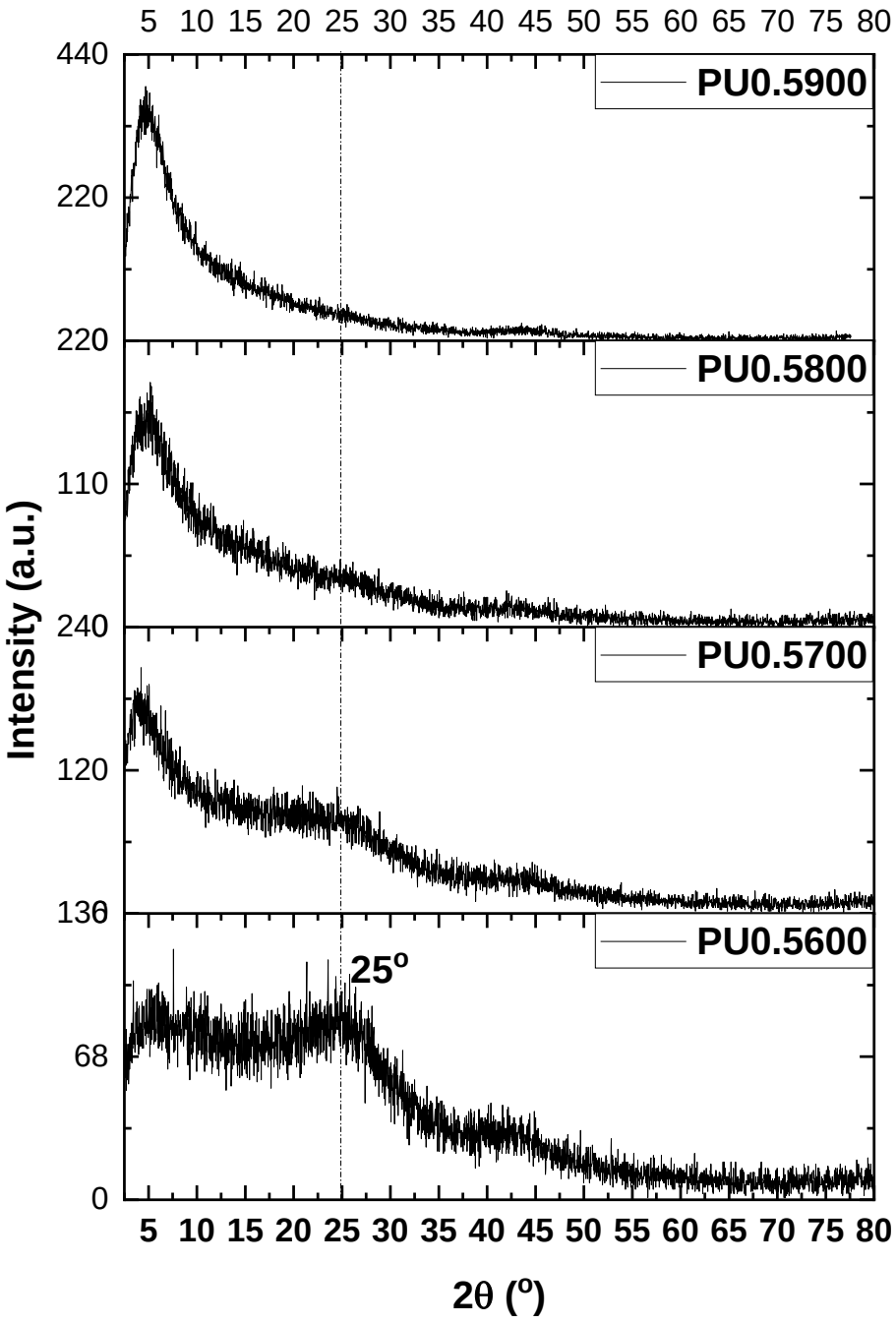


Figure 5-10 Powder XRD patterns of carbons derived from carbonisation ratio 0.5 of U:KHP at different temperatures for 1 h

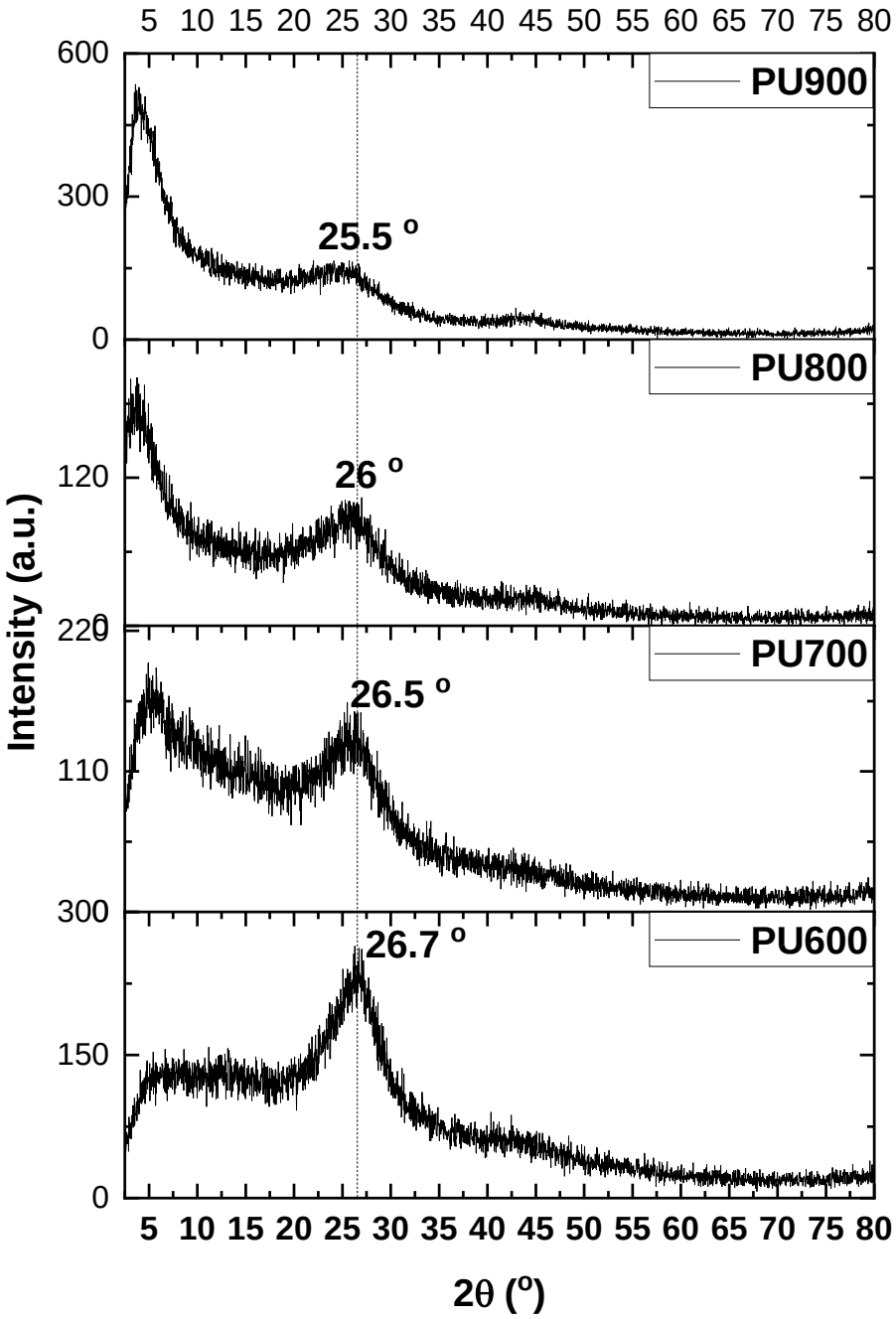


Figure 5-11 Powder XRD patterns of carbons derived from carbonisation ratio 1 of U:KHP at different temperatures for 1 h

From all the results above, we can conclude that the doping happened at low temperatures and after dissociation of all urea decomposition products. It seems the doping was stopped at that point, i.e. at low temperature, as the amount of N% decreased with increased carbonisation temperatures from 600 to 900°C. Contribution of mechanochemical forces cannot be excluded in incorporating the nitrogen into the carbon framework.[21] As observed for sample PU0.25900, development of the porosity depends on the amount of the nitrogen left in the carbon which could be due to destruction of the porosity by removal of the N from the carbon framework. From the comparison between the PN800 sample and other samples, the PN sample has much lower porosity than PU0.25800, even though they have a closely matched N content. However, PN800 has a porosity similar to that of PU0.125800, with a small difference in the microporosity between them. That could be because of the similarity and dissimilarity in the N/K percentage in Table 5-3. The decrease of microporous surface area in PN800 could be due to the high N/C, i.e. due to a decrease in the carbon content in the framework compared to PU0.125800.

The next section is to understand what happened during the carbonisation of KHP in the presence of urea to uncover the factors that control the porosity of the samples. We will start by stating the reactions that took place and some of the findings from our work and previous reports.

3.3.Carbonisation/activation processes

The carbonisation of the KHP itself was described by the Mokaya group,[35] and the possible reactions that happened during its carbonisation were studied as well. In brief, the carbonisation of KHP at 900°C happened in three major steps; first, water and phthalic anhydride are volatised with the formation of

dipotassium phthalate at a low temperature of 330°C; then, at 560°C, the dipotassium phthalate decomposes into K_2CO_3; finally, at 700°C, some of the potassium carbonate dissociates and the final carbon sample is generated. Urea, on the other hand, has been used for N-doping as a precursor of g-C_3N_4[15] and other reducing agents as well, e.g. NH_3.[13, 36, 37] During the carbonisation of urea itself, the elements polymerise at around 500°C to form carbon nitride g-C_3N_4. Depending on the pyrolysis conditions, different morphologies of g-C_3N_4, 1D, 2D or 3D can be achieved.[38]

We pyrolysed urea at ca. 550°C under the same conditions as used to prepare the carbons in this study, and obtained g-C_3N_4. The physical appearance confirms that the product, g-C_3N_4, has different morphologies, as is clear from the observed colours, which ranged from pale yellow to orange,[38] and as the XRD pattern shown in Figure 5-12. The SEM images in Figure 5-13 show the carbonised urea. There are different morphologies produced from the carbonisation of urea to g-C_3N_4. These morphologies exhibit potential congruence with the analysis of XRD peaks. The most intense peak at 28° is generally for graphitic materials (crystal plane, 002) and seems to correspond to g-C_3N_4 but with a shift to a higher angle. The small, wide peak at 14° seems to be a crystal plane (100) related to the tris-s-triazine unit, with a shift to a higher angle as well. While the peaks at 20−26 and 30° could be attributed to g-C_3N_4 nanorods.[39]

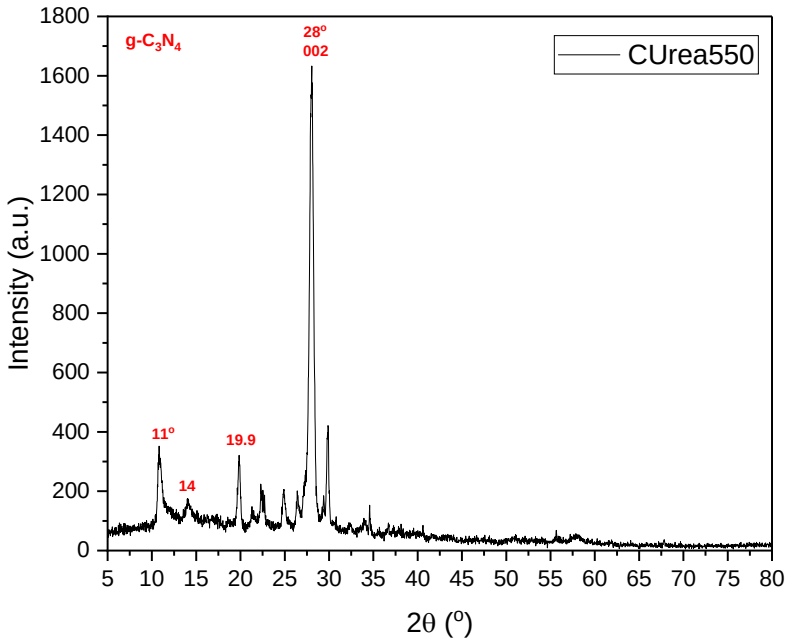


Figure 5-12 Powder XRD patterns of carbon nitride derived from carbonisation of urea at 550°C for 1 h.

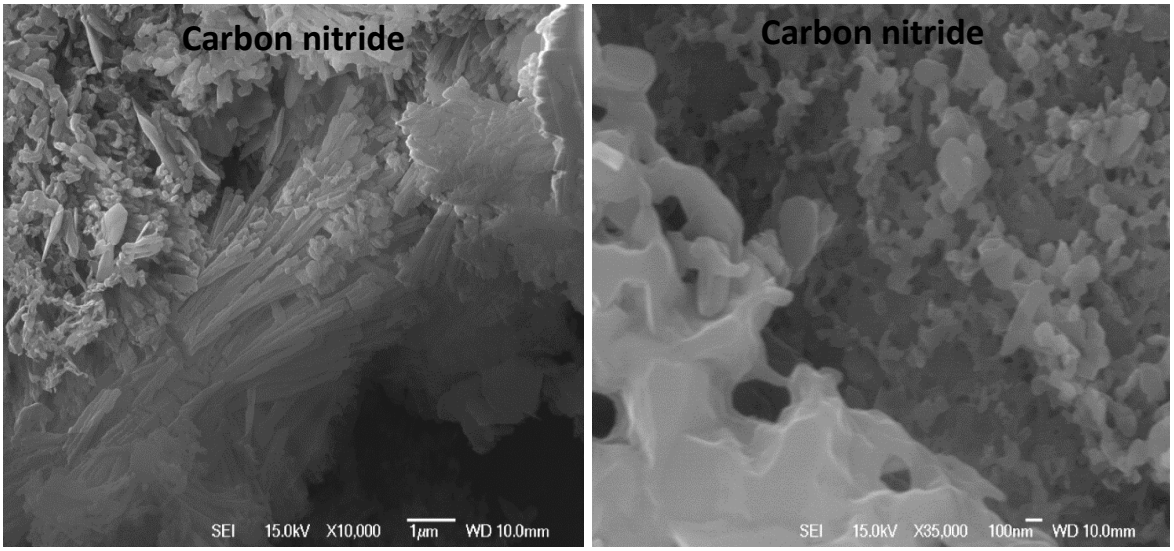


Figure 5-13 SEM images of carbon nitride derived from carbonisation of urea at 550°C for 1 h.

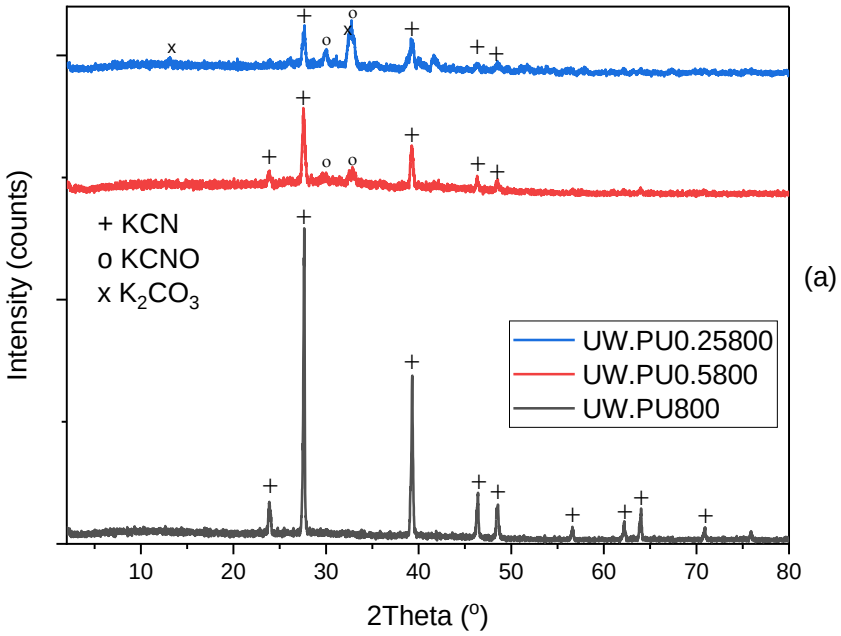
The carbonisation of KHP with urea involves an activation step and according to the literature,[12] the activation mechanism in the presence of urea and K-based activating agents can be described as follows:

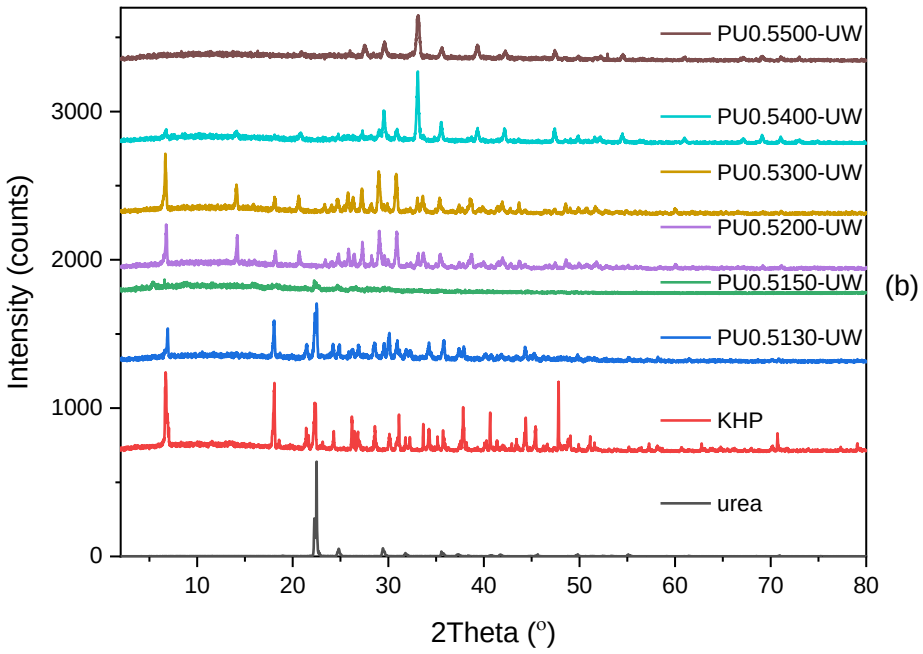
$$OC(NH_2)_2 + K_2CO_3 \rightarrow 2\ KCNO + 2\ NH_3 + H_2O + CO_2 \quad (1)$$

$$KCNO + C \rightarrow KCN + CO \quad (2)$$

The activation of N-containing carbon sources using potassium will produce potassium cyanate and potassium cyanide (equation 1, 2) due to a reaction between the N-functional groups and potassium.[40] The XRD patterns of the N-doped carbon samples collected before the samples were washed and the inorganic residues removed are shown in Figure 5-14. From the interpretation of the XRD patterns in Figure 5-14 and the above reactions, we can summarise some of the possible processes that took place during the carbonisation of our samples. The XRD peaks of KCNO started appearing simultaneously due to a reaction between the decomposition products of KHP 'K_2CO_3 /-CO_2K'[35] and urea at low temperatures. The formation of potassium carbonate and/or -CO_2K from KHP decomposition in the presence of urea was supposed to be at temperatures lower than 470°C. The temperature of dissociation of KHP to potassium carbonate has been reported to be 470°C. That was confirmed by the decrease in the intensity of the main peaks of KHP at around 300°C as shown in Figure 5-14-b and c. Different works have reported a decrease in the decomposition temperature of potassium salts in the presence of urea.[12, 14] After the dissociation of most of the KHP at temperatures higher than 300°C, most of the -CO_2K reacted to create more KCNO, as the intensity of KCNO peaks became dominant. The KCNO in turn decomposed into KCN with the increase in the carbonisation temperatures of all the doped samples, as can be clearly seen in Figure 5-15. The high intensity of the KCNO and KCN peaks in Figure 5-14 could explain the low amount of N-doping in the created carbon from low urea/KHP ratios, as most of the remaining nitrogen had been removed as

potassium cyanide. After the consumption or dissociation of all the urea,[13, 36] there was still extra -CO_2K in K_2CO_3 form. As a result, in the low ratio of urea (PU0.25), the K_2CO_3 peaks' intensities at around 800 °C were visible compared to PU0.5 and PU, which have higher ratios of urea (Figure 5-14-a shows).





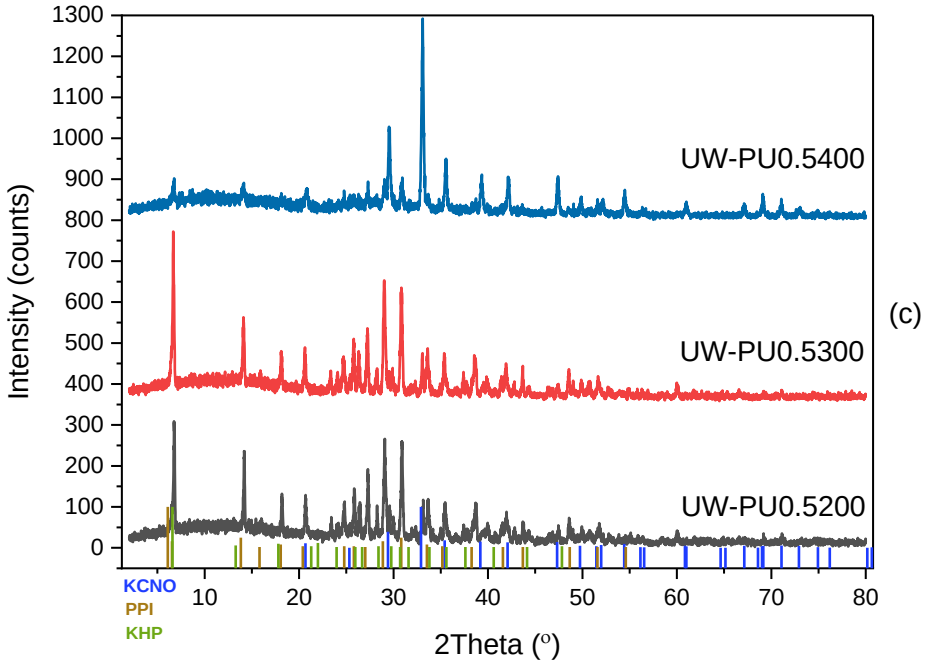
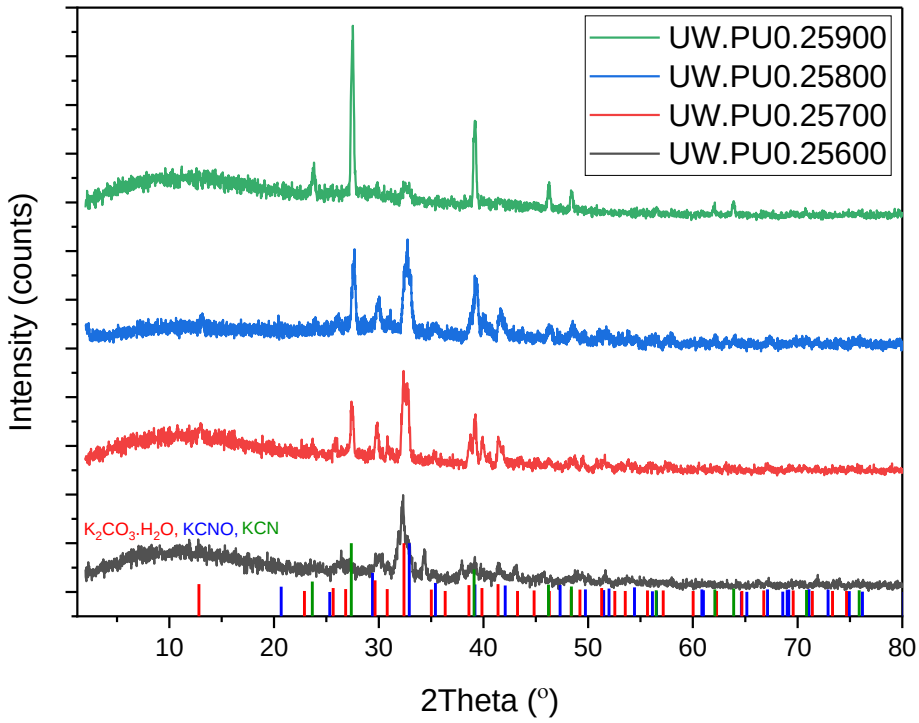


Figure 5-14 PXRD patterns of unwashed carbonised samples



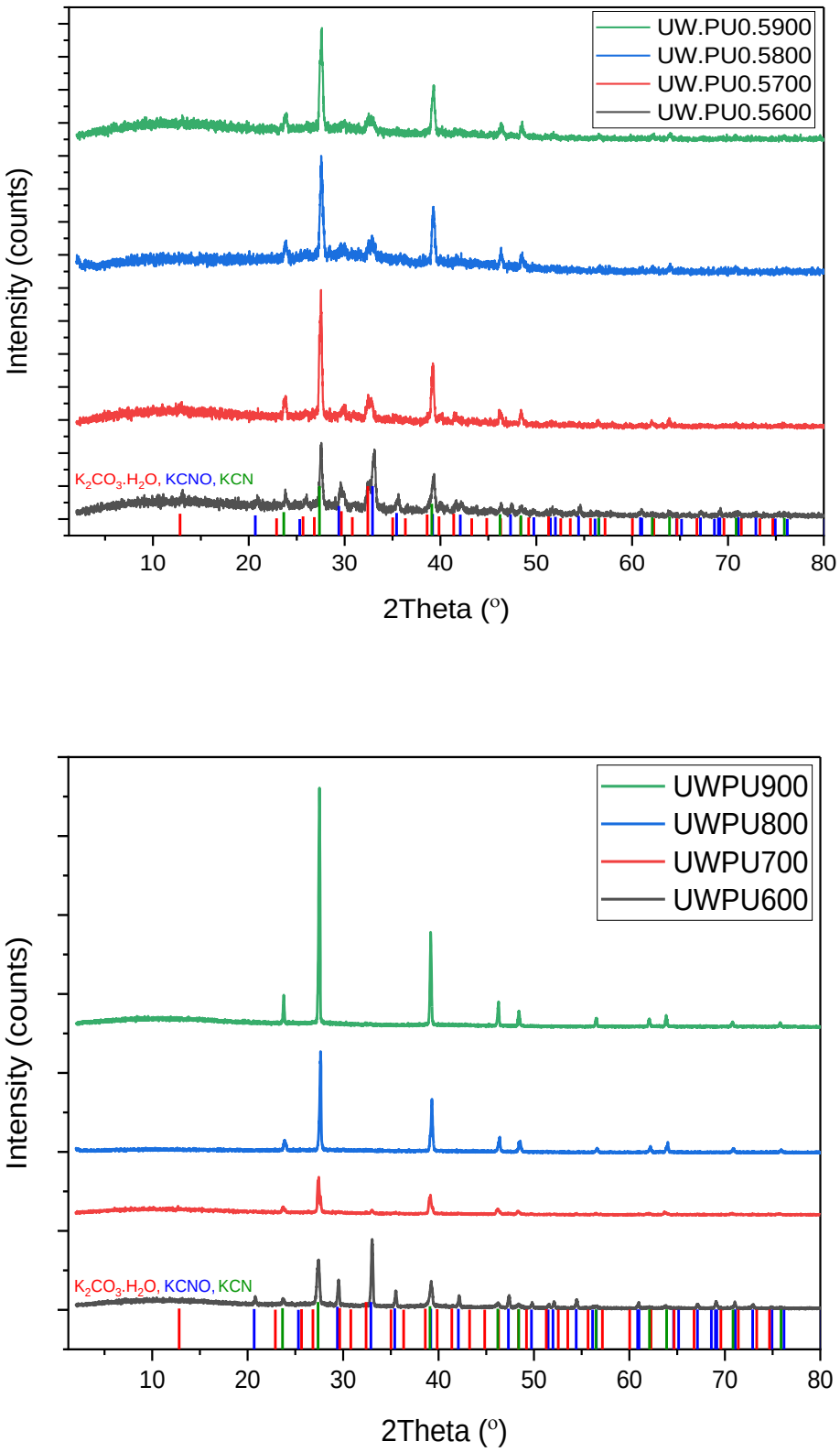


Figure 5-15 PXRD of the carbonised carbons at 600–900°C of different urea/KHP weight ratios

A fluffy white to yellowish powder accumulated in the end of the combustion tube during the carbonisation of KHP in the presence of urea, as shown in Figure 5-16. The XRD peaks suggested the presence of phthalimide. This is likely the result of a reaction between ammonia and phthalic anhydride to generate phthalimide.[41] The ammonia is expected to have come from the thermal dissociation of urea, which produces ammonia at low temperatures (130–150°C).[42] And the phthalic anhydride likely formed when KHP was heated to 300°C without urea.[35]

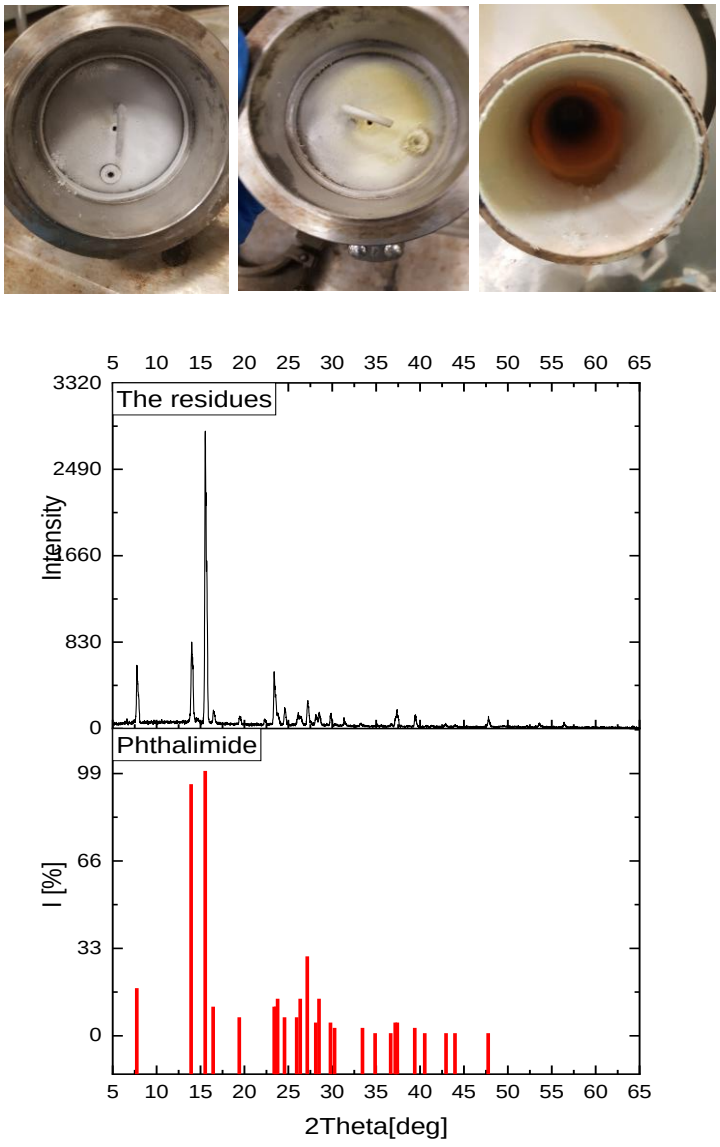


Figure 5-16 White to pale yellow powder accumulated at the ends and plug of the tube at ≥ 300 °C. Most of its PXRD peaks match phthalimide peaks

4. Discussion

The above equations (1 and 2) summarise the activation reaction of carbon in the presence of urea using well-known potassium salts. In order for the above-mentioned reactions to occur, every mole of urea in the reaction mixture must be paired by two moles of potassium. As a result, any increase in the potassium moles will add the effect of the well-known activation reaction of potassium to the above-mentioned activation reaction, while any excess moles of urea will add the effect of its reaction with the carbon to the above-mentioned activation reaction.

As mentioned above the reaction between potassium as an activating agent and carbon materials has been extensively studied.[11] At high temperatures, a reduced potassium ion dissociates into metallic K, which oxidises, intercalates and exfoliates the N-free carbon precursors to have plenty of microporosity. On the other hand and according to the literature,[16, 18, 37, 42] the thermal treatment of carbon with urea mostly reduces the carbon porosity. For example, for using urea for the reduction of graphene oxide (GO) to graphene or for N-doping, urea and GO were mixed and heated together. The result of that treatment was the removal of the oxygen, doping with nitrogen and the formation of graphitic layers. The increase of Van der Waals interactions between the carbon sheets induced by the incorporated nitrogen atoms in the carbon framework[14] was the reason that the N-doping was accompanied by the formation of graphitic layers. Furthermore, in an experiment to exfoliate pure graphite using urea at 600°C, due to the limitations of diffusion between the stacked graphitic layers, the urea was not effective. That went against what was expected, as urea reduces graphite

oxide to graphene.[37] Generally, the thermal treatment of carbon with urea might have a negative effect on the carbon porosity, unlike that of potassium.

Under our carbonisation conditions, the urea decomposed to form a graphitic C_3N_4 at a moderate temperature of ≥ 500°C. Thus, theoretically, the excess urea of the carbonisation of the KHP/urea mixture decomposed at a temperature higher than 600°C.[43] Based on the above statements, the decrease in porosity at a molar ratio 1:3 of KHP to urea (PU sample, 1:1 weight ratio, see Table 5-1) was due to the consumption of all the potassium in the reaction with urea at low temperatures and the excess of urea reacted with the carbon framework, causing high doping amount and formation graphitic layers in PU-samples. That also explained the heterogeneity of the 3D morphology of the PU800 sample due to reacting the decomposed urea with the carbon besides the etching reaction. In the samples of smaller molar ratio 1:1.5 or 1:1, as in samples PU0.25 and PU0.5 (Table 5-1), the surface area was boosted. However, the amount of N-doping was significantly lower compared to ratio 1 in the PU sample (Table 5-2). That means that most of the nitrogen was removed, due to the reaction of the potassium with nitrogen as a salt, KCNO/KCN, or due to vaporisation at the high temperature.

4.1. Effect of P:U ratio

The rise in the ratio of urea to KHP led to increase in porosity until the ratio 0.5 (molar ratio 1:1.5), after which, any increase led to a decrease in the surface area and especially so at ratio 1 (molar ratio 1:3). These results are consistent with those of Eichler et al.;[14] the increase of the molar ratio of nitrogen to potassium was accompanied by an increase in graphitic layers, which, as is well known, affects porosity. Consequently, the development of porosity is governed by the

N/K and N/C ratios.[14] The pores develop by the etching reaction between the potassium and the nitrogen, and in some cases via molten salt templating as well. The molten salt templating also participates in controlling the final porosity when there is a high amount of KCN compared to the carbon during the thermal treatment, which allows the carbon to solvate in the molten KCN at temperature above its melting point. As shown in Figure 5-17 and Table 5-3, the samples with the highest porosities were those with N/K ratios ranging from 1.70 to 3.40 and N/C ratios ranging from 0.19 to 0.35. The increase in N/K ratio from 3.4 to 6.8 was accompanied by a halving of the urea molar ratio from 1:1.5 to 1:3, resulting in a halving of the surface area. These results reliably confirm the importance of the N/K ratio in the pore development process.

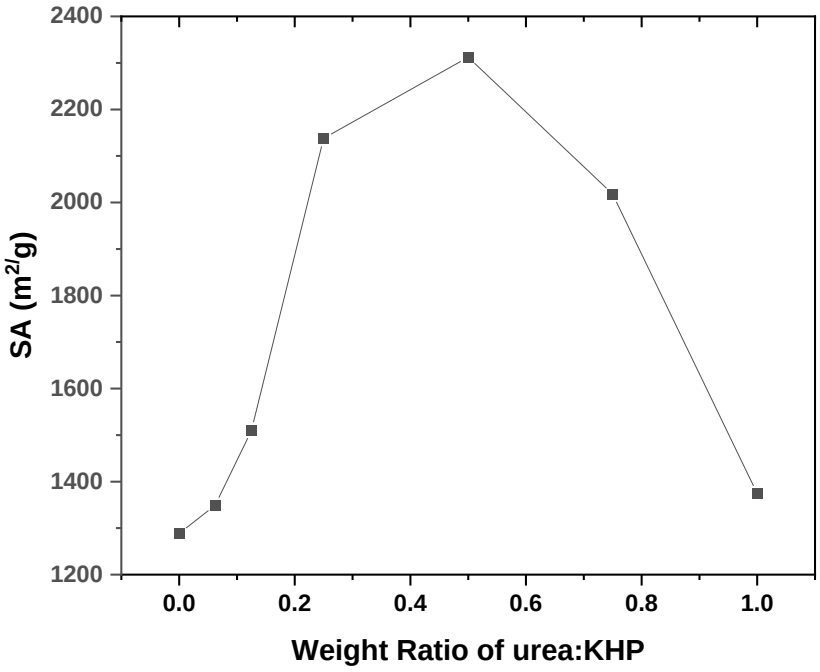


Figure 5-17 Relationship between the surface area and weight ratio of the pre-carbonised (urea:KHP) mixtures.

Besides the N/K ratio, the heating ramp rate and the duration are important factors as well in the overall pore development process. As shown in Table 5-2, two samples (PU800-5 and PU0.5800-5) were prepared at a ramp rate of 5°C/min. They were exposed for longer time to the higher temperature, so their surface area and pore volume were different from those prepared under the 10°C/min ramp rate. The microporosity decreased versus the mesoporosity, which was due to the expansion of the pores by more etching of the framework. However, the side reactions are highly likely to take place and the primary elements (carbon, nitrogen and potassium) in the precursors will be then excluded from the ratio. The formation of phthalimide confirmed the side reactions that may have happened during the carbonisation of KHP with urea. In this case, it seems that when the carbonisation is accompanied by activation in one step, equations 1 and 2 are not enough to describe the changes that will happen.

4.2. CO_2 uptake

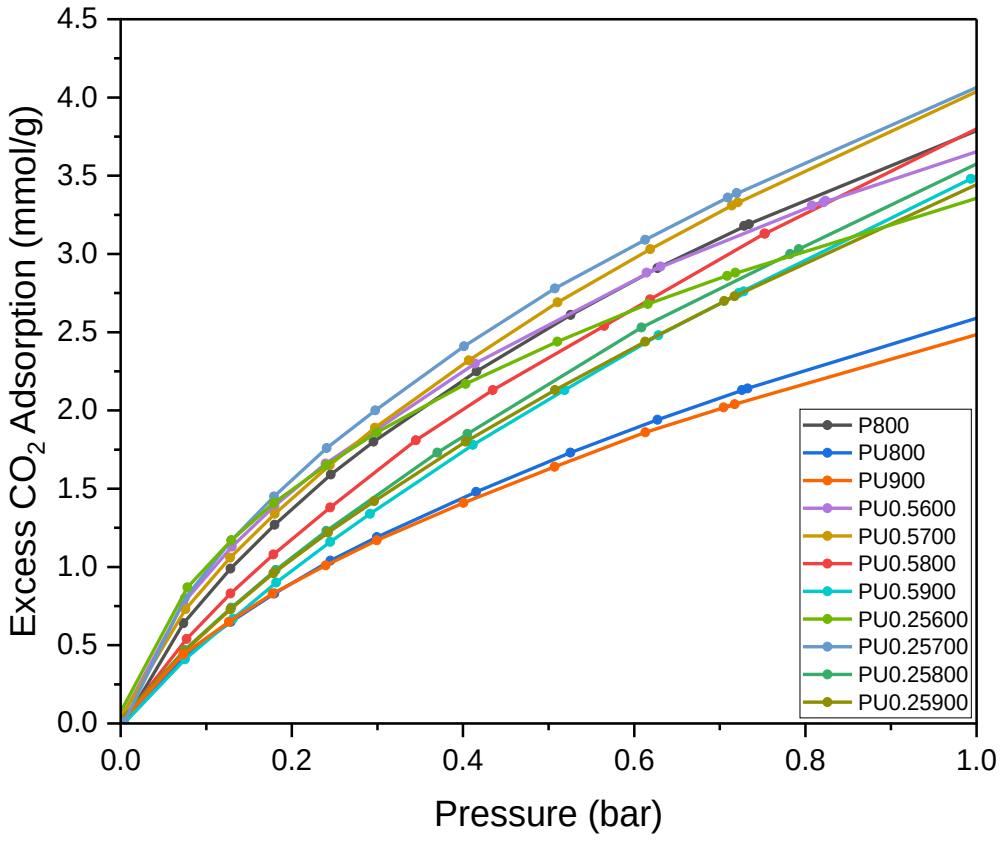
CO_2 uptake measurements were carried out over the pressure range of 0 to 30 bar at 25^{o}C. The results are presented in Figure 5-18 and Table 5-5. The highest CO_2 uptake at 1 bar is for samples PU0.5700 and PU0.25700 at 4.08 and 4.10 mmol/g, respectively. That can be explained by the effect of the pore sizes, which control the uptake at low pressures,[44] as the sample PU0.25700 has the highest number of pores less than 0.5 nm. This uptake capacity is comparable to that of other activated carbons that have to be made in several steps or need corrosive solutions to remove the inorganic residues from the last synthesis step.[1, 45-47]

Several research papers have observed that nitrogen doping contributes to CO_2 adsorption at low pressures, in addition to the impact of small pore sizes.[48-51] To investigate the relationships between the uptake at 1 bar and the BET surface area (SA), total pore volume (Vp), micropore surface area (μ SA), and micropore volume (μ V), Figure 5-19 was plotted. The effect of the BET surface area and the total pore volume on the uptake at 1 bar is hardly to define. However, the micropore volume and surface area could potentially have a positive impact on the uptake. But the poor linear correlations with R^2 values ranging from 0.333 to 0.287 suggested possible effects of N-doping on the uptake at 1 bar.

Compared to CO_2 uptake at 1 bar on the base sample 'P800', adding urea does not significantly improve the uptake at low pressure, as the smallest pore sizes are the key factor for the uptake capacity. While the uptake capacity at 1 bar on PU0.5800 is nearly as much as P800 at 3.9 mmol/g, it is lower for PU0.25800 and PU800 at 3.7 and 2.68 mmol/g, respectively. However, the larger pores that are produced by adding urea enhance the diffusion and the uptake capacity at high pressure, compared to P800. The uptake capacity at higher pressures, e.g. at 30 bar, increases with total pore volume and surface area as shown in Figure 5-20 and Figure 5-21. The uptake capacity (Figure 5-22) increases at 20 bar by ~60% after adding 0.25 and 0.5 weight ratios of urea and only by 6% after adding ratio 1 of urea. At 30 bar, compared to P800, the capacity increased by 68% in PU0.25800 and PU0.5800, while only by 13% in PU800. Consequently, as is expected from the porosity results, adding urea produces wider pore sizes, which leads to an increase in the uptake capacity at higher pressures.

A linear correlation has been observed between the total pore volume and the CO_2 uptake at 20 and 30 bar, with R^2 values ranging from 0.836 to 0.856. A

linear correlation with a root-mean-square error of determination (R2) ranging from 0.937 to 0.939 has been observed between the uptake of CO_2 at 20 and 30 bar and the surface area. These findings potentially indicate the clear effect of the pore volume and surface area on the uptake within the specific range of pressure compared to their effect at low pressure (1 bar as shown in Figure 5-19). The R^2 values being in the range of 0.836 to 0.856 and 0.937 to 0.939 suggest that the nitrogen may potentially affect the CO_2 adsorption capacity at pressures between 20 and 30 bar.



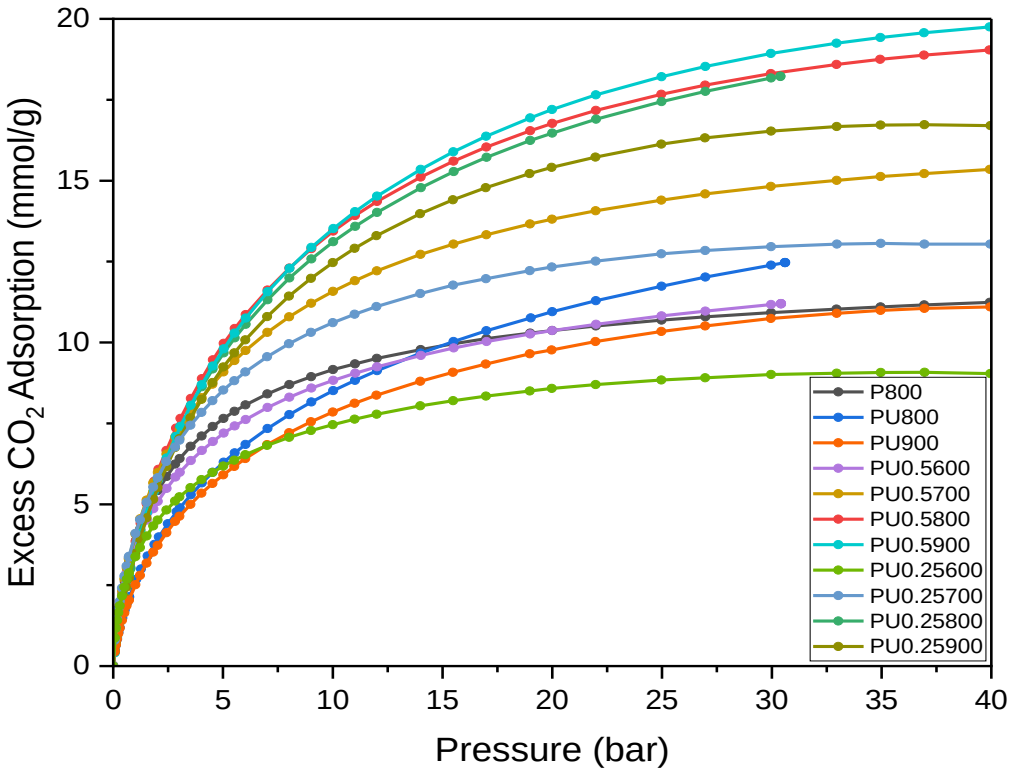


Figure 5-18 Excess Adsorption of CO_2 at RT, until 1 bar and 0–40 bar

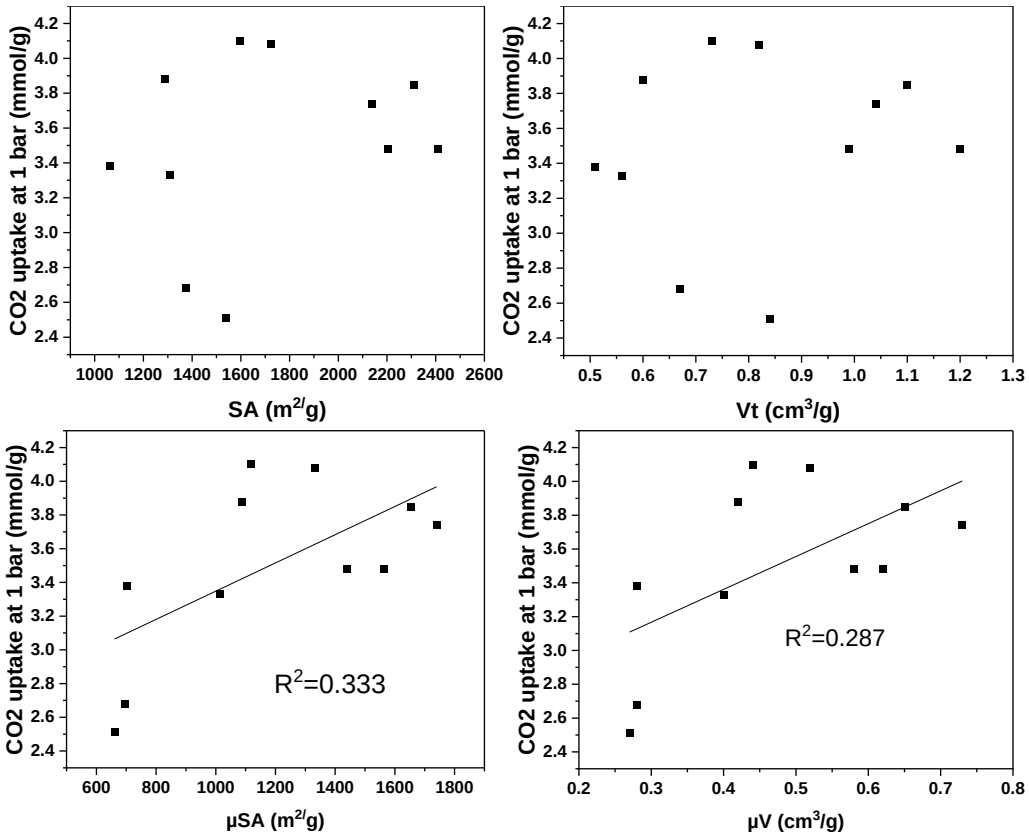


Figure 5-19 Correlation plot of CO_2 uptake data at 1 bar on PU samples with surface area, total pore volume, micropore surface area, and micropore volume.

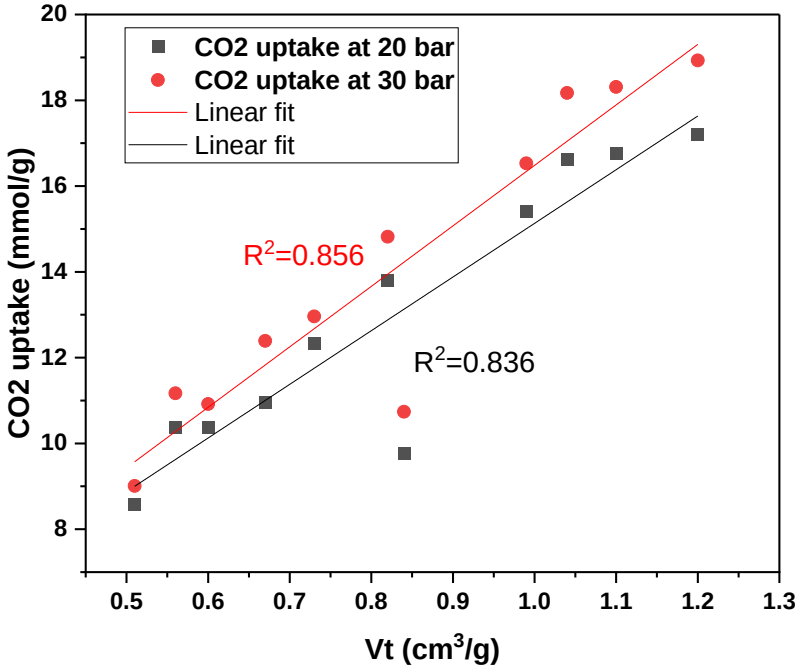


Figure 5-20 Correlation plot of CO_2 uptake data at 20, 30 bar on PU samples with total pore volume

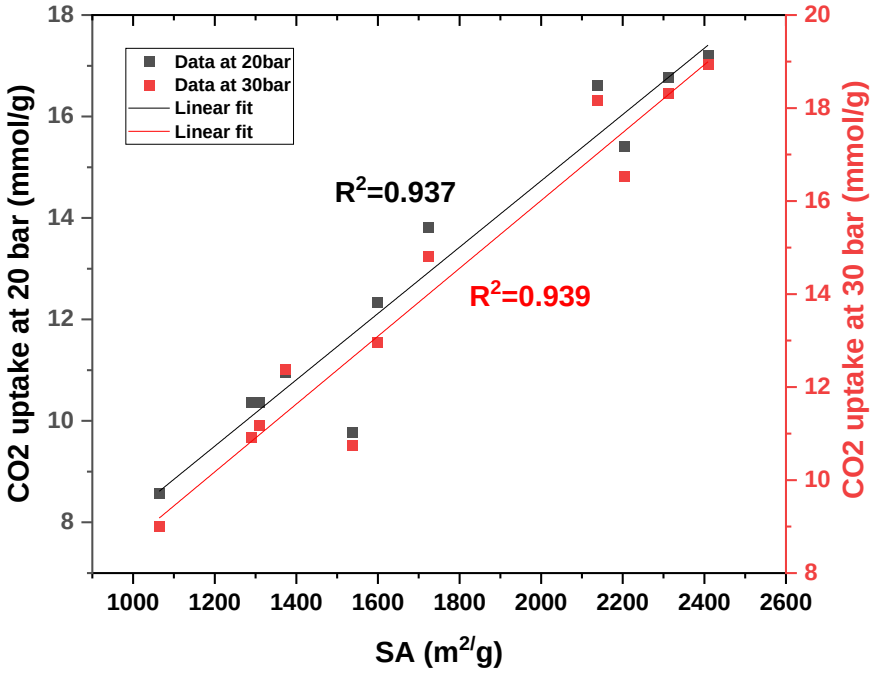


Figure 5-21 Correlation plot of CO_2 uptake data at 20 and 30 bar with surface area for on PU samples

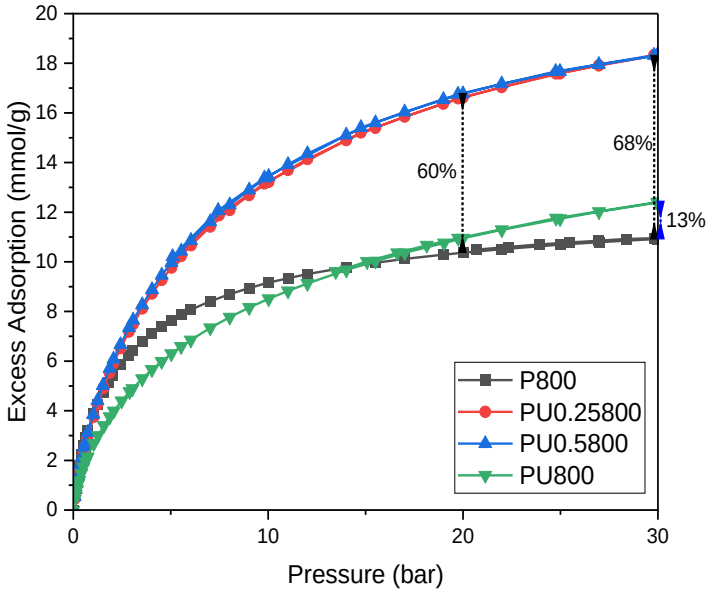


Figure 5-22 CO_2 uptake data on PU samples vs. the base sample

Thus samples PU0.25y, PU0.5y and P800 are suitable for post-combustion CO_2 capture as their uptake is high at low pressure, which meets the required conditions of post-combustion applications.[1] Table 5-6 summarises a comparison of CO_2 uptake of the present carbons with previous reports. For post-composition CO_2 capture, where CO_2 is captured typically from flue gases, the highest uptake at 1 bar and 25°C was for the samples PU0.25700 and PU0.5700. The uptake capacity of these two samples is comparable to benchmark samples that gave the highest uptakes, e.g. AS-2-600 and ACGR2700 (Table 5-6). If we consider the simplicity of the synthesis routes, the minimalism of the synthesis steps of our samples makes them applicable and cost-competitive. On the other hand, a comparison of the uptake capacities of our samples in general at high pressures shows that they show moderate capacities compared to other adsorbents. Samples such as the activated carbon from Camellia japonica 'ACCA2800' and zeolite-templated carbons CZ13XFAET and CZ13XFAETP exhibit higher capacities at 20 bar, and from their isotherm shapes, are expected to accommodate higher amounts of gas at higher pressures. But the porosity of the urea/KHP mix could be slightly improved in some ways, such as by carbonisation at a slower heating ramp rate[19] to target greater CO_2 uptake at moderate to high pressures. In summary, as the uptake is governed at low pressure by the presence of ultramicropores, i.e. by pores of size less than 0.5 nm,[52] the carbonisation of KHP with urea fortunately maintains ultramicropores in that range even with the shift in the pore evolution mechanism. This was reflected in the CO_2 uptake in these two sets of samples. Besides that, as is known, the amount of N-doping might not have a significant effect on the overall uptake capacity except for the uptake at low pressures.[44, 53]

In order to better investigate the effect of N% on the uptake, the relationship between N% and the uptake (mmol/g) at different pressures was plotted in Figure 5-23─25. Based on Figure 5-23, it appears that the uptake seen at a pressure of 0.13 bar was affected by a combination of factors, including the textural properties of the samples and their nitrogen content. Figure 5-23 shows that the uptake trend increased as the N% increased, which is consistent with findings by many groups, e.g., that found by Luo et al.[49] However, the uptake on the two samples prepared starting from a high weight ratio of urea (have the highest N%) at 0.13 bar was low even with the high N%. The samples in the grey area were synthesised using the low weight ratios of urea between 0-0.5, which show an increase in the uptake at 0.13 bar as the N% increases. Figure 5-24 shows the relationship between the uptake at 1 bar and N%, which seems unclear and could tend to be a decrease in the uptake as N% increases. The similar relationship as at 1 bar appeared in the uptake at 20 and 30 bar (see Figure 5-25) suggesting that an increase in nitrogen might lead directly to a decrease in the uptake at these pressure ranges. This behaviour was expected, especially at high pressures, due to the drop in surface areas and pore volumes in our samples accompanied by the increase in N-doping.

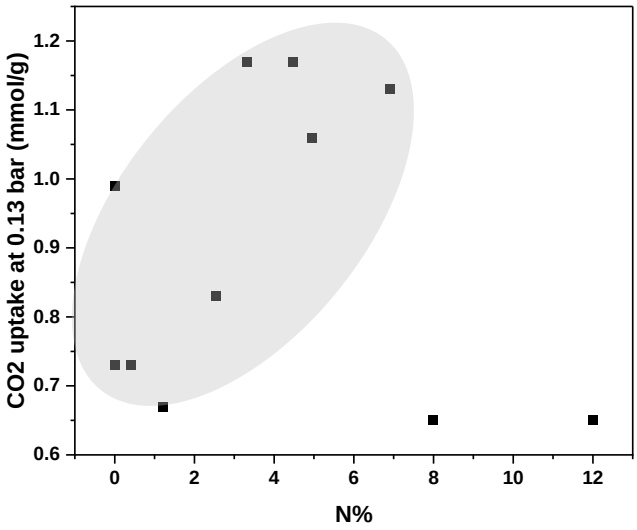


Figure 5-23 Correlation plot of CO_2 uptake data at 0.13 bar on PU samples with N%

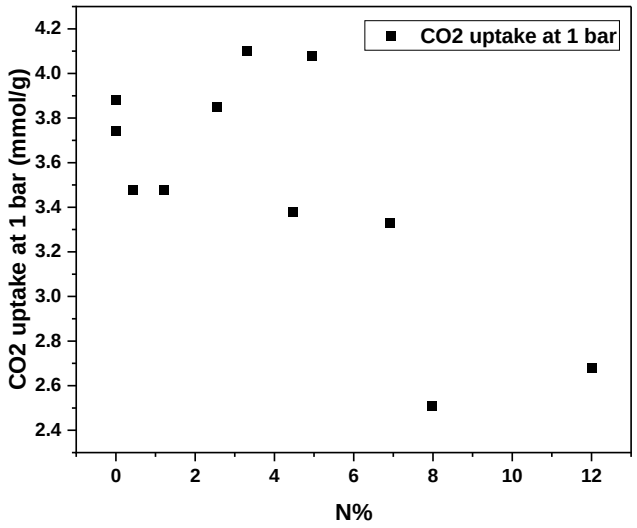


Figure 5-24 Correlation plot of CO_2 uptake data at 1 bar on PU samples with N%

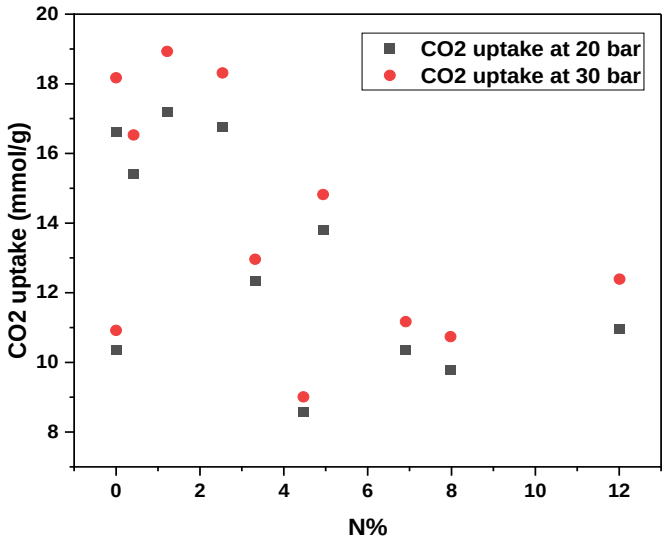


Figure 5-25 Correlation plot of CO_2 uptake data at 20 and 30 bar on PU samples with N%

Table 5-5 textural properties, density, and gravimetric and volumetric CO_2 Uptake at 25°C

Sample	Textural properties		Density[c]	CO_2 uptake (mmol/g) at 25°C			CO_2 uptake (cm^3_{STP}/cm^3) at 25°C		
	SA[a]	V_p[b]	g/cm³	1	20	30	1	20	30
	m²/g	cm³/g		bar	bar	bar	bar	bar	bar
P800	**1289 (1087)**	**0.60 (0.42)**	**0.79**	**3.9**	**10.4**	**10.9**	**68**	**182**	**192**
PU600	577 (500)	0.27 (0.19)		-	-	-			
PU700	1309 (993)	0.61 (0.39)		-	-	-			
PU800	**1374 (695)**	**0.67 (0.28)**	**0.75**	**2.7**	**11**	**12.4**	**45**	**182**	**205**
PU900	1538 (661)	0.84 (0.27)	0.66	2.5	9.8	10.7	37	144	158
PU0.5600	1309 (1014)	0.56 (0.40)	0.82	3.3	10.4	11.2	60	188	202
PU0.5700	1723 (1331)	0.82 (0.52)	0.67	4.1	13.8	14.8	61	206	222
PU0.5800	**2312 (1654)**	**1.1 (0.65)**	**0.57**	**3.9**	**16.8**	**18.3**	**48**	**211**	**230**
PU0.5900	2409 (1565)	1.2 (0.62)	0.54	3.5	17.2	18.9	41	205	225
PU0.25600	1064 (702)	0.51 (0.28)	0.85	3.4	8.6	9	64	162	170
PU0.25700	1598 (1116)	0.73 (0.44)	0.72	4.1	12.3	13	65	196	206
PU0.25800	**2138 (1740)**	**1.04 (0.73)**	**0.59**	**3.7**	**16.6**	**18.2**	**49**	**216**	**239**
PU0.25900	2205 (1441)	0.99 (0.58)	0.60	3.5	15.4	16.5	47	207	222

a) BET surface area and (micropore surface area from t-plot) in m^2/g, b) total pore volume and (micropore pore volume from t-plot) in cm^3/g, c) packing density of carbons calculated from the equation; $d_{carbon} = (1/\rho d + Vt)^{-1}$, where ρd is skeletal density and Vt is total pore volume from nitrogen sorption analysis.

Table 5-6 CO_2 uptake results compared to other carbons at room temperature (25°C)

Sample	CO_2 uptake (mmol/g)	CO_2 uptake (mmol/g)		Reference
	1 bar	20 bar	30 bar	
P800	3.9	10.4	10.9	This work
PU800	2.7	11	12.4	This work
PU900	2.5	10.4	11.7	This work
PU0.5600	3.3	10.4	11.4	This work
PU0.5700	4.1	13.8	14.8	This work
PU0.5800	3.9	16.8	18.3	This work
PU0.5900	3.5	17.2	18.9	This work
PU0.25600	3.4	9.2	10	This work
PU0.25700	4.1	12.9	13.9	This work
PU0.25800	3.7	16.6	18.2	This work
PU0.25900	3.5	16	17.5	This work
H250–800	3.7	-	-	[54]
AS-2-600	4.8	-	-	[55]
Pine sawdust	4.2	-	-	[56]
LHPC-700	4.8	-	-	[57]
ACDS-800-4	4.4	-	-	[58]
G850-5	4.5	-	14.3	[40]
SD6800	4.4	12.6	-	[9]
ACGR2700	4.9	12.7	-	[59]
ACCA2800	3.7	17.5	-	[59]
CZ13XFAET	2.5	18.6	-	[60]
CZ13XFAETP	2.6	22.0	-	[60]
PC poly(vinylidene chloride)-based carbon	4	10.6	-	[45]

5. Conclusion

The work in this chapter investigated a simple and straightforward method to synthesise N-doped carbon from cheap precursors, potassium hydrogen phthalate (KHP) and urea. The findings show that an N-doped carbon can be successfully prepared by in-situ doping using urea. Very high nitrogen doping was achieved, up to nearly 20%. We have found that adding urea to KHP has

boosted the surface area and shown an improvement in CO_2 uptake at high pressure compared to the carbonisation of the organic salt itself. Despite the high N-doping in our study, the increase in the carbonisation temperature leading to the high porosity has reduced the nitrogen amount. Despite being primarily exploratory, this study shows how the N/K and N/C ratios significantly affect the porosity of N-doped potassium-activated carbon.

Acknowledgment

I'm grateful to the Nanoscale and Microscale Research Centre (nmRC) at the University of Nottingham (especially Sabrin Samad) who imaged some of the samples for this project.

6. References

1. S. Wang, P. Bai, Y. Wei, W. Liu, X. Ren, J. Bai, Z. Lu, W. Yan and J. Yu, *ACS Applied Materials & Interfaces*, 2019, **11**, 38955-38963.
2. R.-S. Liu, X.-D. Shi, C.-T. Wang, Y.-Z. Gao, S. Xu, G.-P. Hao, S. Chen and A.-H. Lu, *ChemSusChem*, 2021, **14**, 1428-1471.
3. L. S. Blankenship and R. Mokaya, *Materials Advances*, 2022, **3**, 1905-1930.
4. Y. Zhai, B. Xu, Y. Zhu, R. Qing, C. Peng, T. Wang, C. Li and G. Zeng, *Materials Science and Engineering: C*, 2016, **61**, 449-456.
5. A. Elmouwahidi, E. Bailón-García, L. A. Romero-Cano, A. I. Zárate-Guzmán, A. F. Pérez-Cadenas and F. Carrasco-Marín, *Materials (Basel)*, 2019, **12**, 2458.
6. S. Zhang, X. Shi, R. Wróbel, X. Chen and E. Mijowska, *Electrochimica Acta*, 2019, **294**, 183-191.
7. Z. Yang, Y. Xia, X. Sun and R. Mokaya, *The Journal of Physical Chemistry B*, 2006, **110**, 18424-18431.

8. N. Balahmar and R. Mokaya, *Journal of Materials Chemistry A*, 2019, **7**, 17466-17479.
9. A. M. Aljumialy and R. Mokaya, *Materials Advances*, 2020, **1**, 3267-3280.
10. J. Shi, H. Cui, J. Xu, N. Yan, Y. Liu and S. Zhang, *Journal of CO2 Utilization*, 2020, **39**, 101164.
11. J. Wang and S. Kaskel, *Journal of Materials Chemistry*, 2012, **22**, 23710-23725.
12. M. Sevilla, G. A. Ferrero, N. Diez and A. B. Fuertes, *Carbon*, 2018, **131**, 193-200.
13. N. Tsubouchi, M. Nishio and Y. Mochizuki, *Applied Surface Science*, 2016, **371**, 301-306.
14. J. E. Eichler, J. N. Burrow, Y. Wang, D. C. Calabro and C. B. Mullins, *Carbon*, 2022, **186**, 711-723.
15. Q. Liu, Y. Duan, Q. Zhao, F. Pan, B. Zhang and J. Zhang, *Langmuir*, 2014, **30**, 8238-8245.
16. D.-W. Lee, M.-H. Jin, D. Oh, S.-W. Lee and J.-S. Park, *ACS Sustainable Chemistry & Engineering*, 2017, **5**, 9935-9944.
17. A. Altwala and R. Mokaya, *Energy & Environmental Science*, 2020, **13**, 2967-2978.
18. J. Gao, L. Li, Z. Zeng, X. Ma, R. Chen, C. Wang and K. Zhou, *Journal of Materials Science*, 2019, **54**, 6186-6198.
19. G. Nazir, A. Rehman and S.-J. Park, *Carbon*, 2022, **192**, 14-29.
20. C. Wang, H. Fan, X. Ren, J. Ma, J. Fang and W. Wang, *ChemSusChem*, 2018, **11**, 700-708.
21. C. Schneidermann, N. Jäckel, S. Oswald, L. Giebeler, V. Presser and L. Borchardt, *ChemSusChem*, 2017, **10**, 2416-2424.
22. K. László, E. Tombácz and K. Josepovits, *Carbon*, 2001, **39**, 1217-1228.
23. Q. Wang, Q. Liu, Z. Wang, H. Liu and J. Bai, *Oil Shale*, 2017, **34**, 129.
24. K. Zou, Y. Deng, J. Chen, Y. Qian, Y. Yang, Y. Li and G. Chen, *Journal of Power Sources*, 2018, **378**, 579-588.
25. Y. Liu and Z. Gao, *ChemElectroChem*, 2017, **4**, 1059-1065.
26. Y. Cui, J. Zhang, G. Zhang, J. Huang, P. Liu, M. Antonietti and X. Wang, *Journal of Materials Chemistry*, 2011, **21**, 13032-13039.

27. L. Ma, H. Fan, J. Wang, Y. Zhao, H. Tian and G. Dong, *Applied Catalysis B: Environmental*, 2016, **190**, 93-102.
28. W. E. Ford, A. Jung, A. Hirsch, R. Graupner, F. Scholz, A. Yasuda and J. M. Wessels, *Advanced Materials*, 2006, **18**, 1193-1197.
29. M. Ayiania, M. Smith, A. J. R. Hensley, L. Scudiero, J.-S. McEwen and M. Garcia-Perez, *Carbon*, 2020, **162**, 528-544.
30. A. Bello, N. Manyala, F. Barzegar, A. A. Khaleed, D. Y. Momodu and J. K. Dangbegnon, *RSC Advances*, 2016, **6**, 1800-1809.
31. L. Caracciolo, L. Madec and H. Martinez, *ACS Applied Energy Materials*, 2021, **4**, 11693-11699.
32. Q. Zhong, Y. Yang, L. Chen, Q. Li, B. Xu and T. Jiang, *Metals*, 2018, **8**, 80.
33. V. A. Setyowati, L. Noerochim, D. Susanti, Y. Pradesar, H.-C. Huang, S.-T. Chang, K.-C. Wang and C.-H. Wang, *Ionics*, 2020, **26**, 813-822.
34. Z. Mou, X. Chen, Y. Du, X. Wang, P. Yang and S. Wang, *Applied Surface Science*, 2011, **258**, 1704-1710.
35. B. Adeniran, E. Masika and R. Mokaya, *Journal of Materials Chemistry A*, 2014, **2**, 14696-14710.
36. S. Wakeland, R. Martinez, J. K. Grey and C. C. Luhrs, *Carbon*, 2010, **48**, 3463-3470.
37. N. A. Rashidi and S. Yusup, *Journal of Energy Storage*, 2020, **32**, 101757.
38. W.-J. Ong, L.-L. Tan, Y. H. Ng, S.-T. Yong and S.-P. Chai, *Chemical Reviews*, 2016, **116**, 7159-7329.
39. X. Bai, L. Wang, R. Zong and Y. Zhu, *The Journal of Physical Chemistry C*, 2013, **117**, 9952-9961.
40. M. Sevilla, A. S. M. Al-Jumialy, A. B. Fuertes and R. Mokaya, *ACS Applied Materials & Interfaces*, 2018, **10**, 1623-1633.
41. M. Colaço, J. Dubois and J. Wouters, *CrystEngComm*, 2015, **17**, 2523-2528.
42. P. M. Schaber, J. Colson, S. Higgins, D. Thielen, B. Anspach and J. Brauer, *Thermochimica Acta*, 2004, **424**, 131-142.
43. A. Yadav, R. Kumar and B. Sahoo, *Physical Chemistry Chemical Physics*, 2022, **24**, 1059-1071.
44. B. Adeniran and R. Mokaya, *Chemistry of Materials*, 2016, **28**, 994-1001.

45. J. Cai, J. Qi, C. Yang and X. Zhao, *ACS Applied Materials & Interfaces*, 2014, **6**, 3703-3711.
46. N. A. Rashidi and S. Yusup, *Journal of CO2 Utilization*, 2016, **13**, 1-16.
47. A. A. Abd, M. R. Othman and J. Kim, *Environmental Science and Pollution Research*, 2021, **28**, 43329-43364.
48. M. Sevilla, P. Valle-Vigón and A. B. Fuertes, *Advanced Functional Materials*, 2011, **21**, 2781-2787.
49. J. Luo, B. Liu, R. Shi, Y. Guo, Q. Feng, Z. Liu, L. Li and K. Norinaga, *Microporous and Mesoporous Materials*, 2021, **327**, 111404.
50. A. S. Jalilov, G. Ruan, C.-C. Hwang, D. E. Schipper, J. J. Tour, Y. Li, H. Fei, E. L. G. Samuel and J. M. Tour, *ACS Applied Materials & Interfaces*, 2015, **7**, 1376-1382.
51. F. Bai, Y. Xia, B. Chen, H. Su and Y. Zhu, *Carbon*, 2014, **79**, 213-226.
52. V. Presser, J. McDonough, S.-H. Yeon and Y. Gogotsi, *Energy & Environmental Science*, 2011, **4**, 3059-3066.
53. M. Sevilla, J. B. Parra and A. B. Fuertes, *ACS Applied Materials & Interfaces*, 2013, **5**, 6360-6368.
54. G. K. Parshetti, S. Chowdhury and R. Balasubramanian, *Fuel*, 2015, **148**, 246-254.
55. M. Sevilla and A. B. Fuertes, *Energy & Environmental Science*, 2011, **4**, 1765-1771.
56. C. Quan, R. Su and N. Gao, *International Journal of Energy Research*, 2020, **44**, 4335-4351.
57. M. Demir, T.-D. Tessema, A. A. Farghaly, E. Nyankson, S. K. Saraswat, B. Aksoy, T. Islamoglu, M. M. Collinson, H. M. El-Kaderi and R. B. Gupta, *International Journal of Energy Research*, 2018, **42**, 2686-2700.
58. J. Li, B. Michalkiewicz, J. Min, C. Ma, X. Chen, J. Gong, E. Mijowska and T. Tang, *Chemical Engineering Journal*, 2019, **360**, 250-259.
59. H. M. Coromina, D. A. Walsh and R. Mokaya, *Journal of Materials Chemistry A*, 2016, **4**, 280-289.
60. N. Balahmar, A. M. Lowbridge and R. Mokaya, *Journal of Materials Chemistry A*, 2016, **4**, 14254-14266.

Chapter 6 Direct synthesis approach to porous BCN for CO_2 uptake

Abstract

Borocarbonitride (BCN)-based materials are gaining popularity recently for a variety of applications due to their exceptional properties. There is a need for more effort to develop the synthesis of porous BCN materials. On the other hand, the direct synthesis of N-doped carbons using potassium-based organic salts offers two things: first, a simple and direct way of synthesising N-doped carbons. Second, it provides a straightforward method of studying the potassium activation process of the N-containing carbon sources. There is a lack of information about the potassium activation of a system containing a trio of components (boron, nitrogen, and carbon). Here, examination of the synthesis of BCN using potassium-based organic salt in the presence of N- and B-precursors could help synthesise porous BCN and improve understanding of the nature of potassium activation in the presence of such three elements. In this study, an examination of the synthesis of BCN starting from potassium hydrogen phthalate/urea/boric acid mixtures was done, and the resulting carbons were explored for room temperature CO_2 uptake. The findings revealed a decrease in the surface areas due to the addition of boric acid to the mixture and, as a result, the CO_2 uptake capacities. A further study with more focus on optimization of the current BCN synthesis method is therefore suggested.

1. Introduction

Boron, carbon and nitrogen may be combined in a single system called borocarbonitrides (BxCyNz or BCN) [1], which has shown a variety of exciting and versatile properties and uses, including in the oxygen reduction reaction,[2] supercapacitors,[3-5] in CO_2 adsorption,[6] in dye adsorption,[7] in the removal of heavy metal ions[8] and in photocatalysis.[9] On one hand, it is claimed that N-doped carbons can exhibit high CO_2 uptake due to the presence of N in the carbon framework.[10] On the other hand, the presence of N in activateable carbonaceous matter can increase the reactivity of the activation process, resulting in the enlargement of the carbon framework and the addition of comparatively larger pores.[11] This, in turn, leads to reduction of the packing density. Boron co-doping may increase the packing density of N-doped carbons due to the smaller size of boron in comparison to nitrogen and carbon. Several attempts have been made to synthesise such materials containing the combination of boron, carbon, and nitrogen. For example, Li et al.[12] synthesised porous BCN by dissolving the precursors, stirring them for several hours, followed by polymerisation and then carbonisation steps. The generated sample, BNHC-2, was microporous with 1 nm wide pores. At 30°C and atmospheric pressure, BNHC-2 could store up to 94.07 mg/g (2.14 mmol/g) of CO_2. Besides this, it showed good re-use stability with uptake of more than 80 mg/g (1.82 mmol/g) after eight cycles.

However, synthesis of a low-cost BCN and that has controlled porosity for various applications is still restricted by the difficulty of available synthesis procedures. This is in the context of the fact that the synthesis of highly porous carbons can be achieved via simple and straightforward approaches that include, for example, the direct carbonisation of certain organic salts. In this regard, some potassium- or sodium-containing organic salts that are carbon rich such as potassium hydrogen phthalate or potassium pthalimide, can be converted directly to porous carbons via simple carbonisation. Moreover, the direct carbonisation of these organic salts allows for significant control of the porosity of the resulting carbons.[11, 13]

Based on the above mentioned prior knowledge, this chapter examined the synthesis of BCN by the direct carbonisation of potassium hydrogen phthalate but in the presence of urea (which is N-rich) and boric acid (which provides B). The resulting carbons were applied towards CO_2 uptake. The status of the boron in the samples may not be completely confirmed in this study, but there is evidence of a clear effect on the porosity of N-doped carbon that was made by adding boric acid to the carbonisation of a mixture of potassium hydrogen phthalate and urea.

2. Experimental

2.1. Synthesis

Nitrogen and boron co-doped carbon samples were synthesised by carbonisation of mixtures composed of potassium hydrogen phthalate (P), urea (U) and boric

acid (B). The mixtures were placed in an alumina boat and heated at 800°C for one hour in a tube furnace under N_2 flow (heating rate = 10°C/min). The carbonised samples were then washed with hot (~90°C) distilled water until a neutral pH was attained by the filtrate. The samples were named as PUB0800-abc, where a, b and c was the mass of (P), (U) and (B), respectively, in the carbonisation mixture. The Table 6-1 below shows the amounts (mass) of the precursors for each sample and Figure 6-1 shows the obtained samples.

Table 6-1 starting materials quantities of the samples

Sample name	KHP (g)	Urea (g)	BA (g)	wt. ratio KHP:urea:BA	Molar ratio KHP:urea:BA
P800-4	4	0	0	-	-
PU800-42	4	2	0	1:0.5:0	1:2:0
PU800-41	4	1	0	1:0.25:0	1:1:0
PU800-4:0.5	4	0.5	0	1:0.125:0	2:1:0
PUB800-422	4	2	2	1:0.5:0.5	1:2:2
PUB800-411	4	1	1	1:0.25:0.25	1:1:1
PUB800-424	4	2	4	1:0.5:1	1:2:3
PUB800-421	4	2	1	1:0.5:0.25	1:2:1
PUB800-4:0.5:0.25	4	0.5	0.25	1:0.125:0.0625	5:2:1

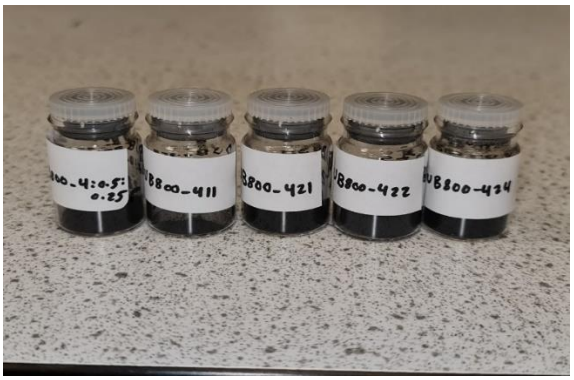


Figure 6-1 A photo depicting the black colour of the samples.

2.2.Characterisation

Powder XRD patterns of the samples were performed using a PANalytical X'Pert PRO diffractometer with a copper Kα and a monochromator (λ = 1.5405Å) at 40 kV and 40 mA with a step size of 0.02 and a 50 s time step. The scan was performed at room temperature. The porosity and determination of textural properties were performed via nitrogen physisorption using a Micromeritics 3Flex sorptometer. Prior to analysis (at –196°C), the carbon samples were degassed under vacuum at 230°C for 32 or 16 h. The surface area was calculated using the BET method applied to adsorption data within the relative pressure (*P/Po*) range of 0.02–0.35. The total pore volume was determined from the nitrogen uptake at close to saturation pressure (*P/Po* = 0.99). The micropore surface area and micropore volume were determined via t-plot analysis. Micromeritics' SAIEUS software was used to obtain PSDs of the samples using the 2D-NLDFT method for heterogeneous surfaces. In order to create the most accurate PSD for carbons, the software's fitting parameter, λ, which affects the roughness of the PSD, was adjusted between 2.75 and 3.00. Scanning electron microscopy (SEM) images were recorded on a JEOL7000 microscope at 15 kV accelerating voltage. Samples were mounted using a conductive carbon double-sided sticky tape and a thin (ca. 8 nm) coating of Iridium sputter was deposited onto the samples to avoid any effects of charging. CHN elemental analysis was performed using an Exeter Analytical CE-440 Elemental Analyser. IR spectroscopy was performed using a Bruker ALPHA FTIR Spectrometer.

3.2 CO_2 uptake measurements

CO_2 uptake capacity of the carbons was measured with a Hiden Isochema Intelligent Gravimetric Analyser (IGA-003) at room temperature and up to 20 bar of pressure. Prior to conducting the CO_2 uptake experiments, the carbons were outgassed for 3 h at 240 °C (at heating ramp rate 10°C/min) under vacuum. The measurements determined the excess CO_2 uptake directly.

3. Results

3.1. Nature, textural properties and chemical composition of carbons

The XRD patterns of the samples shown in Figure 6-2 indicated the formation of carbons that were mainly amorphous. However, there was a small sharp peak at 2θ of 26° attributed to graphitic phases, either graphite or boron nitride but not carbon nitride as shown in Figure 6-3. This narrow graphitic peak was formed in the sample with the lowest added amounts of boric acid and urea. The intensity of the peak decreased as the amount of boric acid and urea increased. That means the low amounts of boric acid and urea generate highly oriented assemblies of graphitic layers. The XRD pattern of the PUB800-422 sample also exhibited a graphitic peak, but which was broader and centred at 26° (see Figure 6-2). This development of the ordering as also evidenced in the XRD pattern of sample PUB800-4:0.5-0.25's acts to enhance the packing density of this sample, as shown in Table 6-2.

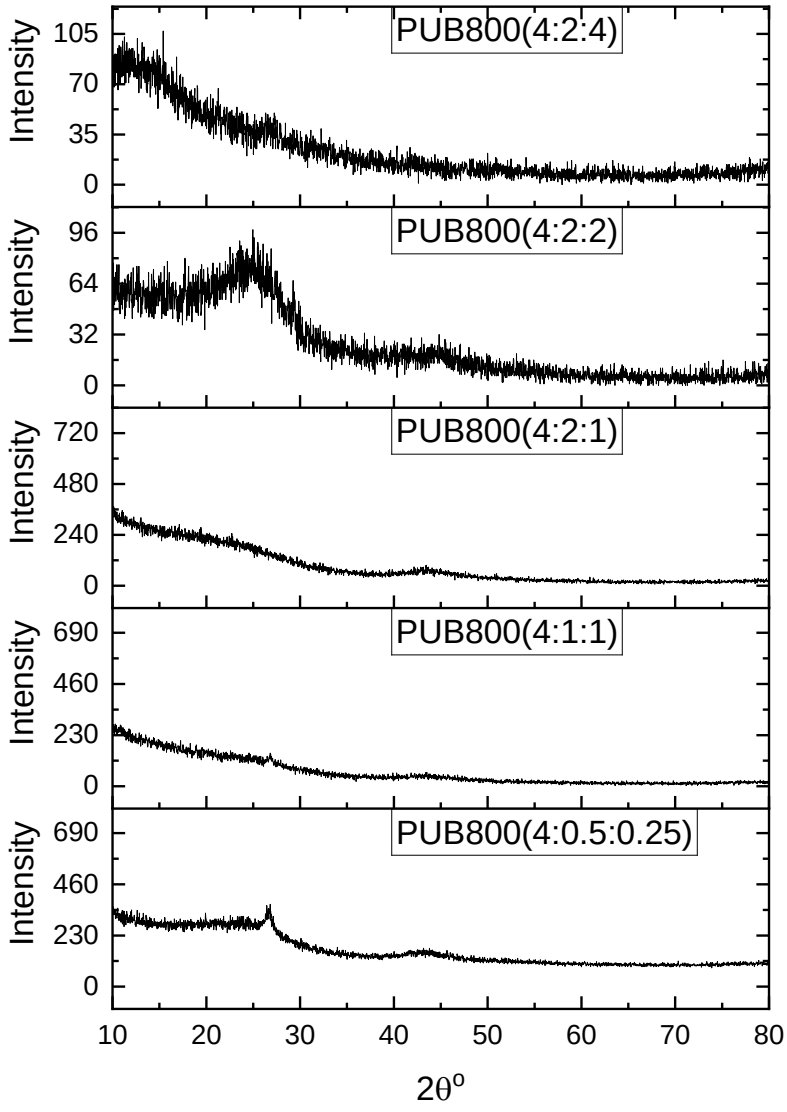


Figure 6-2 XRD patterns of the carbons derived from carbonisation of PUB mixtures

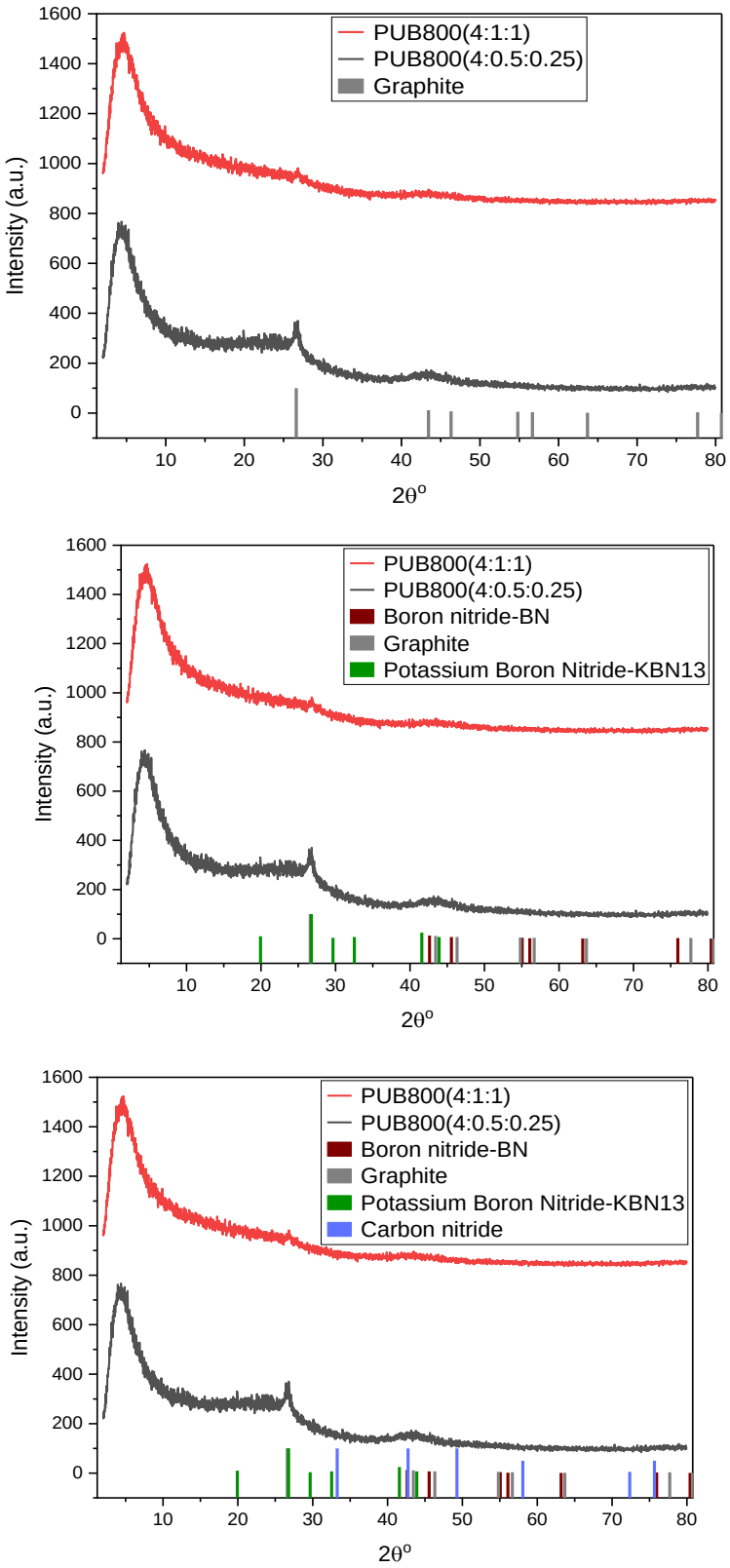


Figure 6-3 XRD patterns of the carbons derived from carbonisation of PUB mixtures along with the reference material stick patterns

Figure 6-4 depicts the nitrogen sorption isotherms of carbons derived from the carbonisation of P-U-B mixtures in comparison to those of P-U mixtures. The amount of nitrogen adsorbed can be related to the level of porosity in the carbons with high amounts signifying greater porosity. The isotherms are mainly type I, which is typical of microporous materials. This is consistent with previous reports on KHP-derived carbons.[13] The porosity of the KHP-derived carbons increases with the amount of added urea. This suggest that the urea acts as an extra porogen, which may be related to the presence of greater amounts of N in the carbonisation mixture. On the other hand, the isotherms show clearly that adding boric acid to the potassium hydrogen phthalate and urea mixture led to a decrease in porosity. As the amount of boric acid increased, the surface area reduced. This is in contrast with the observed increase in the porosity as the amount of urea increases. The isotherm of the sample prepared with the highest amount of boric acid, PUB800-424, exhibited a type IV isotherm with substantial mesoporosity. The pore size distribution curves, Figure 6-4 (b), show that the addition of boric acid in increasing amounts leads to a gradual disappearance of the larger pores that are centred at ca. 9 Å, and which were produced by adding urea to KHP. That was an indication that adding boric acid hindered the activation mechanism of potassium. The pores centred at 9 Å were formed due to the etching reaction between the potassium and the nitrogen, as explained previously in chapter 5. Increasing the amounts of urea and boric acid to a high level generated larger mesopores.

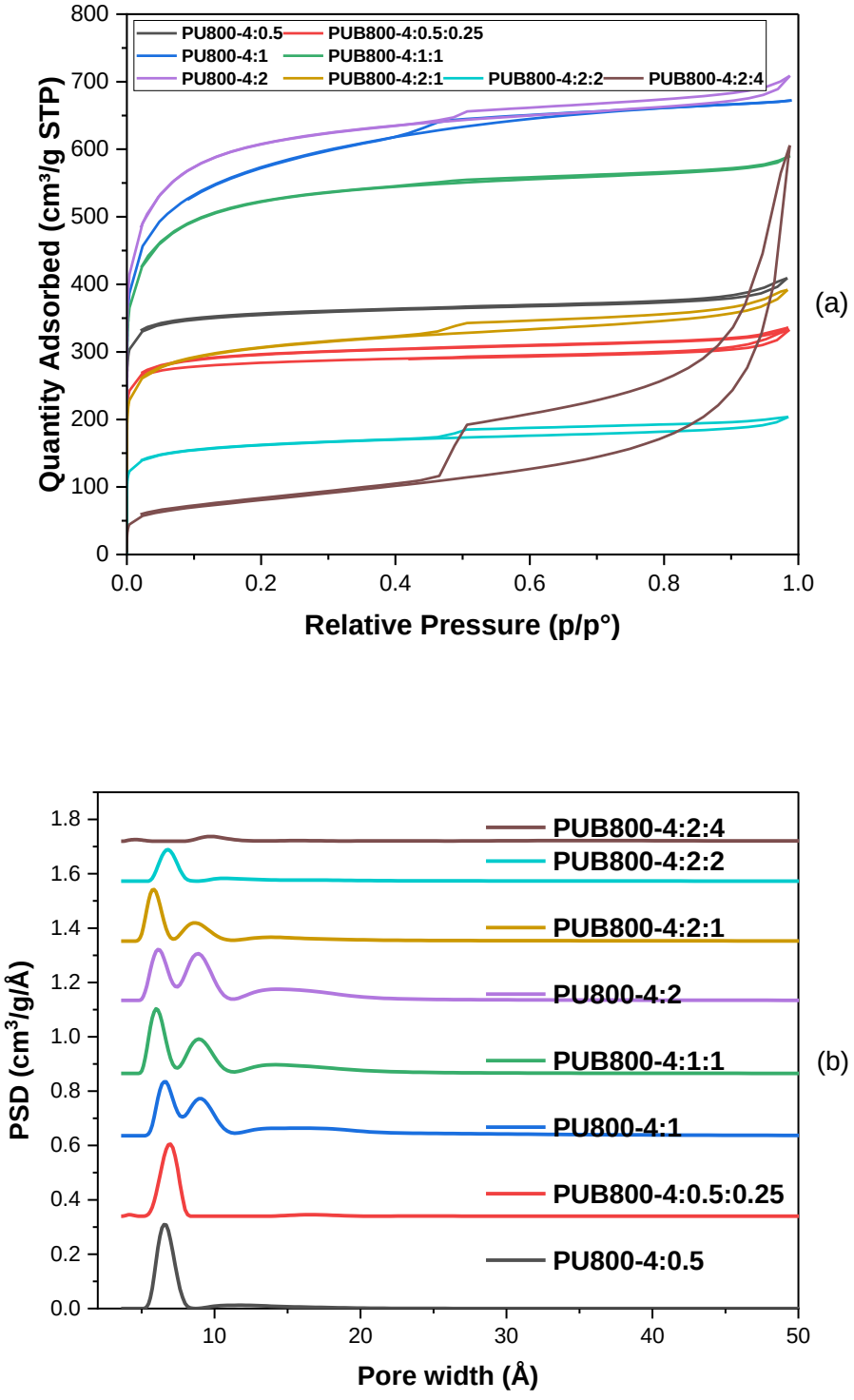


Figure 6-4 N_2 sorption isotherms (a) and pore size distribution curves (b) of PU and PUB samples

As shown in Table 6-2, the surface area and pore volume increase with addition of urea to KHP and appears to reach a maximum of ca. 2300 m^2/g and 1.1 cm^3/g at KHP/urea ratio of 2 for sample PU800-42. Thus the addition of urea improves the porosity (surface area and pore volume) by up to 80%. The level of microporosity reduces but still remains within a high level being 70% of surface area and 60% of pore volume for sample PU800-42. Taking sample PU800-42 as the baseline, the surface area and pore volume decreased with the addition of boric acid resulting in a reduction in surface area and pore volume from 2312 to 287 m^2/g and 1.1 to 0.32 cm^3/g, respectively. Samples PUB800-4:1:1 and PUB800-4:0.5:0.25 also show lower surface area and pore volume that is consistent with the amount of boric acid and urea in their carbonisation mixtures.

Table 6-2 textural properties, elemental analysis (CHN) and densities of the samples

	Textural properties			**Elemental analysis**			
Sample	**Surface area[a]**	**mesoSA[b]**	**Pore volume[c]**	**C**	**H**	**N**	**ρd_{exp}**
	m^2/g	**m^2/g**	**cm^3/g**	**%**	**%**	**%**	**g/cm^3**
P800	1289 (1087)	202 (16)	0.60 (0.42)	87.98	0.20	0	0.43
PU800	1374 (695)	679 (49)	0.67 (0.28)	74.45	0.61	12.01	0.37
PU800-42	2312 (1654)	658 (28)	1.1 (0.65)	84.34	0.46	2.54	0.38
PU800-41	2138 (1740)	398 (19)	1.04 (0.73)	91.34	0	0	0.45
PU800-4:0.5	1417 (1243)	174 (12)	0.63 (0.48)	89.48	0.07	0.58	0.42
PUB800-4:2:4	287 (43)	244 (85)	0.94 (0.02)	48.71	0	20.25	0.10
PUB800-4:2:2	621 (470)	151 (24)	0.32 (0.18)	70.25	0.38	8.03	0.29
PUB800-4:2:1	1171 (873)	298 (25)	0.61 (0.34)	74.87	0.21	8.8	0.42
PUB800-4:1:1	1984 (1430)	554 (28)	0.91 (0.56)	79.98	0.39	5.12	0.24
PUB800-4:0.5:0.25	1121 (1004)	117 (10)	0.52 (0.39)	89.05	0.24	1.63	0.46

[a]The values in parenthesis are micropore surface area. [b] mesopore surface area and the values in parenthesis are the percentages (%) of mesopore surface area as a proportion of surface area. [c] The values in parenthesis are micropore volume.

The high surface area and pore volume of sample PU800-42 may be attributed to an activation mechanism that depends on the etching K–N reaction, where K-species etch the nitrogen and produce KCNO and KCN.[11, 14] The surface area decreased drastically on addition of boric acid, which inhibited this reaction. On the other hand, the porosity of the PU800-4:1 sample was well developed and may be attributed to reactions of conventional K-activation of carbon; the porosity development was less hindered in a manner similar to that of sample PU800-42. It is interesting to note that in the appropriate settings, boric acid can itself act as an activating agent.[15] However, the role of boric acid in the present study and its impact on reducing porosity needs further exploration and consideration. It is also of interest to clarify the specific effect and role of the N:K ratio in porosity development of the present tri-component (P, U and B) derived samples.

SEM images (Figure 6-5) showed heterogeneity in the surface morphology of the PUB samples. The presence of boric acid in the carbonisation mixture results in changes in the morphology, with the formation of thin sheets, which may comprise of graphene or boron nitride.

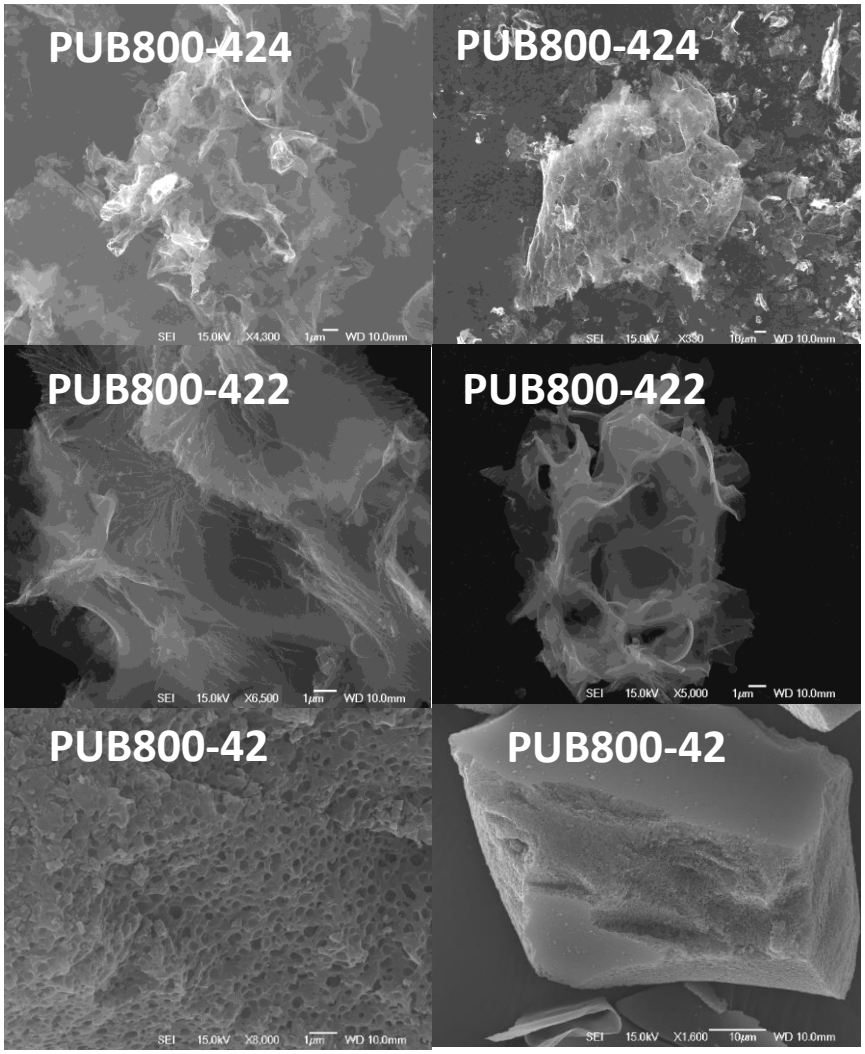


Figure 6-5 SEM images of PUB800-424, PUB800-422 and PUB800-42

The chemical composition from the CHN analysis showed an increase in N content after adding BA in PUB-samples compared to PU-samples without BA. The N content in the two samples, PUB800-421 and -422, was similar. However, the sample with a higher BA ratio, PUB800-422, showed lower carbon content, which suggested that the higher BA ratio may have led to etching more C to create more defects but did not affect the nitrogen content. Increasing amounts of BA also acted to increase the O/C ratio (see Figure 6-6 and Table 6-3). The highest N content is for sample PUB800-424, which was made with the highest ratio of BA. This indicated that increasing the amount of BA etched out more C. This sample has very high N content of ca. 20%, with a low C content of nca. 49%. Besides, the level of mesoporosity in this sample is high (85% of surface area), as seen in Figure 6-4 and Table 6-2.

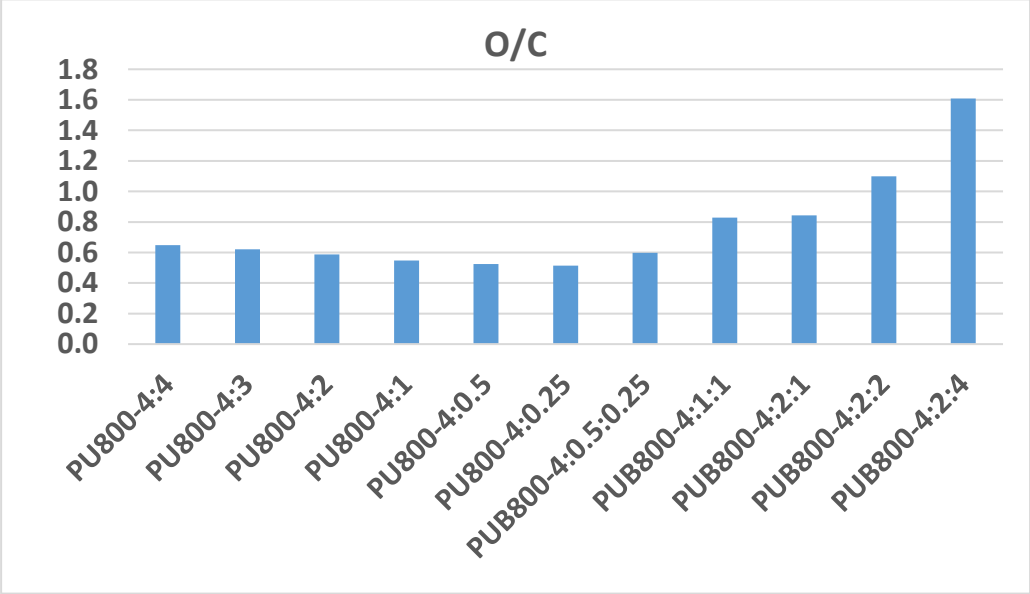


Figure 6-6 O/C atomic ratio of pre-carbonised BA/Urea/KHP mixture

Table 6-3 Elemental composition of pre-carbonised BA/Urea/KHP mixtures

Sample	C %	H%	N%	O%	K%	B%	N/H	N/K	N/C	N/O	O/C
PU-4:4	33.494	4.554	23.310	28.989	9.549		0.366	6.801	0.597	0.919	0.649
PU-4:3	35.425	4.253	19.980	29.325	10.913		0.336	5.100	0.483	0.779	0.621
PU-4:2	37.999	3.852	15.540	29.773	12.731		0.288	3.400	0.351	0.597	0.588
PU-4:1	41.603	3.291	9.324	30.399	15.278		0.202	1.700	0.192	0.351	0.548
PU-4:0.5	44.005	2.916	5.180	30.817	16.975		0.127	0.850	0.101	0.192	0.525
PU-4:0.25	45.418	2.696	2.742	31.062	17.974		0.073	0.425	0.052	0.101	0.513
PUB-4:0.5:0.25	41.689	3.018	4.907	33.281	16.082	0.936	0.116	0.850	0.101	0.169	0.599
PUB-4:1:1	34.669	3.551	7.770	38.271	12.731	2.965	0.156	1.700	0.192	0.232	0.828
PUB-4:2:1	32.570	3.995	13.320	36.610	10.913	2.542	0.238	3.400	0.351	0.416	0.843
PUB-4:2:2	28.499	4.102	11.655	41.737	9.549	4.448	0.203	3.400	0.351	0.319	1.098
PUB-4:2:4	22.799	4.252	9.324	48.916	7.639	7.116	0.157	3.400	0.351	0.218	1.609

The elemental weight percentages were calculated based on the experimental weights, with approximate errors of ±0.09% in each calculated element and ±0.005 in each atomic ratio.

Another elemental analysis of this sample was done using EDS (see Figure 6-7). There was the presence of a small amount of boron (1.2%) in the sample, perhaps as a residue from the boric acid, [16] or accompanied by small amounts of the boron nitride.[17] Consequently, the C/N content can be simply modified by controlling the starting ratios of KHP, urea and boric acid. The FTIR spectra of the samples (Figure 6-8), showed peaks at 820 and 1310 cm^{-1}. The peak located at 820 cm^{-1} could belong to B–N–B in-plane stretching vibrations[18, 19] or for aromatic C–N.[20, 21]. The peak at 1310 cm^{-1} could be attributed to the B–N group, which appeared slightly different in the PUB-samples than in the PU-samples.[22]

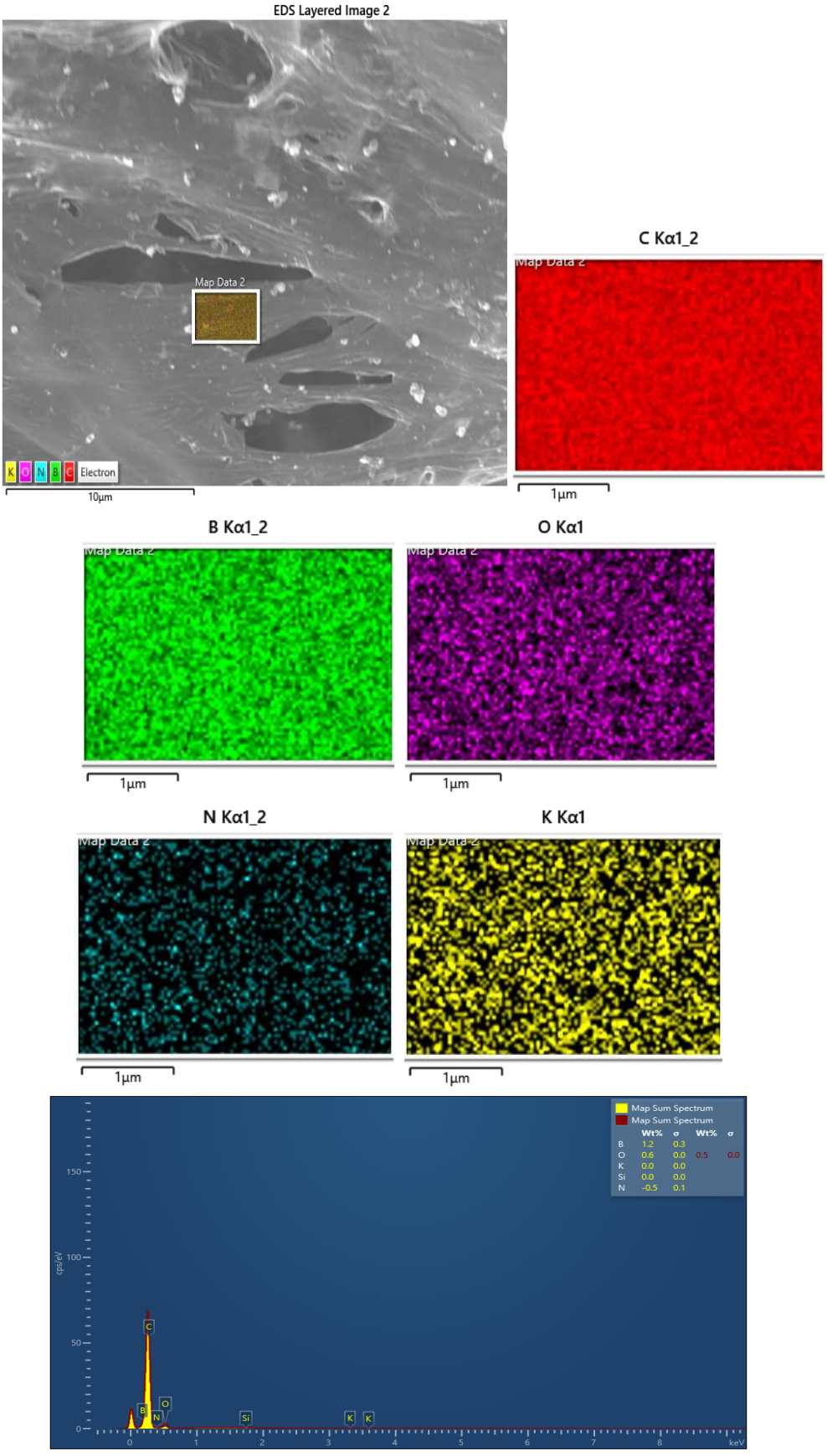


Figure 6-7 SEM/EDS analysis of sample PUB800-424

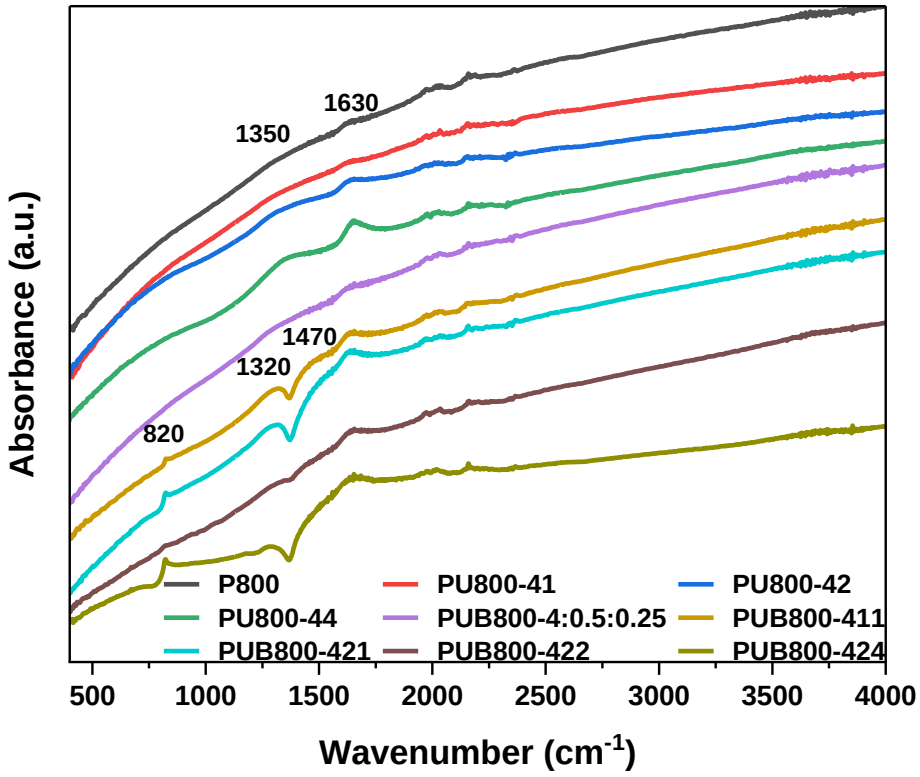


Figure 6-8 FTIR of PUB-samples

There are various possible ways of reacting the boric acid in a mixture of boric acid, urea, and potassium hydrogen phthalate, which will be discussed below:

I. The temperature of the thermal decomposition of the pure precursors in this study is in the following order: urea[23] < boric acid < potassium hydrogen phthalate,[13] with decomposition temperatures of 133, 170.9, and 295°C, respectively. It has reported that heating a mixture of urea and boric acid can generate boron nitride.[24] Based on the decomposition temperatures of BA, urea and KHP, we can hypothesise that there was a reaction between BA and urea, likely forming B–N bonds as the precursors decomposed.

II. On the other hand, the first report on the synthesis of boron nitride was by Balmain, who used molten boric acid and potassium cynide.[25] As potassium cyanide is produced during the carbonisation of the KHP/urea mixture, we can hypothesise that there was a reaction between the produced KCN and the molten boric acid and a bond formation between the B–N of boron nitride.

III. |Potassium borates are usually prepared from boric acid and potassium hydroxide or potassium carbonate.[26] Therefore, we can hypothesise that there was a reaction between the potassium carbonate that was produced during the decomposition of the KHP and the boric acid to produce potassium borates.

Looking at the results, the low concentration of boron in the elemental analysis obtained using EDS possibly confirms the first and second ways of forming boron nitride, while the high reduction in the surface area with the increase in amount of BA suggests that the reaction of the boric acid with the potassium in the potassium hydrogen phthalate can produce any form of the potassium borates. As such the potassium will be hindered and thus reduce the effect of the N:K ratio, which is responsible for the high surface area of the PU-samples. The potassium borates are thermally stable at high temperatures, so it is expected that they will remain at 800°C[27] and be removed in the washing step as they easily dissolve in water. The high thermal stability of the potassium borates at our carbonisation temperature is another probable confirmation of its existence, which would be consistent with the decrease in the surface area and, on the other hand, due to the increase in the N% compared to the same samples without

adding BA (see Table 6-2). In this case, the nitrogen is protected by preventing the formation of KCN or KCNO at 800°C. In case the latter is what happened, that would mean adding BA to potassium activation mixtures of N-containing precursors will keep the formation of hazardous salt, KCN, at low levels or even at zero. It was proposed by L'Hermitte[23] that the condensation of BN started at temperatures higher than 800°C during the carbonisation of a mixture of urea, boric acid and melamine. Their findings suggest that the current mixture could be unlikely to condense a considerable amount of BN, especially if it were heated only to 800°C. This is just in case there was a direct reaction between these two components.

Li and co-workers mixed biomass as a carbon source in a solution of urea and boric acid and heated it at 800°C. Finally, they activated it using potassium hydroxide at 800°C. They found that the carbon that was pre-treated with BA and urea had a slightly higher amount of nitrogen than that pre-treated with urea alone. They also found remains of the boric acid in the filtrate, which was due to B_2O_3.[16] We can conclude from their findings that all or part of the boric acid in the PUB-samples might be still unreacted; it just decomposed into B_2O_3.

Whatever the role of boric acid in our synthesis procedures, a separate systematic study of the possible reactions during carbonisation PUB samples will be needed. In particular, there is a lack of such studies on potassium activation of N-, B- and C-based precursors.

3.2. CO_2 uptake

The CO_2 uptake measurements were carried out from zero to 20 bar at room temperature. The results are presented in Table 6-4. The gravimetric CO_2 uptake capacity at room temperature was dependent on the surface area

and porosity of the samples. As the surface area increased, the uptake at 20 bar increased. The highest gravimetric uptake at 20 bar was 14.7 mmol/g for sample PUB800-411. As is known, the uptake at low pressures is controlled mainly by pores with a size around 5 Å.[28] From the PSD in Figure 6-4, Figure 6-10 and Figure 6-11 CO2 uptake at room temperature

Table 6-4, the uptake at 0.15 and 1 bar increased as the proportion of pores of sizes 5–7 Å increased, and vice versa. As the pores in the range 5–7 Å decreased with amount of BA increased, the BA had a similar effect of the CO_2 uptake. These results were consistent with those obtained by Sathish,[29] who found that the increase in amounts of boron and nitrogen precursors during the synthesis of BCN decreased the surface area and thus the CO_2 uptake capacity.

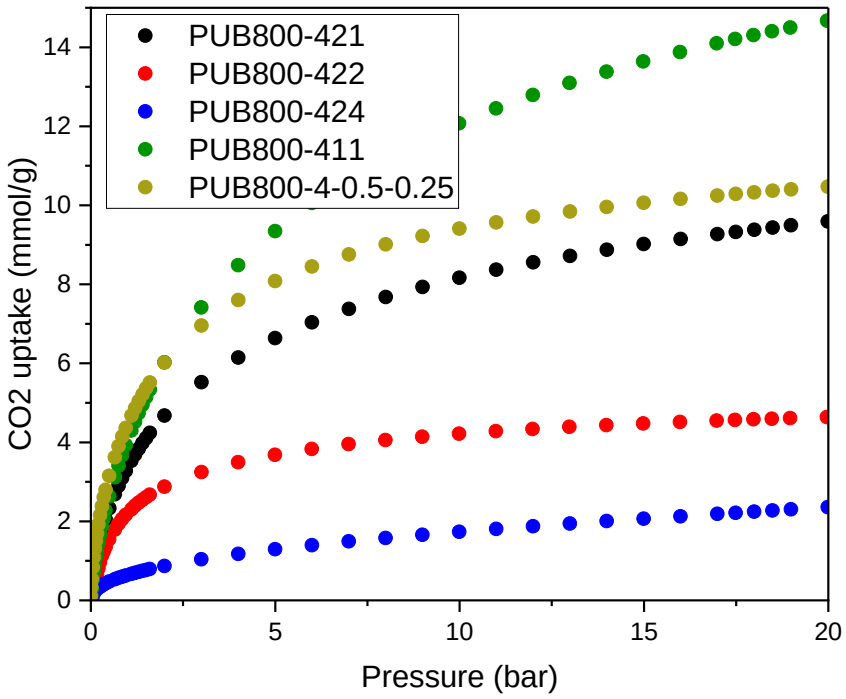


Figure 6-9 CO_2 uptake at room temperature up to 20 bar

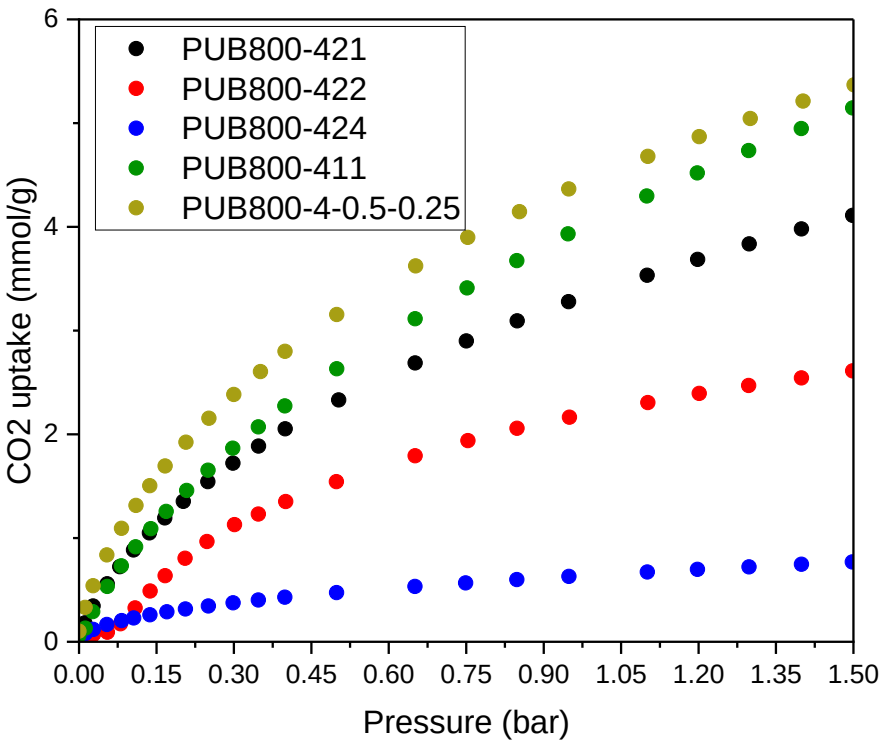


Figure 6-10 CO_2 uptake at room temperature at atmospheric pressure

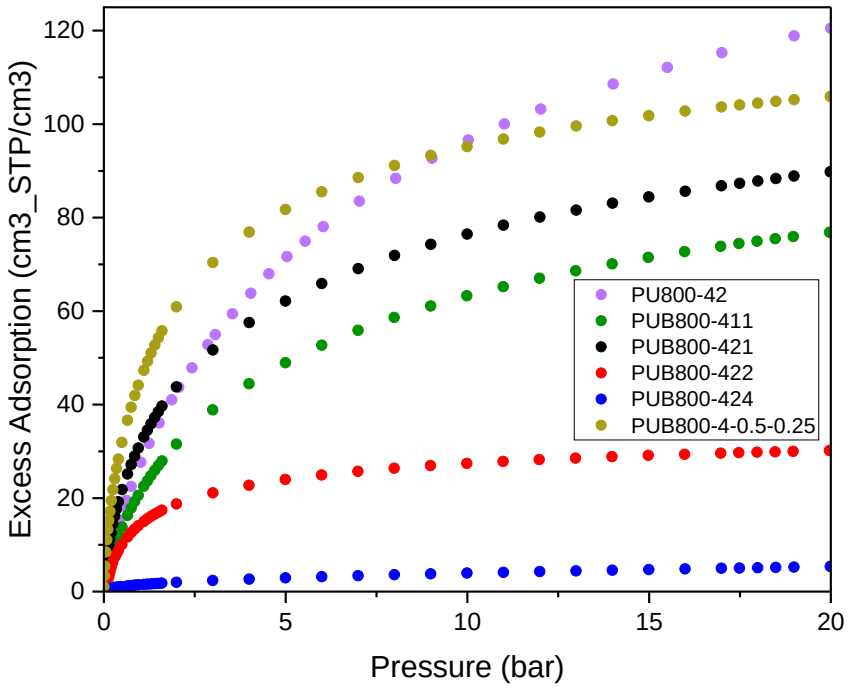


Figure 6-11 CO_2 uptake at room temperature

Table 6-4 Gravimetric and volumetric CO_2 Uptake at 25°C

Sample	CO_2 uptake (mmol/g) at 25°C			CO_2 uptake (cm^3_{STP}/cm^3) at 25°C			$\rho d_{exp.}$ [c]
	0.15 bar	1 bar	20 bar	0.15 bar	1 bar	20 bar	(g/cm^3)
P800	1.0	3.9	10.4				**0.43**
PU800	0.7	2.7	11.0				**0.37**
PU800-42	0.8	3.9	16.8				**0.38**
PU800-41	0.7	3.7	16.6				**0.45**
PU800-4.05							**0.42**
PUB800-4:2:4	0.3	0.6	2.4	0.6	2	5	**0.10**
PUB800-4:2:2	0.6	2.1	4.6	3	15	30	**0.29**
PUB800-4:2:1	1.1	3.5	9.6	10	33	90	**0.42**
PUB800-4:1:1	1.2	4	14.7	6	23	77	**0.24**
PUB800-4:0.5:0.25	1.5	4.4	10.5	15	44	106	**0.46**

[a] packing density of carbons obtained experimentally by compressing ca. 0.4 g of carbon for 5 minutes at 1 tonne loads in a 1.3 cm-diameter die. Then, three sample height measurements were averaged to determine sample volumes. Finally, the packing density was experimentally determined by dividing the measured sample mass by the sample volume.

For samples PUB800-421 and PUB800-4:0.5:0.25, where the ratio of urea to BA was 1:0.5, there were no high variations in the CO_2 uptake. However, in the volumetric uptake, and due to the fact that the packing densities were higher for PUB800-4:0.5:0.25, it showed a higher volumetric uptake than PUB800-421. In the samples with the same urea and KHP amounts, adding BA decreased the packing density (see Table 6-4) and decreased the porosity (as shown above); thus, the volumetric uptake was still in the same order. Briefly, the volumetric uptake was affected by the combination of the overall porosity and the packing density, which are mainly affected by adding BA.

The CO_2 uptake of the samples in this work was comparable to that of various BN, CN, or BCN and N-doped carbon adsorbents as listed in Table 6-5. The results showed that the high uptake capacity of the PUB800-4:0.5:0.25 at 1 bar

and room temperature were comparable to those of previously reported of activated carbons, boron nitride, or the B and N co-doped carbon adsorbent.

Table 6-5 CO_2 uptake (mmol/g) compared to other carbons at room temperature (25 °C), ** (0 °C)*

Sample	CO_2 uptake at 1bar	CO_2 uptake at 20 bar	Ref.	
P800	3.88	10.37	Ch.5	*
PU800	2.68	10.95	Ch.5	*
PU900	2.54	10.37	Ch.5	*
PU0.5600	3.33	10.37	Ch.5	*
PU0.5700	4.08	13.81	Ch.5	*
PU0.5800	3.85	16.77	Ch.5	*
PU0.5900	3.48	17.2	Ch.5	*
PU0.25600	3.41	9.18	Ch.5	*
PU0.25700	4.12	12.93	Ch.5	*
PU0.25800	3.74	16.61	Ch.5	*
PU0.25900	3.51	16.01	Ch.5	*
PUB800-4:2:4	0.63	2.4		*
PUB800-4:2:2	2.1	4.6		*
PUB800-4:2:1	3.5	9.6		*
PUB800-4:1:1	4	14.7		*
PUB800-4:0.5:0.25	4.4	10.5		*
H250–800	3.7	-	[30]	*
AS-2-600	4.8	-	[31]	*
Pine sawdust	4.2	-	[32]	*
LHPC-700	4.8	-	[33]	*
ACDS-800-4	4.36	-	[34]	*
G850-5	4.5	-	[35]	*
SD6800	4.4	12.6	[36]	*
ACGR2700	4.9	12.7	[37]	*
ACCA2800	3.7	17.5	[37]	*
CZ13XFAET	2.5	18.6	[38]	*
CZ13XFAETP	2.6	22.0	[38]	*
PC-poly(vinylidene chloride)-based carbon	3.97	10.56	[39]	*
Porous BN	1.68	8.3	[40]	*
BCN	3.74 5.36	-	[41]	* **
BNHC-2	~5.5 ~7.5	-	[12]	* **
BN-1100	~0.7 ~3.8	-	[42]	* **
BN-900	~0.55 ~2.8	-	[42]	* **
BN pellets	2.26 3.58	-	[43]	* **

4. Conclusion

In this work, the direct carbonisation of a mixture of potassium hydrogen phthalate, urea and boric acid was examined to prepare porous B/N co-doped carbons. The procedures involved grinding the dry precursors together, followed by a carbonisation under nitrogen. As the boric acid ratio increased, the nitrogen content increased in the samples up to ca. 20%. The presence of boron was revealed using the EDS analysis, and a confirmation of its status might be confirmed by the new peak in the FTIR at ca. 820 cm^{-1} of B-N-B. However, because the role of BA in the potassium activation of the N-containing carbon mixture requires further investigation, the boron status in the samples remains unknown.

The produced carbons in this study showed lower porosity compared to the carbons obtained in the absence of BA. As the ratio of BA increased, the surface area decreased. However, the sample with the lowest BA ratio, PUB800-4:0.5:0.25, showed an enhancement in the packing density compared to the same sample without BA, PU800-4:0.5. The experimental packing density increased from 0.42 to 0.46 cm^3/g of PUB800-4:0.5:0.25, which showed CO_2 uptake at 1 bar ca. 4.4 mmol/g. In the sample with the highest ratio of boric acid in the carbonisation mixture, PUB800-424, the porosity transformed towards large mesoporosity.

5. References

1. R. Bahadur, G. Singh, Y. Bando and A. Vinu, *Carbon*, 2022, **190**, 142-169.

2. A. Yamuna, A. Mandalam, A. Karthigaiselvi, M. Balasubramanian, B. Thiruparasakthi, S. Ravichandran and S. Mayavan, *RSC Advances*, 2015, **5**, 69394-69399.
3. D. Chen, Y. Huang, X. Hu, R. Li, Y. Qian and D. Li, *Materials*, 2018, **11**, 209.
4. J. Zhou, N. Li, F. Gao, Y. Zhao, L. Hou and Z. Xu, *Scientific Reports*, 2014, **4**, 6083.
5. S. Dou, X. Huang, Z. Ma, J. Wu and S. Wang, *Nanotechnology*, 2015, **26**, 045402.
6. K. Raidongia, A. Nag, K. P. S. S. Hembram, U. V. Waghmare, R. Datta and C. N. R. Rao, *Chemistry – A European Journal*, 2010, **16**, 149-157.
7. J. Wang, J. Hao, D. Liu, S. Qin, C. Chen, C. Yang, Y. Liu, T. Yang, Y. Fan, Y. Chen and W. Lei, *Nanoscale*, 2017, **9**, 9787-9791.
8. D. Peng, W. Jiang, F.-F. Li, L. Zhang, R.-P. Liang and J.-D. Qiu, *ACS Sustainable Chemistry & Engineering*, 2018, **6**, 11685-11694.
9. L. Chen and X. Wang, *Chemical Communications*, 2017, **53**, 11988-11991.
10. L. Wei, M. Sevilla, A. B. Fuertes, R. Mokaya and G. Yushin, *Advanced Functional Materials*, 2012, **22**, 827-834.
11. M. Sevilla, G. A. Ferrero, N. Diez and A. B. Fuertes, *Carbon*, 2018, **131**, 193-200.
12. J. Li, W. Zhang and A. Bao, *Industrial & Engineering Chemistry Research*, 2021, **60**, 2710-2718.
13. B. Adeniran, E. Masika and R. Mokaya, *Journal of Materials Chemistry A*, 2014, **2**, 14696-14710.
14. J. E. Eichler, J. N. Burrow, Y. Wang, D. C. Calabro and C. B. Mullins, *Carbon*, 2022, **186**, 711-723.
15. C. Akmil-Başar, E. Köseoğlu and Y. Önal, *Particulate Science and Technology*, 2016, **34**, 526-532.
16. D. Li, Y. Huang, C. Yu, Y. Lu, C. Tang and J. Lin, *Diamond and Related Materials*, 2022, **130**, 109432.
17. M. Hubáček, T. Sato and T. Ishii, *Journal of Solid State Chemistry*, 1994, **109**, 384-390.
18. M. Mirzaee, A. Rashidi, A. Zolriasatein and M. Rezaei Abadchi, *Ceramics International*, 2021, **47**, 5977-5984.
19. M. Mirzaee, A. Rashidi, A. Zolriasatein and M. Rezaei Abadchi, *Diamond and Related Materials*, 2021, **115**, 108350.
20. S. Wang, J. Feng, Q. Meng, B. Cao and G. Tian, *Journal of Solid State Electrochemistry*, 2019, **23**, 2377-2390.

21. X. Xu, T. Yuan, Y. Zhou, Y. Li, J. Lu, X. Tian, D. Wang and J. Wang, *International Journal of Hydrogen Energy*, 2014, **39**, 16043-16052.
22. J. Wang, Z. Liu, S. Li, C. Li, S. Liu, J. Feng and R. Tan, *Green Chemical Engineering*, 2021, **2**, 239-249.
23. A. L'Hermitte, D. M. Dawson, P. Ferrer, K. Roy, G. Held, T. Tian, S. E. Ashbrook and C. Petit, *The Journal of Physical Chemistry C*, 2021, **125**, 27429-27439.
24. S. Marchesini, A. Regoutz, D. Payne and C. Petit, *Microporous and Mesoporous Materials*, 2017, **243**, 154-163.
25. W. H. Balmain, *The London, Edinburgh, and Dublin Philosophical Magazine and Journal of Science*, 1842, **21**, 270-277.
26. M. O. Asensio, M. Yildirim, F. T. Senberber, A. S. Kipcak and E. M. Derun, *Research on Chemical Intermediates*, 2016, **42**, 4859-4878.
27. Ö. Şahin, E. S. Cennetkusu, H. Dolaş and M. Özdemir, *Thermochimica Acta*, 2006, **440**, 7-12.
28. V. Presser, J. McDonough, S.-H. Yeon and Y. Gogotsi, *Energy & Environmental Science*, 2011, **4**, 3059-3066.
29. C. Sathish, G. Kothandam, P. Selvarajan, Z. Lei, J. Lee, J. Qu, A. a. H. Al-Muhtaseb, X. Yu, M. B. H. Breese, R. Zheng, J. Yi and A. Vinu, *Advanced Science*, 2022, **9**, 2105603.
30. G. K. Parshetti, S. Chowdhury and R. Balasubramanian, *Fuel*, 2015, **148**, 246-254.
31. M. Sevilla and A. B. Fuertes, *Energy & Environmental Science*, 2011, **4**, 1765-1771.
32. C. Quan, R. Su and N. Gao, *International Journal of Energy Research*, 2020, **44**, 4335-4351.
33. M. Demir, T.-D. Tessema, A. A. Farghaly, E. Nyankson, S. K. Saraswat, B. Aksoy, T. Islamoglu, M. M. Collinson, H. M. El-Kaderi and R. B. Gupta, *International Journal of Energy Research*, 2018, **42**, 2686-2700.
34. J. Li, B. Michalkiewicz, J. Min, C. Ma, X. Chen, J. Gong, E. Mijowska and T. Tang, *Chemical Engineering Journal*, 2019, **360**, 250-259.
35. M. Sevilla, A. S. M. Al-Jumialy, A. B. Fuertes and R. Mokaya, *ACS Applied Materials & Interfaces*, 2018, **10**, 1623-1633.
36. A. M. Aljumialy and R. Mokaya, *Materials Advances*, 2020, **1**, 3267-3280.
37. H. M. Coromina, D. A. Walsh and R. Mokaya, *Journal of Materials Chemistry A*, 2016, **4**, 280-289.

38. N. Balahmar, A. M. Lowbridge and R. Mokaya, *Journal of Materials Chemistry A*, 2016, **4**, 14254–14266.
39. J. Cai, J. Qi, C. Yang and X. Zhao, *ACS Applied Materials & Interfaces*, 2014, **6**, 3703-3711.
40. S. Marchesini, C. M. McGilvery, J. Bailey and C. Petit, *ACS Nano*, 2017, **11**, 10003-10011.
41. S. Chen, P. Li, S. Xu, X. Pan, Q. Fu and X. Bao, *Journal of Materials Chemistry A*, 2018, **6**, 1832-1839.
42. Y. Li, L. Liu, H. Yu, Y. Zhao, J. Dai, Y. Zhong, Z. Pan and H. Yu, *Science of The Total Environment*, 2021, DOI: https://doi.org/10.1016/j.scitotenv.2021.151384, 151384.
43. J. Gou, C. Liu, J. Lin, C. Yu, Y. Fang, Z. Liu, Z. Guo, C. Tang and Y. Huang, *Ceramics International*, 2022, **48**, 11636-11643.

Chapter 7 Conclusion

This thesis studied the synthesis of porous carbons in different aspects, then applied them for CO_2 and CH_4 uptake applications.

A. Template removal (zeolite 13X) via reaction of the carbon/zeolite composite with KOH showed a promising approach for avoiding the use of harsh acids (concentrated HCl and HF). All three temperatures examined in this thesis for the reaction between the KOH and the composites (600, 700, and 800 °C) led to the destruction of a large number of large micropores. The average reduction in the total surface area was 1451 m^2/g, which is nearly half the surface area of the pristine ZTC. That affected the maximum methane uptake capacity of these ZTCs compared to the pristine ZTC sample. Consequently, even if this treatment was successfully offered, which seems like a greener template removal approach, it had negative influences on the resultant porosity and yield. Another study could be built up on the same samples to investigate hydrogen storage uptake. This may provide more knowledge about the effect of the template removal method examined here on their microporosities.
B. The investigation revealed that the porosity of the activated samples derived from ginkgo leaves was influenced by the chemical composition of the starting precursor (char), despite the carbonisation methods employed to generate the char. The activated carbon produced by KOH, starting from the hydrochar of the ginkgo leaves, showed a very high surface area when the hydrochar was prepared at 300 °C. The highest surface of the activated sample from this hydrochar at 800 °C and the weight ratio 4 of KOH were

nearly 3300 m^2/g and 1.65 cm^3/g total pore volume, compared to 2500 m^2/g and 1.47 cm^3/g for that one from the hydrochar prepared at 250 °C. The sample with the highest surface area was accompanied by high CO_2 uptake at 20 bar and room temperature, reaching 23 mmol/g. The change in the hydrothermal carbonisation temperature led to a change in the chemical composition of the hydrochar and, thereby, in the porosities of the activated carbons produced from the hydrochar. Similarly, the activation of the air-carbonised leaves using potassium oxalate lowered meso/microporosity compared to the direct activation of the leaves, which affected their CO_2 uptake capacities. The capacities were 4.6 vs. 4.0 mmol/g at 1 bar and 14.4 vs. 15.5 mmol/g at 20 bar for AcGLF-2ox-800 vs. AcGL-2ox-800-D. This findings showed the importance of the pre-treatment of the leaves (e.g., adopting carbonisation step or directly activating the raw precursor) on the textural properties of the activation using PO. The air-carbonisation led to a decrease in O/C and N/C ratios compared to the raw leaves, which decreased the uptake at 1 bar in the direct activated. And vice versa, the uptake at 20 bar increased in the direct activated due to the higher meso/microporosity ratio. A comparison between the activation of HCl-washed and unwashed air-carbonised leaves using KOH and PO revealed that the presence of inorganic content in the carbon precursor led to a minor widening of the pore sizes in activated carbon.

Future research as well would be recommended to investigate the effects of N/C, O/C, and H/C ratios of different precursors on the textural properties of the PO-activated carbons. This may provide more knowledge for a deeper understanding of the PO activation mechanism.

C. In-situ N-doping using urea for carbons starting from KHP by simple mechanical mixing has successfully produced N-doped carbons with enhanced porosities. The well-controlled amounts of the added urea and the carbonisation conditions helped to control the porosities in addition to the N-doping. The highest surface of the samples reached 2409 m^2/g with a total pore volume 1.2 cm^3/g. The highest nitrogen doping achieved was 22%, but with the lowest porosities at the highest amount of urea and lower carbonisation temperatures. On the other hand, adding a third component, which is boric acid, to the urea and KHP and carbonising it at 800 °C boosted the nitrogen doping against the porosity. As the added BA increased, the N-doping increased. The qualitative elemental analysis using EDX showed the presence of boron, which perhaps indicated boron-doping in addition to the N-doping. However, the reactions that occurred during carbonisation and affected doping or developing porosity remain unclear. In contrast with the N-doped carbons from urea/KHP, which were obviously controlled by N/C and N/K ratios. The CO_2 uptake on these synthesised samples from the carbonisation of KHP mixtures was governed mainly by the porosities, with a limited effect of the doping at low pressure. A further effort would be recommended in regards of investigation existence of the boron in the prepared doped carbons.